Analysis of Reaction Pathways on the Catalytic Conversion of CO_2 using Quantum Mechanical Calculations

by

Yohaselly Santiago Rodríguez

A dissertation submitted in partial fulfillment of the requirements for the degree of

DOCTOR OF PHILOSOPHY

in

CHEMICAL ENGINEERING

UNIVERSITY OF PUERTO RICO

MAYAGÜEZ CAMPUS

2015

Approved by:

_____   _____

María C. Curet Arana, Ph.D.   Date
President, Graduate Committee

_____   _____

Nelson Cardona Martínez, Ph.D.   Date
Member, Graduate Committee

_____   _____

Alberto Santana, Ph.D.   Date
Member, Graduate Committee

_____   _____

Oscar Marcelo Suárez, Ph.D.   Date
Member, Graduate Committee

_____   _____

Héctor Méndez Mella, Ph.D.   Date
Representative of Graduate Studies

_____   _____

Aldo Acevedo Rullán, Ph.D.   Date
Department Chair

Abstract

The greenhouse gas CO_2 is an inexpensive and abundant feedstock that may be used to produce valuable organic compounds. The main goal of this work was to unravel reaction pathways for CO_2 conversion through hydrogenation on heterogeneous catalysts and through the coupling reaction with ethylene oxide facilitated by homogeneous catalysts. The thermochemistry of several adsorption, decomposition, hydrogenation and oxidation reactions on Au(111) was thoroughly analyzed with density functional theory (DFT). Our results indicate that the production of formic acid, formaldehyde and methanol on Au(111) is not thermodynamically favorable. Cu(111) surfaces doped with Ni, Pd, Ti, Mg, Ga and Al were screened using different descriptors. A systematic study of the thermochemistry for elementary steps in the synthesis of formic acid, formaldehyde and methanol from CO_2 and CO were developed to evaluate the performance of Ga/Cu(111), Mg/Cu(111) and Ti/Cu(111) compared to Cu(111). Our results suggest that Ga/Cu(111) and Mg/Cu(111) might be promising catalysts for CO_2 and CO hydrogenation. Each of the doped Cu surfaces exhibited different reaction mechanisms for the synthesis of the desired products. Methanol was predicted to be selectively produced from CO_2 on Ga/Cu(111) and Mg/Cu(111). DFT methods were also used to analyze metal-salen catalysts in the coupling of CO_2 with ethylene oxide. The effect of several metal centers and axial ligands on the reaction energies for the formation of relevant intermediates was investigated. The UOPBE/LANL2DZ and B3LYP/6-311g**/LANL2DZ methods were compared. There were significant differences on the reaction energies estimated with both methods, but they generated similar geometries for the intermediates. The best description of the reaction system was obtained with UOPBE/LANL2DZ. Calculations with

dichloromethane as the solvent were performed. The reaction energies for the CO_2-epoxide-salen complexes were lower with 4-dimethylaminopyridine (DMAP) as axial ligand than with Cl. The DMAP complexes with Al and Cr were the most stable intermediates with UOPBE/LANL2DZ. Furthermore, CO_2 could be activated by DMAP forming a stable CO_2-DMAP complex.

Resumen

El gas de invernadero CO_2 es una materia prima económica y abundante que puede producir compuestos orgánicos de alto valor. La meta principal de este trabajo fue entender los mecanismos de reacción para la conversión de CO_2 mediante hidrogenación sobre catalizadores heterogéneos, y mediante la reacción de acoplamiento con óxido de etileno facilitada por catalizadores homogéneos. La termoquímica de varias reacciones de adsorción, descomposición, hidrogenación y oxidación en Au(111) fueron sistemáticamente analizadas usando la teoría del funcional de densidad (DFT, por sus siglas en inglés). Nuestros resultados indican que la producción de ácido fórmico, formaldehído y metanol sobre Au(111) no es termodinámicamente favorable. Superficies de Cu(111) dopadas con Ni, Pd, Ti, Mg, Ga y Al fueron analizadas usando diferentes descriptores. Un estudio sistemático de la termoquímica para pasos elementales durante la síntesis de ácido fórmico, formaldehído y metanol partiendo de CO_2 y CO fue desarrollado para evaluar el desempeño de Ga/Cu(111), Mg/Cu(111) y Ti/Cu(111) comparadas con Cu(111). Nuestros resultados sugieren que Ga/Cu(111) y Mg/Cu(111) pueden ser catalizadores prometedores para la hidrogenación de CO_2 y CO. Cada una de las superficies de Cu dopadas exhibió distintos mecanismos de reacción para la síntesis de los productos deseados. Estos resultados predicen que metanol será selectivamente producido a partir de CO_2 en Ga/Cu(111) y Mg/Cu(111). Métodos de DFT fueron también usados para analizar catalizadores de salenos metálicos durante la reacción de CO_2 con óxido de etileno. El efecto de varios centros metálicos y ligandos axiales sobre las energías de reacción para la formación de intermediarios relevantes fue investigado. Los métodos UOPBE/LANL2DZ y B3LYP/6-

311g**/LANL2DZ fueron comparados. Hubo diferencias significativas en las energías de reacción estimadas con ambos métodos, pero ellos generaron geometrías similares para los intermediarios. La mejor descripción del sistema de reacción fue obtenida con UOPBE/LANL2DZ. Cálculos con diclorometano como disolvente fueron realizados. Las energías de reacción para los complejos de CO_2-epóxido-salen fueron más bajas con 4-dimetilaminopiridina (DMAP) como ligando axial que con Cl. Los complejos de DMAP con Al y Cr fueron los intermediarios más estables con el método UOPBE/LANL2DZ. Además, CO_2 podría ser activado por DMAP formando un complejo estable de CO_2-DMAP.

The material included in the chapter 4 of this dissertation is a reprint of an article published on the journal Surface Science. The copyright of this material holds to Elsevier. Permission to reprint this material in this thesis was requested and granted by Elsevier: Reprinted from Surface Science, 627, Y. Santiago-Rodríguez, J.A. Herron, M.C. Curet-Arana, M. Mavrikakis, Atomic and molecular adsorption on Au(111), 13, Copyright (2014), with permission from Elsevier. This article is available online at http://dx.doi.org/10.1016/j.susc.2014.04.012.

The material included in the chapter 6 of this dissertation is a reprint of an article published on the journal Reaction Kinetics, Mechanisms and Catalysis. The copyright of this material holds to Springer Science and Business Media. Permission to reprint this material in this thesis was requested and granted by Springer and Business Media: Reaction Kinetics, Mechanisms and Catalysis, 116, 2015, 351, "Quantum mechanical study of the reaction of CO_2 and ethylene oxide catalyzed by metal–salen complexes: effect of the metal center and the axial ligand", Y. Santiago-Rodríguez and M. C. Curet-Arana, 9, Copyright © 2015, Akadémiai Kiadó, Budapest, Hungary) is given to the publication in which the material was originally published, by adding; with kind permission from Springer Science and Business Media. This article is available online at DOI: 10.1007/s11144-015-0904-6.

To my loving husband, Danny, who motivated me to make this possible. He is the person that has always been with me no matter what, with his unconditional love and support in happiness and sadness. He encourages me to do things that I sometimes think are impossible to do, because he has more faith in me than myself. He has always believed in me and that is why I love him and I dedicate this work to him.

To the memory of my sister, Nohelys. Some people dedicate to their loved ones a song or a poem. But, I want to dedicate this work to her, because science is what I do best.

Acknowledgements

I want to thank:

My loving husband Daniel Rivera Vázquez.

My loving family: my parents Nancy Rodríguez and Noel Santiago; my grandparents Acidalia and Roberto; my uncles Ivette and David; my niece "Kikin" and my nephews "Junior" and "Naldy", my parents-in-law Iris and Félix; Denisse, Félix and Leonel, who I love like sister and brothers; Edith and Félix. Thanks for your support and love.

My research partner and friend Paul Meza Morales for his support.

My mentor Dr. María C. Curet-Arana for her guidance and support during the whole process of accomplishing my Ph.D. degree. My thesis committee: Dr. Alberto Santana, Dr. Oscar Marcelo Suárez and Dr. Nelson Cardona for their constructive recommendations to improve my work.

Dr. Jeffrey Herron, Dr. Manos Mavrikakis, Dr. Guangfu Luo, Dr. Dane Morgan and Dr. Izabela Szlufarska for the VASP training and the use of their computational facilities.

The undergraduate students Rafael Soler and Erick Barreto.

Dr. Yomaira Pagán for her feedback on my research work.

Liliana Gamez and Dr. María Martínez for their training in visualization tools.

Wi(PR)$_2$EM and EPSCoR programs and the Alfred P. Sloan foundation for their financial support and providing me opportunities to grow as a researcher and professional.

NERSC Center and Office of Science of the U.S. DOE and IFN-High Performance Computing Facility for their computing resources.

Table of Contents

List of Tables

List of Figures

List of Appendices

Chapter 1: Introduction

1.1   Motivation

Statistical data collected by the National Oceanic & Atmospheric Administration Earth System Research Laboratory indicate that the atmospheric concentration of CO_2 has continuously increased in the last 55 years, as shown in Fig. 1.1 [1]. The constant emissions of this greenhouse gas and others into the atmosphere have caused global warming and climate changes that negatively impact the planet. In 2012, the annual greenhouse gas emissions were quantified, and the major CO_2 emissions were generated by the fossil fuels combustion for electricity and heat generation for industry, residential and commercial services, and transportation [2]. In fact, 31,780.361 million metric tons of CO_2 were emitted by worldwide energy consumption in 2010 [3].
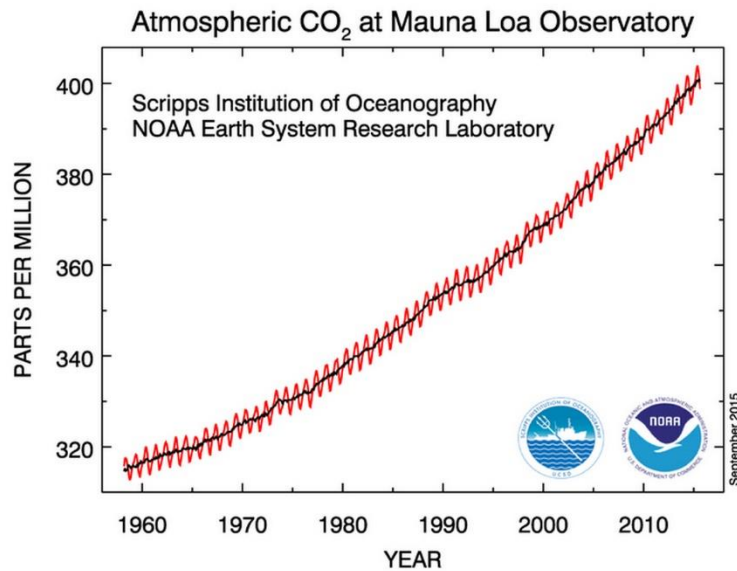
Fig. 1.1. Annual mean concentrations of atmospheric CO_2 measured at Mauna Loa Observatory, Hawaii [1].

Furthermore, the high demand for energy has also triggered fossil fuels depletion, which are currently the main carbon source in the chemical industry. The consumption of

coal, liquid fuels and natural gas has continuously increased during the last 45 years [4]. Projections made with data collected from U.S. Energy Information Administration and British Petroleum, as illustrated in Figure 1.2, predict that these increasing trends on fossil fuels consumption will prevail until 2030 [4]. Moreover, projections based on the World Energy Outlook 2007 predict that, still in 2030, around 84% of the energy will come from fossil fuels [4].
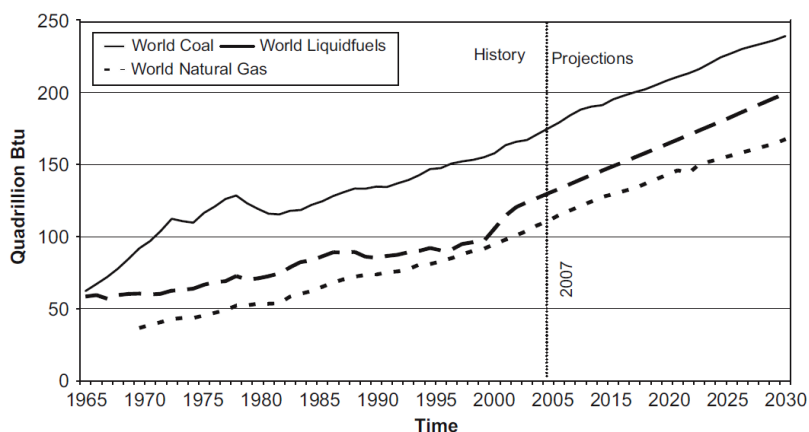
Fig. 1.2. Worldwide consumption of fossil fuels from 1965 to 2030. Data collected from EIA and BP [4].

Because of environmental concerns and the need of alternative sources of fuels and chemicals, efforts have been put forth to reduce CO_2 emissions from industries. Large amounts of fossil fuels are consumed and of CO_2 are emitted through many processes, such as fermentation and combustion reactions, among others. Currently, CO_2 is mainly used as a chemical commodity for meat freezing or a component of carbonated beverages. But, our consumption of fossil fuels, and the generation of CO_2, is too large for carbon-capture technology to manage by itself. Therefore, efficient catalysts still have to be developed, that not only sequester CO_2, but also convert it into valuable organic compounds, such as alcohols (e.g., methanol), carbonate esters (e.g., cyclic carbonates), among others, which in turn can be used as energy sources, chemical substances or

2

feedstocks to produce other materials and chemical compounds (see Figure 1.3). This process has two main advantages: (1) added-value compounds can be produced by using an inexpensive and abundant raw material, and (2) this process could be implemented as a cycle, where CO_2 is generated and re-used.
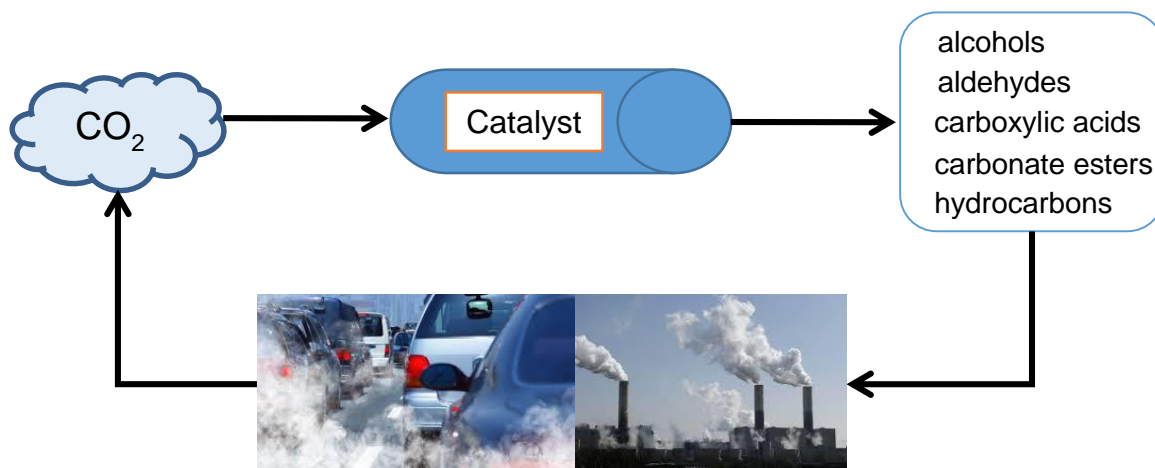
Fig. 1.3. Production of valuable compounds through the catalytic hydrogenation of CO_2/CO.

In this project, homogeneous and heterogeneous catalysts were studied to evaluate their catalytic performance in CO_2 conversion. The high thermodynamic stability of CO_2 imposes a challenge for its conversion. In fact, CO_2 is not extensively used as a chemical feedstock, and its use is limited to a few industrial processes, such as in the synthesis of urea and its derivatives, salicylic acid, and carbonates [5]. Because of this challenge, computational simulations were used for screening plausible catalysts to be employed in CO_2 conversion, reducing the time it usually takes to discover such materials, the operational costs and wastes generated by the trial and error experiments. Furthermore, these computational tools provided insights into the thermochemistry of the surface reactions occurring on the analyzed catalysts to study reaction intermediates that cannot

be experimentally detected and postulate possible reaction mechanisms, which have not been fully clarified.

1.2   Outline of Research Work

This thesis contains our investigation accomplished for the quantum mechanical study of the conversion of CO_2 into value-added compounds using homogeneous and heterogeneous catalysts. In the second chapter, a compendium of the literature revision and theoretical background relevant to our research work is presented. The third chapter summarizes the global goals of this research project and the specific aims of the three case studies performed, for which their methodologies, results and conclusions are discussed in the subsequent chapters. In these studies, we theoretically analyzed three types of catalysts: a pure metal surface, metal-doped surfaces, and metal-salen complexes. The first two types of catalysts are heterogeneous and the last ones are homogeneous catalysts.

The first case study is: "*Atomic and Molecular Adsorption on Au(111)*" and corresponds to chapter 4, which has been reprinted from Y. Santiago-Rodríguez, J.A. Herron, M.C. Curet-Arana, M. Mavrikakis, Surf. Sci. 627 (2014) 57-69: http://dx.doi.org/10.1016/j.susc.2014.04.012. In this study, periodic self-consistent density functional theory (DFT-GGA) calculations were used to analyze the adsorption of several atomic species, molecular species and molecular fragments on the Au(111) surface with a coverage of ¼ ML. Binding geometries, binding energies, and diffusion barriers were calculated for 27 species. Furthermore, we calculated the surface deformation energy associated with the binding events. The intramolecular and adsorbate-surface vibrational frequencies were calculated for all the adsorbates on their

4

most energetically stable adsorption site. The energies of the adsorbed species were used to calculate the thermochemical potential energy surfaces for decomposition of CO, NO, N_2, NH_3 and CH_4, oxidation of CO, and hydrogenation of CO, CO_2 and NO, giving insight into the thermochemistry of these reactions on gold nanoparticles.

The second case study in chapter 5 is: "*Quantum Mechanical Study of CO₂ and CO Hydrogenation on Metal-Doped Cu(111) Surfaces*". In this study, DFT methods were used to analyze metal-doped Cu(111) surfaces to identify novel surface alloys that catalyze selectively the hydrogenation of CO_2. The adsorption of relevant species, such as: H, O, CO and CO_2, HCO, HCOO, HCOOH, CH_2O, CH_3OH, H_2O, among others, were studied on Cu(111) surfaces doped with Ga, Mg and Ti. Preferred adsorption sites, geometries and binding energies were determined for the species involved in CO_2 and CO hydrogenation. A systematic study of the thermochemistry of plausible surface reactions involved in the CO_2/CO hydrogenation was performed for the Ga, Mg and Ti-doped Cu(111) surfaces to postulate reaction mechanisms for the synthesis of formic acid, formaldehyde and methanol. The catalytic activity and selectivity of the metal-doped Cu surfaces were compared with the performance of the pure Cu(111) surface.

In chapter 6, the third case study of this research work: "*Quantum Mechanical Study of the Reaction of CO₂ and Ethylene Oxide Catalyzed by Metal-Salen Complexes: Effect of the Metal Center and the Axial Ligand*" is discussed and this is a reprint from Y. Santiago-Rodríguez and M.C. Curet-Arana, Reac. Kinet. Mech. Catal. 116 (2015) 351-370: DOI: 10.1007/s11144-015-0904-6. DFT calculations were used to evaluate the thermochemistry of plausible elementary steps for the reaction of CO_2 with ethylene oxide catalyzed by metal-salen complexes consisting of Co, Cr, Mn, Fe, Al and Zn. The effect

of the axial ligands on the energies of reaction was studied using chlorine and DMAP. This analysis was performed using UOPBE/LANL2DZ to screen the plausible reaction intermediates. The most favorable intermediates were then studied with B3LYP/6-311g**/LANL2DZ in gas phase and in dichloromethane to evaluate the method and solvent effect on their reaction energies and geometries. Electronic properties, such as the HOMO and LUMO surfaces, LUMO energies, hardness and electronegativity were also evaluated for all the metal-salen catalysts with Cl or DMAP. Energies of reaction were correlated with the hardness of the catalysts.

In chapter 7, we finished with the general conclusions of all results discussed in this document and some recommendations about which could be the next phase in this research project are included. The supplementary material for the chapters 5 and 6 can be found in the Appendices A and B, respectively.

References

[1]   US Department of Commerce, NOAA. Trends in Carbon Dioxide, http://www.esrl.noaa.gov/gmd/ccgg/trends/mlo.html (accessed Sep 26, 2015).
[2]   IEA-Publication: CO_2 Emissions from Fuel Combustion Highlights 2014, https://www.iea.org/publications/freepublications/publication/co2-emissions-from-fuel-combustion-highlights-2014.html (accessed Sep 26, 2015).
[3]   International Energy Statistics, http://www.eia.gov/cfapps/ipdbproject/iedindex3.cfm?tid=90&pid=44&aid=8&cid=ww,&syid=2000&eyid=2010&unit=MMTCD (accessed Sep 26, 2015).
[4]   S. Shafiee, E. Topal, When will fossil fuel reserves be diminished?, Energy Policy. 37 (2009) 181–189.
[5]   W. Wang, S. Wang, X. Ma, J. Gong, Recent advances in catalytic hydrogenation of carbon dioxide, Chem. Soc. Rev. 40 (2011) 3703–3727.

Chapter 2: Literature Revision

2.1 Description of Catalytic Systems

This section discusses two systems used for the conversion of CO_2: (a) the hydrogenation of CO_2; and (b) the coupling reaction of CO_2 with ethylene oxide, as depicted in Fig. 2.1. These catalytic processes used to transform CO_2 involve heterogeneous and homogeneous catalysts, respectively.
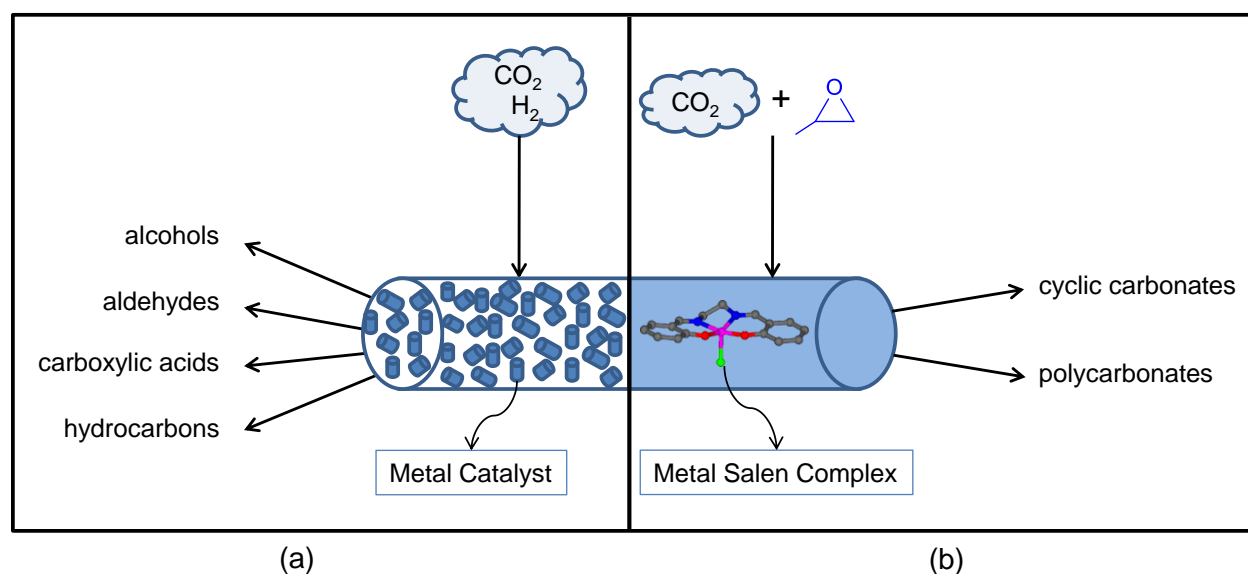
Fig. 2.1. Catalytic conversion of CO_2 via two reactions: (a) hydrogenation of CO_2 and (b) coupling of CO_2 with epoxide.

2.1.1 Heterogeneous catalysis: hydrogenation of CO_2 on metal surfaces

Many valuable chemicals, such as alcohols (e.g., methanol), carboxylic acids (e.g., formic acid) and aldehydes (e.g., formaldehyde) can be produced through the hydrogenation of CO_2 [1]. However, other side products, such as carbon monoxide and carbon could be also generated. These undesired products could poison the catalyst

surface, affect the selectivity or change the reaction pathway. The catalytic systems involved in the production of these value-added chemical compounds will be discussed in detail at the subsequent sections.

2.1.1.1 Methanol synthesis

Methanol is a commodity chemical, and its total global demand reached 59 million metric tons during 2013 and it was projected to continue increasing to arrive at 105 million metric tons in 2023 [2]. Moreover, methanol can be used as a fuel in direct methanol fuel cells, as a medium for the storage and transportation of hydrogen [3], and as a raw material for the production of fuel additives components (e.g., methyl tertiary-butyl ether or MTBE and transesterification of vegetable oils) or other valuable compounds [1].

Currently, methanol is produced via syngas using Cu/ZnO-based catalysts (e.g., Cu/ZnO/Al$_2$O$_3$) [3]. Because of the environmental issues caused by the high concentrations of CO_2 in the atmosphere, the methanol production from CO_2 through its hydrogenation is a potential alternative that are being evaluated by many scientists:

$$CO_2 + 3H_2 \leftrightarrow CH_3OH + H_2O \qquad \text{Reaction 2.1}$$

This reaction is exothermic with a standard reaction enthalpy of -49.8 kJ/mol [4]. Cu-based catalysts have been intensively analyzed for the methanol synthesis through this hydrogenation reaction [5], and the general composition of these catalysts is similar to the ones used in the production of methanol via syngas [6]. However, it has been demonstrated that pure Cu is not an efficient catalyst because it exhibits low activity for this reaction [7,8]. Consequently, the Zn atoms in ZnO play an important role in the reaction imparting catalytic properties to copper. Kanai and coworkers studied the

promotional effect of ZnO in physically-mixed Cu/SiO_2 and ZnO/SiO_2 catalysts, finding by using different characterization techniques that ZnO_x moieties were formed under strong reduction conditions and that they migrated to the surface of the Cu particles, which caused the formation of a surface Cu-Zn alloy [9]. A ZnO_x coverage on the surface of the reduced Cu nanoparticles were also identified by X-Ray photoelectron spectroscopy (XPS) on $Cu/ZnO/Al_2O_3$ [8]. The authors speculate that the migration of ZnO_x to the Cu surface is caused by a strong metal support interaction between Cu and ZnO, which might be related to the fact that the presence of ZnO increases the activity of Cu-based catalysts during the methanol synthesis. The hypothesis is that ZnO_x on the Cu surface stabilizes the Cu^+ sites, which are essential for the reaction progress [9]. The completely reduced state Cu^0 has also been proposed as an active site [9] and in a recent study, methanol was produced when the Cu cluster had a high concentration of Cu^0 sites [10]. The partially oxidized $Zn^{\delta+}$ state, which can be the result of either the strong metal support interaction among Cu and ZnO or of the adsorbate-induced oxidation of Zn in a Cu-Zn surface alloy, is also considered a vital species for a high catalytic activity [8].

Multicomponent catalysts have been developed to improve the performance of the copper catalyst for this reaction. Toyir *et al.* studied the production of methanol from CO_2 and H_2 using Cu/ZnO-based multicomponent catalysts ($Cu/ZnO/ZrO_2/Al_2O_3/SiO_2$) [11]. The main products obtained in this process were methanol, CO and water. The activity of the catalyst was proportional to the surface area of Cu and the highest selectivity obtained was 99.7% for methanol. In addition, catalysts based on other metals such as gold have been proposed as promising candidates for the catalytic hydrogenation of CO_2. Sakurai and Haruta [12], and Hartadi et al. [13] have demonstrated that Au/ZnO has similar

catalytic activity and selectivity to the ones obtained with Cu/ZnO in the methanol synthesis using the same metal loadings and preparation methods. A slightly higher formation rate of methanol by 7.9 x 10^{-7} mol $s^{-1}g_M^{-1}$ (M=Cu for the Cu/ZnO/Al$_2$O$_3$ catalyst and M=Au for the Au/ZnO catalyst) and lower selectivity for methanol by 19.2% were obtained with Cu/ZnO/Al$_2$O$_3$ at 220 °C and 5 bar, when compared to Au/ZnO [13].

2.1.1.2 Formic acid synthesis

Formic acid can be also produced through CO_2 hydrogenation:

$$CO_{2\,(g)} + H_{2\,(g)} \leftrightarrow HCOOH_{(l)} \hspace{4cm} \text{Reaction 2.2}$$

This reaction is exothermic with a standard reaction enthalpy of -32 kJ/mol, but it is not a spontaneous reaction with a standard Gibbs free energy of 33 kJ/mol [14]. Nevertheless, interest in the synthesis of formic acid from CO_2 has emerged as a possibility to convert CO_2 into liquid products that may be used as fuels and chemicals [1]. The synthesis of this product is being investigated because formic acid can be used in fuel cell applications as a hydrogen storage material, due to that the formic acid decomposition only produces H_2 and CO_2 [3]. Thus, if formic acid is used for this application, then the CO_2 by-product yielded in the H_2 generation could be used again as a raw material for the production of formic acid.

Usually, formic acid is produced from high-pressure CO through the carbonylation of methanol to methyl formate followed by the hydrolysis of this intermediate to formic acid and methanol [15]. On the other hand, formic acid can be produced by the hydrogenation of CO_2 in the presence of water, but this reaction requires high CO_2/H_2 pressures and still, high yield of formic acid is not obtained [16]. The most remarkable results for the

hydrogenation of CO_2 to formic acid have been achieved by using Ru, Rh and Ir-complexes as homogeneous catalysts [17–19]. However, these homogeneous catalysts confront the disadvantage of requiring a separation process to recover the catalyst, which could promote the progress of undesired reactions.

In an effort to find a solution for this problem, Preti and coworkers implemented the heterogeneous catalyst Au/TiO_2 for the CO_2 hydrogenation and they obtained free-catalyst $HCOOH$/triethylamine (NEt_3) adducts [20]. Zhang et al. reported satisfactory activity and selectivity for formic acid in the hydrogenation of CO_2 combining a basic ionic liquid with a silica supported ruthenium complex catalyst [21]. Hao et al. also studied the catalytic properties of supported Ru catalysts for this reaction observing that the interaction between active ruthenium components with OH groups is crucial for the reaction [22]. Highly dispersed Ru-OH species present on $Ru/\gamma-Al_2O_3$ enhance the hydrogenation of CO_2, while the formation of crystalline RuO_2 species in the catalyst restricts the production of formic acid. Nevertheless, the design of this type of catalysts with expensive noble metals is not cost-effective for their implementation in industrial processes. Hence, the development of a new process for which formic acid can be efficiently produced by CO_2 hydrogenation using relative inexpensive catalysts results highly attractive.

2.1.1.3 Formaldehyde synthesis

Formaldehyde has several applications as a key building block for the production of other valuable materials. This compound is used as preservative and as an inactivating agent in vaccines [23]. Formaldehyde is also used in the industries of resins, adhesives

and plastics [23]. This chemical compound is industrially produced through a process that consists of three stages: steam reforming of natural gas to produce syngas followed by the methanol synthesis and ultimately, the partial oxidation of methanol or alternatively, via dehydrogenation of methanol [24]. The problem with these industrial processes is that they are carried out using high temperatures and a considerable amount of energy is used in combustion, compression and purification units [24]. In addition, these processes use as feedstock a valuable energy resource as natural gas or a valuable chemical compound as methanol, thus the utilization of a raw material such as CO and/or CO_2 is more attractive for the formaldehyde production through the following reactions:

$$CO + H_2 \leftrightarrow CH_2O \qquad\qquad\qquad\qquad\qquad \text{Reaction 2.3}$$

$$CO_2 + 2H_2 \leftrightarrow CH_2O + H_2O \qquad\qquad\qquad\qquad \text{Reaction 2.4}$$

There are not many studies on the production of formaldehyde from CO_2/CO hydrogenations, but catalysts based on metals that are active for hydrogenation (e.g., Ru and Pt) and that have demonstrated to produce formaldehyde as an intermediate in the methanol synthesis (e.g., Cu and Ni-based catalysts) have been explored for their implementation in the formaldehyde synthesis from CO_2/CO. Formaldehyde was selectively produced from the CO_2 hydrogenation, instead of methanol, using a PtCu/SiO_2 catalyst with an optimum Pt/Cu atomic ratio of 0.03 at 423 K and 600 KPa [25]. The high selectivity of the catalyst for formaldehyde was attributed to the platinum that promotes the reaction by diffusing the adsorbed hydrogen to the Cu surface. Bahmanpour and coworkers recently reported that formaldehyde can be produced from CO hydrogenation in an aqueous medium using a Ru-Ni/Al_2O_3 catalyst at 353 K and 100 bar [24]. In contrast

to the CO hydrogenation in gas phase that has a $\Delta G°=34.6$ kJ/mol [24], the aqueous phase reaction was thermodynamically favorable with a CO conversion of 19.14% and a selectivity of 100%, but was kinetically limited. Water promotes this reaction because it rapidly hydrates formaldehyde to form methylene glycol, which shifts the reaction equilibrium towards the formation of formaldehyde. However, this reaction has the limitation that CO and H_2 have low solubility in water. Therefore, similar to the production of formic acid, novel catalysts based on inexpensive metals for the synthesis of formaldehyde from an abundant feedstock such as CO_2 is worth of being investigated.

2.1.1.4 Carbon monoxide and carbon: undesired products

Carbon monoxide is produced by the reverse water-gas shift (RWGS) reaction:

$$CO_2 + H_2 \leftrightarrow CO + H_2O \qquad\qquad\qquad\qquad \text{Reaction 2.5}$$

This reaction is endothermic and its enthalphy and Gibbs free energy changes at 298K are 41.2 kJ/mol and 28.6 kJ/mol, respectively [1]. In some cases, CO is an undesired product because it competes with CO_2 causing changes in the reaction pathway or decreasing the rate of reaction of the desired product. This reaction is commonly investigated using catalysts active for water-gas shift (WGS) and the methanol synthesis, being the Cu-based catalysts the most popular [18]. Chen and colleagues reported that Cu/SiO_2 with potassium promoter had better catalytic activity for RWGS reaction than Cu/SiO_2 without the promoter, with CO_2 conversions of 12.8% and 5.3% at 600 °C, respectively [26]. The catalysts Cu-ZnO and $Cu-ZnO/Al_2O_3$ with different Cu/Zn ratios were also evaluated by Stone and Waller for this reaction obtaining that the most active ones were those with Cu/Zn >3 supported on Al_2O_3 [27]. Therefore, the activity of this

catalyst for the RWGS reaction is favored with high concentrations of Cu in the catalyst surface. Sakurai et al. [28] and Hartadi et al. [13] analyzed the hydrogenation of CO_2 on gold catalysts supported on different metal oxides and they found that Au/TiO_2 favored the dissociation of CO_2 to CO. Acidic metal oxides as TiO_2 promote the RWGS reaction [29].

On the other hand, another possible byproduct generated by the CO_2 hydrogenation could be carbonaceous species or coke. For example, catalysts used for the methanol synthesis can be also active for the synthesis of hydrocarbons. These hydrocarbons partially convert to coke, which deactivates the catalyst. Thus, the selection of the correct catalyst and reaction conditions to avoid the formation of these byproducts is crucial depending which is the product of interest in the hydrogenation of CO_2.

2.1.2 Homogeneous catalysis: reaction of CO_2 with ethylene oxide catalyzed by metal-salen complexes

Cyclic carbonates and polycarbonates can be produced through the coupling of CO_2 with an epoxide via two competing reactions, as illustrated in Fig. 2.2. The products from Reactions 1 and 2 in this figure have numerous applications in the industries of pharmaceutical, cleaning and personal care products, cosmetics, additives, automotive, plastics and electronics [30,31]. Different catalysts have been developed for these reactions and among these are the metal-salen complexes commonly with Al, Zn, Cr, Mn, Co and Fe as metal centers, which have demonstrated to have a good performance in the reaction of CO_2 with epoxides [32,33]. The metal-salen complexes show advantages over other catalysts, because they are inexpensive, their synthesis, modification, tailoring

14

and immobilization on solid supports are easy, and they are thermal and chemically stable [34]. The cycloaddition of CO_2 to epoxides to form cyclic carbonates or the copolymerization of CO_2 and epoxides to produce polycarbonates will be favored depending on the catalyst used. The nature of the metal center in the catalyst affects the selectivity of the metal-salen complexes. When the metal-oxygen bond of the alkoxide and carbonate intermediates formed during the reaction is weak, it can be displaced by a nucleophile or a solvent molecule, leading to the formation of cyclic carbonates [32]. For instance, Al-salen complexes were highly selective for cyclic carbonates because they facilitate the dissociation of the growing polymer chain more than Cr-salen complexes [32,35]. Lu and coworkers studied the performance of different metal-salen complexes toward the synthesis of ethylene carbonate from the reaction of CO_2 and ethylene oxide at supercritical conditions, obtaining that the catalytic activities increased in the following order: SalenAlCl > SalenCrCl > SalenCo > SalenZn [36].
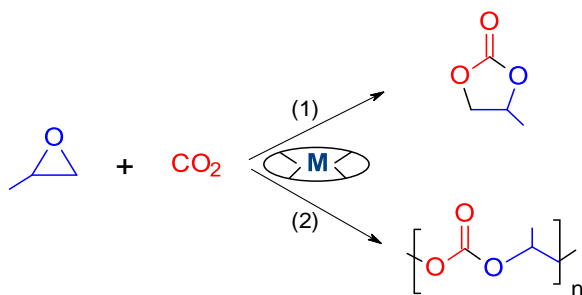
Fig. 2.2. Coupling reactions of CO_2 with epoxide using metal-salen complexes as catalysts.

Reaction 1 in Fig 2.2 with the coupling of ethylene oxide and CO_2 to produce ethylene carbonate is exothermic with a standard reaction enthalpy of -63.6 kJ/mol [37]. The typical experimental conditions for Reactions 1 and 2 when metal-salens are used as catalysts involve high pressures and temperatures, 20-150 atm and 80-130 °C, respectively [36,38,39]. In fact, Jacobsen et al., and Kruper and Dellar found that higher temperatures

promote the formation of cyclic carbonates from CO_2 and an epoxide [40,41], since cyclic carbonates are more thermodynamically stable and a higher activation energy is usually required for their synthesis in comparison with polycarbonates [32]. On the other hand, the effect of CO_2 pressure on the selectivity of Cr-salen complexes was studied, demonstrating that the rate of cyclic carbonate formation increases at low CO_2 pressures [42,43]. CO_2 dissolves into epoxides, but in general, without forming a single phase [32]. In some cases, a solvent is required to carry out the coupling reaction because the catalyst and/or the co-catalyst are not soluble in the epoxide at the reaction conditions [32].

2.2 Computational Chemistry

2.2.1 Quantum mechanical calculations

Computational chemistry has presented itself as an ideal alternative to optimize and understand reaction mechanisms. A screening of possible catalysts for a particular reaction can be performed by studying their interactions with different species and intermediates using computational quantum mechanics. Moreover, the optimum geometry, electronic distribution and energy, vibrational modes and thermodynamic properties of the analyzed species can be obtained by performing quantum mechanical calculations that solve the time-independent Schrödinger equation:

$$\widehat{H}\psi = E\psi \qquad\qquad (2.1)$$

where $\hat{H}$ is the Hamiltonian operator that includes both kinetic energy and potential energy terms, ψ is the wavefunction, which depends on the coordinates of all the electrons, and

E is the electronic energy. For the case of systems with one only electron, Equation 2.1 can be solved analytically. But, when species with more than one electron are analyzed, Equation 2.1 cannot be solved analytically since the electron-electron repulsions must be considered and several assumptions have to be made to determine a numerical solution.

One of these simplifications is the Born-Oppenheimer approximation which assumes that the kinetic energy of the nuclei is neglected and the potential energy of the nucleus is constant, because the mass of a nucleus is much greater than the mass of an electron. Consequently, the total wavefunction for a molecule can be split into electronic and nuclear parts as illustrated in Equation 2.2:

$$\psi_{total}(nuclei, electrons) = \psi(electrons)\psi(nuclei) \tag{2.2}$$

Using this approximation, Equation 2.1 can be solved for the electronic part at a fixed nuclear configuration.

Another simplification is to describe each molecular orbital (ψ_i) in a molecule as a linear combination of atomic orbitals (LCAO) or single-electron orbitals (ϕ_j):

$$\psi_i = \sum_{j=1}^{n} c_{ji}\phi_j \tag{2.3}$$

where c_{ji} is a coefficient and *n* is the total number of atomic orbitals. These single-electron orbitals are a set of functions named basis functions or basis set. There are diverse types of basis sets that have been developed to define atomic orbitals [44,45], but commonly these orbitals are described by Gaussian functions. The simplest basis set is the minimal basis set, in which each filled orbital is strictly described by one function. The split valence double zeta basis sets consists of a rigorous treatment of the valence electrons doubling the number of functions that describe them and the use of a single function for the core

electrons. Polarization and diffuse functions can also be introduced in the basis functions to account for the distortion of electron clouds that could be present in the combination of atoms to form a molecule, and to treat anionic species or molecules with lone pairs, respectively.

To obtain a numerical solution of Equation 2.1, several methods exist and the method selection will depend of the accuracy and speed at which results are expected to be obtained. For instance, there are *ab initio* methods, as Hartree-Fock (HF). HF calculations use the LCAO approach previously mentioned and described by Equation 2.3. These calculations involve a search for the coefficients c_{ji} for each atomic orbital that give the lowest energy for the system:

$$\frac{\partial E}{\partial c_{ji}} = 0 \qquad\qquad (2.4)$$

The main simplification of this wavefunction method is that it assumes the electron-electron interaction energy as an average for each of the electrons in the system. Consequently, the main disadvantage of HF is that the motion of an individual electron is assumed to be independent of the motion of other electrons, which means that it does not include a correlation term. Another method commonly used to optimize the electronic structure and energy of species is density functional theory. DFT methods are based on the Hohenberg-Kohn theorem, which establishes that the ground state electronic energy is a unique functional[1] of the electron density, $\rho(r)$ [45]. In other words, the energy and all other electronic properties of the system on the ground state are uniquely defined by the electron density. The advantage of this method is that the electronic density depends only

---

[1] According to the book "Introduction to Computational Chemistry", a functional is a prescription for producing a number from a function, which in turn depends on variables [45].

on the three spatial coordinates, while the wavefunction method depends on $3n$ coordinates, where n is the number of electrons, and the electron spin. The methodology of DFT is similar to the one of the HF method, but the energy for DFT $E[\rho(r)]$ is given by the kinetic energy $E_{KE}[\rho(r)]$, the repulsion among electrons $V_{ee}[\rho(r)]$ and an external potential v_{ext} that represents the Coulomb interactions between the electrons and the nuclei. DFT methods also include the exchange-correlation potential $v_{xc}(r)$ that is not present in HF equations and is defined by the exchange-correlation functional $E_{xc}[\rho(r)]$ as:

$$v_{XC}(\boldsymbol{r}) = \frac{\delta E_{XC}[\rho]}{\delta \rho(r)} \qquad (2.5)$$

Although this functional is unknown, many approximate functionals have been proposed and tested [45], among which is found the generalized gradient approximation (GGA) methods that are improvements over the most primitive approximation for this functional, the local spin density approximation (LDA).

For DFT calculations, the Kohn-Sham [44] equations are solved to obtain the electron density using an iterative process known as the self-consistent field (SCF) approach:

$$\left(\hat{h}^{(1)}(\boldsymbol{r}_1) + \hat{J}(\boldsymbol{r}_1) + v_{XC}(\boldsymbol{r}_1) \right) \psi_i^{KS}(\boldsymbol{r}_1) = \varepsilon_i^{KS} \psi_i^{KS}(\boldsymbol{r}_1) \qquad (2.6)$$

where $\hat{h}^{(1)}(\boldsymbol{r}_1)$ is the one-electron Hamiltonian, $\hat{J}(\boldsymbol{r}_1)$ is the Coulomb operator, ψ_i^{KS} are the Kohn-Sham (KS) orbitals (which are analogous to the HF wavefunctions) and ε_i^{KS} are the Kohn-Sham energies. The iterative process starts approximating: $\rho(r)$, typically by using a superposition of atomic densities, and the functional $E_{xc}[\rho(r)]$ using for example LDA or GGA functionals [46]. By specifying this functional, the term $v_{xc}(r)$ can be computed. Now, the KS equations can be solved to obtain an initial set of KS orbitals and

these orbitals can be used to calculate an improved electron density by the following relationship:

$$\rho(\mathbf{r}) = \sum_{i=1}^{N} \left| \psi_i^{KS}(\mathbf{r}) \right|^2 \tag{2.7}$$

This process is repeated until the electron density and the exchange-correlation energy converge. Finally, the electronic energy can be calculated as:

$$E[\rho(\mathbf{r})] = E_{KE}[\rho(\mathbf{r})] + V_{ee}[\rho(\mathbf{r})] + E_{XC}[\rho(\mathbf{r})] + \int v_{ext} \, \rho(\mathbf{r}) d\mathbf{r} \tag{2.8}$$

Also, DFT methods used to model infinite systems like a unit cell with periodic boundary conditions (e.g., metal surfaces and alloys) have been developed and they are known as periodic DFT calculations. These calculations use plane wave basis sets to describe the outer valence electrons and Vanderbilt ultrasoft pseudopotentials or effective core potentials to analyze the core electrons. This type of basis sets are ideal for metals (especially transition metals) because many of them have a large number of core electrons. Consequently, the accurate analysis of these systems would require a large amount of basis functions that describe the corresponding orbitals and their interaction with the valence orbitals. Hence, this computational cost problem might be solved by modeling the core electrons with an appropriate function (the pseudo potential) and treating only the valence electrons explicitly, because the former are not involved in bonding [45].

HF methods do not include correlation effects, but they have the solution for the exchange contribution. To exploit this peculiarity of HF methods, some methods known as hybrid methods have been developed, which include a mixture of the HF exchange functional and DFT exchange-correlation functionals. Because GGA methods give a

considerable improvement over LDA, a generalized version of the hybrid method can be defined by writing the exchange energy as a combination of the exchange energy under the local spin density approximation, the exact exchange energy obtained from the Slater determinant of the Kohn-Sham orbitals, and the gradient correction terms for exchange and correlation [44,45].

Once the method and the basis set are selected, the first step in performing quantum mechanical calculations is usually a geometry optimization to find the lowest-energy structure.

2.2.2 Solvent methods

In most quantum mechanical calculations, the system is assumed to be in the gas phase and placed in a vacuum. However, there are some reactions that are carried out in the liquid phase because they require the presence of a solvent to accomplish the reaction. In some cases, the presence of a solvent can considerably change the mechanism, energy and rate of reaction. Thus, taking into account the solvent effect is imperative in these cases.

Interactions between the solute and solvent can be divided into two types: specific solvation effects and non-specific solvation effects [45]. Specific solvation effects, such as hydrogen bonds, van der Waals interactions and so on, can be studied by modeling the system with explicit solvent molecules. These methods are computationally expensive. However, non-specific effects can be modeled by using continuum models, where the solvent is considered as a uniform polarizable medium with a dielectric constant [45]. This approach is used to study long-range effects of the solvent, such as

dipole orientation and solvent polarization. The principle of continuum models is to place the solute molecule into a cavity in the medium. When a molecule is transferred from vacuum to solvent there is a free energy change associated to this process known as the solvation free energy [44]. This energy has three contributions. The first one is the free energy required to form the solute cavity inside the solvent. The second contribution is due to the dispersion interactions between the solute and the solvent and the last one is the electrostatic contribution that takes into account when the charge distribution of the solute polarizes the solvent. The differences among the continuum models are the following: how the size and shape of the cavity are defined, how the cavity/dispersion contributions are calculated, how the charge distribution of the solute is represented, which method (e.g., classical or quantum methods) is used to describe the solute, and how the dielectric medium is described [45].

A method that is commonly used for solvent calculations and has been implemented in a variety of *ab initio* and semi-empirical quantum mechanical programs is the polarizable continuum model (PCM) [47]. This method employs a more realistic cavity shape generated by interlocking atomic van der Waals radii scaled by an empirical factor and a detailed description of the electrostatic potential; and the parameterization of the cavity/dispersion contributions is based on the surface area, as illustrated in Fig. 2.3 [45]. The cavity surface is divided into several small surface elements, and each one of these elements has a point charge. The point charges represent the solvent polarization, and they are initially calculated for each surface element from the electric field gradient caused by the solute [44]. Then, the potential associated to other surface charges, can be initially estimated with Coulomb's law. This potential is added to the Hamiltonian and it is solved

by SCF procedure, where new values of the surface charges are calculated from the wavefunction to obtain a new value of the potential. This iterative process continues until the wavefunction of the solute and the surface charges are self-consistent, obtaining the charge distribution in the cavity that is needed to calculate the electrostatic contribution to the free energy.
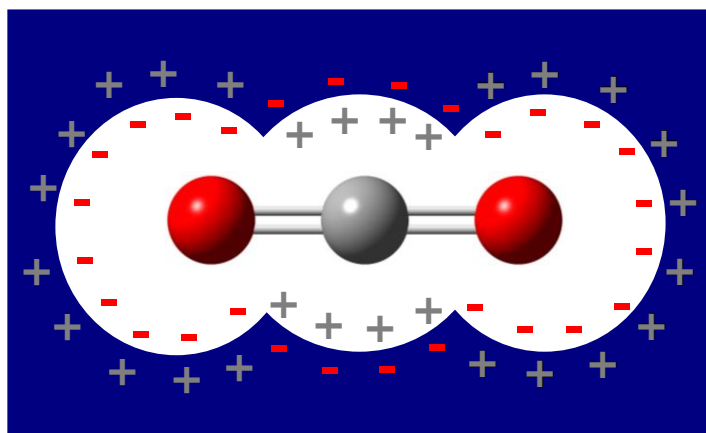
Fig. 2.3. Point charges on the cavity where the solute is located in the polarizable continuum model.

2.2.3 Reaction mechanisms and theoretical studies about CO_2 conversion

2.2.3.1   Hydrogenation of CO_2 and CO

The hydrogenation of CO_2 and CO have been widely studied by theoretical methods such as DFT in order to elucidate many unknowns with respect to its reaction mechanism [7,8,10,18,48–52]. Grabow and Mavrikakis performed a microkinetic study for the methanol synthesis on a slab of Cu(111) through CO_2 and CO hydrogenation using their periodic DFT results and experimental data [48]. They found that both the hydrogenation of CO and CO_2 are active pathways for the methanol production via the formation of the following intermediates: $HCO \rightarrow CH_2O \rightarrow CH_3O$ and $HCOO \rightarrow HCOOH \rightarrow H_2COOH \rightarrow$

$CH_2O \rightarrow CH_3O$, respectively. But according to their thermochemistry and transition state results, CO hydrogenation is the dominant reaction because: it is more exothermic than CO_2 hydrogenation and the large energy barriers required to hydrogenate methoxy and produce water in the hydrogenation of CO_2.

The formation of methanol from CO hydrogenation on a $Pd_{19}(111)$ cluster was predicted to proceed through the same mechanism postulated on Cu(111), being the hydrogenation of CO to HCO a plausible rate-limiting step because this was the only endothermic elementary step [53]. This mechanism is also consistent with the one obtained on Rh(211), because the HCO intermediate is more stable than its isomer COH [54]. However, Remediakis et al. found that the formation of COH is slightly more favorable than HCO on Ni(111), proposing a different mechanism where the following intermediates were considered: COH $\rightarrow$ HCOH $\rightarrow$ CH_2O $\rightarrow$ CH_3O [52]. But, the hydrogenation of CO was also the rate-limiting step in this mechanism being an endothermic reaction with high activation energies of 1.45 and 1.49 eV for COH and HCO, respectively. Lin and coworkers proposed a different mechanism to the ones previously discussed for the conversion of CO to methanol on Pd(111), where the HCO intermediate is more stable than COH, but the next hydrogenation steps produce HCOH and CH_2OH as intermediates, instead of CH_2O and CH_3O [51].

On the other hand, Hu and Nasatsuji proposed another reaction mechanism for CO_2 hydrogenation where formate (HCOO) is hydrogenated to dioxymethylene (CH_2O_2) instead of formic acid as predicted by Grabow and Mavrikakis, and CH_2O_2 is then converted to formaldehyde [55]. They suggested that the steps of formate hydrogenation and the conversion of CH_2O_2 to CH_2O are rate-limiting for the methanol synthesis on

Cu(100). The stability of the intermediates HCOOH and CH_2O_2 on a simulated Cu_{29} nanoparticle were also studied by Yang and coworkers, obtaining that the hydrogenation of formate to CH_2O_2 is more favorable than to HCOOH [7]. The formation of CH_2O_2 is less endothermic by 0.39 eV with a lower activation energy by 0.56 eV than the HCOOH formation. As these researchers, many others have proposed dioxymethylene as intermediate in the methanol synthesis through the hydrogenation of formate on pure or doped Cu surfaces [7,49,50,56,57]. In the literature, the question about which is the product of the hydrogenation of formate, CH_2O_2 or HCOOH, is a motive of debate because it has been theoretically demonstrated that CH_2O_2 is strongly adsorbed on Cu(111), but it is not stable since its dehydrogenation back to HCOO is easier than its hydrogenation to H_2COOH [50]. On the other hand, if HCOOH is favored over CH_2O_2, there is still a problem because HCOOH is easily desorbed from Cu(111) or it can be dissociated back to HCOO and H with a small energy barrier [50]. Therefore, the reaction mechanisms for the hydrogenations of CO_2 and CO are still unclarified.

Similar to experimental studies, many investigators have performed DFT studies to evaluate the catalytic activity and selectivity of different catalysts in the hydrogenations of CO_2 and CO [8,48,54,58,59]. For instance, Filot and coworkers very recently published a microkinetic study of the formation of several products, among them formaldehyde and methanol, from CO hydrogenation catalyzed by the Rh(211) surface [54]. They found that this catalyst is predicted to be more selective for formaldehyde at temperatures below 600 K, because the low rate of CO dissociation and the desorption of CH_2O was preferred to its hydrogenation to CH_3O due to the high energy barrier associated to this step. However, this reaction was also studied on the Ni(111) surface and the obtained results

demonstrate that this catalyst is not selective for formaldehyde or methanol because the overall energy barrier for both reaction routes was estimated to be 2.0 eV [52]. Similar to Rh(211) at temperatures below 600 K and Ni(111), on the $Pd_{19}(111)$ cluster, the dissociation of CO leading to a possible reaction of methanation or chain-growth was highly energetically unfavorable in comparison with the hydrogenation of CO [53]. It is consistent with the DFT results obtained by Lin and coworkers in which the synthesis of methane through CO dissociation is more unfavorable than via the hydrogenation of CO on Pd(111) [51]. Despite this, the methanol production is favored over the methane synthesis on this catalytic surface.

By using the dipped adcluster model with *ab initio* second-order Møller-Plesset methods, researchers found that the addition of Zn to the Cu(100) catalyst creates Cu-Zn sites that enhance the reactivity of HCOO and CH_2O_2 by decreasing the activation energies for the hydrogenation of these two species and they increase the catalyst activity by stabilizing the intermediate CH_2O_2 [55]. Behrens et al. studied the effect of Zn on the catalytic properties of a CuZn(211) surface using DFT calculations [8]. They observed that the incorporation of Zn in the surface steps of Cu(211) increased the rate of methanol synthesis, because it caused an increase in the adsorption strength of the intermediates HCO, CH_2O and CH_3O and a decrease in the energy barriers. One of main conclusions of this work is that other dopants with the same oxygen binding strength as Zn may have the same promotional effect on the methanol synthesis.

2.2.3.2 Coupling of CO_2 with ethylene oxide

Many researchers have investigated the reaction mechanism for the coupling of CO_2 and epoxide catalyzed by metal-salen complexes, and they have debated on how the epoxide ring opens and postulated different reaction intermediates for the interaction of the reactants with the catalyst. Most of the postulated reaction mechanisms agree that the reaction starts with the formation of an epoxide-salen complex where the oxygen of the epoxide coordinates to the metal center, followed by the epoxide ring opening through a nucleophilic attack to a C-O bond in the epoxide by the axial ligand of the catalyst or a cocatalyst [37,60,61]. The subsequent step in the reaction is the direct insertion of CO_2 into the metal-alkoxide bond of the radical epoxide-salen complex that acts as a nucleophile and activates CO_2 through its electrophilic C and nucleophilic O atom. The growing polymeric chain might backbite to form cyclic carbonates while it is bonded to the metal center of the catalyst or after its dissociation, which generates a free anionic polymer. On the other hand, if the alternating insertion of epoxide and CO_2 is sustained without the backbiting reaction, polycarbonates are formed. Luinstra et al. investigated plausible routes for the formation of cyclic carbonates via either free or metal-bound alkoxy or carbonate chain end using DFT calculations [60]. They found that the backbiting of the carbonate end chain is more favorable than of the alkoxy chain end because the former has lower activation barriers in both free and metal-bound conformations. However, the free carbonate end chains were decomposed to cyclic carbonates more easily than the metal-bound ones. On the other hand, Darensbourg and Yeung also evaluated these routes for the backbiting reaction with composite *ab initio* methods,

demonstrating that the metal-free carbonate backbiting has higher free energies barriers than the alkoxide backbiting for most of analyzed epoxides [37].

The interaction of epoxide with metal-salens has been extensively studied by DFT methods, because these complexes are commonly used as catalysts for epoxidation reactions [62–64]. However, limited information about the activation of CO_2 by the epoxide-salen complex or by another substance involved in the reaction (e.g., cocatalyst) is known and the reaction mechanism has not been entirely clarified. Curet-Arana and her research group analyzed the interaction of CO_2 with chlorinated Co, Cr, Mn, Fe, Al and Zn salen complexes using DFT calculations [34]. Their study demonstrated that the bonding of CO_2 on these metal-salen complexes is not thermodynamically favorable, even when the epoxide is included in the system.

References

[1] G. Centi, S. Perathoner, Opportunities and prospects in the chemical recycling of carbon dioxide to fuels, Catal. Today. 148 (2009) 191–205.

[2] Methanol Data, IGP Energy, http://igpenergy.com/products/methanol-overview/methanol/ (accessed Sep 19, 2015).

[3] N. Homs, J. Toyir, P.R. de la Piscina, Catalytic Processes for Activation of CO_2, in: S.L. Suib (Ed.), New Future Dev. Catal., Elsevier, Amsterdam, 2013: pp. 1–26.

[4] A. Ota, E.L. Kunkes, I. Kasatkin, E. Groppo, D. Ferri, B. Poceiro, R. Navarro, M. Behrens, Comparative study of hydrotalcite-derived supported Pd_2Ga and PdZn intermetallic nanoparticles as methanol synthesis and methanol steam reforming catalysts, J. Catal. 293 (2012) 27–38.

[5] N.A.M. Razali, K.T. Lee, S. Bhatia, A.R. Mohamed, Heterogeneous catalysts for production of chemicals using carbon dioxide as raw material: A review, Renew. Sustain. Energy Rev. 16 (2012) 4951–4964.

[6] G.A. Olah, A. Goeppert, G.K.S. Prakash, Chemical Recycling of Carbon Dioxide to Methanol and Dimethyl Ether: From Greenhouse Gas to Renewable, Environmentally Carbon Neutral Fuels and Synthetic Hydrocarbons, J. Org. Chem. 74 (2009) 487–498.

[7] Y. Yang, J. Evans, J.A. Rodriguez, M.G. White, P. Liu, Fundamental studies of methanol synthesis from CO_2 hydrogenation on Cu(111), Cu clusters, and Cu/ZnO(000), Phys. Chem. Chem. Phys. 12 (2010) 9909–9917.

[8] M. Behrens, F. Studt, I. Kasatkin, S. Kühl, M. Hävecker, F. Abild-Pedersen, S. Zander, F. Girgsdies, P. Kurr, B.-L. Kniep, M. Tovar, R.W. Fischer, J.K. Nørskov, R. Schlögl, The Active Site of Methanol Synthesis over $Cu/ZnO/Al_2O_3$ Industrial Catalysts, Science. 336 (2012) 893–897.

[9] Y. Kanai, T. Watanabe, T. Fujitani, M. Saito, J. Nakamura, T. Uchijima, Role of ZnO in promoting methanol synthesis over a physically-mixed Cu/SiO_2 and ZnO/SiO_2 catalyst, Energy Convers. Manag. 36 (1995) 649–652.

[10] C. Liu, B. Yang, E. Tyo, S. Seifert, J. DeBartolo, B. von Issendorff, P. Zapol, S. Vajda, L.A. Curtiss, Carbon Dioxide Conversion to Methanol over Size-Selected Cu_4 Clusters at Low Pressures, J. Am. Chem. Soc. 137 (2015) 8676–8679.

[11] J. Toyir, R. Miloua, N.E. Elkadri, M. Nawdali, H. Toufik, F. Miloua, M. Saito, Sustainable process for the production of methanol from CO_2 and H_2 using Cu/ZnO-based multicomponent catalyst, Phys. Procedia. 2 (2009) 1075–1079.

[12] H. Sakurai, M. Haruta, Carbon dioxide and carbon monoxide hydrogenation over gold supported on titanium, iron, and zinc oxides, Appl. Catal. Gen. 127 (1995) 93–105.

[13] Y. Hartadi, D. Widmann, R.J. Behm, CO_2 Hydrogenation to Methanol on Supported Au Catalysts under Moderate Reaction Conditions: Support and Particle Size Effects, ChemSusChem. 8 (2015) 456–465.

[14] F. Joó, Activation of Carbon Dioxide, in: A. Bakac (Ed.), Phys. Inorg. Chem., John Wiley & Sons, Inc., 2010: pp. 247–279.

[15] Q. Ge, Mechanistic Understanding of Catalytic CO_2 Activation from First Principles Theory, in: S.L. Suib (Ed.), New Future Dev. Catal., Elsevier, Amsterdam, 2013: pp. 49–79.

[16] H. Hayashi, S. Ogo, S. Fukuzumi, Aqueous hydrogenation of carbon dioxide catalysed by water-soluble ruthenium aqua complexes under acidic conditions, Chem. Commun. (2004) 2714–2715.

[17] C. Federsel, R. Jackstell, M. Beller, State-of-the-Art Catalysts for Hydrogenation of Carbon Dioxide, Angew. Chem. Int. Ed. 49 (2010) 6254–6257.

[18] W. Wang, S. Wang, X. Ma, J. Gong, Recent advances in catalytic hydrogenation of carbon dioxide, Chem. Soc. Rev. 40 (2011) 3703–3727.

[19] S. Moret, P.J. Dyson, G. Laurenczy, Direct synthesis of formic acid from carbon dioxide by hydrogenation in acidic media, Nat. Commun. 5 (2014).

[20] D. Preti, C. Resta, S. Squarcialupi, G. Fachinetti, Carbon Dioxide Hydrogenation to Formic Acid by Using a Heterogeneous Gold Catalyst, Angew. Chem. Int. Ed. 50 (2011) 12551–12554.

[21] Z. Zhang, Y. Xie, W. Li, S. Hu, J. Song, T. Jiang, B. Han, Hydrogenation of Carbon Dioxide is Promoted by a Task-Specific Ionic Liquid, Angew. Chem. Int. Ed. 47 (2008) 1127–1129.

[22] C. Hao, S. Wang, M. Li, L. Kang, X. Ma, Hydrogenation of CO_2 to formic acid on supported ruthenium catalysts, Catal. Today. 160 (2011) 184–190.

[23] Formaldehyde Applications, Formaldehyde Facts, http://www.formaldehydefacts.org/applications (accessed Sep 19, 2015).

[24] A.M. Bahmanpour, A. Hoadley, A. Tanksale, Formaldehyde production via hydrogenation of carbon monoxide in the aqueous phase, Green Chem. 17 (2015) 3500–3507.

[25] D.-K. Lee, D.-S. Kim, S.-W. Kim, Selective formation of formaldehyde from carbon dioxide and hydrogen over $PtCu/SiO_2$, Appl. Organomet. Chem. 15 (2001) 148–150.

[26] C.-S. Chen, W.-H. Cheng, S.-S. Lin, Study of reverse water gas shift reaction by TPD, TPR and CO_2 hydrogenation over potassium-promoted Cu/SiO_2 catalyst, Appl. Catal. Gen. 238 (2003) 55–67.

[27] F.S. Stone, D. Waller, Cu–ZnO and $Cu–ZnO/Al_2O_3$ Catalysts for the Reverse Water-Gas Shift Reaction. The Effect of the Cu/Zn Ratio on Precursor Characteristics and on the Activity of the Derived Catalysts, Top. Catal. 22 (2003) 305–318.

[28] H. Sakurai, S. Tsubota, M. Haruta, Hydrogenation of CO_2 over gold supported on metal oxides, Appl. Catal. Gen. 102 (1993) 125–136.

[29] G.C. Bond, D.T. Thompson, Catalysis by Gold, Catal. Rev. 41 (1999) 319–388.

[30] A.-A.G. Shaikh, S. Sivaram, Organic Carbonates, Chem. Rev. 96 (1996) 951–976.

[31] Q. Ashton (ed.), Alkalies—Advances in Research and Application: 2013 Edition: ScholarlyBrief, ScholarlyEditions, 2013.

[32] P.P. Pescarmona, M. Taherimehr, Challenges in the catalytic synthesis of cyclic and polymeric carbonates from epoxides and CO_2, Catal. Sci. Technol. 2 (2012) 2169–2187.

[33] T. Sakakura, J.-C. Choi, H. Yasuda, Transformation of Carbon Dioxide, Chem. Rev. 107 (2007) 2365–2387.

[34] M. Curet-Arana, P. Meza, R. Irizarry, R. Soler, Quantum Chemical Determination of Stable Intermediates on CO_2 Adsorption Onto Metal(Salen) Complexes, Top. Catal. 55 (2012) 260–266.

[35] K.V. Raghavan, B.M. Reddy, Industrial Catalysis and Separations: Innovations for Process Intensification, CRC Press, 2014.

[36] X.-B. Lu, X.-J. Feng, R. He, Catalytic formation of ethylene carbonate from supercritical carbon dioxide/ethylene oxide mixture with tetradentate Schiff-base complexes as catalyst, Appl. Catal. Gen. 234 (2002) 25–33.

[37] D.J. Darensbourg, A.D. Yeung, Thermodynamics of the Carbon Dioxide–Epoxide Copolymerization and Kinetics of the Metal-Free Degradation: A Computational Study, Macromolecules. 46 (2013) 83–95.

[38] R.L. Paddock, S.T. Nguyen, Chiral (salen)CoIII catalyst for the synthesis of cyclic carbonates, Chem. Commun. (2004) 1622–1623.

[39] D.J. Darensbourg, J.L. Rodgers, R.M. Mackiewicz, A.L. Phelps, Probing the mechanistic aspects of the chromium salen catalyzed carbon dioxide/epoxide copolymerization process using in situ ATR/FTIR, Catal. Today. 98 (2004) 485–492.

[40] E.N. Jacobsen, Asymmetric Catalysis of Epoxide Ring-Opening Reactions, Acc. Chem. Res. 33 (2000) 421–431.

[41] W.J. Kruper, D.D. Dellar, Catalytic Formation of Cyclic Carbonates from Epoxides and CO_2 with Chromium Metalloporphyrinates, J. Org. Chem. 60 (1995) 725–727.

[42] D.J. Darensbourg, R.M. Mackiewicz, D.R. Billodeaux, Pressure Dependence of the Carbon Dioxide/Cyclohexene Oxide Coupling Reaction Catalyzed by Chromium Salen Complexes. Optimization of the Comonomer-Alternating Enchainment Pathway, Organometallics. 24 (2005) 144–148.

[43] R. Eberhardt, M. Allmendinger, B. Rieger, DMAP/Cr(III) Catalyst Ratio: The Decisive Factor for Poly(propylene carbonate) Formation in the Coupling of CO_2 and Propylene Oxide, Macromol. Rapid Commun. 24 (2003) 194–196.

[44] A.R. Leach, Molecular Modelling: Principles and Applications, 2nd ed., Pearson Education, Harlow, England, 2001.

[45] F. Jensen, Introduction to Computational Chemistry, 2nd ed., John Wiley & Sons, Ltd, West Sussex, England, 2007.

[46] P. Atkins, R. Friedman, Molecular Quantum Mechanics, 5th ed., Oxford University Press, Oxford, N.Y., 2011.

[47] S. Miertuš, E. Scrocco, J. Tomasi, Electrostatic interaction of a solute with a continuum. A direct utilization of AB initio molecular potentials for the prevision of solvent effects, Chem. Phys. 55 (1981) 117–129.

[48] L.C. Grabow, M. Mavrikakis, Mechanism of Methanol Synthesis on Cu through CO_2 and CO Hydrogenation, ACS Catal. 1 (2011) 365–384.

[49] Y. Yang, M.G. White, P. Liu, Theoretical Study of Methanol Synthesis from CO_2 Hydrogenation on Metal-Doped Cu(111) Surfaces, J. Phys. Chem. C. 116 (2012) 248–256.

[50] Y.-F. Zhao, Y. Yang, C. Mims, C.H.F. Peden, J. Li, D. Mei, Insight into methanol synthesis from CO_2 hydrogenation on Cu(1 1 1): Complex reaction network and the effects of H_2O, J. Catal. 281 (2011) 199–211.

[51] S. Lin, J. Ma, X. Ye, D. Xie, H. Guo, CO Hydrogenation on Pd(111): Competition between Fischer–Tropsch and Oxygenate Synthesis Pathways, J. Phys. Chem. C. 117 (2013) 14667–14676.

[52] I.N. Remediakis, F. Abild-Pedersen, J.K. Nørskov, DFT Study of Formaldehyde and Methanol Synthesis from CO and H_2 on Ni(111), J. Phys. Chem. B. 108 (2004) 14535–14540.

[53] M. Neurock, First-principles analysis of the hydrogenation of carbon monoxide over palladium, Top. Catal. 9 (1999) 135–152.

[54] I.A.W. Filot, R.J.P. Broos, J.P.M. van Rijn, G.J.H.A. van Heugten, R.A. van Santen, E.J.M. Hensen, First-Principles-Based Microkinetics Simulations of Synthesis Gas Conversion on a Stepped Rhodium Surface, ACS Catal. 5 (2015) 5453–5467.

[55] Z.-M. Hu, H. Nakatsuji, Active sites for methanol synthesis on a Zn/Cu(100) catalyst, Chem. Phys. Lett. 313 (1999) 14–18.

[56] J.R.B. Gomes, J.A.N.F. Gomes, A theoretical study of dioxymethylene, proposed as intermediate in the oxidation of formaldehyde to formate over copper, Surf. Sci. 446 (2000) 283–293.

[57] D. Mei, L. Xu, G. Henkelman, Dimer saddle point searches to determine the reactivity of formate on Cu(111), J. Catal. 258 (2008) 44–51.

[58] F. Studt, F. Abild-Pedersen, Q. Wu, A.D. Jensen, B. Temel, J.-D. Grunwaldt, J.K. Nørskov, CO hydrogenation to methanol on Cu–Ni catalysts: Theory and experiment, J. Catal. 293 (2012) 51–60.

[59] F. Studt, I. Sharafutdinov, F. Abild-Pedersen, C.F. Elkjær, J.S. Hummelshøj, S. Dahl, I. Chorkendorff, J.K. Nørskov, Discovery of a Ni-Ga catalyst for carbon dioxide reduction to methanol, Nat. Chem. 6 (2014) 320–324.

[60] G.A. Luinstra, G.R. Haas, F. Molnar, V. Bernhart, R. Eberhardt, B. Rieger, On the Formation of Aliphatic Polycarbonates from Epoxides with Chromium(III) and Aluminum(III) Metal–Salen Complexes, Chem. – Eur. J. 11 (2005) 6298–6314.

[61] D.J. Darensbourg, A.D. Yeung, A concise review of computational studies of the carbon dioxide–epoxide copolymerization reactions, Polym. Chem. 5 (2014) 3949–3962.

[62] L. Cavallo, H. Jacobsen, Electronic Effects in (salen)Mn-Based Epoxidation Catalysts, J. Org. Chem. 68 (2003) 6202–6207.

[63] M.-A. Munoz-Hernandez, M.L. McKee, T.S. Keizer, B.C. Yearwood, D.A. Atwood, Six-coordinate aluminium cations: characterization, catalysis, and theory, J. Chem. Soc. Dalton Trans. (2002) 410–414.

[64] Y.G. Abashkin, J.R. Collins, S.K. Burt, (Salen)Mn(III)-Catalyzed Epoxidation Reaction as a Multichannel Process with Different Spin States. Electronic Tuning of Asymmetric Catalysis: A Theoretical Study, Inorg. Chem. 40 (2001) 4040–4048.

Chapter 3: Goal and Specific Aims

The global goal of this project is to use DFT methods to study homogeneous and heterogeneous catalysts for the conversion of CO_2 into useful organic compounds. As mentioned in the previous chapters, two main reactions have been considered for the conversion of CO_2: the hydrogenation of CO_2 and the coupling reaction of CO_2 with ethylene oxide. The specific objectives for each reaction system analyzed in this research project are summarized in the next subsections.

3.1 Heterogeneous Catalysis: Hydrogenation of CO_2 on Metal Surfaces

1) To analyze the adsorption of relevant species involved in the hydrogenation of CO_2 and CO over metal catalysts using DFT calculations to determine how these species interact with the catalytic surface.

   - Relevant adsorbed species to be analyzed include: CO_2, H_2, H, CO, H_2O, C, O, OH, CH_3OH, HCOOH, CH_2O, CH_2OH, CH_2O_2, CH_3O, CH_3O_2, HCO, COH, COOH, HCOO, HCO_3 and CO_3.

   - The metal catalysts to be analyzed include the pure Au(111) surface and Cu-based surface alloys. Potential catalysts for CO_2/CO hydrogenation to be determined through a screening of Cu(111) surfaces doped with Ni, Pd, Ti, Mg, Ga and Al by comparing various descriptors, such as the binding energies of H, O, CO and CO_2, and the work functions of these surfaces.

2) To study the thermochemistry of the formation of formic acid, formaldehyde and methanol from CO_2 and CO hydrogenation, and to determine which intermediates are more thermodynamically favorable on each of the surfaces.

3) To postulate reaction mechanisms for the hydrogenation of CO_2 and CO on each of the catalytic materials.

4) To compare the energies of reactions on the copper-based surface alloys to determine the effect of the addition of metal dopants on the thermochemistry of CO_2 and CO hydrogenation reactions.

5) To study the stability of these catalysts against poisoning by species such as adsorbed carbon atoms.

3.2 Homogeneous Catalysis: Reaction of CO_2 with Ethylene Oxide Catalyzed by Salen Complexes

1) To understand, at the molecular level, how the metal-salen catalysts can activate CO_2 and to unravel the role of these catalysts on the coupling reaction of CO_2 and ethylene oxide for the formation of ethylene carbonate.

2) To perform a systematic analysis of the possible interactions of CO_2 and ethylene oxide with metal-salen complexes by employing DFT calculations to determine the effect of the metal center and axial ligand on the reaction energies for the formation of relevant intermediate species.

- Metal centers to be analyzed are: Co, Cr, Mn, Fe, Zn, and Al

- Axial ligands to be suited are chlorine and DMAP

- To study the interaction of the cocatalyst, DMAP with CO_2.

3) To analyze the thermochemistry of plausible reaction intermediates to determine the most favorable interactions

Chapter 4: Atomic and Molecular Adsorption on Au(111)[1]

4.1. Introduction

Interest in the catalytic properties of gold nanoparticles emerged in the late 1980s, when Haruta and coworkers reported that these particles are effective catalysts for the oxidation of CO at low temperature [1, 2]. In the same decade, another key discovery was made by Hutchings, when he reported that gold nanoparticles are very selective catalysts for the hydrochlorination of acetylene [3]. However, the commercialization of gold catalysts did not start until a decade later, c.a. 1992, when they were proven to decompose ammonia and trimethylamine at room temperature, and were used mainly to decompose odors [4]. A particular feature that made these catalysts so effective for this application is that moisture enhances their catalytic activity. Since this commercialization, gold nanoparticles have also showed high activities and selectivities for many other reactions, in particular for selective oxidation and hydrogenation reactions. Some of the reactions in which gold catalysts have been proven useful include: propylene epoxidation [5, 6], oxidation of glycerol [7–9], oxidation of ethylene glycol [10], direct synthesis of hydrogen peroxide from hydrogen and oxygen [11–13], hydrogenation of acetylene to ethylene [14] and reduction of NO by H_2 [15]. Reviews by Hashmi and Hutchings [16], Corma and Garcia [17], Pina et al. [18] and Wittstock and Bäumer [19] provide comprehensive summaries of gold catalyzed reactions.

Many adsorbates and reactions have been studied on gold surfaces using a variety of experimental and theoretical methods. Because the main applications of gold catalyst are related to oxidation of CO and hydrogenation of CO, CO_2 [20–25] and NO [20, 26], the species involved in those reaction systems have been extensively studied on gold surfaces. Several experimental surface science techniques have been used to study the adsorption of O_2 and/or O on Au(111), such as: temperature-programmed desorption (TPD) [20, 27–32], high-resolution electron energy loss spectroscopy (HREELS) [28, 32], He diffraction [33], scanning tunneling microscopy (STM) [34], low-energy electron diffraction (LEED) [31, 32], XPS [32, 34] and Auger electron spectroscopy (AES) [32]. The adsorption of the atomic and molecular oxygen has been widely analyzed with density functional theory (DFT) calculations [27, 28, 35–37]. Oxygen does not chemisorb, molecularly or dissociatively, on clean gold surfaces under UHV conditions, nor at elevated temperature and pressure [20, 27]. To study the interaction between oxygen and gold surfaces, different approaches have been developed such as: thermal dissociation of gaseous O_2 on hot filaments, ozone decomposition, coadsorption of NO_2 and H_2O, O^+ sputtering, electron-induced adsorption of oxygen, and electron bombardment of condensed NO_2 [27]. Also, the oxidation of CO by gold catalysts has motivated a number of reaction studies and fundamental surface science investigations into the relevant intermediates. Stolcic et al. showed evidence of CO oxidation on small Au particles proceeding via molecular oxygen rather than atomic oxygen when O_2 is absorbed on free Au_2^- and Au_4^- particles at room temperature [38]. Moreover, an $^{18}O_2$ isotope study performed by Stiehl and coworkers with nanoparticles of Au supported on TiO_2 demonstrated a reaction pathway that does not require the dissociation of molecular

oxygen, such that O_2 can react directly with CO to form CO_2 [39]. These results were further substantiated with DFT calculations by Molina and coworkers showing that O_2 can react with CO adsorbed at the edge sites of Au particles leading to the formation of CO_2 with a low energy barrier of ~ 0.15 eV [40]. Among the experimental methods that have been employed for studying CO on Au(111) are: TPD [20, 41], infrared reflection absorption spectroscopy (IRAS) [41, 42], Fourier transform infrared spectroscopy (FTIR) [20, 43], [129]Xenon nuclear magnetic resonance ([129]Xe NMR) spectroscopy [20], diffuse-reflectance infrared Fourier transform spectroscopy (DRIFTS) [20], STM [42]. Fourier transform ion cyclotron resonance (FT-ICR) mass spectroscopy has been applied to study the co-adsorption of oxygen and CO on anionic gold clusters [44]. Several DFT studies have been performed for the adsorption of CO and the co-adsorption of CO with O or O_2 on Au(111) [45–48].

The chemisorption of molecular hydrogen on gold has been achieved on unsintered thin gold films at low temperature [49, 50]. For supported gold particles, the chemisorption of H_2 molecule has been reported, but amounts are small [20, 51]. H_2 dissociation is favorable on supported surfaces as proved by Fujitani and coworkers, and the active sites for H_2 dissociation on gold catalysts are thought to be at the interface between gold and the metal oxide support [52]. Despite the limited circumstances under which gold surfaces are found to chemisorb molecular hydrogen, the literature reveals a number of observations in which hydrogen molecules or atoms participate in reactions on gold. Some of these reactions include the hydrogenation of hydrocarbons (e.g., alkenes [53–55], alkadienes [56, 57] and alkynes [57]), both saturated and unsaturated ketones [57, 58] and carbon oxides [22, 57], hydrogenolysis [59, 60], dehydrogenation [61, 62] and

water-gas shift (WGS) reaction [16]. Furthermore, Azar and coworkers demonstrated with TPD experiments that hydrogen can regenerate their Au catalyst through the removal of the poisoning carbonate-like species produced during CO oxidation [63]. Sugawara et al. studied the reactions of cationic gold clusters Au_n^+ ($n = 1–12$) with H_2 using FT-ICR mass spectrometry [64]. Pessoa et al. analyzed the adsorption of several ionic and non-ionic species, among which is H, on the low-index gold surfaces Au(100), Au(110) and Au(111) using DFT calculations (B3LYP and GGA-PW91) [35]. Many other DFT studies of hydrogen adsorption on gold clusters have been performed [65–68].

It has been suggested that hydroxyl groups present on the surface of gold in aqueous solution promote reactions such as the oxidation of CO and glycerol [69–72]. Sanchez-Castillo and coworkers observed CO oxidation by O_2 at room temperature on gold nanotubes in polycarbonate membranes without the presence of a catalyst support, finding that the activity can be enhanced by performing the reaction in the aqueous phase, increasing the pH of the solution and using H_2O_2 as the oxidizing agent [73]. Ketchie et al. investigated the promotional effect of OH on the oxidation of both CO and glycerol in the aqueous phase, as a function of pH, over Au/C and Au/TiO_2 using transmission electron microscopy (TEM), near-edge X-ray absorption fine structure (NEXAFS) and X-ray absorption near edge structure (XANES) spectroscopy, high performance liquid chromatography (HPLC) and ultraviolet-visible (UV-VIS) spectroscopy [71]. They concluded that the hydroxyl groups adsorbed on the Au surface increase CO oxidation rates by facilitating the adsorption and activation of O_2 on the Au surface. Similarly, OH groups are necessary in order to activate glycerol by deprotonation of the primary alcohol group prior to the selective oxidation to glyceric acid over both gold catalysts. The

adsorption of the OH ion on Au(100), Au(110) and Au(111) was also analyzed by Pessoa and coworkers using DFT calculations [35].

For many reactions involving CO, CO_2, H_2 and water (e.g., WGS reaction), reaction intermediates such as formyl (HCO), COH, formate (HCOO), carboxyl (COOH) and bicarbonate (HCO_3) have been proposed as relevant species [69]. For that reason, Senanakaye and coworkers have investigated the role of formate, carbonate, and carboxyl as possible intermediates in the WGS reaction through the interaction of CO with OH ($OH_{ads} + CO_{gas} \rightarrow CO_{2,gas} + 0.5H_{2,gas}$) on Au(111) and O/Au(111) using synchrotron-based core level photoemission, NEXAFS, infrared absorption spectroscopy (IR) and DFT calculations [74]. Their results indicate that formate is not a key intermediate at low temperatures because HCOO is stable on Au(111) up to temperatures near 350 K. In fact, they suggest that the formation of this species could provoke surface poisoning. Moreover, the results of IR spectroscopy and photoemission spectroscopy point to HO-CO interactions, which are consistent with the formation of a COOH intermediate with a short lifetime on the gold surface [74]. On the other hand, Bond and Thompson, based on a reaction mechanism developed by Costello and coworkers [72], proposed a mechanism for CO oxidation on Au/Al_2O_3 where a bicarbonate species is involved. In this mechanism, an Au-OH species reacts with a CO molecule adsorbed on an under-coordinated gold atom to form a carboxyl species, which is then oxidized to bicarbonate. They suggest that the decomposition of bicarbonate would yield CO_2, and in the presence of water, COOH is formed. Thus, water and OH groups play an important role on this mechanism to facilitate CO oxidation through the formation of COOH [69].

Gold catalysts are very susceptible to poisoning, particularly with chloride ions. Supported Au catalysts are often prepared using $HAuCl_4$ as a precursor. Yang and coworkers have demonstrated using X-ray fluorescence (XRF), NEXAFS, XANES and high-resolution scanning transmission electron microscopy (STEM) that residual chloride can cause agglomeration of Au particles during heat treatment and suppresses its catalytic activity by poisoning active sites [75, 76]. On the other hand, the adsorption of chloride on gold can be advantageous for various applications in homogeneous and heterogeneous catalysis. Mercury can be removed from coal-fired boiler gas effluents by oxidizing it to $HgCl_2$ with chlorinating reagents over a gold catalyst [77] and chlorine also increases the selectivity of styrene epoxidation on Au(111) [78]. These potential applications of Cl on catalytic systems motivated Baker and coworkers to perform first-principles DFT calculations to study the nature of the interaction between Cl and the Au(111) surface, and they have reported evidence that this bonding is primarily of covalent character [79]. Lemoine and coworkers also studied the Eley-Rideal type reaction of Cl adsorbed on Au (111) with gas-phase H atoms using DFT [80]. The adsorption of chlorine on Au (111) also has been studied by various experimental (e.g., AES, XPS and UV photoelectron spectroscopy (UPS), LEED, TPD [81] and STM [82]) and theoretical techniques [82].

Although the catalytic properties of nanoscale gold have been extensively studied, the intrinsic mechanism of the heterogeneous catalysis at the atomic and molecular level has not been fully clarified. DFT studies can provide further insight into the fundamental surface science of gold catalysis. Similar to previous works on Pt(111) [83], Rh(111) [84], Ir(111) [85], Pd(111) [86], Ru(0001) [87] and Re(0001) [88] this work aims at performing

a systematic study of the chemisorption of several atomic and molecular species, and molecular fragments involved in gold catalyzed reactions. We study the adsorption of these species on the Au(111) facet, which is the thermodynamically most stable and prevalent configuration of supported gold nanoparticles [27]. While it has been observed that this surface reconstructs to the characteristic herringbone structure [89, 90] with an additional 4% of Au atoms incorporated into the surface layer, our calculations only account for reactions on the unreconstructed Au(111) surface. For this analysis, we have used periodic self-consistent DFT calculations to determine preferred binding sites, binding energies, vibrational modes and estimated diffusion barriers. The thermochemistry of several surface reactions on Au(111) is also examined. These DFT-derived results present a database of benchmarks that can be used for comparison with experiments, including state-of-the-art single crystal adsorption microcalorimetry [91, 92], and we compare our results to experimental results when available. Our data can be added to other electronically accessible databases, which have started appearing recently [93].

4.2 Methods

We have used DACAPO, a periodic self-consistent DFT-based total energy code [94], to analyze the adsorption of atoms, molecules and molecular fragments on the surface of Au(111) and to study the thermochemistry of simple reactions, such as hydrogenation of CO, CO_2 and NO. For these calculations, a 2x2 unit cell is used to construct a four-layer Au(111) slab with five equivalent layers of vacuum separating successive slabs. The top two layers of the slab are relaxed and the surface Brillouin zone is sampled at 54 Chadi-

Cohen *k*-points. The Kohn-Sham one-electron valence states are expanded in a basis of plane waves with kinetic energies up to 25 Ry [94], and the core electrons are described by ultrasoft pseudopotentials [95]. The exchange-correlation potential and energy are described self-consistently using the GGA-PW91 functional [96]. Energies are also calculated non-self-consistently using the RPBE [94] functional, and are provided in the text enclosed by square brackets next to the PW91 values (e.g., -2.01 [-1.97] eV). We note in passing that we also evaluated the binding energies of NH, HCO_3, and HCOO (species that have very large differences between the PW91 and RPBE results) self-consistently with the RPBE functional and found that the difference between the self-consistent and non-self-consistent results was < 0.1 eV. Therefore, we suggest that the differences in the PW91 and RPBE values reported, herein, are due to differences in the functional and not due to non-self-consistency. The self-consistent densities are determined by iterative diagonalization of the Kohn-Sham Hamiltonian, Fermi-population of the Kohn-Sham states ($k_BT = 0.1$ eV), and Pulay mixing of the resulting electronic density. All total energies are extrapolated to $k_BT = 0$ eV [94]. The results of our calculations are used to determine preferred binding sites, chemisorbed structures, binding energies, estimated diffusion barriers, surface deformation energies and the thermochemistry of molecular dissociation/formation, hydrogenation and oxidation reactions.

The calculated PW91 equilibrium lattice constant for bulk Au is 4.18 Å, which closely agrees with the experimental value of 4.0783 Å [97]. The binding energy (E_b) of an adsorbate X is calculated with respect to a clean relaxed Au(111) slab and the respective adsorbate in the gas phase as described by the following equation: $E_b = E_{substrate+adsorbate}$

$-\ E_{substrate}\ -\ E_{gas\text{-}phase\ adsorbate}$, where $E_{substrate+adsorbate}$ is the total energy of the relaxed Au(111) surface with an adsorbate, $E_{substrate}$ is the total energy of the relaxed clean Au(111) surface and $E_{gas\text{-}phase\ adsorbate}$ is the total energy of the isolated adsorbate. A negative binding energy is associated with an exothermic adsorption process. The deformation energy is defined as the change in surface energy upon the adsorption of a species. It is the energy difference between the relaxed clean surface and the deformed surface frozen after the adsorption with the adsorbate removed. Based on this definition, deformation energy is a positive quantity. Harmonic vibrational frequencies for each adsorbate are calculated by diagonalizing the mass-weighted Hessian matrix. The second derivatives of the energy were evaluated using a finite difference approximation [98]. The diffusion barrier of an adsorbate is estimated by first identifying a probable diffusion path that connects neighboring minima on the potential energy surface through a metastable state. Then, the energy of the lowest minimum is subtracted from the energy of the metastable site to give an estimated diffusion barrier. In general, for the atomic species, the diffusion path is from the fcc site to the adjacent hcp site by passing through a metastable bridge site.

4.3   Results and Discussion

In this section, properties obtained for different adsorbates on the Au(111) surface are described and compared with available experimental results. Results include binding energies (Tables 4.1 and 4.6, and Fig. 4.4), adsorption site preferences, adsorption geometries (Table 4.5 and Fig. 4.1), surface deformation energies (Table 4.4) and estimated diffusion barriers (Table 4.3 and Fig. 4.2). In addition, the vibrational modes

and their associated frequencies are given for the most stable configuration of each adsorbate on Au(111) (Tables 4.2, 4.7 and 4.8). Finally, we develop thermochemical potential energy surfaces (Figs. 4.5 and 4.6) for the decomposition of CO, NO, N_2, NH_3, CH_4, for the oxidation of CO, and for the hydrogenation of CO, CO_2 and NO, to assess the favorability of these processes on Au(111).

4.3.1 Adsorption of atomic species

4.3.1.1 Hydrogen (H)

Similar to Pt(111), as demonstrated by Ford et al., hydrogen is the least strongly bound atomic species to the Au(111) surface among those we studied [83]. Hydrogen prefers to bind on the fcc site as illustrated in Fig. 4.1. However, adsorption on the hcp site is only 0.04 eV higher in energy. As shown in Table 4.1, the calculated binding energy of H on the fcc site is -2.18 [-2.00] eV. The calculated Au-H vibrational frequency for the adsorbed H on the fcc site is 794 cm^{-1} (Table 4.2). The diffusion barrier from an fcc site to its adjacent hcp site passing through a bridge site is estimated to be only 0.15 [0.16] eV (Table 4.3 and Fig. 4.2). The estimated deformation caused by hydrogen adsorption on Au(111) is small with a value of 0.06 [0.03] eV (Table 4.4). This deformation is caused by pulling the contacting gold atom up 0.07 Å from its position in a clean relaxed slab and increasing the average distance between two adjacent Au atoms in contact with the adsorbate by 0.08 Å. Additional geometric information, as defined in Fig. 4.3, is supplied in Table 4.5.

Table 4.1. Binding energies (PW91 [RPBE]) and site preferences of atomic species on Au(111); the binding energies for the most stable site for each species are shown in bold.

Adsorbate	Preferred site		Binding Energy (eV)				
	Calc.	Exp.	top	hcp	fcc	bridge	Exp.
H	fcc		-1.87 [-1.72]	-2.14 [-1.96]	**-2.18 [-2.00]**		
C	fcc		-2.12 [-1.79]	-3.86 [-3.39]	**-4.03 [-3.54]**		
N	fcc		-0.88 [-0.64]	-1.94 [-1.53]	**-2.22 [-1.77]**		
O	fcc		-1.41 [-1.02]	-2.53 [-1.97]	**-2.77 [-2.19]**		-2.43[a]
F	fcc		-2.56 [-2.27]	-2.75 [-2.39]	**-2.77 [-2.41]**	-2.74 [-2.39]	
S	fcc	fcc[b]	-1.99 [-1.63]	-3.30 [-2.81]	**-3.50 [-2.98]**		
Cl	fcc		-2.10 [-1.79]	-2.29 [-1.88]	**-2.30 [-1.89]**	-2.28 [-1.89]	-2.34[c]

[a] O_2, TPD [35]; [b] S, STM [100]; [c] Cl_2, TPD [81]

4.3.1.2 Oxygen (O)

The preferred adsorption site for atomic oxygen is fcc (see Fig. 4.1), with an associated binding energy of -2.77 [-2.19] eV (Table 4.1). This value is in good agreement with the Au–O bond dissociation energy of -2.43 eV estimated by Saliba and collaborators in their TPD study of the adsorption of oxygen on Au(111) by exposure to ozone at 300 K [32, 35]. The calculated vibrational frequency of the Au-O stretch on the fcc site is 382 cm^{-1} (Table 4.2). Baker et al. observed this mode at 380 cm^{-1} using HREELS for atomic oxygen deposited by ozone decomposition on Au(111) at a surface temperature of 200 K and low oxygen coverage, concurring with our result [28]. In our analysis, the adsorption of the O atoms occurs at a height of 1.15 Å above the Au surface layer, corresponding to an Au-O bond length of 2.14 Å. This result is 0.10 Å longer than the experimental value of Au-O bond length obtained for oxygen coordinated to three Au atoms in bulk gold (III) oxide [99]. When oxygen is adsorbed, the contacting Au atoms are displaced 0.06 Å above their original position and the Au-Au bond distance between oxygen-adjacent Au atoms increases by 0.18 Å (Table 4.5). These changes on the Au surface produce a deformation energy of 0.22 [0.23] eV (Table 4.4). For the O atom, the diffusion path from

45

an fcc site to an hcp site passing through a bridge site has an estimated barrier of 0.56

[0.47] eV (Table 4.3 and Fig. 4.2).
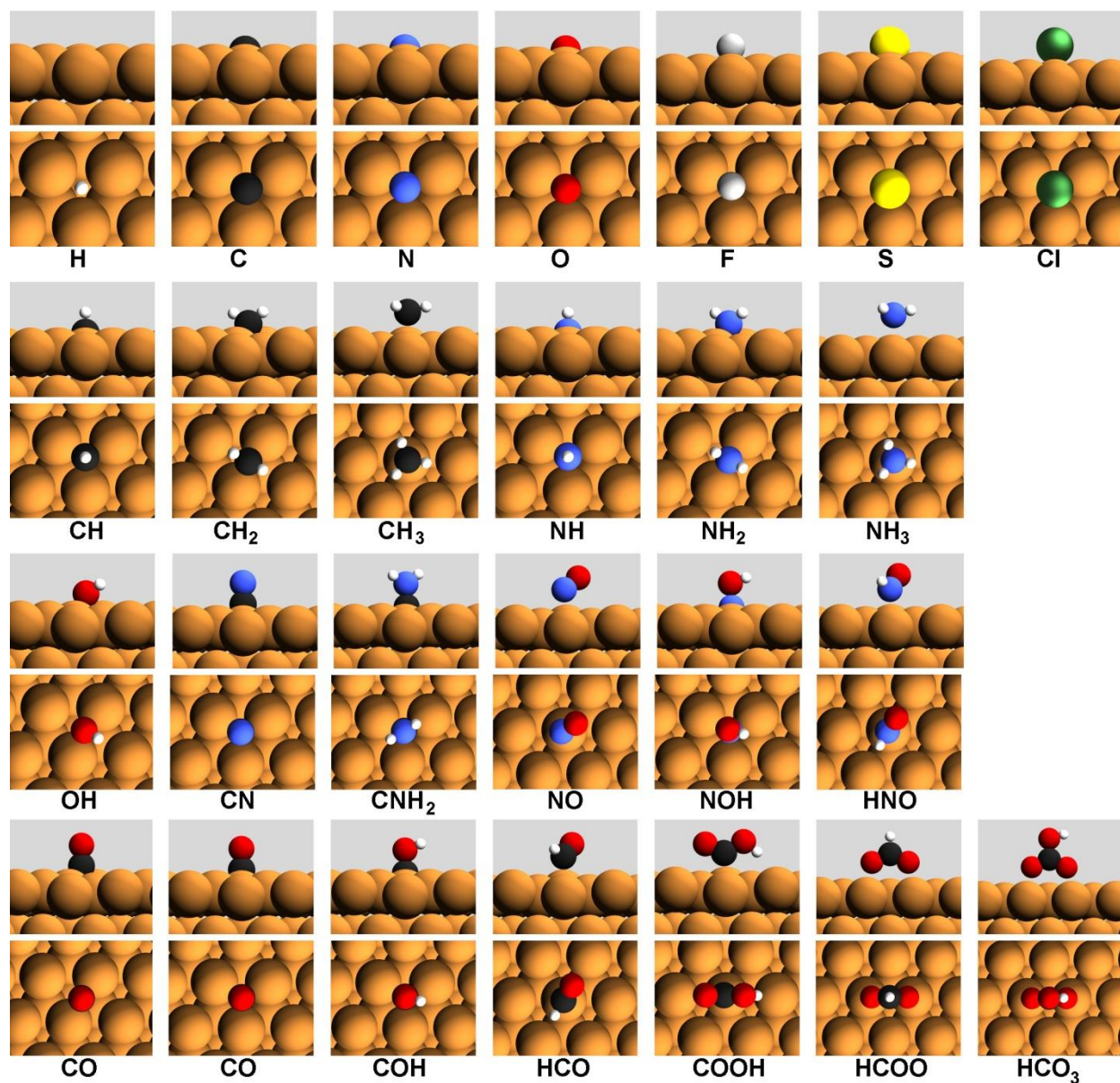
Fig. 4.1. Top and side views of the most stable configurations for the adsorption of selected adsorbates on Au(111). Table 5 provides the geometric details for these structures.

4.3.1.3   Nitrogen (N)

The fcc site is the most stable adsorption site for N with a binding energy of -2.22

[-1.77] eV. The calculated Au-N stretching frequency for this site is 430 cm^{-1}. A diffusion

barrier from an fcc to an hcp site passing through a bridge site was estimated and is 0.84 [0.78] eV, which is the highest barrier among the atomic species that we studied. Table 4.5 shows that nitrogen is adsorbed at a distance of 1.05 Å from the plane of Au(111) while the gold atoms in contact with this adsorbate move up by 0.08 Å from their position in a clean relaxed surface. These modifications in the structure of Au(111) result in a deformation energy of 0.15 [0.14] eV.

Table 4.2. Vibrational frequencies of adsorbed atomic species at fcc sites on Au(111).

Adsorbate	Calculated (cm^{-1})	Experimental (cm^{-1})
H	794	
C	415	
N	430	
O	382	380[a]
F	292	
S	289	
Cl	204	260[b]

[a] O, HREELS [28]; [b] Cl$^-$, SERS [103]

4.3.1.4   Sulfur (S)

Sulfur is the atomic species with the second strongest binding energy. This energy is -3.50 [-2.98] eV and it corresponds to adsorption at the fcc site. Our findings are in agreement with the experimental results obtained by Kurokawa et al., who confirmed that sulfur adsorbs on the fcc site of Au(111) using STM at 77 K [100]. Our results are also in agreement with the DFT work done by Rodríguez et al. [101], which showed that the adsorption of sulfur at low coverage on fcc hollow sites of Au(111) is energetically more favorable than adsorption on bridge or top sites. The S atom is adsorbed 1.61 Å above the surface, corresponding to a Au-S bond length of 2.40 Å. McGuirk et al. detected three adsorption phases using LEED: a (1 x 1) phase at low coverage, a (5 x 5) phase above 0.28 ML coverage, and a ($\sqrt{3}$ x $\sqrt{3}$)R30° phase above 0.30 ML [102]. From the (5 x 5)-7S

47

phase, they found that the S atoms occupy fcc sites, resting 1.57 Å above the Au surface (a 2.29 Å Au-S bond length), in good agreement with our results. Upon adsorption, the contacting plane of Au atoms is moved 0.05 Å upward from its relaxed position and the distance between two adjacent Au atoms is increased by 0.14 Å. This corresponds to a deformation energy of 0.19 [0.20] eV. Among the atomic species, sulfur is the adsorbate with the second highest deformation energy. This is consistent with the structural changes observed by Min and coworkers on the Au(111) surface when sulfur is adsorbed [89]. In particular, they demonstrated that the Au(111) herringbone reconstruction lifts during sulfur adsorption, which releases Au atoms from the surface. These structural changes were attributed to the reduction of tensile surface stress on Au(111) by charge redistribution, which is caused by the electronegativity of sulfur. The adsorption of other electronegative species, such as oxygen, also causes restructuring of Au(111). Min and coworkers indicate that the release of gold atoms caused by the adsorption of sulfur or oxygen on Au(111) enhances the catalytic activity for O_2 dissociation and SO_2 decomposition because of the formation of low-coordinated Au sites. Our DFT calculations estimated a vibrational frequency for S adsorbed at the fcc site of 289 cm^{-1}. The barrier to diffusion of S from an fcc to an hcp site through a bridge site is estimated to be 0.54 [0.47] eV.

4.3.1.5   Carbon (C)

As observed with other metal surfaces, such as Pt(111) [83], carbon binds more strongly to the Au(111) surface than all seven atomic species analyzed in this study, with a binding energy of -4.03 [-3.54] eV at the fcc site. Diffusion of a C atom from fcc to hcp

passing through a bridge site has an estimated barrier of 0.72 [0.69] eV. Vibrational

frequency calculations for C at the fcc site give an Au-C stretching frequency of 415 cm^{-1}. The calculated adsorption height for C on Au(111) is 0.96 Å. In addition, the outward

displacement of the Au atoms caused by the adsorbed C is 0.09 Å and the distance

between two neighboring Au atoms increases by 0.12 Å. These modifications on the

geometry yield a deformation energy of 0.13 [0.10] eV.

Table 4.3. Estimated diffusion barriers for various adsorbates on Au(111).

Adsorbate	Diffusion Barrier (eV)		Diffusion Path
	PW91	RPBE	
H	0.15	0.16	fcc-br-hcp[a]
C	0.72	0.69	fcc-br-hcp[a]
O	0.56	0.47	fcc-br-hcp[a]
N	0.84	0.78	fcc-br-hcp[a]
S	0.54	0.47	fcc-br-hcp[a]
Cl	0.02	0.00	fcc-br-hcp
F	0.03	0.02	fcc-br-hcp
OH	0.10	0.15	br-fcc
CO	0.00	*	fcc-br
NO	0.14	0.29	top-fcc
NH	0.73	0.63	fcc-br-hcp[a]
NH$_2$	0.31	0.17	br-top
NH$_3$	0.21	0.05	top-fcc
CH	0.90	0.90	fcc-br-hcp[a]
CH$_2$	0.87	0.81	br-top
CN	0.07	0.03	fcc-br
HNO	0.11	0.18	top-br
NOH	0.51	0.45	fcc-br-hcp[a]
COH	1.32	1.19	fcc-top
CNH$_2$	0.31	0.29	fcc-br-hcp[a]
HCO$_3$	0.53	0.44	top-br

* The diffusion barrier cannot be estimated because the calculated binding energy is positive (i.e. does not adsorb).
[a] The energy of the adsorbate at the metastable site was calculated by fixing the x and y coordinate of the atom through which the adsorbate binds over the metastable site with the x,y, and z coordinates of the slab atoms were fixed. All other degrees of freedom were relaxed.

4.3.1.6   Fluorine (F)

The most stable adsorption site for F is the fcc site with a binding energy of -2.77 [-2.41] eV. Slightly less stable adsorption of F occurs at the hcp and the bridge sites with binding energies of -2.75 [-2.39] and -2.74 [-2.39] eV, respectively. Consequently, the diffusion of F on Au(111) from an fcc site to an hcp site through the bridge site has an estimated barrier of only 0.03 [0.02] eV. The calculated Au-F stretching frequency for F adsorbed at the fcc site is 292 cm^{-1}. The adsorption of F takes place at a height of 1.65 Å from the Au surface. The deformation energy for the interaction of F with the Au(111) surface is 0.07 [0.10] eV, which is generated by the downward displacement by 0.03 Å of the Au atoms in contact with F and an increase of 0.09 Å in the distance between two contacting Au atoms.
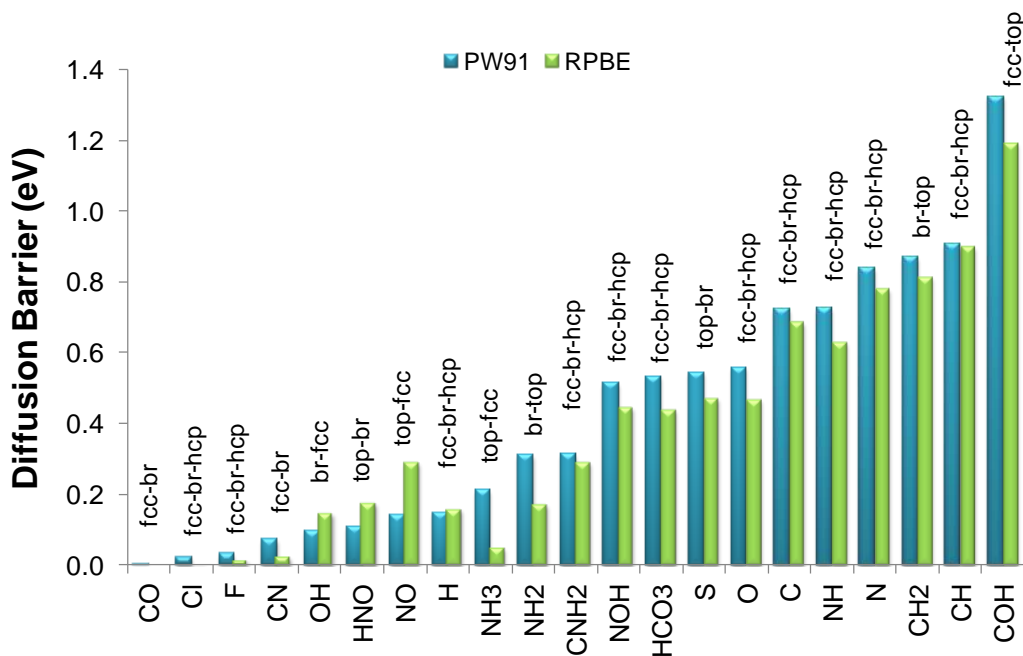
Fig. 4.2. Estimated diffusion barriers for various adsorbate species on Au(111).

Table 4.4. Deformation energy (ΔE) upon adsorption of each species on Au(111).

Adsorbate	Site	ΔE (eV)	
		PW91	RPBE
H	fcc	0.06	0.03
C	fcc	0.13	0.10
N	fcc	0.15	0.14
O	fcc	0.22	0.23
S	fcc	0.19	0.20
Cl	fcc	0.07	0.10
F	fcc	0.07	0.10
CO	fcc	0.09	0.06
CH	fcc	0.16	0.13
CH_2	bridge	0.20	0.16
CH_3	top	0.07	0.06
COH	fcc	0.16	0.12
HCO	top	0.07	0.06
CN	fcc	0.11	0.10
OH	bridge	0.09	0.10
NO	top	0.04	0.04
NH	fcc	0.34	0.33
NH_2	bridge	0.20	0.20
NH_3	top	0.01	0.01
NOH	fcc	0.27	0.26
HNO	top	0.02	0.03
COOH	top-H down	0.06	0.05
HCOO	top	0.03	0.06
CNH_2	fcc	0.16	0.14
HCO_3	top	0.03	0.07

4.3.1.7   Chlorine (Cl)

Atomic chlorine binds to the fcc site on Au(111) with a binding energy of -2.30 [-1.89] eV. This calculated energy agrees with a -2.34 eV Cl-Au bond dissociation energy estimated by Kastanas and Koel using TPD [81]. Moreover, the preferred site according to our calculations is consistent with the findings of Gao and coworkers in their DFT study, where they confirmed that the adsorption of chlorine on fcc site is the configuration of lowest energy [82]. Our calculated difference in energy between the fcc, hcp and bridge sites is within the error of the calculation, with a difference less than 0.02 eV. Hence, chlorine is the atomic species with the smallest estimated diffusion barrier, 0.02 [0.00] eV, to move from fcc to hcp through bridge. The calculated vibrational frequency for the Au-

Cl stretching is 204 cm^{-1}, which is similar to the experimental value of 260 cm^{-1} obtained by Tadayyoni and Weaver with surface-enhanced Raman spectroscopy (SERS) [103]. Chlorine is adsorbed at a height of 2.03 Å from the Au surface. The adjacent Au atoms are shifted 0.01 Å downwards from their original position. Using XRD, the Au-Cl bond length in bulk Au(III)Cl was found to be 2.23 Å [104], which is close to our calculated value of 2.69 Å. The deformation energy caused by these changes on the surface is 0.07 [0.10] eV.

Table 4.5. Adsorption geometry on Au(111).

Adsorbate	Z_{A-Au} (Å)	ΔZ_{Au} (Å)	d_{Au-Au} (Å)	d_{A-B} (Å)
H (fcc)	0.69	0.07	3.04	
C (fcc)	0.96	0.09	3.08	
N (fcc)	1.05	0.08	3.09	
O (fcc)	1.15	0.06	3.13	
F (fcc)	1.65	-0.03	3.05	
S (fcc)	1.61	0.05	3.10	
Cl (fcc)	2.03	-0.01	3.04	
CO (fcc)	1.36	0.09	3.05	1.19
CH (fcc)	1.04	0.12	3.09	1.10
CH$_2$ (bridge)	1.47	0.22	3.03	1.10
CH$_3$ (top)	2.13	0.22	2.97	1.09
COH (fcc)	1.11	0.13	3.09	1.34 (CO) 0.99 (OH)
HCO (top)	2.10	0.24	2.97	1.21 (CO) 1.11 (CH)
OH (bridge)	1.76	0.06	3.04	0.99
NO (top)	2.21	0.16	2.95	1.18
NH (fcc)	1.02	0.12	3.16	1.03
NH$_2$ (bridge)	1.58	0.15	3.08	1.02
NH$_3$ (top)	2.45	0.03	2.96	1.02
NOH (fcc)	1.12	0.10	3.14	1.41 (NO) 0.99 (OH)
HNO (top)	2.20	0.09	2.95	1.24 (NO) 1.05(NH)
COOH (top-H down)	2.13	0.20	2.96	1.21 (CO) 0.99 (OH) 1.33 (C-OH)
HCOO (top)	2.28	0.02	2.93	1.27 (CO) 1.11 (CH)
CN (fcc)	1.38	0.07	3.05	1.20
CNH$_2$ (fcc)	1.26	0.10	3.08	1.35 (CN) 1.02 (NH)
HCO$_3$ (top)	2.26	0.00	2.94	1.27 (CO*) 1.28 (CO$^\#$) 0.96 (OH) 1.11 (CH) 1.36 (C-OH)

See Fig. 4.3 for geometric definitions of these parameters.
* means CO group of the left side in HCO$_3$ molecule as depicted in Fig. 4.1.
# means CO group of the right side in HCO$_3$ molecule as depicted in Fig. 4.1.
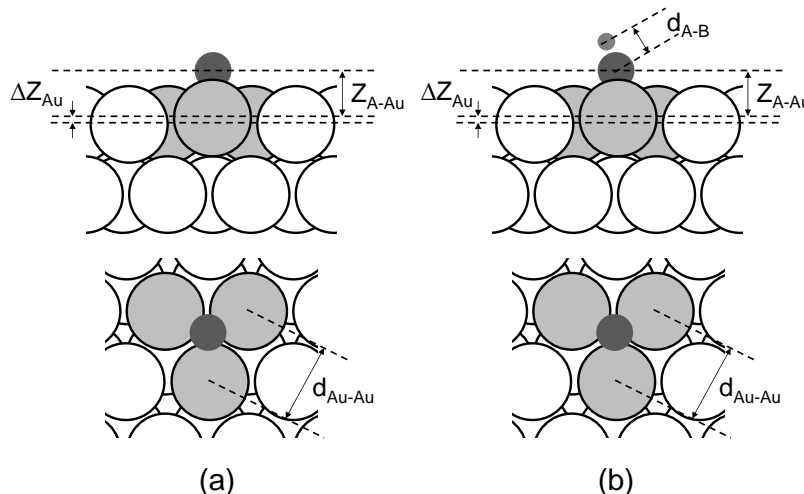
Fig. 4.3. Top and side view of geometric parameters for (a) atomic and (b) molecular adsorbates. Z_{A-Au} (Å) is the vertical distance between the adsorbate and the plane of Au in contact with it; ΔZ_{Au} (Å) is the change in vertical distance of the Au atoms in contact with the adsorbate and the plane of Au atoms on a clean relaxed surface; d_{Au-Au} is the average distance between adjacent Au atoms in contact with the adsorbate and this distance for two adjacent Au atoms on a relaxed clean surface is 2.96 Å; d_{A-B} is the bond length within an adsorbed species.

4.3.2 Adsorption of molecules and molecular fragments

4.3.2.1   Carbon monoxide (CO)

Our DFT calculations of CO adsorption on Au(111) indicate that adsorption at the fcc and bridge sites has the same binding energy of -0.36 [0.10] eV, while CO adsorbs at hcp and top sites with binding energies of -0.32 [0.14] eV and -0.31 [0.07] eV, respectively (Table 4.6). The preferred adsorption site for CO on Au(111) is different for the two DFT functionals used in this study. According to PW91, the preferred adsorption site is either the fcc or the bridge site. However, with the RPBE functional the lowest energy adsorption site for CO is the top site. A previous combined experimental and theoretical study (IRAS and DFT-GGA) concluded that CO adsorbs on top sites at low coverage [42], which is not in agreement with the adsorption site preferences obtained with PW91. It has been reported in the literature that DFT with non-hybrid functionals such as PW91 and RPBE

functionals tend to fail in predicting the correct adsorption site for strong pi-acceptor molecules such as CO [45, 46, 105]. Empirical corrections for the adsorption energy have been developed by Mason et al. [105] to improve the prediction of CO adsorption sites on metal surfaces obtaining results in agreement with experimental data. The binding energy for CO has been estimated using TPD and it is -0.43 eV [106]. Yim and coworkers also reported adsorption energies close to our results: -0.46 eV and -0.56 eV for the low-temperature programmed desorption peak and the high-temperature peak, respectively, which were calculated with experimental data obtained on Au(111) surfaces roughened by argon ion bombardment using a scanning tunneling microscopy / TPD system [107]. Yim et al. also studied the adsorption of CO on this surface using infrared spectroscopy, obtaining a C-O vibrational frequency of 2120 cm^{-1}. Our calculated vibrational frequency for the C-O vibrational mode when CO is adsorbed at the bridge site is 1983 cm^{-1} (Table 4.7), while it is at 1898 cm^{-1} when adsorbed at the fcc site. Our results, however, are in closer agreement to the frequency reported by Sun et al. of 1925-1975 cm^{-1} [108] using surface-enhanced infrared absorption spectroscopy (SEIRAS) on a Au film electrode. In contrast, Piccolo and coworkers found the mode at 2060 cm^{-1} between 1-100 torr pressure using IRAS [42], and they concluded that it is due to linearly adsorbed CO at the top site. This experimental frequency is similar to our calculated C-O stretch frequency at the top site, which is 2142 cm^{-1}. We also calculated frequencies for the Au-CO stretch at the fcc and bridge site at 233 cm^{-1} and 263 cm^{-1}, respectively. The latter value is close to the 290 cm^{-1} band determined by Tadayyoni and Weaver using SERS, which corresponds to the carbon-surface vibration generated during the CO adsorption on gold electrodes [103]. The diffusion path from fcc site to bridge site has an estimated barrier of 0.00 eV.

This diffusion barrier is the smallest of all the species analyzed in this study (see Fig. 4.2). According to our calculations, CO is adsorbed at the fcc site with the C atom bound to the surface at a distance of 1.36 Å from the surface. The C-O bond is parallel to the surface normal with a C-O bond length of 1.19 Å. A deformation energy of 0.09 [0.06] eV is caused by a vertical outward displacement of the contacting Au atoms from their original positions of 0.09 Å and a separation of 0.09 Å between adjacent Au atoms.

4.3.2.2 Methyl (CH_3), methylene (CH_2) and methylidyne (CH)

According to our calculations, CH_3 adsorbs only at the top site of Au(111), with a binding energy of -1.19 [-0.86] eV. CH_2 adsorbs most strongly to the bridge site, with a binding energy of -2.45 [-1.97] eV. Similar to other metal surfaces, such as Pt(111) [83], CH is the CH_x fragment and adsorbate with the strongest binding as illustrated in Fig. 4.4, with a binding energy of -4.34 [-3.75] eV at the fcc site.

The calculated frequency for the C-H stretching mode in CH is 3092 cm^{-1}. For CH_2, the estimated symmetric stretching mode has a frequency of 3041 cm^{-1}. Similarly, the calculated frequency for the C-H asymmetric stretching mode of CH_2 is 3137 cm^{-1}, for the scissoring mode of CH_2 is 1312 cm^{-1} and for the C-H twisting mode of CH_2 is 640 cm^{-1}. Our DFT calculations provided frequencies of 3032 and 3152-3153 cm^{-1} for the symmetric and asymmetric modes of CH_3, respectively.

As shown in Fig. 4.1, CH_3 is bound on a top site in a tetrahedral geometry through its carbon atom 2.13 Å above the surface and the C-H bonds (C-H bond lengths are 1.09 Å) are oriented 74° from the surface normal. The adsorption of CH_3 pulls the bound Au atom 0.22 Å out of the surface plane at a deformation cost of 0.07 [0.06] eV. On bridge sites,

CH$_2$ is bound through its carbon atom 1.47 Å above the surface with the 1.10 Å C-H bonds oriented 54° from the surface normal. This adsorption deforms the surface by 0.20 [0.16] eV. CH is adsorbed on fcc sites through its carbon atom, which is adsorbed 1.04 Å above the surface, corresponding to a Au-C bond length of 2.07 Å. The 1.10 Å C-H bond is oriented parallel to the surface normal. This adsorption slightly displaces the adjacent surface Au atoms by 0.12 Å vertically, and expands their Au-Au bond lengths to 3.09 Å. This deformation costs 0.16 [0.13] eV. The diffusion barriers have been estimated as 0.90 [0.90] eV for CH and 0.87 [0.81] eV for CH$_2$. We were unable to locate a metastable adsorption site for CH$_3$, therefore we have not estimated its diffusion barrier.

Table 4.6. Binding energies (PW91 [RPBE]) and site preferences of molecules and molecular fragments on Au(111). Entries in bold face signify preferred adsorption configurations.

Adsorbate	Preferred site		Binding Energy (eV)				
	Calc.	Exp.	top	fcc	hcp	bridge	Exp.
CO	fcc/bridge (PW91) top (RPBE)	top[d]	-0.31 [0.07]	**-0.36 [0.10]**	-0.32 [0.14]	**-0.36 [0.09]**	-0.43[a] -0.46[b], -0.56[c]
CH	fcc		--	**-4.34 [-3.75]**	-4.09 [-3.54]		
CH$_2$	bridge		-1.58 [-1.16]	--	--	**-2.45 [-1.97]**	
CH$_3$	top		**-1.19 [-0.86]**	--	--	--	
COH	fcc		-0.95 [-0.50]	**-2.27 [-1.70]**	--	--	
HCO	top		**-1.33 [-0.97]**	--	--	--	
CN	fcc		-2.52 [-2.23]	**-2.69 [-2.27]**	-2.62 [-2.22]	-2.62 [-2.25]	
OH	bridge		-1.51 [-1.08]	-1.60 [-1.03]	-1.55 [-1.00]	**-1.70 [-1.18]**	
NO	top		**-0.30 [0.06]**	-0.16 [0.35]	-0.10 [0.39]	--	-0.40[e]
NH	fcc		-0.67 [-0.27]	**-2.22 [-1.60]**	-1.93 [-1.34]		
NH$_2$	bridge		-1.12 [-0.73]	--	--	**-1.43 [-0.90]**	
NH$_3$	top		**-0.29 [0.00]**	-0.08 [0.05]	--	--	-0.34[f]
NOH	fcc		-1.61 [-1.09]	**-2.26 [-1.55]**	-2.04 [-1.35]		
HNO	top		**-2.74 [-2.26]**	--	--	-2.63 [-2.08]	
COOH	top-H down		**-1.47 [-1.01]** -1.40 [-0.98][#]	--	--	--	
HCOO	top*	top*[g]	**-1.86 [-1.29]**	--	--	--	
CNH$_2$	fcc		--	**-2.08 [-1.53]**	-1.90 [-1.39]	--	
HCO$_3$	top*		**-2.36 [-1.43]**	--	-1.72 [-0.86]	-1.83 [-0.99]	

No stable adsorption structure was obtained for entries indicated with "--"

[#] Two stable carboxyl (COOH) binding geometries were found over the top site, but they differ on the orientation of O-H bond. This value corresponds to the binding energy of the top site with the O-H bond oriented away from the surface.

* Indicates that two oxygen atoms of the species are respectively adsorbed on two gold atoms by the preferred site specified. This conformation is also named bidentate (η^2-O,O) configuration.

[a] CO, TPD [106]
[b] LTP, CO, STM/TPD [107]
[c] HTP, CO, STM/TPD [107]
[d] CO, STM [42]
[e] NO, TPD [111]
[f] NH$_3$, TPD [109]
[g] HCOOH/HCOO, bidentate (η^2-O,O) configuration, NEXAFS/IRAS/DFT [74]

4.3.2.3   COH intermediate and formyl (HCO) intermediate

The most stable adsorption site for COH is the fcc site, with a binding energy of -2.27 [-1.70] eV. The formyl intermediate (HCO) has a weaker interaction with Au(111), binding at the top site with a binding energy of -1.33 [-0.97] eV. Comparing the total reaction energies for the formation of both isomers on the gold surface, HCO adsorbed on Au(111) is more stable than the adsorbed COH isomer by 0.83 [1.03] eV. At fcc sites, COH is bound through its carbon atom, with the C-O bond axis parallel to the surface normal and the O-H bond oriented 69° away from the surface normal (see Fig. 4.1). The C-O bond length is 1.34 Å, while the O-H bond length is 0.99 Å. This adsorption causes a displacement of the gold atom bonded to COH outward by 0.13 Å and it increases the distance for two adjacent Au atoms by 0.13 Å. These geometric changes produce a surface deformation of 0.16 [0.12] eV on Au(111). HCO bound at the top site, has its C-H bond oriented 69° with respect to the surface normal and the C-O bond oriented 55° from the normal (the H-C-O bond angle is 124°). The C-O bond in adsorbed HCO is 1.21 Å, significantly shorter than in COH, and the C-H bond length is 1.11 Å. The adsorption of HCO pulls the bound Au atom 0.24 Å out of the surface plane, which has a deformation cost of 0.07 [0.06] eV. Additional geometric parameters are reported in Table 4.5. The diffusion barrier for COH was estimated to be 1.32 [1.19] eV, while we were unable to locate a metastable site to estimate the barrier for HCO diffusion. Vibrational modes for COH and HCO are reported in Table 4.8. For COH, we find the asymmetric O-H stretch at 3717 cm^{-1}, the asymmetric C-O stretch at 1239 cm^{-1}, the Au-COH stretch at 324 cm^{-1}, a scissoring mode at 1120 cm^{-1}, rocking modes at 389 and 437 cm^{-1}, and a twisting mode at 153 cm^{-1}. For HCO we found the asymmetric C-H stretch at 2897 cm^{-1}, the Au-HCO

stretch at 471 cm^{-1} and 223 cm^{-1}, a scissoring mode at 1166 cm^{-1}, a wagging mode at 729 cm^{-1}, and a twisting mode at 85 cm^{-1}.

Table 4.7. Vibrational frequencies (in cm^{-1}) of adsorbed diatomic species in their lowest energy configurations on Au(111).

Adsorbate	Calculated (cm^{-1})		Experimental (cm^{-1})	
	(IM)	(AS)	(IM)	(AS)
CO (fcc)	1898	233	2060[a]	
CO (br)	1983	263	1925-1975[b], 2060[a] 2120[c]	290[d]
CH (fcc)	3092	500		
CN (fcc)	2012	239	2100	370[e,h], 300[e,i]
OH (br)	3776	332	3750[f]	
NH (fcc)	3500	423		
NO (top)	1800	342	1810[g]	

IM stands for intramolecular, and AS stands for adsorbate-surface.
[a] CO (top site), IRAS [42]; [b] CO (bridge site), SEIRAS [108]; [c] CO, FTIR [107]
[d] CO, SERS [103]; [e] CN$^-$, SERS [114]; [f] O$_2$, FTIR [115]; [g] NO, DRIFTS [112]
[h] v(Au-CN); [i] δ(Au-CN)

4.3.2.4   Ammonia (NH$_3$), amide (NH$_2$) and imide (NH)

NH$_3$ prefers to bind at the top site of Au(111) with a binding energy of -0.29 [0.00] eV. This low binding energy is in excellent agreement with the experimental value of -0.34 eV estimated by Kay and coworkers using TPD [109]. NH$_2$ and NH bind more strongly to Au(111), with binding energies of -1.43 [-0.90] at the bridge site and -2.22[-1.60] eV at the fcc site, their preferred adsorption sites respectively. The calculated vibrational frequencies for NH are 3500 cm^{-1} for the N-H stretching and 423 cm^{-1} for Au-NH stretching. The symmetric and asymmetric mode of NH$_2$, and the symmetric stretching for NH$_3$ have frequencies of 3473, 3598 and 3442 cm^{-1}, respectively. NH$_3$ shows the N-H asymmetric stretching mode at 3609 and 3611 cm^{-1}. NH$_3$ is adsorbed at a height of 2.45 Å from the surface and the N-H bond lengths are 1.02 Å, which are in good agreement with the experimental gas phase value of 1.012 Å [110]. The adsorption of NH$_3$ slightly distorts the surface, with a deformation energy of 0.01 [0.01] eV. NH$_2$ is adsorbed through its N atom 1.58 Å above the surface with a Au-N bond length of 2.20 Å

and the 1.02 Å N-H bonds oriented 55° from the surface normal. The Au atoms bound to NH$_2$ are pulled 0.15 Å out of the relaxed surface and their Au-Au bond distance expands to 3.08 Å, which causes a surface deformation of 0.20 [0.20] eV. NH binds 1.02 Å above the surface, corresponding to a Au-N bond length of 2.09 Å. The N-H bond is 1.03 Å and is oriented parallel to the surface normal. Interestingly, NH adsorption induces the most-positive deformation energy of all adsorbates in this study, with a value of 0.34 [0.33] eV. This adsorption stretches the Au-Au bond lengths between N-adjacent Au atoms by 0.21 Å. Diffusion barriers are estimated for NH$_3$, NH$_2$, and NH as 0.21 [0.05] eV, 0.31 [0.17] eV, and 0.73 [0.63] eV.
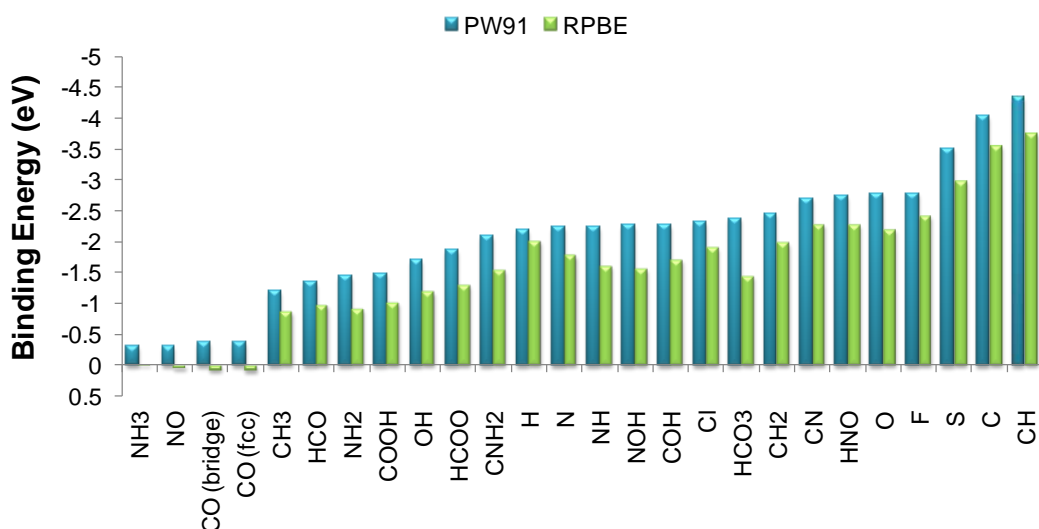
Fig. 4.4. Binding energies on Au(111) for the most stable site of each species.

4.3.2.5   Nitric oxide (NO)

Nitric oxide adsorbs at the top, fcc, and hcp sites with binding energies of -0.30 [0.06], -0.16 [0.35], and -0.10 [0.39] eV, respectively. An experimentally estimated binding energy of -0.4 eV was reported by McClure and coworkers using TPD [111], in agreement with our calculated top site adsorption mode. We calculated the N-O stretching frequency

at 1800 cm^{-1} and the Au-NO stretching at 342 cm^{-1}. Debeila and coworkers reported an experimental N-O stretching frequency of 1810 cm^{-1} on Au/TiO$_2$ using DRIFTS [112] in reasonable agreement with our results. NO adsorbs on Au(111) through its N atom at a height of 2.21 Å from the surface. The N-O bond axis is tilted 63° away from the surface normal with an N-O bond length of 1.18 Å (see Fig. 4.1). The deformation on the surface caused by the NO adsorption has an energy of 0.04 [0.04] eV. NO adsorbed on Au(111) is estimated to diffuse from the top site to the fcc site with an energy barrier of 0.14 [0.29] eV.

4.3.2.6   Nitrosyl hydride (NOH, HNO)

The minimum energy site for the adsorption of NOH on Au(111) is the fcc site, while HNO adsorbs most strongly at the top site. The binding energies of these species were calculated with respect to isolated NO and isolated H, both in the gas phase. They are -2.26 [-1.55] eV and -2.74 [-2.26] eV, respectively. Since these binding energies are referenced to the same state, we can conclude that HNO is more stable on Au(111) than NOH. The vibrational modes calculated for NOH are at 3704 cm^{-1}, 1271 cm^{-1}, 896 cm^{-1}, 399 cm^{-1}, 393 cm^{-1}, 247 cm^{-1}, and 166 cm^{-1}, while HNO has the following vibrational frequencies: 3078 cm^{-1}, 1504 cm^{-1}, 1381 cm^{-1}, 353 cm^{-1}, 194 cm^{-1}, 112 cm^{-1}, and 55 cm^{-1} (see Table 4.8). NOH binds through its N atom 1.12 Å above the surface with the N-O bond oriented nearly parallel with the surface normal. The N-O bond length is 1.41 Å, which is significantly longer than that of NO. The N-O-H bond angle is 106° and the O-H bond is 0.99 Å. HNO is adsorbed through its N atom at a height of 2.20 Å above the surface. The N-H bond length is 1.05 Å and it is oriented 65° away from the surface

normal. The N-O bond length is 1.24 Å and it is oriented 48° away from the surface normal. The Au surface is deformed more significantly upon the adsorption of NOH compared to the adsorption of HNO, with calculated deformation energies of 0.27 [0.26] eV and 0.02 [0.03] eV, respectively. The diffusion barrier for NOH is estimated to be 0.51 [0.45] eV and for HNO 0.11 [0.18] eV.

Table 4.8. Vibrational frequencies (in cm^{-1}) of adsorbed polyatomic species in their lowest energy configurations on Au(111).

Modes	NH$_3$	NH$_2$	CNH$_2$	NOH	HNO	CH$_3$	CH$_2$
	top	bridge	fcc	fcc	top	top	bridge
Symmetric IM stretch	3442	3473	3486[c] 1298[d]			3032	3041
Asymmetric IM stretch	3609 3611	3598	3602[c]	896[b] 3704[a]	1504[b] 3078[c]	3152 3153	3137
AS stretch	152	373	321	247	353 194	432	478
Scissoring	1570 1571	1450	1545	1271	1381	1388 1391	1312
Rocking	389 405	551	1072 398	399/ 393	112	709 714	636
Wagging	929	617	291	166		1105	778
Twisting	43	671	391		55		640

[a] v(O-H); [b] v(N-O); [c] v(N-H); [d] v(C-N)

Modes	HCO	COH	HCOO		COOH	HCO$_3$	
	top	fcc	top*	Exp.	top-H down	top*	Exp.
Symmetric IM stretch			1308[g] 2935[e]	1332[g, i] 2824[e, i]	1821[f] 3618[a]	1023[h] 1394[g] 3782[a]	1440[g, j] 3610[a, j]
Asymmetric IM stretch	2897[e] 1821[f]	3717[a] 1239[f]	1574[g]		1115 1183	1558[g]	1650[g, j]
AS stretch	471 223	324	72 90 248		83 96 230	58 79 222	
Scissoring	1166	1120	732		633	598 650	
Rocking		389 437	259 1285		219	190	
Wagging	729		965		443	91 537 1199	
Twisting	85	153	63		86 592	54 750	

* means that two atoms of the species are adsorbed on the preferred site specified.
[e] v(C-H); [f] v(C-O); [g] v(O-C-O); [h] v(CO$_3$); [i] HCOOH/HCOO, IRAS [74]; [j] CO, FTIR [113]

4.3.2.7   Carboxyl (COOH), formate (HCOO) and bicarbonate (HCO$_3$)

The minimum energy adsorption structure for carboxyl is obtained when the species adsorbs at the top site through its carbon atom at a distance of 2.13 Å from the bound Au atom, with the hydrogen atom of the hydroxyl group oriented towards the surface (see Fig. 4.1). The bond lengths of C-O, O-H and C-OH for COOH are: 1.21 Å, 0.99 Å and 1.33 Å, respectively. The binding energy for this configuration is -1.47 [-1.01] eV. When the hydrogen atom of the hydroxyl group is oriented away from the surface, the binding energy is 0.07 [0.03] eV more positive (see Table 4.6). Formate adsorbs in a bidentate (η^2-O,O) configuration as illustrated in Fig. 4.1, with its two oxygen atoms bonded to the surface by a Au-O length of 2.28 Å. This result is in agreement with the experimental observations reported by Senanayake and coworkers using NEXAFS and IR spectroscopy [74].This preferred configuration has both C-O bond lengths corresponding to 1.27 Å and a C-H bond length of 1.11 Å. The binding energy for HCOO adsorbed on Au(111) is -1.86 [-1.29] eV. Adsorbed formate and carboxyl are isomers of each other, and in that form, adsorbed HCOO is more stable than adsorbed COOH by 0.12 [0.10] eV. The binding energy for HCO$_3$ was calculated with respect to isolated CO$_2$ and OH gas phase species, and it is -2.36 [-1.43] eV. The preferred site for the adsorption of bicarbonate is the top site, also with two O atoms absorbed on Au(111) at a height of 2.26 Å, see Fig. 4.1. Details of calculated bond lengths of adsorbed HCO$_3$ are provided in Table 4.5.

A deformation energy of only 0.06 [0.05] eV was estimated for the adsorption of COOH on Au(111). This deformation results by the outward displacement of 0.20 Å for the bound Au atom from its relaxed position. The Au-Au bond lengths between neighboring Au

atoms remained unchanged. The adsorptions of HCOO and HCO_3 cause similar surface deformations, with energies of 0.03 [0.06] eV and 0.03 [0.07] eV, respectively. When HCOO is adsorbed on Au(111), the vertical displacement of the Au atoms is only 0.02 Å and the distance between two adjacent Au atoms increases by 0.03 Å. Similarly, when HCO_3 is adsorbed, no vertical displacement of the upper gold plane in the surface is observed and the Au-Au bond length is expanded by 0.02 Å.

The vibrational modes for COOH were calculated obtaining the C-O symmetric stretching at 1821 cm^{-1} and the O-H symmetric stretching at 3618 cm^{-1}. Senanayake et al. found the O-C-O symmetric stretching mode and the C-H stretching mode for HCOO at 1332 and 2824 cm^{-1} using IRAS [74]. These experimental values are in good agreement with our vibrational frequencies of 1308 and 2935 cm^{-1} that correspond to the symmetric stretching of the bonds O-C-O and C-H in HCOO, respectively. HCO_3 has three symmetric stretching modes at 1023 cm^{-1} for CO_3, 1394 cm^1 for O-C-O and 3782 cm^{-1} for O-H, and an asymmetric stretching mode at 1558 cm^{-1} for O-C-O. Similar vibrational modes were obtained by Roze and coworkers for the O-C-O and O-H symmetric stretching, and the O-C-O asymmetric stretching in HCO_3 using FTIR: 1440, 3610 and 1650 cm^{-1}, respectively [113]. Other vibrational modes for COOH, HCOO and HCO_3 are summarized on Table 4.8. The diffusion of HCO_3 on the surface through the path from top site to bridge site has an estimated energy barrier of 0.53 [0.44] eV. Diffusion barriers for COOH and HCOO were not calculated because we were unable to locate a metastable site for the adsorption of these species.

4.3.2.8   Hydrogen cyanide (HCN), cyanide (CN) and aminomethylidyne (CNH$_2$)

According to our calculations, HCN does not adsorb on Au(111), while CN adsorbs with a binding energy of -2.69 [-2.27] eV and CNH$_2$ adsorbs with a binding energy of -2.08 [-1.53] eV. Both of these species prefer adsorption at fcc sites. CN is adsorbed on Au(111) through its C atom 1.38 Å above the surface. The C-N bond length is 1.20 Å and it is oriented parallel to the surface normal. The plane of Au atoms in contact with CN is moved 0.07 Å upward and the distance between the contacting Au atoms increases by 0.09 Å. The overall cost of this deformation is 0.11 [0.10] eV. CNH$_2$ adsorbs through its carbon atom at 1.26 Å above the surface with the C-N bond axis (bond length of 1.35 Å) oriented parallel to the surface normal. The N-H bonds lengths are 1.02 Å and the H-N-H bond angle is 117°. Adsorption causes the Au atoms in contact with CNH$_2$ to rise by 0.10 Å from their relaxed positions with an associated deformation energy of 0.16 [0.14] eV. The calculated vibrational frequencies for CN include the C-N stretching mode at 2012 cm^{-1} and the Au-CN stretch at 239 cm^{-1}. Beltramo et al. used SERS to evaluate the vibrational modes of CN$^-$ adsorbed on a gold electrode finding the C-N stretch at around 2100 cm^{-1} and the Au-CN stretching and bending modes at ~370 and ~300 cm^{-1}, respectively [114], which are in reasonable agreement with our calculated results. We find a number of CNH$_2$ vibrational modes, including a symmetric N-H stretch at 3486 cm^{-1}, a symmetric C-N stretch at 1298 cm^{-1}, an asymmetric N-H stretch at 3602 cm^{-1}, the Au-CNH$_2$ stretch at 321 cm^{-1}, a scissoring mode at 1545 cm^{-1}, rocking modes at 1072 and 398 cm^{-1}, a wagging mode at 291 cm^{-1}, and a twisting mode at 391 cm^{-1}. CN diffuses easily from the fcc to the bridge site with an estimated energy barrier of 0.07 [0.03] eV. CNH$_2$ has an estimated diffusion barrier from the fcc to the hcp site of 0.31 [0.29] eV.

4.3.2.9 Hydroxyl (OH)

OH adsorbs preferentially at the bridge site with a binding energy of -1.70 [-1.18] eV. The OH adsorption occurs at a height of 1.76 Å from the Au(111) surface and the bond length between O and H is 0.99 Å. Adsorption pulls the O-adjacent Au atoms out from the surface by 0.06 Å and expands their Au-Au bond distance by 0.08 Å. The energy associated with this deformation is 0.09 [0.10] eV. The vibrational frequency corresponding to the OH stretching, v(OH), is 3776 cm^{-1}, which approaches a sharp v(OH) band at 3750 cm^{-1} observed by Brooker and coworkers analyzing the reduction of O_2 on a Au electrode in alkaline solution using FTIR [115]. The stretching mode for Au-OH is 332 cm^{-1}. The diffusion barrier of OH from the bridge site to the fcc site is estimated to 0.10 [0.15] eV.

4.3.3 Thermochemistry of possible surface reactions

The PW91 binding energies of all the species in their preferred adsorption sites, along with their gas phase energies, were used to calculate reaction energies for the decomposition, hydrogenation, and oxidation of various species. Energy diagrams which describe possible pathways for these surface reactions are shown in Fig. 4.5 and Fig. 4.6. Some of these reactions are discussed below.

4.3.3.1 CO₂ hydrogenation to carboxyl or formate; and OC-O bond dissociation:

$$CO_{2\,(g)} + \tfrac{1}{2}H_{2\,(g)} \rightarrow CO_{2\,(g)} + H_{(a)} \rightarrow COOH_{(a)} \qquad \Delta E_{rxn} = 0.46\ eV$$
$$CO_{2\,(g)} + \tfrac{1}{2}H_{2\,(g)} \rightarrow CO_{2\,(g)} + H_{(a)} \rightarrow HCOO_{(a)} \qquad \Delta E_{rxn} = 0.34\ eV$$
$$COOH_{(a)} \rightarrow CO_{(a)} + OH_{(a)} \qquad \Delta E_{rxn} = 1.33\ eV$$
$$HCOO_{(a)} \rightarrow HCO_{(a)} + O_{(a)} \qquad \Delta E_{rxn} = 2.70\ eV$$
$$CO_{2\,(g)} \rightarrow CO_{(a)} + O_{(a)} \qquad \Delta E_{rxn} = 3.04\ eV$$

This thermochemistry suggests that CO_2 hydrogenation is unfavorable on Au(111). For hydrogenation, first hydrogen must dissociatively adsorb on Au(111) ($H_{2\,(g)} \rightarrow 2H_{(a)}$), which is endothermic by 0.20 eV. Subsequently, CO_2 is hydrogenated to COOH or HCOO. These reactions are endothermic by 0.36 eV and 0.24 eV, respectively (see Fig. 5). The direct scission of the OC-O bond in CO_2 is endothermic by 3.04 eV. The OC-O bond in COOH can be broken to produce CO and OH, which is endothermic by 1.33 eV, while the decomposition of HCOO to HCO and O is endothermic by 2.70 eV. Overall, these results suggest that Au(111) would be a poor catalyst for CO_2 hydrogenation. It is thermodynamically favorable for any adsorbed hydrogen to desorb rather than to hydrogenate CO_2. Furthermore, our results suggest that the most thermochemically efficient method of breaking the OC-O bond is through the COOH intermediate, producing $CO_{(a)}$ + $OH_{(a)}$.

4.3.3.2 Formation of COH and HCO via hydrogenation of CO; and C-O bond scission:

$$CO_{(g)} + \tfrac{1}{2}H_{2\,(g)} \rightarrow CO_{(a)} + H_{(a)} \qquad\qquad \Delta E_{rxn} = -0.26\ eV$$
$$CO_{(g)} + \tfrac{1}{2}H_{2\,(g)} \rightarrow COH_{(a)} \qquad\qquad \Delta E_{rxn} = 0.47\ eV$$
$$CO_{(g)} + \tfrac{1}{2}H_{2\,(g)} \rightarrow HCO_{(a)} \qquad\qquad \Delta E_{rxn} = -0.37\ eV$$
$$COH_{(a)} \rightarrow C_{(a)} + OH_{(a)} \qquad\qquad \Delta E_{rxn} = 2.44\ eV$$
$$HCO_{(a)} \rightarrow CH_{(a)} + O_{(a)} \qquad\qquad \Delta E_{rxn} = 2.86\ eV$$
$$CO_{(a)} \rightarrow C_{(a)} + O_{(a)} \qquad\qquad \Delta E_{rxn} = 4.52\ eV$$

The hydrogenation of CO requires the adsorption of CO (ΔE_{rxn} = -0.36 eV) and the adsorption of H_2 (ΔE_{rxn} = 0.20 eV), as illustrated in Fig. 4.5. CO hydrogenation can occur at the carbon atom to produce HCO (ΔE_{rxn} = -0.11 eV) or at the oxygen atom to produce COH (ΔE_{rxn} = 0.73 eV). The net reaction energies (starting from CO(g) and ½H$_2$(g)) are -

0.37 eV and 0.47 eV, respectively. The direct dissociation of adsorbed CO is endothermic

by 4.52 eV (see Fig. 4.6). Alternatively, the C-O bond can be broken by the decomposition

of COH or HCO to C + OH or CH + O, respectively. The reaction energies for these

respective pathways are 2.44 eV and 2.86 eV. Overall, these results show that CO

hydrogenation to HCO is more thermodynamically favorable than to COH on Au (111). In

fact, it is more favorable for CO to be hydrogenated to HCO than for CO and H to desorb

from Au(111). Also, the C-O bond is most favorably broken by proceeding through an

HCO intermediate on Au(111).
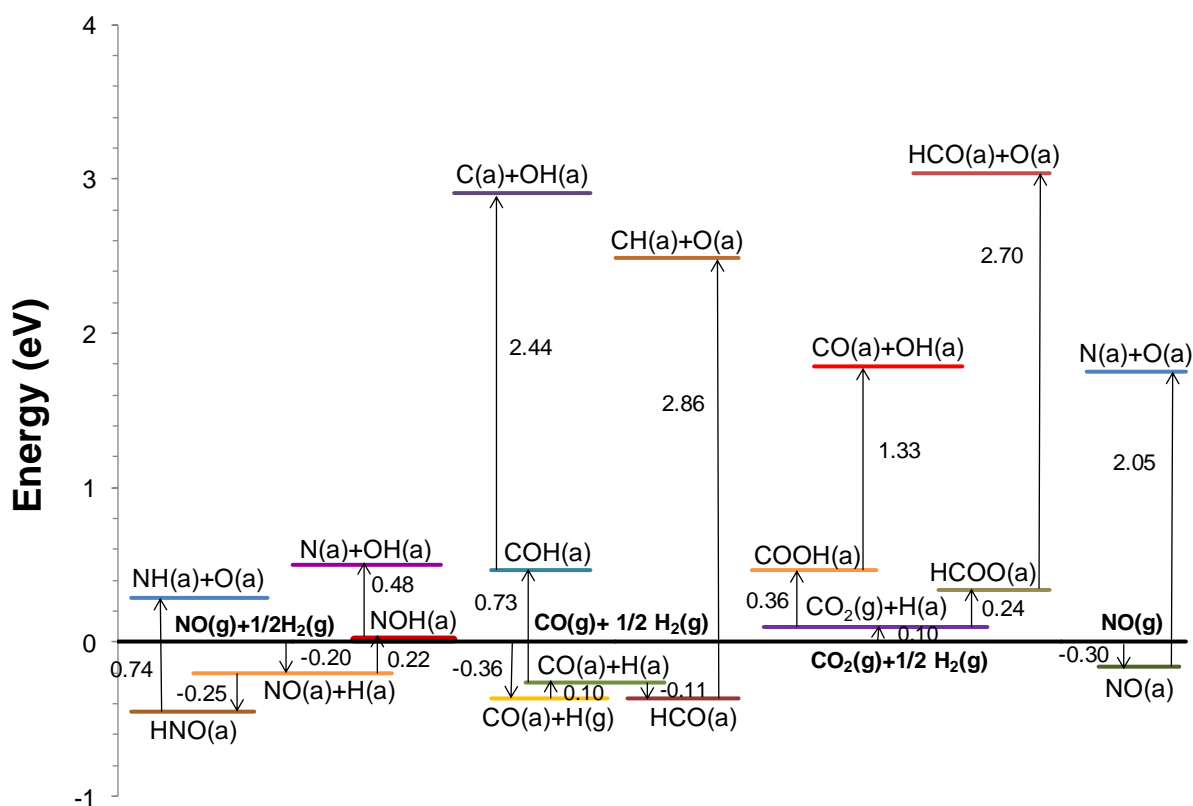
Fig. 4.5. Thermochemistry for the hydrogenation of NO, CO and CO_2, and for the molecular decomposition of NO. The reference zero corresponds to the energy of the isolated species in gas-phase and the energy of the clean relaxed Au(111) slab at infinite separation. Energies are calculated using the PW91 functional and the change in energy is labeled next to each arrow on the diagram.

4.3.3.3 Formation of NOH and HNO through the hydrogenation of NO; and N-O bond scission:

$NO_{(g)} + \frac{1}{2}H_{2\,(g)} \rightarrow NO_{(a)} + H_{(a)}$	$\Delta E_{rxn} = -0.20\ eV$
$NO_{(g)} + \frac{1}{2}H_{2\,(g)} \rightarrow NOH_{(a)}$	$\Delta E_{rxn} = 0.02\ eV$
$NO_{(g)} + \frac{1}{2}H_{2\,(g)} \rightarrow HNO_{(a)}$	$\Delta E_{rxn} = -0.45\ eV$
$NOH_{(a)} \rightarrow N_{(a)} + OH_{(a)}$	$\Delta E_{rxn} = 0.48\ eV$
$HNO_{(a)} \rightarrow NH_{(a)} + O_{(a)}$	$\Delta E_{rxn} = 0.74\ eV$
$NO_{(a)} \rightarrow N_{(a)} + O_{(a)}$	$\Delta E_{rxn} = 2.05\ eV$

NO adsorbs on Au(111) with a binding energy of -0.30 eV (see Fig. 4.5), while the dissociative adsorption of H_2 requires 0.20 eV. As shown in Fig. 4.5, $NO_{(a)}$ would more favorably be hydrogenated at the N atom to produce HNO (ΔE_{rxn} = -0.25 eV) than on the O atom to produce NOH, which has a reaction energy of 0.22 eV. The net reaction (beginning from NO(g) and ½H₂(g)) for formation of HNO is thermochemically favorable, while the corresponding net reaction for NOH is practically thermoneutral. The N-O bond in adsorbed NO can be directly dissociated with a reaction energy of 2.05 eV. The N-O bond can be dissociated in hydrogenated NO via NOH to N + OH (ΔE_{rxn} = 0.48 eV) or HNO to NH + O (ΔE_{rxn} = 0.74 eV). Similar to CO, all of this thermochemistry suggests that NO, in the presence of hydrogen, is more likely to be hydrogenated to HNO than to desorb from Au(111). Furthermore, these results indicate that the most efficient method of breaking the N-O bond is by first hydrogenating to HNO and then breaking the bond to form NH + O.

4.3.3.4 CO oxidation to CO₂:

$CO_{(g)} \rightarrow CO_{(a)}$	$\Delta E_{rxn} = -0.36\ eV$
$O_{2\,(g)} \rightarrow 2O_{(a)}$	$\Delta E_{rxn} = 0.10\ eV$
$CO_{(a)} + O_{(a)} \rightarrow CO_{2\,(g)}$	$\Delta E_{rxn} = -3.04\ eV$

The oxidation of CO proceeds by adsorption of CO and O_2 on the surface. CO adsorbs mildly with an adsorption energy of -0.36 eV, while the activated dissociative adsorption of O_2 is endothermic by 0.10 eV. The reaction between adsorbed CO and adsorbed atomic oxygen to liberate gas phase CO_2 is very exothermic, with ΔE_{rxn} = -3.04 eV (see Fig. 4.6). Compared to other reactions studied on Au(111), this is the most thermodynamically favorable reaction. This result is in agreement with the experiments that show that this catalyst has high catalytic activity for the oxidation of CO [16, 116, 117]. Clearly, kinetic limitations to activating the O-O bond control the overall reaction rate.

4.3.3.5   Decomposition of CH_4, NH_3, and N_2:

We find that N_2 does not adsorb on Au(111) and that its activated dissociative adsorption is highly unfavorable (ΔE_{rxn} = 5.20 eV), as illustrated in Fig. 4.6. Also, methane does not adsorb on Au(111), and its activated dissociative adsorption, $CH_{4(g)} \rightarrow CH_{3(a)}$ + $H_{(a)}$ is endothermic by 1.31 eV. All subsequent dehydrogenation steps, leading to the formation of adsorbed atomic carbon, are also endothermic with reaction energies of 1.47 eV, 0.77 eV and 1.77 eV for the second, third and fourth dehydrogenation steps, respectively. Ammonia binds to Au(111) with a binding energy of -0.29 eV. The dehydrogenation of ammonia is endothermic with reaction energies of 1.47 eV, 1.24 eV, and 1.57 eV for the first, second, and third dehydrogenation steps, respectively. As a result, it is more favorable for ammonia to desorb from Au(111) than to be dehydrogenated.
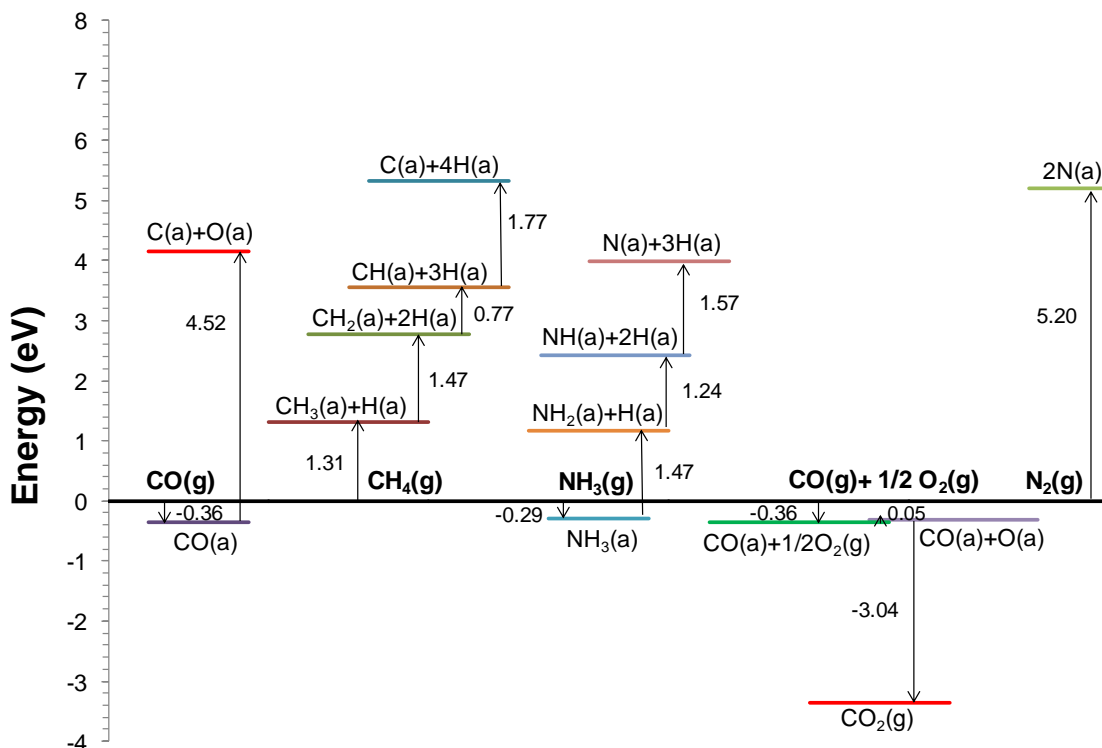
Fig. 4.6. Thermochemistry for the molecular decomposition of CO, CH_4, NH_3 and N_2, and for the oxidation of CO. The reference zero corresponds to the energy of the isolated species in gas-phase and the energy of the clean relaxed Au(111) slab at infinite separation. Energies are calculated using the PW91 functional and the change in energy is labeled next to each arrow on the diagram.

4.4 Conclusions

The adsorption of several atomic (H, O, N, S, C, F and Cl) and molecular species (CO, NO, N_2, HCN and NH_3), and molecular fragments (CH_3, CH_2, CH, COH, HCO, NH_2, NH, OH, NOH, HNO, COOH, HCOO, HCO_3, CN and CNH_2) on Au(111) has been studied using periodic self-consistent DFT calculations. The preferred binding sites, binding energies and binding geometries of the species along with their estimated diffusion energy barriers were determined. For all the adsorbates on their most energetically stable adsorption site, the intramolecular and adsorbate-surface vibrational frequencies were calculated. The theoretical results were compared with experimental values found in the

literature, when available, and most of these values are in good agreement, indicating that our calculations can correctly predict the experimental observations. In general, the PW91 functional is more accurate than RPBE for estimating the binding energies of the species adsorbed on Au(111). The RPBE functional tends to underestimate these energies. Our results demonstrate that atomic species tend to bind on Au(111) more strongly than molecular fragments. All the atomic species analyzed adsorb preferentially at fcc sites. Molecular species and fragments do not show any clear preference for the adsorption site.

The thermochemistry for the adsorption and decomposition reactions of CH_4, CO, NO, NH_3 and N_2, hydrogenation of CO, CO_2 and NO, and oxidation of CO were also studied on Au(111). Reaction energies were calculated and used to determine the most thermodynamically favorable reactions. These reaction energies demonstrate that the decomposition of species is not favorable on Au(111), showing that the desorption of NH_3, NO and CO is preferable to the decomposition of these species. Thus, these theoretical results suggest that in general, bond-making events are facile on Au(111) while bond-breaking events are more difficult. Moreover, the oxidation of CO and hydrogenation of CO and NO to HCO and HNO, respectively, are thermodynamically favored on Au(111). The intermediates COOH and HCOO can be formed by the hydrogenation of CO_2 requiring moderately endothermic reaction energies, HCOO being more stable than COOH. Of all the reactions analyzed on Au(111), the oxidation of CO is the most favored on this surface, in accord with numerous experimental reports on the subject.

References

[1]   M. Haruta, T. Kobayashi, H. Sano, N. Yamada, Novel gold catalysts for the oxidation of carbon monoxide at a temperature far below 0°C, Chem. Lett. 16 (1987) 405–408.

[2]   M. Haruta, N. Yamada, T. Kobayashi, S. Iijima, Gold catalysts prepared by coprecipitation for low-temperature oxidation of hydrogen and of carbon monoxide, J. Catal. 115 (1989) 301–309.

[3]   G.J. Hutchings, Vapor phase hydrochlorination of acetylene: Correlation of catalytic activity of supported metal chloride catalysts, J. Catal. 96 (1985) 292–295.

[4]   G.J. Hutchings, M. Haruta, A golden age of catalysis: A perspective, Appl. Catal. A 291 (2005) 2–5.

[5]   A.K. Sinha, S. Seelan, S. Tsubota, M. Haruta, A Three-Dimensional Mesoporous Titanosilicate Support for Gold Nanoparticles: Vapor-Phase Epoxidation of Propene with High Conversion, Angew. Chem. Int. Ed. 43 (2004) 1546–1548.

[6]   T. Hayashi, K. Tanaka, M. Haruta, Selective Vapor-Phase Epoxidation of Propylene over Au/TiO_2 Catalysts in the Presence of Oxygen and Hydrogen, J. Catal. 178 (1998) 566–575.

[7]   S. Carrettin, P. McMorn, P. Johnston, K. Griffin, C.J. Kiely, G.A. Attard, G.J. Hutchings, Oxidation of Glycerol Using Supported Gold Catalysts, Top. Catal. 27 (2004) 131–136.

[8]   F. Porta, L. Prati, Selective oxidation of glycerol to sodium glycerate with gold-on-carbon catalyst: an insight into reaction selectivity, J. Catal. 224 (2004) 397–403.

[9]   S. Demirel-Gülen, M. Lucas, P. Claus, Liquid phase oxidation of glycerol over carbon supported gold catalysts, Catal. Today 102–103 (2005) 166–172.

[10]   F. Porta, L. Prati, M. Rossi, S. Coluccia, G. Martra, Metal sols as a useful tool for heterogeneous gold catalyst preparation: reinvestigation of a liquid phase oxidation, Catal. Today 61 (2000) 165–172.

[11]   G. Li, J. Edwards, A.F. Carley, G.J. Hutchings, Direct synthesis of hydrogen peroxide from H_2 and O_2 using zeolite-supported Au catalysts, Catal. Today 114 (2006) 369–371.

[12]   P. Landon, P.J. Collier, A.J. Papworth, C.J. Kiely, G.J. Hutchings, Direct formation of hydrogen peroxide from H_2/O_2 using a gold catalyst, Chem. Commun. (2002) 2058–2059.

[13]   J. Edwards, B. Solsona, P. Landon, A. Carley, A. Herzing, C. Kiely, G. Hutchings, Direct synthesis of hydrogen peroxide from H_2 and O_2 using TiO_2-supported Au–Pd catalysts, J. Catal. 236 (2005) 69–79.

[14]   T.V. Choudhary, C. Sivadinarayana, A.K. Datye, D. Kumar, D.W. Goodman, Acetylene Hydrogenation on Au-Based Catalysts, Catal. Lett. 86 (2003) 1–8.

[15]   T.M. Salama, R. Ohnishi, T. Shido, M. Ichikawa, Highly Selective Catalytic Reduction of NO by H_2 over Au^0 and Au(I) Impregnated in NaY Zeolite Catalysts, J. Catal. 162 (1996) 169–178.

[16]   A.S.K. Hashmi, G.J. Hutchings, Gold Catalysis, Angew. Chem. Int. Ed. 45 (2006) 7896–7936.

[17] A. Corma, H. Garcia, Supported gold nanoparticles as catalysts for organic reactions, Chem. Soc. Rev. 37 (2008) 2096–2126.

[18] C.D. Pina, E. Falletta, L. Prati, M. Rossi, Selective oxidation using gold, Chem. Soc. Rev. 37 (2008) 2077–2095.

[19] A. Wittstock, M. Bäumer, Catalysis by Unsupported Skeletal Gold Catalysts, Acc. Chem. Res. 47 (2014) 731-739.

[20] G.C. Bond, D.T. Thompson, Catalysis by Gold, Catal. Rev.: Sci. Eng. 41 (1999) 319–388.

[21] H. Sakurai, M. Haruta, Synergism in methanol synthesis from carbon dioxide over gold catalysts supported on metal oxides, Catal. Today 29 (1996) 361–365.

[22] H. Sakurai, M. Haruta, Carbon dioxide and carbon monoxide hydrogenation over gold supported on titanium, iron, and zinc oxides, Appl. Catal. A 127 (1995) 93–105.

[23] Baiker, M. Kilo, M. Maciejewski, S. Menzi, A. Wokaun, Hydrogenation of CO_2 Over Copper, Silver and Gold/Zirconia Catalysts: Comparative Study of Catalyst Properties and Reaction Pathways, in: Studies in Surface Science and Catalysis, Elsevier, 1993, pp. 1257–1272.

[24] H. Sakurai, S. Tsubota, M. Haruta, Hydrogenation of CO_2 over gold supported on metal oxides, Appl. Catal. A 102 (1993) 125–136.

[25] M. Shibata, N. Kawata, T. Masumoto, H. Kimura, CO hydrogenation over an amorphous gold-zirconium alloy, Chem. Lett. (1985) 1605–1608.

[26] A. Ueda, M. Haruta, Nitric Oxide Reduction with Hydrogen, Carbon Monoxide, and Hydrocarbons over Gold Catalysts, Gold Bull. 32 (1999) 3–11.

[27] J. Gong, C.B. Mullins, Surface Science Investigations of Oxidative Chemistry on Gold, Acc. Chem. Res. 42 (2009) 1063–1073.

[28] T.A. Baker, B. Xu, X. Liu, E. Kaxiras, C.M. Friend, Nature of Oxidation of the Au(111) Surface: Experimental and Theoretical Investigation, J. Phys. Chem. C 113 (2009) 16561–16564.

[29] R.A. Ojifinni, J. Gong, N.S. Froemming, D.W. Flaherty, M. Pan, G. Henkelman, C.B. Mullins, Carbonate Formation and Decomposition on Atomic Oxygen Precovered Au(111), J. Am. Chem. Soc. 130 (2008) 11250–11251.

[30] R.A. Ojifinni, J. Gong, D.W. Flaherty, T.S. Kim, C.B. Mullins, Annealing Effect on Reactivity of Oxygen-Covered Au(111), J. Phys. Chem. C 113 (2009) 9820–9825.

[31] K.A. Davis, D.W. Goodman, Propene Adsorption on Clean and Oxygen-Covered Au(111) and Au(100) Surfaces, J. Phys. Chem. B 104 (2000) 8557–8562.

[32] N. Saliba, D.. Parker, B.. Koel, Adsorption of oxygen on Au(111) by exposure to ozone, Surf. Sci. 410 (1998) 270–282.

[33] K.D. Gibson, S.J. Sibener, O Atom Induced Gradual Deconstruction of the 23 × √3 Au(111) Surface, J. Phys. Chem. A 111 (2007) 12398–12401.

[34] B.K. Min, A.R. Alemozafar, D. Pinnaduwage, X. Deng, C.M. Friend, Efficient CO Oxidation at Low Temperature on Au(111), J. Phys. Chem. B 110 (2006) 19833–19838.

[35] A.M. Pessoa, J.L.C. Fajín, J.R.B. Gomes, M.N.D.S. Cordeiro, Ionic and radical adsorption on the Au(hkl) surfaces: A DFT study, Surf. Sci. 606 (2012) 69–77.

[36] D. Torres, K.M. Neyman, F. Illas, Oxygen atoms on the (111) surface of coinage metals: On the chemical state of the adsorbate, Chem. Phys. Lett. 429 (2006) 86–90.

[37] L. Barrio, P. Liu, J.A. Rodriguez, J.M. Campos-Martin, J.L.G. Fierro, Effects of Hydrogen on the Reactivity of O_2 toward Gold Nanoparticles and Surfaces, J. Phys. Chem. C 111 (2007) 19001–19008.

[38] D. Stolcic, M. Fischer, G. Ganteför, Y.D. Kim, Q. Sun, P. Jena, Direct Observation of Key Reaction Intermediates on Gold Clusters, J. Am. Chem. Soc. 125 (2003) 2848–2849.

[39] J.D. Stiehl, T.S. Kim, S.M. McClure, C.B. Mullins, Reaction of CO with Molecularly Chemisorbed Oxygen on TiO_2-Supported Gold Nanoclusters, J. Am. Chem. Soc. 126 (2004) 13574–13575.

[40] L.M. Molina, M.D. Rasmussen, B. Hammer, Adsorption of O_2 and oxidation of CO at Au nanoparticles supported by TiO_2(110), J. Chem. Phys. 120 (2004) 7673–7680.

[41] C. Lemire, R. Meyer, S.K. Shaikhutdinov, H.-J. Freund, CO adsorption on oxide supported gold: from small clusters to monolayer islands and three-dimensional nanoparticles, Surf. Sci. 552 (2004) 27–34.

[42] L. Piccolo, D. Loffreda, F.J. Cadete Santos Aires, C. Deranlot, Y. Jugnet, P. Sautet, J.C. Bertolini, The adsorption of CO on Au(1 1 1) at elevated pressures studied by STM, RAIRS and DFT calculations, Surf. Sci. 566–568, Part 2 (2004) 995–1000.

[43] J.H. Yang, J.D. Henao, M.C. Raphulu, Y. Wang, T. Caputo, A.J. Groszek, M.C. Kung, M.S. Scurrell, J.T. Miller, H.H. Kung, Activation of Au/TiO_2 Catalyst for CO Oxidation, J. Phys. Chem. B 109 (2005) 10319–10326.

[44] I. Balteanu, O.P. Balaj, B.S. Fox, M.K. Beyer, Z. Bastl, V.E. Bondybey, Very low rate constants of bimolecular CO adsorption on anionic gold clusters: Implications for catalytic activity, Phys. Chem. Chem. Phys. 5 (2003) 1213–1218.

[45] F. Abild-Pedersen, M.P. Andersson, CO adsorption energies on metals with correction for high coordination adsorption sites – A density functional study, Surf. Sci. 601 (2007) 1747–1753.

[46] M. Gajdoš, A. Eichler, J. Hafner, CO adsorption on close-packed transition and noble metal surfaces: trends from ab initio calculations, J. Phys. : Condens. Matter 16 (2004) 1141–1164.

[47] N. Lopez, T.V.. Janssens, B.. Clausen, Y. Xu, M. Mavrikakis, T. Bligaard, J.. Nørskov, On the origin of the catalytic activity of gold nanoparticles for low-temperature CO oxidation, J. Catal. 223 (2004) 232–235.

[48] I.N. Remediakis, N. Lopez, J.K. Nørskov, CO oxidation on gold nanoparticles: Theoretical studies, Appl. Catal. A 291 (2005) 13–20.

[49] L. Stobiński, L. Zommer, R. Duś, Molecular hydrogen interactions with discontinuous and continuous thin gold films, Appl. Surf. Sci. 141 (1999) 319–325.

[50] A. Corma, M. Boronat, S. González, F. Illas, On the activation of molecular hydrogen by gold: a theoretical approximation to the nature of potential active sites, Chem. Commun. (2007) 3371–3373.

[51] P. Claus, Heterogeneously catalysed hydrogenation using gold catalysts, Appl. Catal. A 291 (2005) 222–229.

[52] T. Fujitani, I. Nakamura, T. Akita, M. Okumura, M. Haruta, Hydrogen Dissociation by Gold Clusters, Angew. Chem. Int. Ed. 48 (2009) 9515–9518.

[53] G.C. Bond, P.A. Sermon, Gold catalysts for olefin hydrogenation, Gold Bull. 6 (1973) 102–105.

[54] S. Naito, M. Tanimoto, Mechanism of deuterium addition and exchange of propene over silica-supported gold and silver catalysts, J. Chem. Soc., Faraday Trans. 1 84 (1988) 4115–4124.

[55] P.A. Sermon, G.C. Bond, P.B. Wells, Hydrogenation of alkenes over supported gold, J. Chem. Soc., Faraday Trans. 1 75 (1979) 385–394.

[56] D.A. Buchanan, G. Webb, Catalysis by group IB metals. Part 1.—Reaction of buta-1,3-diene with hydrogen and with deuterium catalysed by alumina-supported gold, J. Chem. Soc., Faraday Trans. 1 71 (1975) 134–144.

[57] M. Haruta, Size- and support-dependency in the catalysis of gold, Catal. Today 36 (1997) 153–166.

[58] C.T.H. Stoddart, C. Kemball, The catalytic hydrogenation of acetone on evaporated metallic films, J. Colloid Sci. 11 (1956) 532–542.

[59] M. Boudart, L.D. Ptak, Reactions of neopentane on transition metals, J. Catal. 16 (1970) 90–96.

[60] G. Meitzner, W.J. Mykytka, J.H. Sinfelt, Metal-catalyzed reactions of methylamine in the presence of hydrogen, J. Catal. 98 (1986) 513–521.

[61] J. Erkelens, C. Kemball, A.K. Galwey, Some reactions of cyclohexene with hydrogen and deuterium on evaporated gold films, Trans. Faraday Soc. 59 (1963) 1181–1191.

[62] J.G. Hardy, M.W. Roberts, Mechanism of the catalytic decomposition of methanol on gold filaments, J. Chem. Soc. D (1971) 494–495.

[63] M. Azar, V. Caps, F. Morfin, J.-L. Rousset, A. Piednoir, J.-C. Bertolini, L. Piccolo, Insights into activation, deactivation and hydrogen-induced promotion of a Au/TiO_2 reference catalyst in CO oxidation, J. Catal. 239 (2006) 307–312.

[64] K. Sugawara, F. Sobott, A.B. Vakhtin, Reactions of gold cluster cations Au_n^+(n=1–12) with H_2S and H_2, J. Chem. Phys. 118 (2003) 7808–7816.

[65] L. Barrio, P. Liu, J.A. Rodríguez, J.M. Campos-Martín, J.L.G. Fierro, A density functional theory study of the dissociation of H_2 on gold clusters: Importance of fluxionality and ensemble effects, J. Chem. Phys. 125 (2006) 164715-1–164715-5.

[66] S. Zhao, Y. Ren, Y. Ren, J. Wang, W. Yin, Density Functional Study of Hydrogen Binding on Gold and Silver−Gold Clusters, J. Phys. Chem. A 114 (2010) 4917–4923.

[67] G.-J. Kang, Z.-X. Chen, Z. Li, X. He, A theoretical study of the effects of the charge state and size of gold clusters on the adsorption and dissociation of H_2, J. Chem. Phys. 130 (2009) 034701–034701–6.

[68] H.W. Ghebriel, A. Kshirsagar, Adsorption of molecular hydrogen and hydrogen sulfide on Au clusters, J. Chem. Phys. 126 (2007) 244705–244705–9.

[69] the late David Thompson, G. Bond, Formulation of mechanisms for gold-catalysed reactions, Gold Bull. 42 (2009) 247–259.

[70] H.H. Kung, M.C. Kung, C.K. Costello, Supported Au catalysts for low temperature CO oxidation, J. Catal. 216 (2003) 425–432.

[71] W.C. Ketchie, M. Murayama, R.J. Davis, Promotional effect of hydroxyl on the aqueous phase oxidation of carbon monoxide and glycerol over supported Au catalysts, Top. Catal. 44 (2007) 307–317.

[72] C.K. Costello, J.H. Yang, H.Y. Law, Y. Wang, J.-N. Lin, L.D. Marks, M.C. Kung, H.H. Kung, On the potential role of hydroxyl groups in CO oxidation over Au/Al$_2$O$_3$, Appl. Catal. A 243 (2003) 15–24.

[73] M.A. Sanchez-Castillo, C. Couto, W.B. Kim, J.A. Dumesic, Gold-Nanotube Membranes for the Oxidation of CO at Gas–Water Interfaces, Angew. Chem. Int. Ed. 43 (2004) 1140–1142.

[74] S.D. Senanayake, D. Stacchiola, P. Liu, C.B. Mullins, J. Hrbek, J.A. Rodriguez, Interaction of CO with OH on Au(111): HCOO, CO$_3$, and HOCO as Key Intermediates in the Water-Gas Shift Reaction, J. Phys. Chem. C 113 (2009) 19536–19544.

[75] J.H. Yang, J.D. Henao, C. Costello, M.C. Kung, H.H. Kung, J.T. Miller, A.J. Kropf, J.-G. Kim, J.R. Regalbuto, M.T. Bore, H.N. Pham, A.K. Datye, J.D. Laeger, K. Kharas, Understanding preparation variables in the synthesis of Au/Al$_2$O$_3$ using EXAFS and electron microscopy,Appl. Catal. A 291 (2005) 73–84.

[76] H.-S. Oh, J.H. Yang, C.K. Costello, Y.M. Wang, S.R. Bare, H.H. Kung, M.C. Kung, Selective Catalytic Oxidation of CO: Effect of Chloride on Supported Au Catalysts, J. Catal. 210 (2002) 375–386.

[77] Y. Zhao, M.D. Mann, J.H. Pavlish, B.A.F. Mibeck, G.E. Dunham, E.S. Olson, Application of Gold Catalyst for Mercury Oxidation by Chlorine, Environ. Sci. Technol. 40 (2006) 1603–1608.

[78] D.S. Pinnaduwage, L. Zhou, W. Gao, C.M. Friend, Chlorine Promotion of Styrene Epoxidation on Au(111), J. Am. Chem. Soc. 129 (2007) 1872–1873.

[79] T.A. Baker, C.M. Friend, E. Kaxiras, Nature of Cl Bonding on the Au(111) Surface: Evidence of a Mainly Covalent Interaction, J. Am. Chem. Soc. 130 (2008) 3720–3721.

[80] D. Lemoine, J.G. Quattrucci, B. Jackson, Efficient Eley-Rideal Reactions of H Atoms with Single Cl Adsorbates on Au(111), Phys. Rev. Lett. 89 (2002) 268302.

[81] G.N. Kastanas, B.E. Koel, Interaction of Cl$_2$ with the Au(111) surface in the temperature range of 120 to 1000 K, Appl. Surf. Sci. 64 (1993) 235–249.

[82] W. Gao, T.A. Baker, L. Zhou, D.S. Pinnaduwage, E. Kaxiras, C.M. Friend, Chlorine Adsorption on Au(111): Chlorine Overlayer or Surface Chloride?, J. Am. Chem. Soc. 130 (2008) 3560–3565.

[83] D.C. Ford, Y. Xu, M. Mavrikakis, Atomic and molecular adsorption on Pt(111), Surf. Sci. 587 (2005) 159–174.

[84] M. Mavrikakis, J. Rempel, J. Greeley, L.B. Hansen, J.K. Nørskov, Atomic and molecular adsorption on Rh(111), J. Chem. Phys. 117 (2002) 6737–6744.

[85] W.P. Krekelberg, J. Greeley, M. Mavrikakis, Atomic and Molecular Adsorption on Ir(111), J. Phys. Chem. B 108 (2004) 987–994.

[86] J.A. Herron, S. Tonelli, M. Mavrikakis, Atomic and molecular adsorption on Pd(111), Surf. Sci. 606 (2012) 1670–1679.

[87] J.A. Herron, S. Tonelli, M. Mavrikakis, Atomic and molecular adsorption on Ru(0001), Surf. Sci. 614 (2013) 64–74.

[88] K. Hahn, M. Mavrikakis, Atomic and Molecular Adsorption on Re(0001), Top. Catal. 57 (2014) 54–68.

[89] B.K. Min, A.R. Alemozafar, M.M. Biener, J. Biener, C.M. Friend, Reaction of Au(111) with Sulfur and Oxygen: Scanning Tunneling Microscopic Study, Top. Catal. 36 (2005) 77–90.

[90] H. Bulou, C. Massobrio, Dynamical behavior of Co adatoms on the herringbone reconstructed surface of Au(111), Superlattices Microstruct. 36 (2004) 305–313.

[91] C.E. Borroni-Bird, N. Al-Sarraf, S. Andersoon, D.A. King, Single crystal adsorption microcalorimetry, Chem. Phys. Lett. 183 (1991) 516–520.

[92] M.C. Crowe, C.T. Campbell, Adsorption Microcalorimetry: Recent Advances in Instrumentation and Application, Annu. Rev. Anal. Chem. 4 (2011) 41–58.

[93] J.S. Hummelshøj, F. Abild-Pedersen, F. Studt, T. Bligaard, J.K. Nørskov, CatApp: A Web Application for Surface Chemistry and Heterogeneous Catalysis, Angew. Chem. Int. Ed. 51 (2012) 272–274.

[94] B. Hammer, L.B. Hansen, J.K. Nørskov, Improved adsorption energetics within density-functional theory using revised Perdew-Burke-Ernzerhof functionals, Phys. Rev. B 59 (1999) 7413–7421.

[95] D. Vanderbilt, Soft self-consistent pseudopotentials in a generalized eigenvalue formalism, Phys. Rev. B 41 (1990) 7892–7895.

[96] J.P. Perdew, J.A. Chevary, S.H. Vosko, K.A. Jackson, M.R. Pederson, D.J. Singh, C. Fiolhais, Atoms, molecules, solids, and surfaces: Applications of the generalized gradient approximation for exchange and correlation, Phys. Rev. B 46 (1992) 6671–6687.

[97] V. Milman, B. Winkler, J.A. White, C.J. Pickard, M.C. Payne, E.V. Akhmatskaya, R.H. Nobes, Electronic structure, properties, and phase stability of inorganic crystals: A pseudopotential plane-wave study, Int. J. Quantum Chem. 77 (2000) 895–910.

[98] J. Greeley, M. Mavrikakis, A first-principles study of surface and subsurface H on and in Ni(1 1 1): diffusional properties and coverage-dependent behavior, Surf. Sci. 540 (2003) 215–229.

[99] T.A. Baker, C.M. Friend, E. Kaxiras, Atomic Oxygen Adsorption on Au(111) Surfaces with Defects, J. Phys. Chem. C 113 (2009) 3232–3238.

[100] S. Kurokawa, Y. Miyawaki, A. Sakai, Scanning Tunneling Microscopy Observation of Sulfur Adsorbates on Au(111) at Liquid Nitrogen Temperature, Jpn. J. Appl. Phys. 48 (2009) 08JB12-1–08JB12-5.

[101] J.A. Rodriguez, J. Dvorak, T. Jirsak, G. Liu, J. Hrbek, Y. Aray, C. González, Coverage Effects and the Nature of the Metal−Sulfur Bond in S/Au(111): High-Resolution Photoemission and Density-Functional Studies, J. Am. Chem. Soc. 125 (2002) 276–285.

[102] G.M. McGuirk, H. Shin, M. Caragiu, S. Ash, P.K. Bandyopadhyay, R.H. Prince, R.D. Diehl, Au(111) surface structures induced by adsorption: LEED I(E) analysis of (1 × 1) and (5 × 5) Au(111)–S phases, Surf. Sci. 610 (2013) 42–47.

[103] M.A. Tadayyoni, M.J. Weaver, Adsorption and electrooxidation of carbon monoxide at the gold-aqueous interface studied by surface-enhanced Raman spectroscopy, Langmuir 2 (1986) 179–183.

[104] E.S. Clark, D.H. Templeton, C.H. MacGillavry, The crystal structure of gold(III) chloride, Acta Crystallogr. 11 (1958) 284–288.

[105] S.E. Mason, I. Grinberg, A.M. Rappe, First-principles extrapolation method for accurate CO adsorption energies on metal surfaces, Phys. Rev. B 69 (2004) 161401.

[106] G.S. Elliott, Miller D. R., Helium scattering from carbon monoxide adsorbed on gold(111), in: Rarefied Gas Dynamics: Proc. 14th Int. Symp., University of Tokyo Press, Japan, 1984, pp. 349–358.

[107] W.-L. Yim, T. Nowitzki, M. Necke, H. Schnars, P. Nickut, J. Biener, M.M. Biener, V. Zielasek, K. Al-Shamery, T. Klüner, M. Bäumer, Universal Phenomena of CO Adsorption on Gold Surfaces with Low-Coordinated Sites, J. Phys. Chem. C 111 (2007) 445–451.

[108] S.-G. Sun, W.-B. Cai, L.-J. Wan, M. Osawa, Infrared Absorption Enhancement for CO Adsorbed on Au Films in Perchloric Acid Solutions and Effects of Surface Structure Studied by Cyclic Voltammetry, Scanning Tunneling Microscopy, and Surface-Enhanced IR Spectroscopy, J. Phys. Chem. B 103 (1999) 2460–2466.

[109] B.D. Kay, K.R. Lykke, J.R. Creighton, S.J. Ward, The influence of adsorbate–absorbate hydrogen bonding in molecular chemisorption: NH_3, HF, and H_2O on Au(111), J. Chem. Phys. 91 (1989) 5120-5121.

[110] D.R. Lide, CRC Handbook of Chemistry and Physics, 89th ed., CRC Press/Taylor and Francis, Boca Raton, Florida, 2009.

[111] S.M. McClure, T.S. Kim, J.D. Stiehl, P.L. Tanaka, C.B. Mullins, Adsorption and Reaction of Nitric Oxide with Atomic Oxygen Covered Au(111), J. Phys. Chem. B 108 (2004) 17952–17958.

[112] M.A. Debeila, N.J. Coville, M.S. Scurrell, G.R. Hearne, DRIFTS studies of the interaction of nitric oxide and carbon monoxide on Au–TiO_2, Catal. Today 72 (2002) 79–87.

[113] E. Roze, P. Gravejat, E. Quinet, J.L. Rousset, D. Bianchi, Impact of the Reconstruction of Gold Particles on the Heats of Adsorption of Linear CO Species Adsorbed on the Au Sites of a 1% Au/Al_2O_3 Catalyst, J. Phys. Chem. C 113 (2009) 1037–1045.

[114] G.L. Beltramo, T.E. Shubina, S.J. Mitchell, M.T.M. Koper, Cyanide adsorption on gold electrodes: a combined surface enhanced Raman spectroscopy and density functional theory study, J. Electroanal. Chem. 563 (2004) 111–120.

[115] J. Brooker, P.A. Christensen, A. Hamnett, R. He, C.A. Paliteiro, Combined scanning tunnelling microscopy and in situ Fourier transform infrared study of dioxygen reduction on gold, Faraday Discuss. 94 (1992) 339–360.

[116] V. Aguilar-Guerrero, B. Gates, Kinetics of CO Oxidation Catalyzed by Supported Gold: A Tabular Summary of the Literature, Catal. Lett. 130 (2009) 108–120.

[117] M. Chen, D.W. Goodman, Catalytically active gold on ordered titania supports, Chem. Soc. Rev. 37 (2008) 1860-1870.

Chapter 5: Quantum Mechanical Study of CO_2 and CO Hydrogenation on Metal-Doped Cu(111) Surfaces

5.1 Introduction

Fossil fuels are currently the main carbon source in the chemical industry. Because these resources are expected to be depleted and their combustion is the major cause of CO_2 emissions to the atmosphere, the need for finding alternative carbon sources has sparked interest in using renewable sources. The conversion of CO_2 into valuable organic compounds promises to be a potential approach to reduce the environmental impact of CO_2 emissions, and to generate alternate sources of energy and feedstock.

Cu-based catalysts (e.g., copper oxides, supported and composite Cu catalysts) have been employed for the synthesis of methanol [1–5] and carbon monoxide [6,7] through the hydrogenation of CO_2. Methanol is industrially produced from CO, H_2 and small amounts of CO_2 using $Cu/ZnO/Al_2O_3$ as catalyst at high pressures (50-100 bar) [8]. This catalyst, however, has three limitations: it is susceptible to poisons usually present in syngas sources, it has been observed that the methanol productivity is low in the absence of CO [9] and at low pressures, significant amounts of CO are formed through the reverse water-gas shift (RWGS) reaction [10]. The RWGS reaction competes with the methanol synthesis from CO_2 hydrogenation. Experimental and theoretical results indicate that the rate of the RWGS reaction is approximately two to three orders of magnitude faster than the methanol synthesis on Cu nanoparticles, resulting in CO accumulation on the catalyst surface [5]. The RWGS reaction is endothermic, while the hydrogenation of CO_2 to methanol is an exothermic reaction, as described in Table 5.1 [11]. However, the

hydrogenation of CO to methanol is even more exothermic than CO_2 hydrogenation [12].

Consequently, in addition to high pressures, relative low temperatures (>240 °C) are

required to favor the hydrogenation of CO_2 to methanol. High reaction temperatures (e.g.,

500-873 K) typically favor the formation of undesired products, such as CO, hydrocarbons

and higher alcohols [4].

Table 5.1. Reactions involved in the hydrogenation of CO_2 and CO.

	Reaction	$\Delta H_{rxn}°$ (kJ/mol)	Ref.
Methanol Synthesis from CO_2	$CO_{2(g)} + 3H_{2(g)} \leftrightarrow CH_3OH_{(g)} + H_2O_{(g)}$	-50	[11,12]
Reverse Water Gas Shift	$CO_{2(g)} + H_{2(g)} \leftrightarrow CO_{(g)} + H_2O_{(g)}$	41	[11]
Methanol Synthesis from CO	$CO_{(g)} + 2H_{2(g)} \leftrightarrow CH_3OH_{(g)}$	-91	[12]
Formic Acid Synthesis from CO_2	$CO_{2(g)} + H_{2(g)} \leftrightarrow HCOOH_{(g)}$	15[a]	
Formaldehyde Synthesis from CO	$CO_{(g)} + H_{2(g)} \leftrightarrow CH_2O_{(g)}$	-5	[13]
Formaldehyde Synthesis from CO_2	$CO_{2(g)} + 2H_{2(g)} \leftrightarrow CH_2O_{(g)} + H_2O_{(g)}$	36[a]	

[a] Values calculated by using thermodynamic data provided from NIST [14].

In an effort to find efficient catalysts for the hydrogenation of CO_2, different metal

dopants or promoters have been studied to modify the conventional catalyst used for CO_2

hydrogenation and improve the catalytic performance. Toyir and coworkers studied Ga-

promoted Cu-based catalysts on SiO_2 and ZnO supports and obtained high activity,

selectivity and stability for Cu-Zn-Ga/SiO_2 (hydrophobic silica) [15]. Methanol was the

main product, with a selectivity of 99% and a conversion of 5.6% at 543 K. They found

that Ga increased the activity of the catalyst and selectivity for methanol, when compared

to Cu/ZnO/Al_2O_3. In another study, Toyir et al. also proved that the addition of Ga onto

Cu/ZnO improved the catalyst stability [16]. In addition, they determined that higher

Ga/Cu ratios increased the methanol production [15,16]. Melián-Cabrera and coworkers

studied the effect of Pd incorporation on the performance of a CuO–ZnO catalyst for the

methanol synthesis [17]. They found that there is a synergetic effect of Pd on the active

Cu sites, and that Pd facilitates the H_2 spillover and transport of hydrogen to the active

sites while maintaining CuO in a more reduced state. Nerlov et al. investigated the effect of CO in the methanol synthesis from CO_2 hydrogenation on the Cu(100) surface modified by Ni [18]. They reported that the methanol production increased when CO is fed into the reaction system, because CO activates the catalyst by inducing segregation of Ni to the surface. Studt and coworkers tested the catalytic performance of a CuNi alloy supported on silica in the hydrogenation of CO to methanol, obtaining similar turnover frequencies and slightly higher selectivities for methanol, when compared against the commercial $Cu/ZnO/Al_2O_3$ catalyst [19].

Catalysts based on other metals (e.g., Ni, Ga and Pd) have been investigated and they have demonstrated to be potential promoters for the hydrogenation of CO_2 [10, 20, 21]. Recently, it has been demonstrated that a Ni-Ga intermetallic compound has comparable or better catalytic activity to reduce CO_2 and it is more selective for methanol (significantly lower production of CO) than $Cu/ZnO/Al_2O_3$ [10]. Fujitani et al. studied Pd-based catalysts for methanol production from CO_2 and H_2 and they reported that Pd/Ga_2O_3 was more active than Cu/ZnO on the basis of yields and turnover frequencies [20].

Some of these potential catalysts for the hydrogenation of CO_2 have been also investigated with density functional theory (DFT) calculations. The adsorption and activation of CO_2 were theoretically studied on Cu-Ni bimetallic clusters by evaluating distinct metal compositions and geometry configurations in the clusters [22]. The authors found that the cluster with higher composition of Ni ($Cu_{42}Ni_{13}$) and the icosahedral conformation exhibited the highest adsorption of CO_2. Yang et al. investigated the effects of the metal dopants Pd, Au, Pt, Ni and Rh on the catalytic activity of Cu(111) for the

methanol synthesis through CO_2 hydrogenation using DFT methods with kinetic Monte Carlo (KMC) simulations [23]. They determined that Ni, Pt, Pd, and Rh promote the CH_3OH synthesis reaction, while Au deactivates the reaction, being Ni/Cu(111) the surface with the best catalytic performance.

Experimental and theoretical observations indicate that CO_2 is chemically adsorbed on Ni(110) under UHV conditions [24]. Dissociative adsorption of CO_2 has been observed on Ni, Al and Mg surfaces [25]. Behrens and coworkers demonstrated, with DFT calculations that Zn substituted into the Cu(211) surface at the step sites increased the catalyst activity because it increased the adsorption strengths of the intermediates and decreased the energy barriers [8]. They proposed that the use of other promoters with the same oxophilicity of Zn might increase the catalytic activity of Cu. They reported that there is a synergistic effect between Cu and Zn, because Cu sites near Zn atoms serve as adsorption sites for oxygen-bound intermediates.

The hydrogenation of CO_2 and CO has also been studied by DFT methods in order to elucidate the elementary steps in the reaction mechanisms that have not been fully clarified. There are two major routes that have been proposed for the methanol synthesis from CO_2 hydrogenation: the formate (HCOO) pathway [5,8,23,26] and the RWGS reaction followed by CO hydrogenation [23,26], as illustrated in Fig. 5.1. In the formate pathway, there is a debate on whether dioxymethylene (CH_2O_2) or formic acid (HCOOH) [8,25,26] is the intermediate that leads to the formation of methanol. Most researchers have proposed dioxymethylene as reaction intermediate [5,23,28–31]. The hydrogenation of formic acid or dioxymethylene could produce hydroxymethoxy (H_2COOH) [8,26,27,30], which could decompose to form formaldehyde (CH_2O). Formaldehyde could be directly

generated from dioxymethylene [31]. Finally, methoxy (CH_3O) or hydroxymethyl (CH_2OH) formed by the hydrogenation of formaldehyde could lead to methanol when either of these intermediates are hydrogenated, being methoxy more stable than hydroxymethyl [26]. In the route of RWGS reaction and CO hydrogenation, the formation of CO has been proposed through the decomposition of CO_2 [26] or carboxyl (COOH) [23,26,30]. Formyl, formaldehyde and methoxy have been established as the main reaction intermediates in this pathway. Works in which the HCOO pathway and the RGSW reaction-CO hydrogenation are considered have reported that the latter is the dominant pathway because it is faster than the formate pathway [23]. However, the dominant pathway depends on the slow steps, HCO hydrogenation for the RWGS reaction-CO hydrogenation pathway and HCOOH hydrogenation for the HCOO pathway, and the reaction conditions, as determined in a microkinetic analysis of the methanol synthesis on Cu(111) [26]. For instance, Yang et al. reported that CH_3OH is not produced from CO hydrogenation despite the fast kinetics of the RWGS reaction, because HCO is not a stable intermediate and its dissociation back to CO* + H* is preferred over the HCO hydrogenation on Cu(111) [5].

The metal employed as the catalyst and the reaction conditions, ultimately determine the rate-limiting steps of these reaction mechanisms. In the formate pathway, the hydrogenation of formate [5], dioxymethylene [5,23] and methoxy [26,32] have been proposed as the rate-limiting steps in the synthesis of methanol. While in the CO hydrogenation pathway, the reaction is limited by hydrogenation of CO and HCO [5].
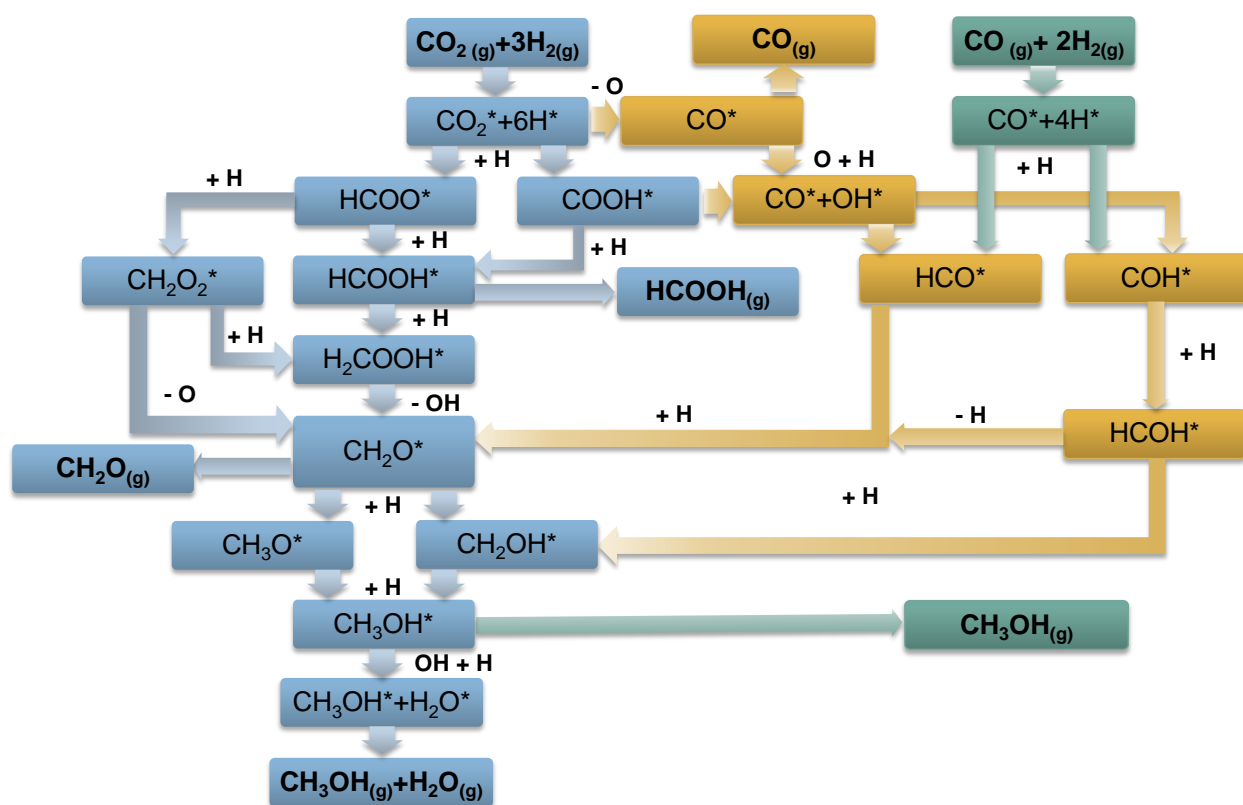
Fig. 5.1. Proposed reaction pathways for the hydrogenation of CO_2 and CO.

In this work, DFT methods have been used to analyze heterogeneous catalysts for the conversion of CO_2 into formic acid, formaldehyde and methanol. To our knowledge, the performance of modified Cu-based catalysts has not been extensively explored for the production of formic acid and formaldehyde. Therefore, we want to fill this lack of information by investigating novel Cu-based catalysts, since Cu has the potential of being an efficient catalyst for the synthesis of these products. Taylor et al. reported that the hydrogenation of formate on Cu(100) most 1likely produces formaldehyde and/or formic acid instead of methanol [33]. Cu(111) surfaces doped with Ni, Pd, Ga, Ti, Mg and Al were investigated to identify potential surface alloys that might selectively catalyze the hydrogenation of CO_2. Studt et al. identified a Ni-Ga alloy [10] and Yang et al. [23]

proposed Ni-doped Cu surface as potential catalysts to convert CO_2 into methanol using the binding energy of O and of CO, respectively, as a descriptor. In this study, the binding energies of H, O, CO and CO_2, and the work function of metal (M)-doped Cu(111) surfaces were used as descriptors in the screening to select the most promising catalysts. The binding energy of CO_2 was analyzed because one of the main challenges of this type of reaction is the activation and direct conversion of CO_2. The performance of these potential catalysts was examined by conducting a systematic analysis of the adsorption of relevant species and intermediates involved in CO_2/CO hydrogenation. Moreover, insights into the thermochemistry of plausible elementary steps for the synthesis of formic acid, formaldehyde and methanol from these hydrogenations were provided to postulate reaction mechanisms for the novel M-doped Cu surfaces. We also analyzed the hydrogenation of CO to determine how feasible is the RWGS reaction over these doped surfaces and if the formation of desired products via this reaction is favored over other reaction pathways. The stability of these catalysts was also studied by determining if the adsorption of species, such as carbon are energetically favorable. The catalytic activity and the selectivity for formic acid, formaldehyde and methanol of these doped surfaces and of the pure Cu surface are compared in order to determine if the dopant addition in the Cu(111) surface improves the performance of Cu-based catalysts. Furthermore, the reliability of the descriptors used for the catalyst screening is discussed based on the thermochemistry results.

5.2 Theoretical Methods

5.2.1 Methodology for the screening of the metal-doped Cu(111) surfaces

Periodic DFT calculations were used to screen copper surface alloys with different descriptors to evaluate the feasibility of employing these novel catalysts for CO/CO_2 hydrogenation. Surface alloys were simulated with a simple model in which the Cu(111) surface was doped with another metal (M). For this screening, we analyzed Ni, Pd, Ti, Mg, Al and Ga as dopant metals on Cu(111). The energies of solution and segregation were used to verify if the formation of these M-doped Cu surfaces is favorable. We calculated the solution energy for an M atom in a pure Cu crystal (E_S^{CuM}) and the segregation energy (E_{seg}) using Equations 5.1 and 5.2, respectively, when these energies were not available in the literature.

$$E_S^{CuM} = \Delta E_{CuM} + E_{Cu} - E_M \tag{5.1}$$

$$E_{seg} = E_{CuM}{}^{surf} - E_{CuM}{}^{bulk} \tag{5.2}$$

In these equations, E_{Cu} and E_M are the energies per atom of the pure metals, ΔE_{CuM} is the energy difference between a Cu crystal with a substitutional M dopant and the pure Cu crystal ($\Delta E_{CuM} = E_{Cu_{n-1}M} - E_{Cu_n}$), n is the total number of Cu atoms, $E_{CuM}{}^{surf}$ is the energy of a Cu surface with M on the surface, and $E_{CuM}{}^{bulk}$ is the energy of a Cu surface with M in the material bulk. For dopants that are not segregated to the surface, the adsorbate-induced segregation energy ($E_{seg}{}^A$) was calculated using Equation 5.3.

$$E_{seg}{}^A = E_{A-CuM}{}^{surf} - E_{A-CuM}{}^{bulk} \tag{5.3}$$

In this equation, $E_{A-CuM}{}^{surf}$ is the energy of a Cu surface with M on the surface in the presence of the adsorbate A, and $E_{A-CuM}{}^{bulk}$ is the energy of a Cu surface with M in the material bulk in the presence of the adsorbate A. Negative energies of solution,

segregation and adsorbate-induced segregation indicate that the substitution of a Cu atom by a dopant is favorable and that the dopant is segregated to the surface, either without the help of an adsorbate or induced by the adsorbate, respectively.

We have analyzed the adsorption of small molecules, such as H, O, CO and CO_2 on Cu(111) and Cu(111) surfaces doped with Ni, Pd, Ti, Mg, Al and Ga. The Cu(111) surface was modeled by a 2x2x4 slab and a vacuum layer of 14 Å-thick separating successive slabs. The top two layers of the slab and the adsorbates were allowed to relax, while the atoms on the bottom two layers were fixed in their optimized bulk coordinates. The calculated equilibrium lattice constant for bulk Cu was 3.63 Å, which closely agrees with the experimental value of 3.62 Å [34]. The M-doped Cu surfaces for the adsorption studies were modeled by substituting a Cu atom in the top layer of the 2x2x4 Cu(111) slab by a metal dopant, obtaining a dopant coverage of 1/4 ML. For the segregation calculations, a 2x2x6 slab was used to correctly model the material bulk. The solubility of the dopant in Cu(111) was evaluated by performing bulk calculations with 32 atoms Cu(111) and M/Cu(111) supercells. The generalized gradient approximation proposed by Perdew and Wang (GGA-PW91) [35] was used as the exchange-correlation functional to optimize the geometries of the species and calculate the energy of each system. For these calculations, plane wave functions with a cutoff energy of 400 eV were used to expand the Kohn-Sham one-electron valence states, while the core electrons were described by projector-augmented wave (PAW) potentials [36,37]. Brillouin zone sampling was performed using Gamma centered k-point meshes of: 8x8x1 for the adsorption studies, 6x6x1 and 6x6x6 for the segregation and solubility calculations, respectively. All these

calculations were performed using the Vienna *ab initio* simulation package (VASP) [38,39].

Four possible adsorption sites: *fcc*, *hcp*, *top* and *bridge* were analyzed in the adsorption calculations for the Cu(111) surface. A visual representation of these sites is illustrated in Fig. 5.2a. For the M-doped Cu(111) surfaces, eight high symmetry sites were explored instead of four sites because the addition of another element to the surface breaks the symmetry. Doped surfaces have two of each adsorption site named: fcc1, fcc2, hcp1, hcp2, top1, top2, bridge1 and bridge2, as illustrated in Fig. 5.2b. Number 1 denotes sites with Cu atoms only, while number 2 corresponds to mixed sites that have Cu and the dopant. Energies of isolated species (E_A), surface (E_S) and adsorbed species (E_{A-S}) on the different adsorption sites were obtained, and used to calculate the binding energies (E_b) with Equation 5.4. The preferred binding site for each adsorbate was the one with the lowest binding energy.

$$E_b = E_{A-S} - (E_A + E_S) \tag{5.4}$$

(a)　　　　　　　　(b)　　　　　　　　(c)
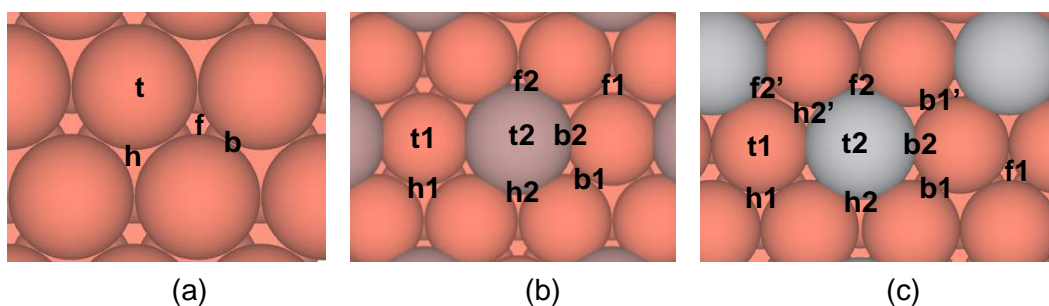
Fig. 5.2. Adsorption sites on the surfaces of (a) Cu(111), (b) M/Cu(111) used in the screening and (c) Ti/Cu(111). M = Ni, Pd, Ti, Mg, Al, or Ga. t=top, h=hcp, f=fcc and b=bridge.

The work function of the M-doped Cu surfaces was also used as a descriptor for the screening analysis. This property is defined as the minimum energy or potential that the

electrons in the solid must overcome to be ejected into the vacuum outside the solid [40], as schematized on Fig. A.1 in Appendix A. Thus, if the work function is low, we expected that the surface would be more reactive because the electrons would be more easily released from the surface; and the electrophilic carbon of CO_2 would be attracted to the catalytic surface, achieving its activation. The work function (ϕ) for the pure Cu(111) surfaces and the doped Cu surfaces was calculated using Equation 5.5, where E_F is the Fermi energy and E_{vac} is the vacuum level, which is estimated from the plot of the electrostatic potential for the surface as a function of the z-coordinate. For Cu(111), the work function was 4.82 eV, which is in good agreement with the theoretical and experimental results for these surface of 4.78 eV and 4.82 eV [41], and 4.94 eV [34], respectively.

$$\phi = E_{vac} - E_F \qquad\qquad\qquad\qquad (5.5)$$

We have compared the binding energies of H, O, CO and CO_2, and the work functions for all the M-doped Cu surfaces with the pure Cu(111) surface to study the effect of the dopants in the adsorption strength and reactivity of the copper surface.

5.2.2 Methodology for the systematic study of the Cu(111) surface doped with Ga, Mg and Ti

The adsorption of key species and intermediates involved in the hydrogenation of CO and CO_2 has been studied using periodic DFT calculations. Adsorbed species, such as: H, O, C, CO, CO_2, OH, H_2O, COH, HCO, COOH, HCOO, HCOOH, CH_2O_2, CH_2O, CH_2OH, CH_3O, CH_3O_2 and CH_3OH on M/Cu(111) were thoroughly analyzed to evaluate the performance of these catalysts. For this systematic study on the M-doped Cu(111)

surfaces, a larger slab with dimensions of 3x3x4 and 36 atoms was used to accommodate larger coadsorbates and avoid the interaction between them through repeated slabs. The M-doped Cu surfaces were constructed by substituting two Cu atoms in the top layer of the 3x3x4 Cu(111) slab by the metal dopant, obtaining a dopant coverage of 2/9 ML in the surface. In this manner, the concentration of the dopant used in the screening is consistent with the one used in the analysis of M/Cu(111) described in Section 5.2.1. The level of theory employed was the Perdew, Burke and Ernzerhof (PBE) exchange-correlation functional [42,43] and we also used the DFT-D2 method of Grimme [44] to account for the dispersion effects. Plane wave functions with a cutoff energy of 400 eV and the PAW potentials were also used for these calculations. The Gamma centered k-point mesh used for the Brillouin zone sampling was reduced to 6x6x1 because the system is larger than the one used in the screening. For the evaluated adsorption sites on M/Cu(111), we included an additional bridge, fcc and hcp site between the two dopant atoms denoted with ('), as illustrated in Fig. 5.2c.

5.3 Results and Discussion

5.3.1 Screening results for Cu(111) and M-doped Cu(111) surfaces

The negative values of the theoretical and experimental solution energies shown in Table 5.2 demonstrate that the formation of these substitutional surface alloys is favorable. Segregation energies reported in the literature indicate that Pd, Mg and Al could be segregated to the surface of Cu [45,46]. For Ga in Cu, the segregation energy has been estimated, obtaining a favorable segregation. While for Ti in Cu, there is no segregation, and Ni is anti-segregated in Cu. However, it has been experimentally

observed and predicted with DFT calculations that CO induces segregation of Ni in Cu(100) [18] and Cu(211) [19]. Furthermore, our results indicate that O and CO induce segregation of Ti in Cu(111) (Table 5.2).

Table 5.2. Theoretical and experimental solution energies, and estimated energies of segregation and adsorbate-induced segregation of the solutes Ni, Pd, Ti, Mg, Al and Ga in Cu.

Solute (M) in Cu	$E_S^{AB,calc}$ (eV)	$E_S^{AB,exp}$ (eV)	E_{seg}^{calc} (eV/atom)	E_{A-seg}^{calc} (eV)
Ni	-0.20 [47], -0.08 [48]	0.03, 0.06 [47]	0.17 [45]	A=CO [18,19]
Pd	-0.86 [47]	-0.44 [47]	-0.20 [45]	
Ti	-0.11 [48]	-2.5 [48]	0.01 [45]	-1.72 (A=O, this work) -0.24 (A=CO, this work)
Mg	-0.14 (this work)		-1.24^a [46]	
Al	-0.58 (this work)		-0.45^a [46]	
Ga	-0.31 (this work)		-0.50 (this work)	

^{a} E_{seg} for Mg and Al in Cu(110).

The adsorption of H, O, CO and CO_2 on Cu(111) and Cu(111) surfaces doped with Ni, Pd, Ti, Mg, Al and Ga and the work functions of these surfaces have been studied using periodic self-consistent DFT calculations to compare these surface alloys against the pure Cu surface, and investigate the effect of these impurities in its catalytic properties. In Appendix A, we have included a detailed discussion of the adsorption or binding energies of these species that have been used as descriptors to predict which of these M-doped Cu surfaces might be a potential catalyst for CO_2/CO hydrogenation. The binding energies on M/Cu(111) are illustrated in Fig. A.2 (Appendix A) relative to the pure Cu(111) surface. The screening results have demonstrated that when Cu(111) is doped with Ti, the adsorption of CO is moderate and CO_2 is activated by chemisorption with the

lowest binding energy. The Mg-doped Cu(111) surface also activates CO_2 and has moderate adsorption of O. The adsorption of CO on both Mg/Cu(111) and Ga/Cu(111) is weaker than on Cu(111), which could favor the formation of the desired products from CO_2 hydrogenation instead of the hydrogenation of CO. The adsorption of H was not a useful descriptor to screen the evaluated M-doped Cu surfaces, because most energy differences between the doped surfaces and Cu(111) are not significant, except for Ni/Cu(111). However, H is chemically adsorbed on Cu(111) doped with Ti, Mg and Ga. The results for the comparison of the work functions of the M-doped Cu(111) against Cu(111) are illustrated in Fig. A.4. These results indicate that Mg/Cu(111) has the lowest work function, followed by Ti/Cu(111) and Ga/Cu(111). Therefore, Cu(111) doped with Mg, Ti and Ga are expected to be more reactive than Cu(111) and the other M-doped Cu(111) surfaces. For these reasons, we have selected the Cu surfaces doped with Ga, Mg and Ti as a potential catalysts for the hydrogenation of CO and CO_2.

5.3.2 Results for the systematic study of the M-doped Cu(111) surfaces

In order to evaluate the performance of Cu(111) doped with M (e.g., Ga, Mg or Ti) as catalysts for the hydrogenation of CO_2 and CO, we have analyzed the adsorption of relevant species for these reactions on M/Cu(111). The PBE energies of the species in their preferred adsorption sites together with the energies of the adsorbates in the gas phase and the surface, have been used to calculate reaction energies of plausible elementary steps for the hydrogenations of CO_2 and CO on the M-doped Cu(111) surfaces. This thermochemistry analysis enables us to postulate plausible pathways for

the synthesis of formic acid, formaldehyde and methanol on the M/Cu(111) surfaces, and quantify the effect of the dopants Ga, Mg and Ti on the energetics of reactions.

5.3.2.1 Ga-doped Cu(111) surface as catalyst for CO_2/CO hydrogenation

Adsorption study and binding energies for Ga/Cu(111)

The adsorption of several species involved in the hydrogenation of CO_2 and CO has been studied on the Ga-doped Cu(111) surface. From this analysis, the preferred adsorption sites along with the minimum energy geometries of the analyzed adsorbates have been determined, as shown in Fig. 5.3 and detailed in Table 5.3. The geometrical parameters for the configurations illustrated in Fig. 5.3 have been included on Table A.1. Most species adsorbed on Ga/Cu(111) adopt monodentate conformations, where the adsorbate is bonded to the surface through one atom. Few adsorbates, such as HCOO, CH_2O, CH_2O_2, CO_3 and HCO_3, have a bidentate configuration, in which the species are adsorbed by two atoms on the surface. The binding energies associated with the adsorption of these species at the minimum energy sites on Ga/Cu(111) have been also estimated (see Table 5.3 and Fig. 5.4). On the basis of our results, CO_2 is not activated by the Ga-doped Cu(111) surface. CO_2 is physically adsorbed on the Ga/Cu(111) surface with a binding energy of -0.23 eV (Table 5.3), and maintains a linear configuration. The average Cu-O bond distance is 3.13 Å (Table A.1). Similar observations have been reported for the CO_2 adsorption on the pure Cu(111) surface using DFT methods [26]. However, experimental observations indicate that CO_2 is not physically adsorbed on Cu(111) [49,50]. Fig. 5.4 depicts that CO_2 is the species with the lowest adsorption strength on Ga/Cu(111). Other species such as H_2O, HCOOH and CH_3OH also exhibit

physical adsorption. The rest of the adsorbates analyzed are chemically adsorbed, and C is the species with the strongest adsorption on Ga/Cu(111) (see Fig. 5.4). Most adsorbates have adsorption sites with degenerate binding energies, which are described in Table 5.3 enclosed by parentheses. CO, HCO and CH_3O are predicted to have two equally stable adsorption sites, which are shown in Fig. 5.3.
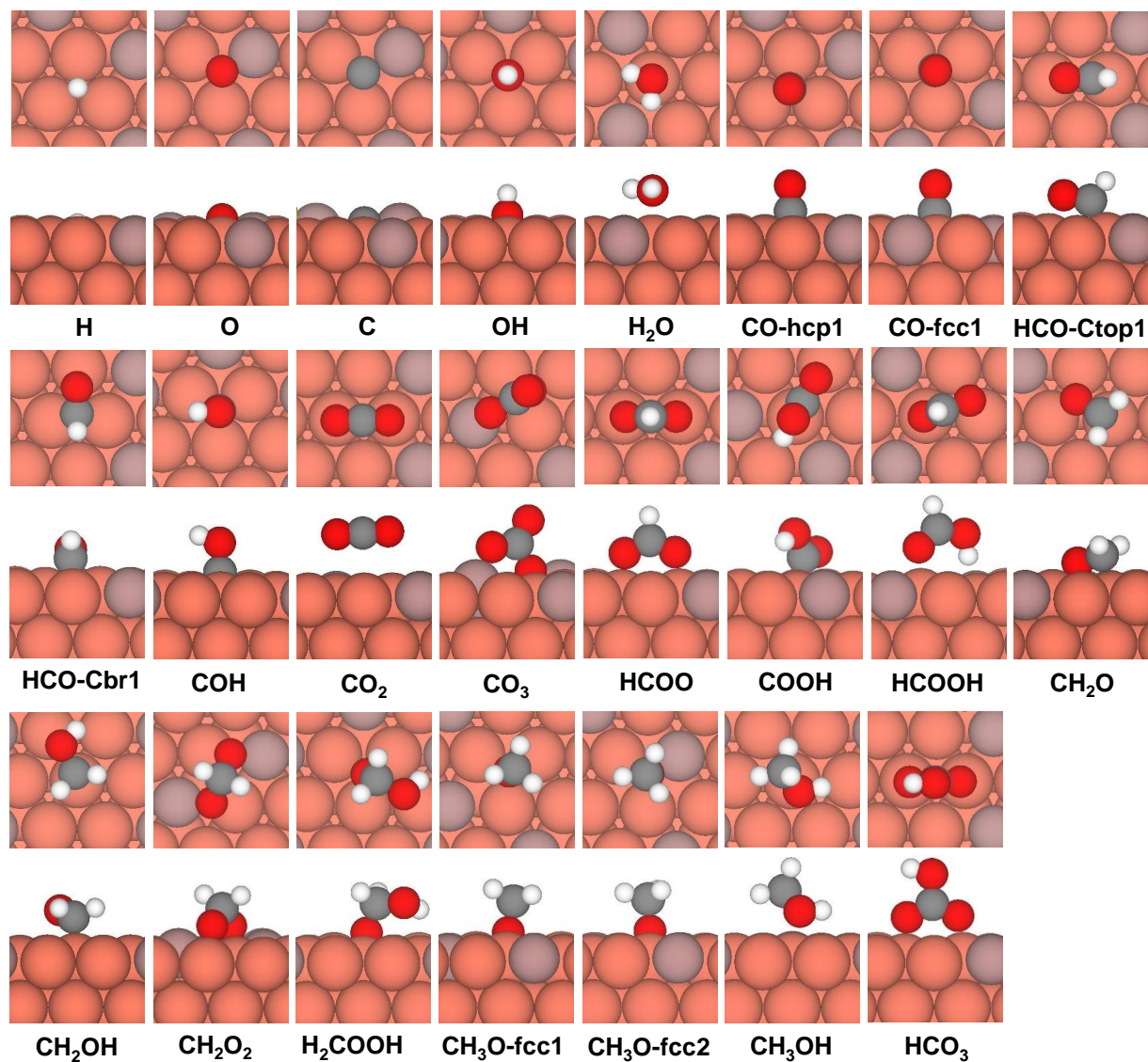
Fig. 5.3. Top and side views of the preferred adsorption sites on the Ga/Cu(111) surface for the species studied. Table A.1 provides the geometric details for these structures.

Table 5.3. Preferred adsorption sites with their binding energies for each species adsorbed on Ga/Cu(111).

Adsorbate	Preferred adsorption site	Binding energy (eV)
H	hcp1(fcc1)	-1.75 (-1.74)
O	fcc2 (hcp2')	-4.93 (-4.86)
C	fcc2 (fcc1)	-5.01 (-5.00)
CO	hcp1(fcc1)	-1.00 (-1.00)
OH	fcc1 (hcp1)	-3.10 (-3.05)
CO_2	Physisorption	-0.23
H_2O	Physisorption	-0.32
COH	fcc1 (hcp1)	-2.99 (-2.94)
HCO	Ctop1 (Cbr1)	-1.48 (-1.48)
COOH	Ctop1-H down (Ctop1-H up) [a]	-2.38 (-2.37)
HCOO	Otop1-Otop1 (Otop2-Otop1)	-3.05 (-2.98)
HCOOH	Physisorption	-0.51
CO_3	Otop2-Obr1 (Otop2-Ofcc2')	-4.34 (-4.28)
HCO_3	Otop1-Otop1 (Otop2-Otop1)	-2.89 (-2.82)
CH_2O	Ctop1-Obr1 (Ctop1-Otop2)	-0.41 (-0.30)
CH_2OH	Ctop1	-1.39
CH_2O_2	Obr2-Obr2	-4.47
H_2COOH	Obr1 (Obr2)	-2.46 (-2.37)
CH_3O	fcc1 (fcc2)	-2.62 (-2.62)
CH_3OH	Physisorption	-0.49

[a] Two stable carboxyl (COOH) binding geometries were found over the top site, but they differ on the orientation of the H atom in the OH group when the species is adsorbed on Ga/Cu(111). H down indicates that H is looking to the downward direction near the surface while H up means that H is oriented away from the surface because is looking to the upward direction.
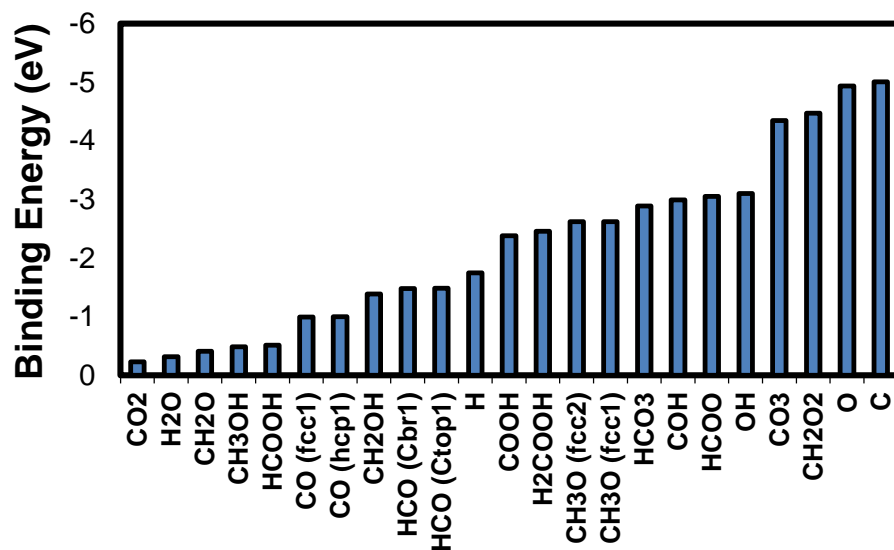
Fig. 5.4. Binding energies for species relevant to CO_2/CO hydrogenation at their preferred adsorption site on Ga/Cu(111).

Thermochemistry of possible surface reactions on Ga/Cu(111)

- Hydrogenation of CO_2 and CO to formic acid (HCOOH)

Plausible reaction pathways have been evaluated for the synthesis of formic acid via CO_2 hydrogenation over the Ga-doped Cu(111) surface, as depicted in Fig. 5.5a. These routes are mediated by the formation of the formate (HCOO) intermediate (pink route in Fig. 5.5a) and the carboxyl (COOH) intermediate (green route), and the dissociation of CO_2 (brown route). In the formate pathway, formic acid might be produced by either the formate hydrogenation (pink line) or the decomposition of HCOO to formyl (HCO*) and O* followed by the hydrogenation of oxygen and the coupling reaction of formyl and hydroxyl (pink, purple and orange lines). In the carboxyl pathway, two routes have been postulated. The first one is the hydrogenation of carboxyl to formic acid (green line) and the second one is the decomposition of carboxyl to CO* and OH* together with the hydrogenation of CO* to formyl and the coupling of HCO* and OH* (green and orange lines). The formyl intermediate could be also generated after the dissociation of CO_2, as illustrated by the brown and orange routes. We have also evaluated the formation of COH, but this reaction is more endothermic than CO* + H* → HCO* + * (R22 in Table 5.4) by 0.33 eV. The hydrogenation of CO to formic acid is slightly more thermodynamically favorable via the formation of carboxyl than the CO_2 dissociation. However, the direct synthesis of formic acid through the formate intermediate is favored over the routes with carboxyl as intermediate and the decomposition of formate. The CO_2 hydrogenation to HCOO is an exothermic reaction, but the hydrogenation is endothermic for the formation of COOH. Moreover, the HCOO decomposition is estimated to require 1.40 eV more than the hydrogenation of HCOO. Therefore, the minimum energy pathway to produce formic

acid from CO_2 hydrogenation on the Ga-doped Cu(111) surface is the formate pathway (blue and pink lines) with a total electronic energy of reaction of -0.17 eV (Fig. 5.6).
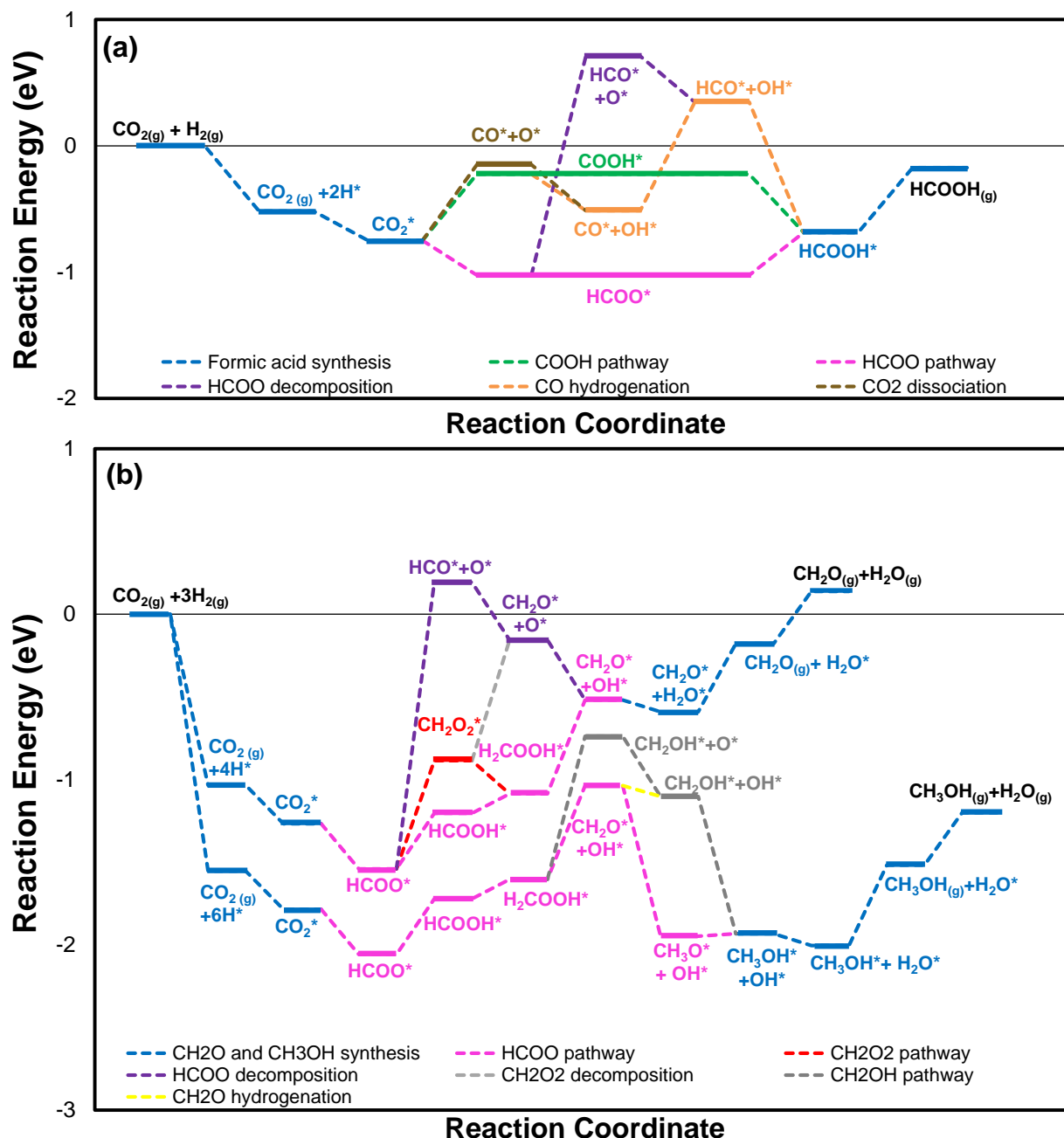
Fig. 5.5. Thermochemistry for the synthesis of: (a) formic acid, (b) formaldehyde and methanol via CO_2/CO hydrogenation on Ga/Cu(111). The reference zero corresponds to the energies of the isolated species in gas phase and the clean relaxed Ga/Cu(111) slab. Gas-phase species are indicated with (g) and adsorbed species are indicated with (*). The spectator $H_{2(g)}$ in the reaction mechanism of formaldehyde and formic acid, and the adsorbed hydrogen (H*) have been omitted from the labels to improve legibility.

Table 5.4. The elementary steps evaluated in the thermochemistry analysis for the hydrogenation of CO_2 and CO on the M-doped Cu(111) surfaces where M=Ga, Ti, Mg.

Reaction No.	Reaction	ΔE (eV) Ga/Cu(111)	Ti/Cu(111)	Mg/Cu(111)
R1	$H_2 + 2^* \rightarrow 2H^*$	-0.52	-1.23	-0.69
R2	$CO_2 + {}^* \rightarrow CO_2{}^*$	-0.23	-2.40	-1.15
R3	$CO_2{}^* + {}^* \rightarrow CO^* + O^*$	0.60	-0.55	0.29
R4	$CO_2{}^* + H^* \rightarrow HCOO^* + {}^*$	-0.27	-0.05	-0.45
R5	$CO_2{}^* + H^* \rightarrow COOH^* + {}^*$	0.53	1.37	0.59
R6	$HCOO^* + H^* \rightarrow HCOOH^* + {}^*$	0.34	1.88	1.02
R7	$HCOO^* + H^* \rightarrow CH_2O_2{}^* + {}^*$	0.65	-0.18	0.60
R8	$COOH^* + H^* \rightarrow HCOOH^* + {}^*$	-0.46	0.46	-0.02
R9	$HCOOH^* + H^* \rightarrow H_2COOH^* + {}^*$	0.12	-0.79	-0.39
R10	$CH_2O_2{}^* + H^* \rightarrow H_2COOH^* + {}^*$	-0.20	1.27	0.03
R11	$CH_2O_2{}^* + {}^* \rightarrow CH_2O^* + O^*$	0.73	0.21	0.37
R12	$H_2COOH^* + {}^* \rightarrow CH_2O^* + OH^*$	0.57	-0.90	0.49
R13	$H_2COOH^* + {}^* \rightarrow CH_2OH^* + O^*$	0.87	0.11	0.35
R14	$CH_2O^* + H^* \rightarrow CH_3O^* + {}^*$	-0.91	-0.19	-0.80
R15	$CH_2O^* + H^* \rightarrow CH_2OH^* + {}^*$	-0.07	1.17	0.01
R16	$CH_3O^* + H^* \rightarrow CH_3OH^* + {}^*$	0.01	1.37	0.17
R17	$CH_2OH^* + H^* \rightarrow CH_3OH^* + {}^*$	-0.83	0.01	-0.64
R18	$O^* + H^* \rightarrow OH^* + {}^*$	-0.36	0.17	0.15
R19	$OH^* + H^* \rightarrow H_2O^* + {}^*$	-0.07	1.09	0.13
R20	$COOH^* + {}^* \rightarrow CO^* + OH^*$	-0.29	-1.76	-0.16
R21	$HCOO^* + {}^* \rightarrow HCO^* + O^*$	1.73	-0.15	1.01
R22	$CO^* + H^* \rightarrow HCO^* + {}^*$	0.86	0.35	0.27
R23	$CO^* + H^* \rightarrow COH^* + {}^*$	1.19	1.27	1.22
R24	$CO^* + {}^* \rightarrow C^* + O^*$	2.71	0.95	1.12
R25	$HCO^* + H^* \rightarrow CH_2O^* + {}^*$	-0.35	0.18	-0.03
R26	$HCO^* + OH^* \rightarrow HCOOH^* + {}^*$	-1.03	1.87	-0.14
R27	$CO_2{}^* + O^* \rightarrow CO_3{}^* + {}^*$	0.18	-	0.26

R28	$CO_2{}^* + OH^* \rightarrow HCO_3{}^* + {}^*$	-0.33	-	-0.03
R29	$CO_3{}^* + H^* \rightarrow HCO_3{}^* + {}^*$	-0.87	-	-0.14
R30	$HCO_3{}^* + {}^* \rightarrow COOH^* + O^*$	1.22	-	0.47
R31	$HCOOH^* \rightarrow HCOOH_{(g)} + {}^*$	0.51	1.62	1.09
R32	$CH_2O^* \rightarrow CH_2O_{(g)} + {}^*$	0.41	2.54	0.99
R33	$CH_3OH^* \rightarrow CH_3OH_{(g)} + {}^*$	0.49	1.25	0.97
R34	$H_2O^* \rightarrow H_2O_{(g)} + {}^*$	0.32	1.21	0.86
R35	$CO^* \rightarrow CO_{(g)} + {}^*$	1.00	2.44	1.14

- Hydrogenation of CO_2 and CO to formaldehyde (CH_2O) and methanol (CH_3OH)

Because adsorbed formic acid is a possible reaction intermediate for the synthesis of formaldehyde and methanol, the reaction pathway obtained from the previous analysis for the formic acid production, involving the formate intermediate, has been proposed for the formation of formaldehyde and methanol (see Fig. 5.5b). Formate can be hydrogenated to either formic acid (pink line in Fig. 5.5b) or dioxymethylene (CH_2O_2) (red line), or it might be decomposed to formyl (purple line). Formaldehyde could be produced through the hydroxymethoxy (H_2COOH) intermediate from the hydrogenation of formic acid or dioxymethylene. On the other hand, formaldehyde could be directly generated from the hydrogenation of formyl or by the decomposition of CH_2O_2. From these pathways, the route that involves the formation of the intermediates HCOO*, HCOOH* and H_2COOH^* (blue and pink lines) is the most favorable one (Fig. 5.6), because HCOOH* is more stable than $CH_2O_2^*$ and HCO* + O* by -0.32 and -1.40 eV, respectively. The total electronic energy for the formaldehyde synthesis from $CO_{2(g)}$ and $H_{2(g)}$ has been calculated to be 0.14 eV.

The thermochemistry for the methanol synthesis has been analyzed through formaldehyde and hydroxymethyl (CH_2OH) as reaction intermediates, which are illustrated with the pink and gray lines in Fig. 5.5b. The reaction $H_2COOH^* + ^* \rightarrow CH_2O^* + OH^*$ (R12) is energetically more favorable than $H_2COOH^* + ^* \rightarrow CH_2OH^* + O^*$ (R13) by -0.30 eV. However, hydroxymethyl could also be produced by the hydrogenation of the oxygen atom of formaldehyde (R15) (pink, yellow and gray lines), which is almost thermoneutral step, with an electronic reaction energy of -0.07 eV. If the carbon atom of formaldehyde is hydrogenated to form methoxy (CH_3O) (R14), the reaction is more exothermic than the previous one by -0.85 eV. For the synthesis of methanol from CO_2 hydrogenation on the Ga/Cu(111) surface, the minimum energy pathway is the formate pathway with HCOOH, H_2COOH, CH_2O and CH_3O as reaction intermediates (blue and pink lines in Fig. 5.6). Methoxy is more stable than hydroxymethyl and the hydrogenation of methoxy is thermoneutral, with an electronic reaction energy of 0.01 eV. The overall electronic energy of reaction for $CO_{2(g)} + 3H_{2(g)} \rightarrow CH_3OH_{(g)} + H_2O_{(g)}$ is estimated to be -1.20 eV.

The thermochemistry analysis indicates that the reaction mechanisms for the synthesis of formic acid, formaldehyde and methanol over the Ga-doped Cu(111) surface is through the formate pathway, as summarized in Fig. 5.6. Based on the Brønsted-Evans-Polanyi (BEP) relation, the most endothermic step in the reaction mechanism is most likely to be the rate-limiting step because the activation energy is directly proportional to the reaction energy. Thus, the decomposition of H_2COOH^* into CH_2O^* and OH^* is the step that thermodynamically limits the reaction progress over the Ga/Cu(111) surface. The Cu surface doped with Ga is predicted to be more selective to methanol than

formic acid and formaldehyde because the hydrogenation of formic acid to the H_2COOH intermediate requires less energy than its desorption and the hydrogenation of CO_2 to methanol is an exothermic reaction while the reaction to formaldehyde is endothermic.
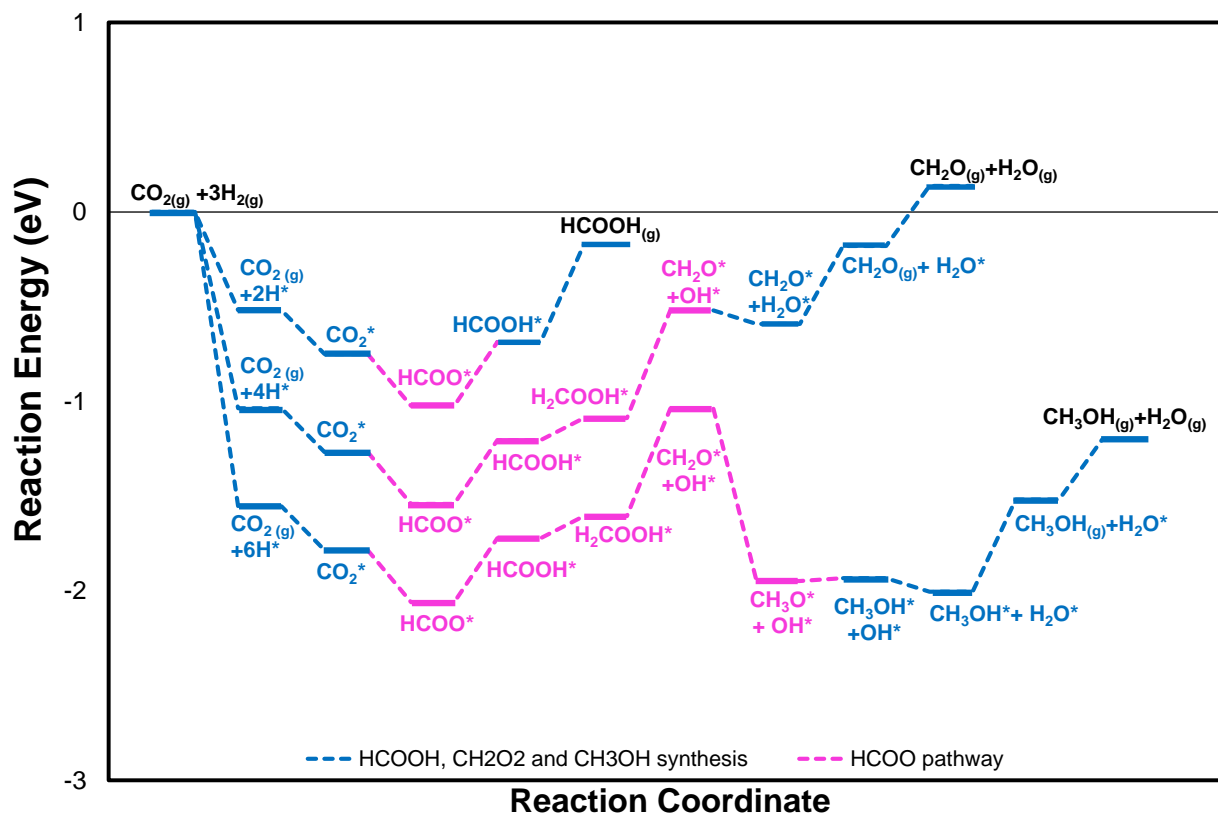
Fig. 5.6. Minimum energy pathways for the synthesis of formic acid, formaldehyde and methanol via CO_2 hydrogenation on Ga/Cu(111). The reference zero corresponds to the energies of the isolated species in gas phase and the clean relaxed Ga/Cu(111) slab. Gas-phase species are indicated with (g) and adsorbed species are indicated with (*). The spectator molecules of $H_{2(g)}$ in the reaction mechanism of formic acid and formaldehyde, and the adsorbed hydrogen (H*) have been omitted from the labels to improve legibility.

5.3.2.2 Ti-doped Cu(111) surface as catalyst for CO_2/CO hydrogenation

Adsorption study and binding energies for Ti/Cu(111)

Fig. 5.7 and Table 5.5 show the preferred adsorption sites for some of the adsorbates analyzed on Ti/Cu(111). Most species preferentially adsorb on sites between Ti atoms, adopting bidentate or tridentate conformations, and on the top site at the Ti atom. The calculated binding energies for these adsorption sites are depicted in Table 5.5 and Fig. 5.8. This chart shows that the binding strength on Ti/Cu(111) increases to the right, being H_2O the species with the lowest binding strength and CH_2O_2 the species with the strongest adsorption, followed by O. CH_2O_2 is adsorbed on Ti/Cu(111) through the two oxygen atoms on the Ti atoms adopting a bidentate top configuration. Thus, oxygen has a very strong interaction with this surface, which is expected because of the high oxophilicity of Ti.
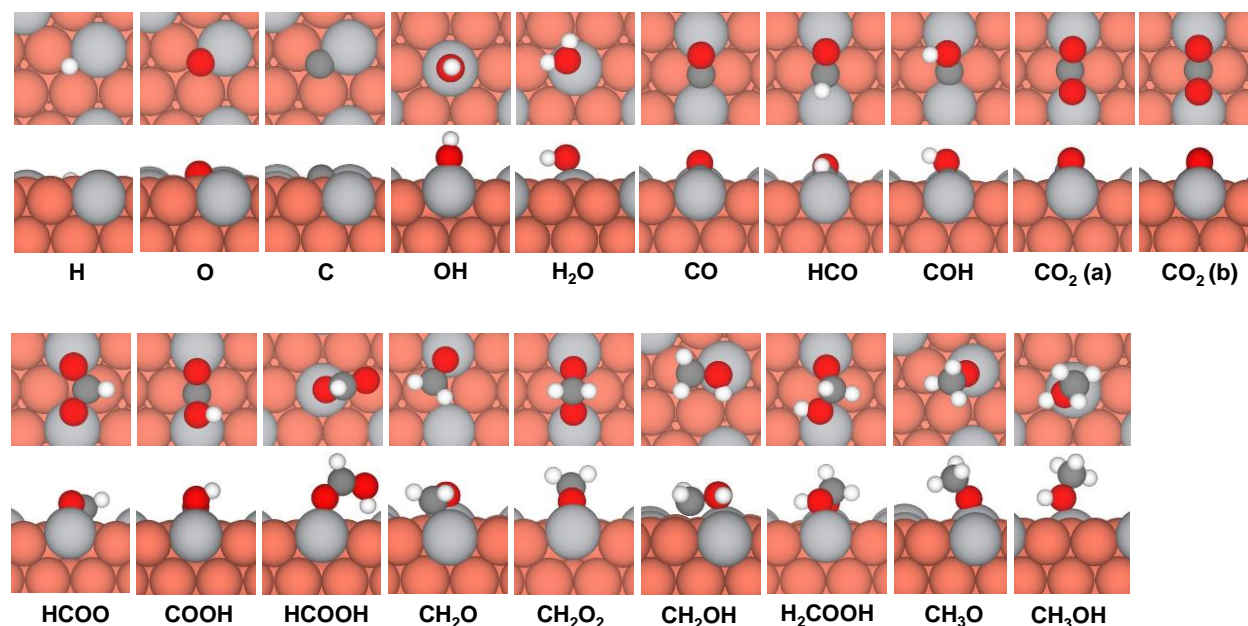
Fig. 5.7. Top and side views of the preferred adsorption sites on the Ti/Cu(111) surface for the species studied. For CO_2, configuration (a) is Otop2-Ctop1 and (b) is Otop2-Cbr1'. Table A.2 provides the geometric details for these structures.

Table 5.5. Preferred adsorption sites with their binding energies for each species adsorbed on Ti/Cu(111).

Adsorbate	Preferred adsorption site	Binding energy (eV)
H	br1 (br1')	-2.88 (-2.76)
O	fcc2 (fcc2')	-6.81 (-6.73)
C	fcc2 (hcp2)	-6.33 (-6.24)
CO	Otop2-Cfcc2'	-2.44
OH	top2	-4.81
CO_2	Otop2-Ctop1 [a] (Otop2-Cbr1' [a])	-2.40 (-2.40)
H_2O	top2	-1.21
COH	Cfcc2'	-4.71
HCO	Cfcc2'-Otop2	-3.79
COOH	Otop2-Cbr1' [b] (Otop2-Ctop1 [c])	-3.62 (-3.54)
HCOO	Otop2-Ctop1[a] (Otop2-Otop2)	-5.35 (-5.27)
HCOOH	top2-H down	-1.62
CH_2O	Otop2-Ctop1 (Otop2)	-2.54 (-2.49)
CH_2OH	Otop2-Ctop1 (Otop2)	-2.63 (-2.59)
CH_2O_2	Otop2-Otop2	-7.96
H_2COOH	Otop2	-4.83
CH_3O	top2	-4.38
CH_3OH	top2	-1.25

[a] Indicates that two oxygen atoms of the species are respectively adsorbed on two metal atoms at the preferred site specified, forming a tridentate configuration because the C atom is also bonded to the surface at the preferred site specified.
[b] Indicates that COOH is adsorbed with the H atom oriented away from the Ti/Cu(111) surface because it is looking to the upward direction.
[c] Indicates that COOH is adsorbed with the H atom looking to the downward direction near the Ti/Cu(111) surface.

The structural parameters for the geometries of the adsorbates illustrated on Fig. 5.7 are detailed in Table A.2. CO_2 is chemically adsorbed on Ti/Cu(111) with a highly favorable binding energy of -2.40 eV (Table 5.5) and adopting a bent configuration that is depicted in Fig. A.6a. The O-C-O angle is 122°, the two O atoms are bonded to the Ti atoms at top2 sites with an average bond distance of 1.98 Å, and the C atom is bonded to a Cu atom at the top1 site with a bond length of 2.05 Å (Table A.2). The results in Table A.2 also show that among the atomic species, the adsorption of C causes more deformation in the Ti/Cu(111) surface than O and H. This deformation is caused by increasing the average distance Cu-Cu and Ti-Cu of the atoms in contact with carbon by

0.16 and 0.14 Å, respectively. Adsorbed species, such as CO, CO_2, COH, HCO, COOH, on Ti/Cu(111) cause surface deformations with considerable increments (0.10-0.42 Å) in the average distance between the two Cu atoms at the bridge1' site. However, the adsorption of other molecular species, such as OH, H_2O and HCOO, do not cause a significant change in d_{Cu-Cu}, when compared with the relaxed clean Ti/Cu(111) surface. In fact, a major deformation caused by increasing or decreasing d_{Ti-Cu} is not observed after the adsorption of the molecular species, with the exception of COOH, for which a increment of 0.13 Å is estimated. A notable upward displacement of the Ti atoms in the Cu surface corresponding to 0.02 Å is observed after the adsorption of the species OH, CO, CO_2, HCOO, CH_2O, CH_3O, CH_2O_2 and H_2COOH on Ti/Cu(111), as illustrated in Fig. 5.7 and detailed in Table A.2.
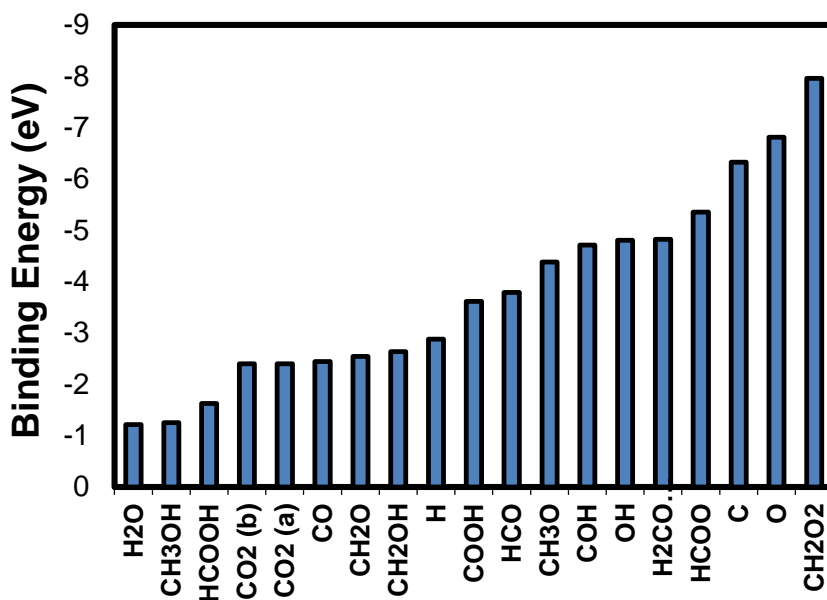
Fig. 5.8. Binding energies for species relevant to CO_2/CO hydrogenation at their preferred adsorption site on Ti/Cu(111). For CO_2, configuration (a) is Otop2-Ctop1 and (b) is Otop2-Cbr1'.

Thermochemistry of possible surface reactions on Ti/Cu(111)

- Hydrogenation of CO_2 and CO to formic acid (HCOOH)

The synthesis of formic acid has been studied through the hydrogenations of CO_2 and CO analyzing various pathways, as depicted in Fig. 5.9a. These results indicate that the production of formic acid through CO_2 hydrogenation is more favorable by the formation of formate than carboxyl (pink and green lines in Fig. 5.9a, respectively). Formic acid could also be generated from formyl via the decomposition of HCOO (purple line) or the hydrogenation of CO formed by the decomposition of CO_2 (orange line). The CO hydrogenation could produce the COH intermediate, but this hydrogenation requires 0.92 eV more than the reaction to form HCO. For this reason, the COH intermediate is not considered in the reaction mechanism depicted in Fig. 5.9a. The HCOO decomposition is thermodynamically more favorable than CO hydrogenation, with reaction energies of -0.15 and 0.35 eV, respectively. However, the decomposition of CO_2 to CO and O is more favorable than any formate route. Thus, the minimum energy pathway to produce formic acid from $CO_{2(g)}$ and $H_{2(g)}$ on Ti/Cu(111) is via the decomposition of CO_2 followed by the hydrogenation of CO (the blue and orange routes).

- Hydrogenation of CO_2 and CO to formaldehyde (CH_2O) and methanol (CH_3OH)

Fig. 5.9b shows plausible reaction pathways that were evaluated for the synthesis of formaldehyde and methanol via CO_2 and CO hydrogenation. Formaldehyde could be produced through formic acid and hydroxymethoxy by the routes of COOH (green and pink lines in Fig. 5.9b) or HCOO (pink line), being the latter more favorable than the former, as discussed in the previous section. However, dioxymethylene as product of the

hydrogenation of HCOO is favored over formic acid. A competitive route for the CH_2O_2 pathway (red line) is the decomposition of formate (purple line) followed by the hydrogenation of CO (orange line). These pathways are very similar because the electronic energies of reaction for $HCOO^* + H^* \rightarrow CH_2O_2^* + ^*$ (R7) and $HCOO^* + ^* \rightarrow HCO^* + O^*$ (R21) are -0.18 and -0.15 eV, respectively. The reaction energies for $CH_2O_2^* + ^* \rightarrow CH_2O^* + O^*$ (R11) and $HCO^* + O^* + H^* \rightarrow HCO^* + OH^* + ^*$ (R18) are also similar, with an energy difference of 0.02 eV. The main difference between the CO hydrogenation and CH_2O_2 pathways is that the decomposition of CO_2 is more thermodynamically favorable than the HCOO formation by -0.50 eV. Therefore, the CO_2 decomposition followed by the CO hydrogenation is the minimum energy pathway to synthesize formaldehyde through the hydrogenation of CO_2.

Formaldehyde is a reaction intermediate in the methanol synthesis. Thus, the minimum energy pathway obtained from the analysis of reaction mechanism for formaldehyde is also the most favorable route to produce methanol on Ti/Cu(111). In the last steps of the methanol synthesis, formaldehyde can be hydrogenated to two possible intermediates, CH_3O or CH_2OH. As illustrated in Fig. 5.9b, the hydrogenation of CH_2O to CH_3O (orange line) requires less energy than the hydrogenation to CH_2OH (gray line).

The RWGS reaction might be a competitive reaction for the hydrogenation of CO (R22). The hydrogenation of O^* (R18) is slightly more favorable than R22 by 0.18 eV. The hydrogenation of OH^* (R19) is less endothermic than the $HCOOH^*$ formation (R26) by 0.87 eV. However, the desorption of CO^* from Ti/Cu(111) is highly unfavorable, with a reaction energy of 2.44 eV. The adsorbed CO could be oxidized back to CO_2 or hydrogenated to HCO, which is favored over the oxidation by 0.20 eV.
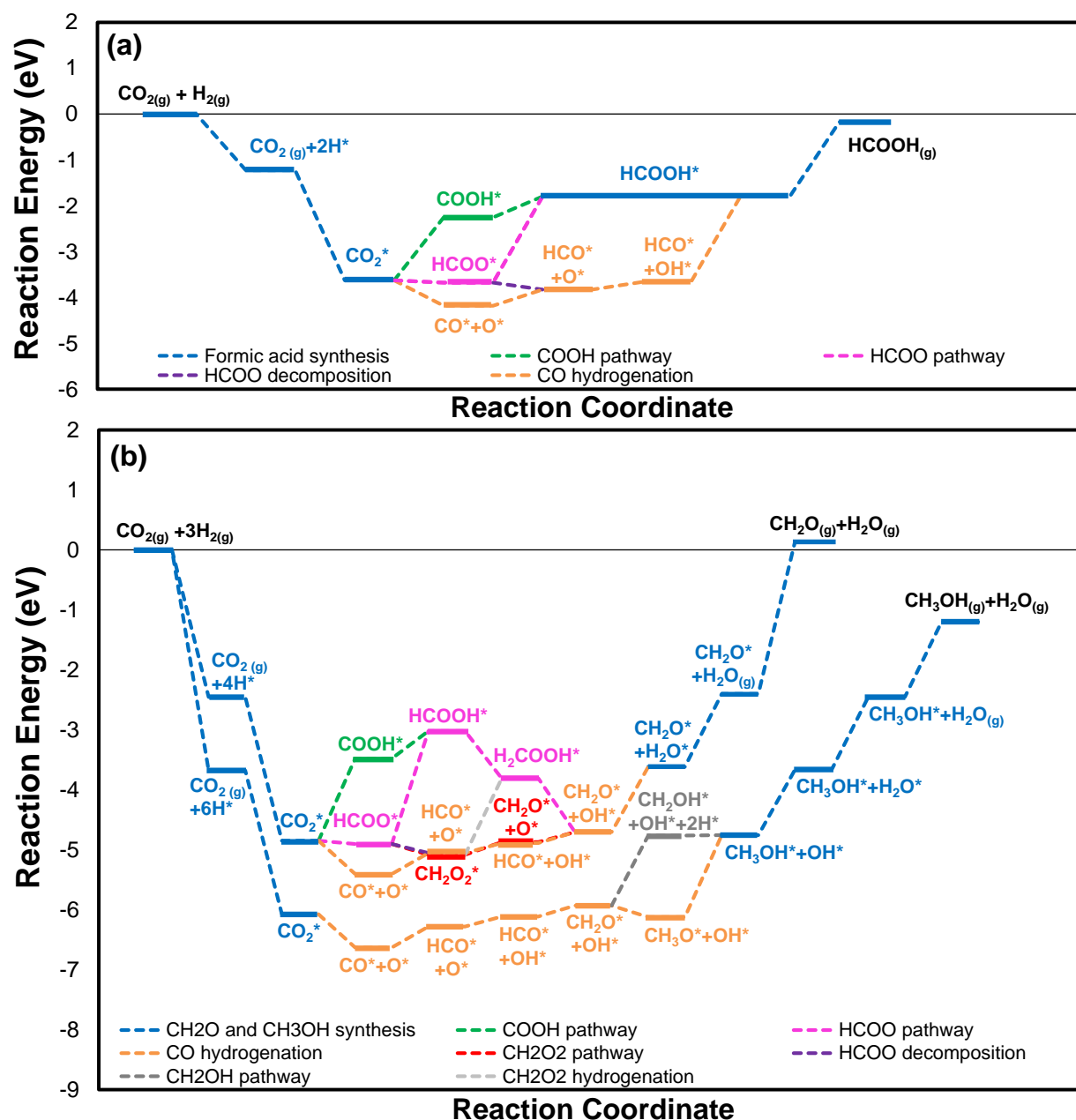
Fig. 5.9. Thermochemistry for the synthesis of: (a) formic acid, (b) formaldehyde and methanol via CO_2/CO hydrogenation on Ti/Cu(111). The reference zero corresponds to the energies of the isolated species in gas phase and the clean relaxed Ti/Cu(111) slab. Gas-phase species are indicated with (g) and adsorbed species are indicated with (*). The spectator $H_{2(g)}$ in the reaction mechanism of formaldehyde and formic acid, and the adsorbed hydrogen (H*) have been omitted from the labels to improve legibility.

The reaction mechanisms obtained for the synthesis of formic acid, formaldehyde and methanol from CO hydrogenation on the Ti-doped Cu(111) surface have two similarities. The first similarity is the downhill in the potential energy (Region A in Fig. 5.10) during the adsorption steps and the second one is the uphill region (Region B) in the coupling of HCO* and OH*, the hydrogenation of the oxygen in OH* and CH₃O*, and the desorption steps. This high request of energy in the last steps of the hydrogenation reactions is because of the strong interaction between O and Ti. Thus, the syntheses of formic acid, formaldehyde and methanol are not thermodynamically favored on Ti/Cu(111).
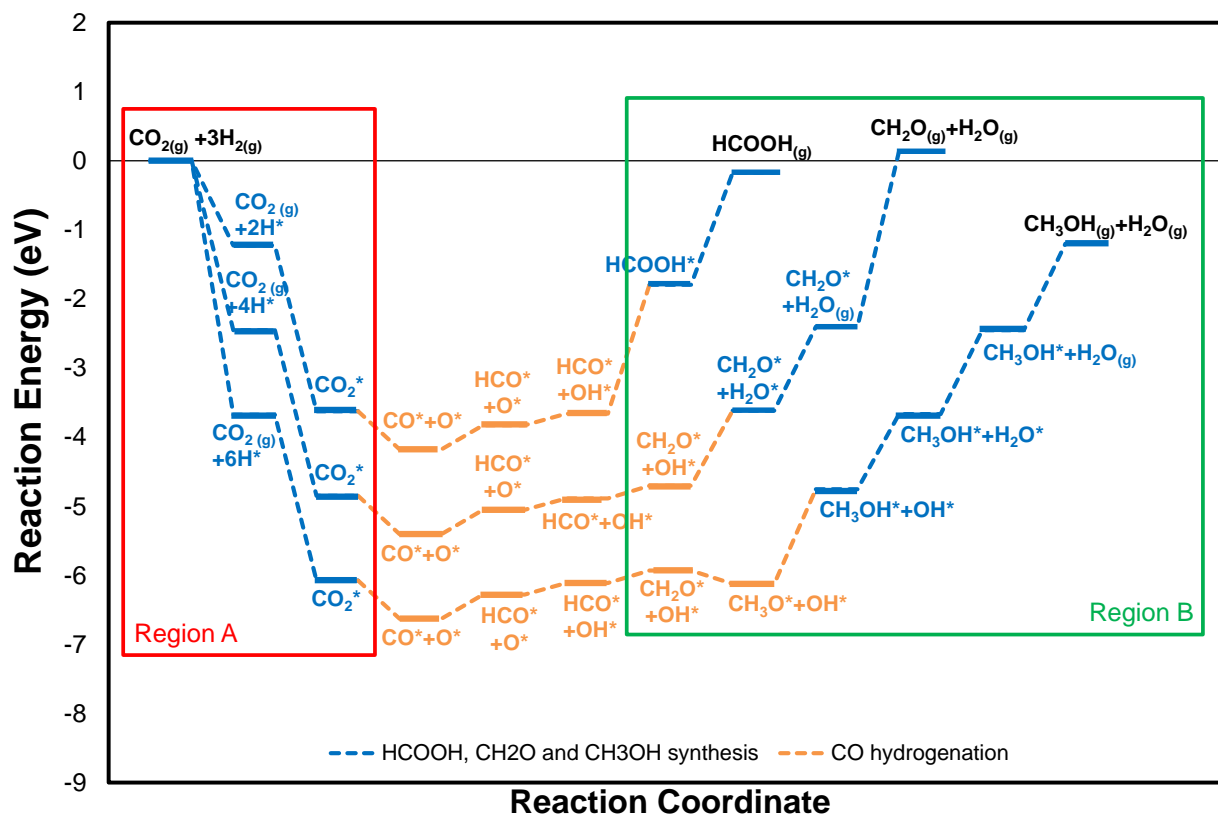
Fig. 5.10. Minimum energy pathways for the synthesis of formic acid, formaldehyde and methanol via CO hydrogenation on Ti/Cu(111). The reference zero corresponds to the energies of the isolated species in gas phase and the clean relaxed Ti/Cu(111) slab. Gas-phase species are indicated with (g) and adsorbed species are indicated with (*). The spectator molecules of $H_{2(g)}$ in the reaction mechanism of formic acid and formaldehyde, and the adsorbed hydrogen (H*) have been omitted from the labels to improve legibility.

5.3.2.3   Mg-doped Cu(111) surface as catalyst for CO_2/CO hydrogenation

Adsorption study and binding energies for Mg/Cu(111)

The preferred adsorption sites for the atomic and molecular species analyzed on Mg/Cu(111) are illustrated on Fig. 5.11 and Table 5.6. Most species adsorb preferentially on mixed adsorption sites, in which the molecule is bonded to Cu and Mg atoms, adopting monodentate, bidentate or tridentate conformations. This is probably because most adsorbates are adsorbed through oxygen and the oxophilicity of Mg. However, Mg does not demonstrate to have an interaction with oxygen as strong as it was observed with Ti. On the Mg/Cu(111) surface, the species that do not have oxygen (e.g., H and C) or the ones that are not bonded to the surface through oxygen (e.g., CO and COH) prefer the adsorption sites on Cu atoms.
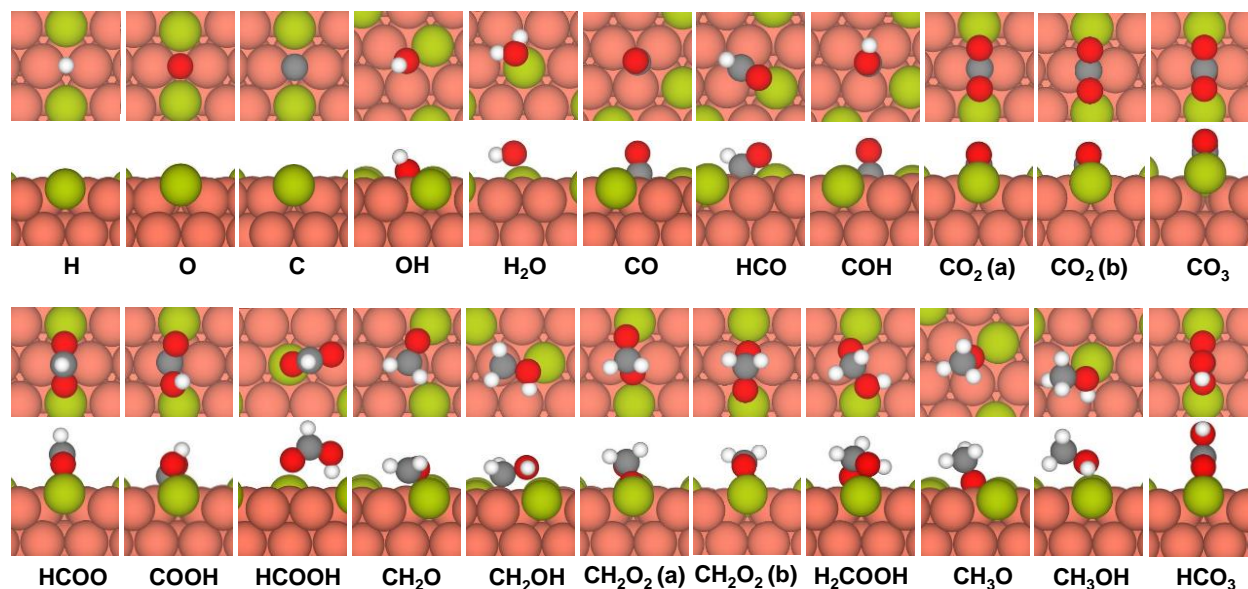
Fig. 5.11. Top and side views of the preferred adsorption sites on the Mg/Cu(111) surface for the species studied. For CO_2, configuration (a) is Otop2-Otop2 and (b) is Otop2-Ctop1. For CH_2O_2, configuration (a) is Otop2-Ofcc2' and (b) is Otop2-Ohcp2'. Table A.3 provides the geometric details for these structures.

Table 5.6. Preferred adsorption sites with their binding energies for each species adsorbed on Mg/Cu(111).

Adsorbate	Preferred adsorption site	Binding energy (eV)
H	br1' (hcp1)	-2.61 (-2.57)
O	br1'[a]	-6.03
C	br1'	-5.65
CO	fcc1	-1.14
OH	fcc2 (hcp2)	-3.77 (-3.74)
CO_2	Otop2-Otop2 (Otop2-Ctop1 [b])	-1.15 (-1.15)
H_2O	physisorption	-0.86
COH	fcc1 (Cbr1'-Otop2)	-3.18 (-3.15)
HCO	Otop2-Cbr1 (Otop2-Cbr1')	-2.29 (-2.26)
COOH	Ctop1-H up [c] (Otop2-Ctop1 [d])	-2.88 (-2.82)
HCOO	Otop2-Otop2	-4.23
HCOOH	top2-H down	-1.09
CO_3	Otop2-Ofcc2'	-6.27
HCO_3	Otop2-Otop2	-4.17
CH_2O	Otop2-Ctop1 (Otop2)	-0.99 (-0.88)
CH_2OH	Ctop1	-1.98
CH_2O_2	Otop2-Ofcc2' (Otop2-Ohcp2')	-5.78 (-5.78)
H_2COOH	Otop2	-3.63
CH_3O	fcc2 (hcp2)	-3.17 (-3.15)
CH_3OH	physisorption	-0.97

[a] Indicates that this species is adsorbed through four metal atoms (two Cu and two Mg) on Mg/Cu(111).
[b] Indicates that two oxygen atoms of the species are respectively adsorbed on two metal atoms at the top site, forming a tridentate configuration because other atom (C or O) is also bonded to the surface at the preferred site specified.
[c] Indicates that COOH is adsorbed with the H atom oriented away from the Mg/Cu(111) surface because it is looking to the upward direction.
[d] Indicates that COOH is adsorbed with the H atom looking to the downward direction near the Mg/Cu(111) surface.

The calculated binding energies for the adsorption sites shown in Fig. 5.11 are detailed in Table 5.6 and Fig. 5.12. For some of the studied species on Mg/Cu(111), we obtained adsorption sites that have degenerate binding energies, which are described in Table 5.6 and enclosed by parentheses. Fig. 5.12 presents the binding energies on Mg/Cu(111) in ascending order, which indicates that water is the species with the lowest binding strength, while carbonate has the strongest adsorption. Water and methanol have

been predicted to be weakly adsorbed on the Mg/Cu(111) surface at the Mg atom with bond distances of 2.12 and 2.11 Å, as shown in Table A.3. The high adsorption strength observed for carbonate is because this species adopts an interesting configuration, which is illustrated in Fig. A.6b, where its two oxygen atoms interact with the Mg-doped Cu(111) surface. CO_2 is activated in the Mg/Cu(111) surface adopting two stable configurations (Otop2-Otop2 and Otop2-Ctop1), one bidentate and another tridentate, with a binding energy of -1.15 eV, which are shown in Fig. 5.11. CO_2 absorbed on the Otop2-Otop2 site with average O-Mg bond lengths of 1.99 Å and a O-C-O angle of 124° is also illustrated in Fig. A.6c.
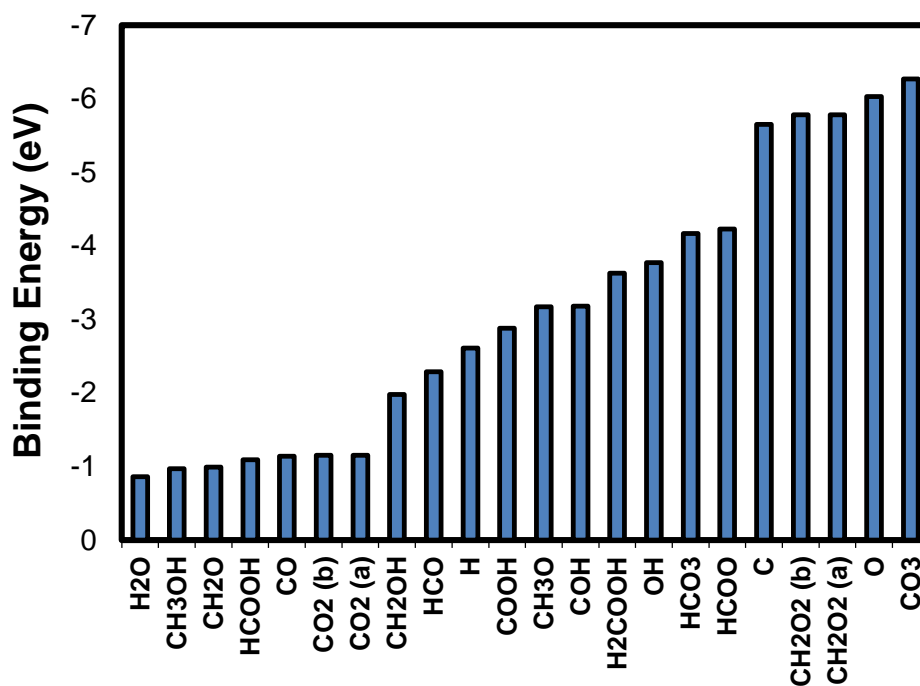
Fig. 5.12. Binding energies for species relevant to CO_2/CO hydrogenation at their preferred adsorption site on Mg/Cu(111). For CO_2, configuration (a) is Otop2-Otop2 and (b) is Otop2-Ctop1. For CH_2O_2, configuration (a) is Otop2-Ofcc2' and (b) is Otop2-Ohcp2'.

Thermochemistry of possible surface reactions on Mg/Cu(111)

- Hydrogenation of CO_2 and CO to formic acid (HCOOH)

The production of formic acid via the hydrogenation of CO_2 on the Mg-doped Cu(111) surface was evaluated through the formation of formate and carboxyl, and the hydrogenation of CO as illustrated on Fig. 5.13a. As shown in this figure, the generation of HCOO (pink line in Fig. 5.13a) is more favorable than the COOH pathway (green line) and the decomposition of CO_2 to CO* and O* (orange line) by -1.04 eV and -0.73, respectively. In fact, the formation of the HCO intermediate through the decomposition of HCOO (purple line) is favored over the CO hydrogenation. Thus, the minimum energy route for the synthesis of formic acid from CO_2 hydrogenation on Mg/Cu(111) is the formate pathway.

- Hydrogenation of CO_2 and CO to formaldehyde (CH_2O) and methanol (CH_3OH)

Fig. 5.13b shows the different pathways that were analyzed to produce formaldehyde and methanol from CO_2 hydrogenation on Mg/Cu(111). As discussed in the previous section, the formation of HCOO is more favorable than the COOH and CO_2 decomposition pathways. However, the hydrogenation of HCOO could generate two intermediates, HCOOH or CH_2O_2, being the hydrogenation at the C atom to produce CH_2O_2 (red line) favored over the hydrogenation at the O atom to produce HCOOH (pink line) by -0.42 eV, as shown in Fig. 5.13b. The next step in the CH_2O_2 pathway could be the C-O bond breaking in CH_2O_2 (R11) or the hydrogenation of CH_2O_2 (R10), where the former is endothermic by 0.37 eV and the last one is thermoneutral, indicating that the formation of H_2COOH* is favored over CH_2O* + O*. However, the hydrogenation of O* (R18), which

is the next step for CH_2O_2 route, is less endothermic than the C-OH bond breaking in H_2COOH^* (R12) for the H_2COOH pathway. Therefore, the minimum energy path depends on the activation energy barriers for these elementary steps. For Cu(111), Grabow and Mavrikakis [26] found that the reactions $CH_2O_2^* + ^* \rightarrow CH_2O^* + O^*$ (R11) and $H_2COOH^* + ^* \rightarrow CH_2O^* + OH^*$ (R12) are spontaneous in the reverse direction, obtaining only thermodynamic barriers for these reactions. This has been also reported by Sakong for the R11 reaction on Cu(110) [51]. If on Mg/Cu(111), the same trends prevail, then the activation energy barriers for the hydrogenation of O (R18) and CH_2O_2 (R10) would dictate the most favorable route in the hydrogenation of CO_2 to formaldehyde. Following the BEP relation, we proposed the H_2COOH pathway (red line) as the most favorable route for the synthesis of formaldehyde from CO_2 on Mg/Cu(111), because the reaction R10 is expected to have a lower activation barrier than R18.

Fig. 5.13. Thermochemistry for the synthesis of: (a) formic acid, (b) formaldehyde and methanol via CO_2/CO hydrogenation on Mg/Cu(111). The reference zero corresponds to the energies of the isolated species in gas phase and the clean relaxed Mg/Cu(111) slab. Gas-phase species are indicated with (g) and adsorbed species are indicated with (*). The spectator $H_{2(g)}$ in the reaction mechanism of formaldehyde and formic acid, and the adsorbed hydrogen (H*) have been omitted from the labels to improve legibility.

115

The methanol synthesis on Mg/Cu(111) was also studied through the reaction pathways analyzed for the formaldehyde synthesis, as depicted in Fig. 5.13b. The H_2COOH pathway followed by the CH_3O pathway (red and green lines in Fig. 5.13b), are also possible routes to produce methanol from CO_2 hydrogenation. In addition, we evaluated other route that involves the C-O bond breaking in H_2COOH^* to yield CH_2OH^* and O^* and the hydrogenation of CH_2OH^* to methanol (the gray line). This pathway could be competitive for the H_2COOH-CH_3O pathway because the intermediate CH_2O^* is more stable than CH_2OH^* by only -0.01 eV. Furthermore, the reaction $CH_2OH^* + H^* \rightarrow CH_3OH^* + ^*$ (R17) is exothermic with an electronic energy of -0.64 eV, while the reaction $CH_3O^* + H^* \rightarrow CH_3OH^* + ^*$ (R16) is endothermic by 0.17 eV. It has been observed in experimental studies with Cu/ZnO and Cu/ZnO/Cr$_2$O$_3$ catalysts [32] as well as in DFT studies with Cu(111) [26], that the hydrogenation of methoxy to methanol is the rate-limiting step in the hydrogenation of CO_2, due to the high energy barrier of this step. A third pathway involves the formation of CH_2OH from the hydrogenation of CH_2O at the O atom instead of the C atom, which connects the red and gray lines. Energy barriers can be used to determine which route yields the minimum energy path. However, we proposed the H_2COOH-CH_2OH pathway (red and gray lines in Fig. 5.14) as the most probable minimum energy route for the hydrogenation of CO_2 to methanol on Mg/Cu(111).

Carbonate (CO_3) has been proposed as a key intermediate for catalysts in which the dissociation of CO_2 is favorable or the hydrogenation of CO_2 is carried on surfaces treated with oxygen or supported on metal oxides. While for Mg/Cu(111), none of these conditions are met, bicarbonate could be formed if CO_2^* reacts with OH^* (R28) with an

almost thermoneutral reaction energy of -0.03 eV. From HCO_3^*, formate might be produced via the following steps: $HCO_3^* \rightarrow CO_3^* \rightarrow CO_2^* + O^* \rightarrow HCOO^*$.
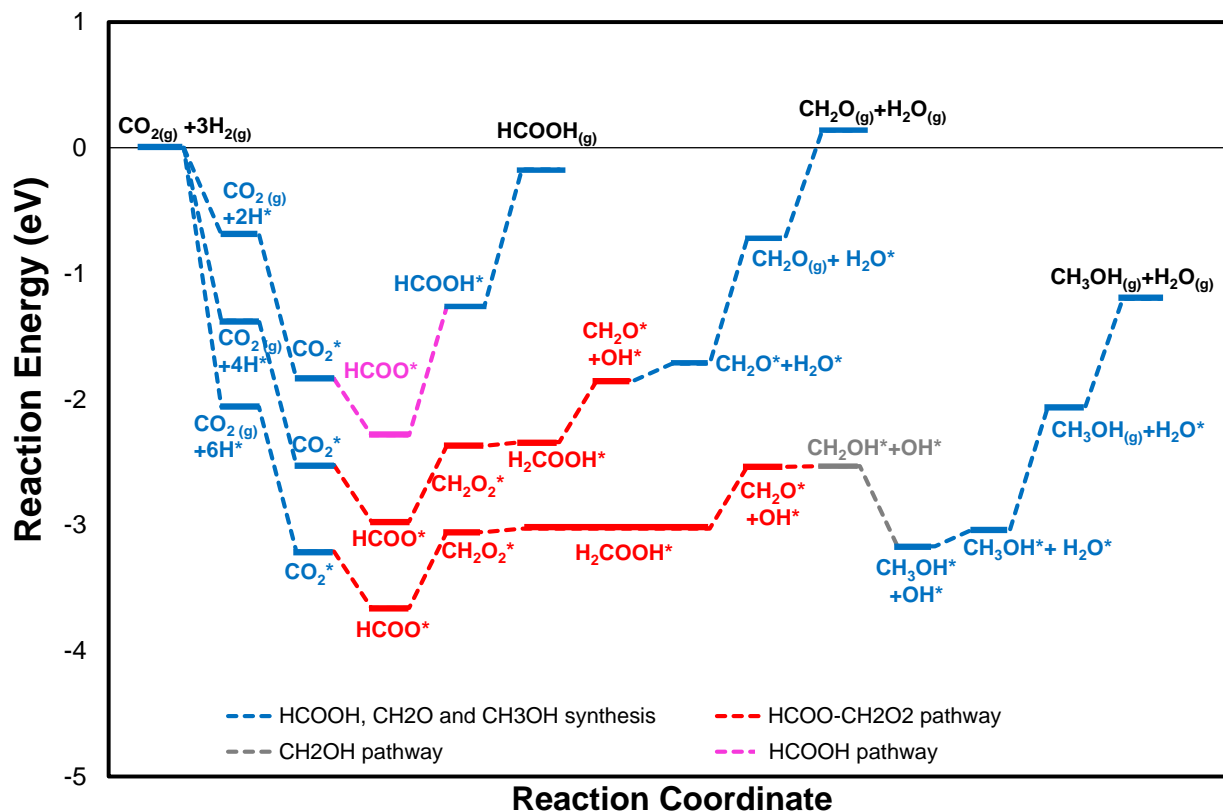
Fig. 5.14. Minimum energy pathways for the synthesis of formic acid, formaldehyde and methanol via CO_2 hydrogenation on Mg/Cu(111). The reference zero corresponds to the energies of the isolated species in gas phase and the clean relaxed Mg/Cu(111) slab. Gas-phase species are indicated with (g) and adsorbed species are indicated with (*). The spectator molecules of $H_{2(g)}$ in the reaction mechanism of formic acid and formaldehyde, and the adsorbed hydrogen (H*) have been omitted from the labels to improve legibility.

The most favorable mechanism of reaction for the CO_2 hydrogenation to produce formic acid, formaldehyde and methanol on Mg/Cu(111) surface is through the formation of formate. As illustrated in Fig. 5.14, the hydrogenation of CO_2 on the Mg-doped Cu(111) surface is downhill in the potential energy on the adsorption steps and uphill in the hydrogenation of the oxygen in formate and on the desorption steps. On this surface, the formaldehyde and methanol formation is thermodynamically favorable while the formic

acid synthesis is not favored, because CH_2O_2 is more stable than HCOOH. However, the desorption of these products and water requires a significant amount of energy. The thermochemistry results indicate that Mg/Cu(111) is more selective to methanol than to formic acid or formaldehyde. However, the activation barriers would be useful to determine the behavior of the catalyst selectivity dictated by the reaction kinetics.

5.3.3 Comparison for the M-doped Cu(111) surfaces

The adsorption strength of most of the species adsorbed on Ti/Cu(111) and Ga/Cu(111) surfaces follow similar trends as on Mg/Cu(111). However, a comparison of the charts depicted in Figs. 4, 8, and 12 reveals that for Ga/Cu(111) and Mg/Cu(111), CO_2, carbonate and bicarbonate do not follow similar adsorption strength tendencies. Furthermore, the most favorable adsorption sites are different for most adsorbates on the three M-doped Cu surfaces and for species adsorbed at the same sites on these surfaces (e.g., H_2O, CH_2O, HCOOH and CH_3OH), different adsorption strengths are obtained. The binding energies of these species estimated on Ti/Cu(111) are, on average, 0.7 eV lower than the energies obtained for Mg/Cu(111). Differences in energies are also observed when comparing binding energies of adsorbates at the same mixed site on Ga/Cu(111) with the energies obtained on Cu(111) doped with Ti and Mg. For instance, C and O have the same adsorption preference on Ga and Ti/Cu(111) and their binding energies with the Ti dopant are lower than Ga by 1.6 eV on average. If the surfaces doped with Ga and Mg are compared, the difference between the binding energies of CH_3O is 0.6 eV. For the species adsorbed on Ga and Mg/Cu(111) at sites with only Cu (e.g., CO and COH), there are no significant differences in their binding energies. Therefore, these results indicate

that the adsorption strength increases by following this order of the dopant in Cu(111): Ga < Mg < Ti. This is consistent with the order of the binding energy of O, which has been used as descriptor for the catalyst screening, where this energy increases in the same order of dopant: Ga < Mg < Ti.

The reaction mechanism and energies for the hydrogenation of CO_2 to formic acid, formaldehyde and methanol considerably change with the dopant added on the Cu(111) surface used as catalyst. When the dopant is Ga and Mg, the most favorable pathway is through the formate intermediate, while for the Cu(111) surface doped with Ti, the CO_2 decomposition followed by CO hydrogenation is the favored route. For the synthesis of formaldehyde and methanol via the formate pathway, HCOOH is more stable than CH_2O_2 on Ga/Cu(111), which is consistent with the observations of Grabow and Mavrikakis on a pure Cu(111) surface [26]. The opposite trends are observed on Ti and Mg/Cu(111). On the other hand, CH_3O is proposed as a more stable reaction intermediate than CH_2OH on Ti and Ga/Cu(111), similar to proposed mechanisms for Cu(111) [26,30]. However, CH_2OH might be a key intermediate for the methanol synthesis on Mg/Cu(111) because it is equally stable to CH_2O and its hydrogenation is highly exothermic in contrast with the hydrogenation of CH_3O, which is considered a rate-limiting step for this reaction in some cases [26,32]. Thus, the addition of Ga, Ti or Mg considerably changes the thermochemistry for the hydrogenation of CO_2.

The thermochemistry analysis indicates that Ti/Cu(111) does not have a good catalytic performance for the hydrogenation of CO (generated from CO_2 decomposition) despite it activates the CO_2 molecule, due to the extremely high energy requirements in the last reaction steps. The Cu(111) surface doped with Ga or Mg are promising catalysts for the

hydrogenation of CO_2. The activation of CO_2 and the formation of the desired products are accomplished on Mg/Cu(111). However, the hydrogenation catalyzed by Mg/Cu(111) requires more energy than Cu(111) or Ga/Cu(111) in order to desorb the products. Ga/Cu(111) does not activate CO_2, but the hydrogenation of HCOO and the desorption steps are less endothermic on this surface than on Mg/Cu(111), and the hydrogenation of CH_3O is thermoneutral. Both Mg/Cu(111) and Ga/Cu(111) are thus attractive materials for the CO_2 conversion into useful chemical compounds. On both, the formate route is thermodynamically favored over the RWGS reaction and CO hydrogenation. Moreover, Mg and Ga/Cu(111) are selective to methanol and the formation C from CO decomposition on these surfaces is not thermodynamically favorable.

5.4   Conclusions

In this study, DFT calculations were used to screen metal-doped Cu(111) surfaces using different descriptors to evaluate the feasibility of employing these surfaces for CO_2/CO hydrogenation. From the screening analysis, Cu(111) doped with Ga, Ti and Mg were identified as potentials catalysts for these reactions. The adsorption of relevant species and key intermediates involved in the CO_2/CO hydrogenation and thermochemistry for the synthesis of methanol, formic acid and formaldehyde on M/Cu(111) with M= Ti, Mg or Ga were studied to evaluate catalytic performance of these surfaces.

The minimum energy pathway to produce formic acid, formaldehyde and methanol from $CO_{2(g)}$ and $H_{2(g)}$ on Ti/Cu(111) is via the decomposition of CO_2 followed by the hydrogenation of CO. On Ga/Cu(111), the most favorable route for the synthesis of these

products is through the formation of the intermediates: HCOO* → HCOOH* → H_2COOH^* → CH_2O^* → CH_3O^*. While for Mg/Cu(111), the following species are the key intermediates in the reaction mechanism to produce formaldehyde and methanol: HCOO* → $CH_2O_2^*$ → H_2COOH^* → CH_2O^* → CH_2OH^*.

The synthesis of formic acid, formaldehyde and methanol are not thermodynamically favored on Ti/Cu(111) because the high energy requirement in the last reaction steps due to the strong interaction between O and Ti. Ga/Cu(111) and Mg/Cu(111) are predicted to be potential catalysts for the direct and selective conversion of CO_2 to methanol. However, the desorption of CH_3OH and H_2O from Mg/Cu(111) required a considerable amount of energy, and CO_2 is not activated by Ga/Cu(111). The stability of these M-doped Cu surfaces was not affected by the carbon accumulation in the surface, because the decomposition of CO was not thermodynamically favorable.

The binding energies of CO_2 and O were good descriptors for the catalyst screening because they predicted that CO_2 can be activated by Ti and Mg/Cu(111) surfaces and that the adsorption strength of species adsorbed by oxygen on mixed sites increases with the following dopant order: Ga < Mg < Ti. Nevertheless, we propose that an effective approach for a catalyst screening is to use as descriptor the reaction energy for the formation of key intermediates in the hydrogenation of CO_2 and CO. We have identified these key intermediates as: HCOO, CH_2O and CH_3O and HCO.

References

[1] G.A. Olah, A. Goeppert, G.K.S. Prakash, Chemical Recycling of Carbon Dioxide to Methanol and Dimethyl Ether: From Greenhouse Gas to Renewable, Environmentally Carbon Neutral Fuels and Synthetic Hydrocarbons, J. Org. Chem. 74 (2009) 487–498.

[2] N.A.M. Razali, K.T. Lee, S. Bhatia, A.R. Mohamed, Heterogeneous catalysts for production of chemicals using carbon dioxide as raw material: A review, Renew. Sustain. Energy Rev. 16 (2012) 4951–4964.

[3] J. Toyir, R. Miloua, N.E. Elkadri, M. Nawdali, H. Toufik, F. Miloua, et al., Sustainable process for the production of methanol from CO_2 and H_2 using Cu/ZnO-based multicomponent catalyst, Phys. Procedia. 2 (2009) 1075–1079.

[4] W. Wang, S. Wang, X. Ma, J. Gong, Recent advances in catalytic hydrogenation of carbon dioxide, Chem. Soc. Rev. 40 (2011) 3703–3727.

[5] Y. Yang, J. Evans, J.A. Rodriguez, M.G. White, P. Liu, Fundamental studies of methanol synthesis from CO_2 hydrogenation on Cu(111), Cu clusters, and Cu/ZnO(000), Phys. Chem. Chem. Phys. 12 (2010) 9909–9917.

[6] C.-S. Chen, W.-H. Cheng, S.-S. Lin, Study of reverse water gas shift reaction by TPD, TPR and CO_2 hydrogenation over potassium-promoted Cu/SiO_2 catalyst, Appl. Catal. Gen. 238 (2003) 55–67.

[7] F.S. Stone, D. Waller, Cu–ZnO and Cu–ZnO/Al_2O_3 Catalysts for the Reverse Water-Gas Shift Reaction. The Effect of the Cu/Zn Ratio on Precursor Characteristics and on the Activity of the Derived Catalysts, Top. Catal. 22 (2003) 305–318.

[8] M. Behrens, F. Studt, I. Kasatkin, S. Kühl, M. Hävecker, F. Abild-Pedersen, et al., The Active Site of Methanol Synthesis over Cu/ZnO/Al_2O_3 Industrial Catalysts, Science. 336 (2012) 893–897.

[9] S. Lee, Handbook of Alternative Fuel Technologies, CRC Press, Boca Raton, FL, 2007.

[10] F. Studt, I. Sharafutdinov, F. Abild-Pedersen, C.F. Elkjær, J.S. Hummelshøj, S. Dahl, et al., Discovery of a Ni-Ga catalyst for carbon dioxide reduction to methanol, Nat. Chem. 6 (2014) 320–324.

[11] N. Homs, J. Toyir, P.R. de la Piscina, Catalytic Processes for Activation of CO_2, in: S.L. Suib (Ed.), New Future Dev. Catal., Elsevier, Amsterdam, 2013: pp. 1–26.

[12] S. Lin, J. Ma, X. Ye, D. Xie, H. Guo, CO Hydrogenation on Pd(111): Competition between Fischer–Tropsch and Oxygenate Synthesis Pathways, J. Phys. Chem. C. 117 (2013) 14667–14676.

[13] A.M. Bahmanpour, A. Hoadley, A. Tanksale, Formaldehyde production via hydrogenation of carbon monoxide in the aqueous phase, Green Chem. 17 (2015) 3500–3507.

[14] H.Y. Affefy, J.F. Liebman, S.E. Stein, Neutral Thermochemical Data, in: P.J. Linstrom and W.G. Mallard (Eds.), NIST Chem. WebBook NIST Stand. Ref. Database Number 69, National Institute of Standards and Technology, Gaithersburg MD, 2015. http://webbook.nist.gov (accessed October 31, 2015).

[15] J. Toyir, P.R. de la Piscina, J.L.G. Fierro, N. Homs, Highly effective conversion of CO_2 to methanol over supported and promoted copper-based catalysts: influence of support and promoter, Appl. Catal. B Environ. 29 (2001) 207–215.

[16] J. Toyir, P. Ramírez de la Piscina, J.L.G. Fierro, N. Homs, Catalytic performance for CO_2 conversion to methanol of gallium-promoted copper-based catalysts: influence of metallic precursors, Appl. Catal. B Environ. 34 (2001) 255–266.

[17] I. Melián-Cabrera, M.L. Granados, J.L.G. Fierro, Pd-Modified Cu–Zn Catalysts for Methanol Synthesis from CO_2/H_2 Mixtures: Catalytic Structures and Performance, J. Catal. 210 (2002) 285–294.

[18] J. Nerlov, S. Sckerl, J. Wambach, I. Chorkendorff, Methanol synthesis from CO_2, CO and H_2 over Cu(100) and Cu(100) modified by Ni and Co, Appl. Catal. Gen. 191 (2000) 97–109.

[19] F. Studt, F. Abild-Pedersen, Q. Wu, A.D. Jensen, B. Temel, J.-D. Grunwaldt, et al., CO hydrogenation to methanol on Cu–Ni catalysts: Theory and experiment, J. Catal. 293 (2012) 51–60.

[20] T. Fujitani, M. Saito, Y. Kanai, T. Watanabe, J. Nakamura, T. Uchijima, Development of an active Ga_2O_3 supported palladium catalyst for the synthesis of methanol from carbon dioxide and hydrogen, Appl. Catal. Gen. 125 (1995) L199–L202.

[21] O. Oyola-Rivera, M.A. Baltanás, N. Cardona-Martínez, CO_2 hydrogenation to methanol and dimethyl ether by Pd–Pd_2Ga catalysts supported over Ga_2O_3 polymorphs, J. CO_2 Util. 9 (2015) 8–15.

[22] Y. Yang, D. Cheng, Role of Composition and Geometric Relaxation in CO_2 Binding to Cu–Ni Bimetallic Clusters, J. Phys. Chem. C. 118 (2014) 250–258.

[23] Y. Yang, M.G. White, P. Liu, Theoretical Study of Methanol Synthesis from CO_2 Hydrogenation on Metal-Doped Cu(111) Surfaces, J. Phys. Chem. C. 116 (2012) 248–256.

[24] X. Ding, L. De Rogatis, E. Vesselli, A. Baraldi, G. Comelli, R. Rosei, et al., Interaction of carbon dioxide with Ni(110): A combined experimental and theoretical study, Phys. Rev. B. 76 (2007) 195425.

[25] M.M. Halmann, Chemical Fixation of Carbon DioxideMethods for Recycling CO_2 into Useful Products, CRC Press, 1993.

[26] L.C. Grabow, M. Mavrikakis, Mechanism of Methanol Synthesis on Cu through CO_2 and CO Hydrogenation, ACS Catal. 1 (2011) 365–384.

[27] C. Liu, B. Yang, E. Tyo, S. Seifert, J. DeBartolo, B. von Issendorff, et al., Carbon Dioxide Conversion to Methanol over Size-Selected Cu_4 Clusters at Low Pressures, J. Am. Chem. Soc. 137 (2015) 8676–8679.

[28] J.R.B. Gomes, J.A.N.F. Gomes, A theoretical study of dioxymethylene, proposed as intermediate in the oxidation of formaldehyde to formate over copper, Surf. Sci. 446 (2000) 283–293.

[29] D. Mei, L. Xu, G. Henkelman, Dimer saddle point searches to determine the reactivity of formate on Cu(111), J. Catal. 258 (2008) 44–51.

[30] Y.-F. Zhao, Y. Yang, C. Mims, C.H.F. Peden, J. Li, D. Mei, Insight into methanol synthesis from CO_2 hydrogenation on Cu(1 1 1): Complex reaction network and the effects of H_2O, J. Catal. 281 (2011) 199–211.

[31] Z.-M. Hu, H. Nakatsuji, Active sites for methanol synthesis on a Zn/Cu(100) catalyst, Chem. Phys. Lett. 313 (1999) 14–18.

[32] J.F. Edwards, G.L. Schrader, In situ fourier transform infrared study of methanol synthesis on mixed metal oxide catalysts, J. Catal. 94 (1985) 175–186.

[33] P.A. Taylor, P.B. Rasmussen, I. Chorkendorff, Is the observed hydrogenation of formate the rate-limiting step in methanol synthesis?, J. Chem. Soc. Faraday Trans. 91 (1995) 1267–1269.

[34] D.R. Lide, CRC Handbook of Chemistry and Physics, 89th Edition (Internet Version 2009), CRC Press/Taylor and Francis, Boca Raton FL, 2009.

[35] J.P. Perdew, J.A. Chevary, S.H. Vosko, K.A. Jackson, M.R. Pederson, D.J. Singh, et al., Atoms, molecules, solids, and surfaces: Applications of the generalized gradient approximation for exchange and correlation, Phys. Rev. B. 46 (1992) 6671–6687.

[36] P.E. Blöchl, Projector augmented-wave method, Phys. Rev. B. 50 (1994) 17953–17979.

[37] G. Kresse, D. Joubert, From ultrasoft pseudopotentials to the projector augmented-wave method, Phys. Rev. B. 59 (1999) 1758–1775.

[38] G. Kresse, J. Furthmüller, Efficiency of ab-initio total energy calculations for metals and semiconductors using a plane-wave basis set, Comput. Mater. Sci. 6 (1996) 15–50.

[39] G. Kresse, J. Furthmüller, Efficient iterative schemes for ab initio total-energy calculations using a plane-wave basis set, Phys. Rev. B. 54 (1996) 11169–11186.

[40] G.A. Somorjai, Introduction to Surface Chemistry and Catalysis, John Wiley & Sons, Inc., New York, NY, 1994.

[41] J.L.F. Da Silva, C. Stampfl, M. Scheffler, Converged properties of clean metal surfaces by all-electron first-principles calculations, Surf. Sci. 600 (2006) 703–715.

[42] J.P. Perdew, K. Burke, M. Ernzerhof, Generalized Gradient Approximation Made Simple, Phys. Rev. Lett. 77 (1996) 3865–3868.

[43] J.P. Perdew, K. Burke, M. Ernzerhof, Generalized Gradient Approximation Made Simple [Phys. Rev. Lett. 77, 3865 (1996)], Phys. Rev. Lett. 78 (1997) 1396.

[44] S. Grimme, Semiempirical GGA-type density functional constructed with a long-range dispersion correction, J. Comput. Chem. 27 (2006) 1787–1799.

[45] A. Ruban, H. Skriver, J. Nørskov, Surface segregation energies in transition-metal alloys, Phys. Rev. B. 59 (1999) 15990–16000.

[46] G. Lanzani, T. Kangas, K. Laasonen, Copper passivation by metal doping, J. Alloys Compd. 482 (2009) 33–42.

[47] B. Drittler, M. Weinert, R. Zeller, P.H. Dederichs, First-principles calculation of impurity-solution energies in Cu and Ni, Phys. Rev. B. 39 (1989) 930–939.

[48] M. Baskes, Modified embedded-atom potentials for cubic materials and impurities, Phys. Rev. B. 46 (1992) 2727–2742.

[49] U. Burghaus, Surface chemistry of CO_2 – Adsorption of carbon dioxide on clean surfaces at ultrahigh vacuum, Prog. Surf. Sci. 89 (2014) 161–217.

[50] F. Solymosi, The bonding, structure and reactions of CO_2 adsorbed on clean and promoted metal surfaces, J. Mol. Catal. 65 (1991) 337–358.

[51] S. Sakong, A. Gross, Total Oxidation of Methanol on Cu(110): A Density Functional Theory Study, J. Phys. Chem. A. 111 (2007) 8814–8822.

Chapter 6: Quantum Mechanical Study of the Reaction of CO_2 and Ethylene Oxide Catalyzed by Metal-Salen Complexes: Effect of the Metal Center and the Axial Ligand[1]

6.1. Introduction

Fossil fuels are currently the main carbon source in chemical industry. Because these resources are expected to be depleted within the next century, the need for alternative carbon sources has sparked interest in using biorenewable sources, such as CO_2. The coupling reaction of CO_2 with epoxides is a good example of a chemical process in which valuable chemicals can be formed from an inexpensive and abundant feedstock. Cyclic carbonates and polycarbonates can be produced using CO_2 and an epoxide as raw material. These products are widely used in industry. Cyclic carbonates are used as precursors in fine chemical and pharmaceutical synthesis, electrolytes in lithium ion batteries and polar aprotic solvents [1,2]. Polycarbonates are one of the most widely used engineering plastics [1], and its demand in the U.S.A. was estimated at 360 thousand metric tons in 2011 [3]. Polycarbonates have applications in automotive and electronics industries [3].

Inoue and coworkers were the first to demonstrate, in 1969, that CO_2 and propylene oxide can be copolymerized with a Zn-based catalyst [4]. Since the work of Inoue was published, various catalysts have been used for the CO_2/epoxide coupling reaction, and salen complexes (bis(salicylidene)ethylenediamine) with various metal centers, such as Co or Cr among others, have exhibited excellent catalytic properties with turnover frequencies of up to 3070 h^{-1} at 120 °C [5–12]. A schematic diagram of a metal-salen complex is shown in Fig. 6.1.

| **1**(M)-Cl | **1**(M)-DMAP |
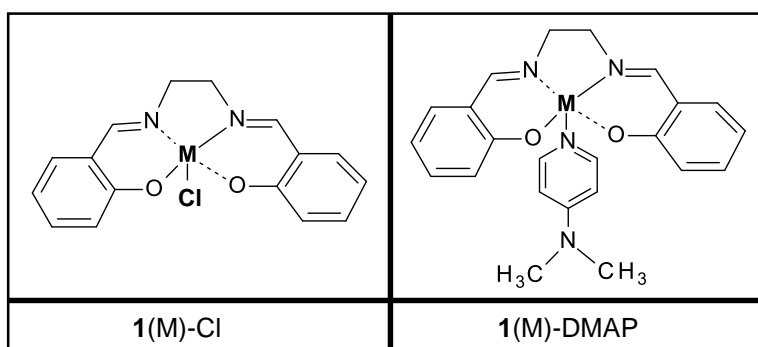
Fig. 6.1. Schematics of a metal-salen molecule and the salen models used for the DFT calculations, **1**(M)-L. M is the metal center (M=Co, Cr, Mn, Fe, Al or Zn). L is the axial ligand (L= Cl or DMAP).

The selectivity for cyclic carbonates or polycarbonates produced through the coupling reactions of CO_2 and epoxides illustrated in Fig. 6.2a depends on the catalyst, cocatalyst and on the reaction conditions, such as temperature, CO_2 pressure and cocatalyst loading [13]. Independent works by Kruper and Dellar, Inoue et al., Jacobsen et al. and Lu et al. proved that the selectivity, reaction rates and yields of reaction can be modified by changing the axial ligand of the catalyst and by using different cocatalysts [5,14–17]. It has also been observed that the production of cyclic carbonates increases at temperatures above 80°C, because their formation usually involve higher activation barriers than the polymeric products [5,12,18]. Similarly, structural changes in the catalyst

and nucleophilic promoters may also impact the reaction conditions. For instance, Lu and coworkers performed the CO_2/epoxide coupling reaction at room temperature obtaining high turnover frequencies, conversions and selectivities for propylene carbonate using Co and Al-salen complexes and quaternary ammonium salts as cocatalysts [19,20] Shen et al. studied the reaction of CO_2 and propylene oxide catalyzed by binaphthyldiamino Cu(III), Zn(II) or Co(II)-salen complexes in the presence of various Lewis bases, obtaining higher turnover numbers and yields for propylene carbonates with triethylamine, pyridine, diazabicycloundecene and DMAP [21]. In fact, the authors reported that the reaction of an epoxide with CO_2 does not take place if an organic base is not used along with the binaphthyldiamino salen catalysts [21]. Paddock and Nguyen also found that Cr(III)-salen complexes along with DMAP can provide yields in the range of 94-100%, with 100% selectivity for cyclic carbonates [22]. Furthermore, Rieger and coworkers demonstrated that the DMAP/catalyst ratio, in this case a chlorinated Cr(III)-salen complex, affects the selectivity [23]. They found that higher DMAP/salen ratios favored the production of propylene carbonate over the polycarbonate product and a selectivity of 100% for the cyclic carbonate was obtained when 2 equivalents of DMAP were used in the reaction. It has been suggested that DMAP favors the cycloaddition reaction because of its high nucleophilicity, which facilitates the dissociation of the growing polymer chain when another molecule of DMAP coordinates the Cr center, and this dissociation can be followed by the backbiting reaction to form cyclic products [12,23,24].

While the role of the DMAP in these reaction systems has not been fully understood, it is clear, from experimental works, that DMAP by itself does not catalyze the reaction [22]. Two hypotheses have been postulated on the role of DMAP when it is coordinated

to the metal atom as an axial ligand of the catalyst: DMAP could act as a nucleophile that dissociates from the metal center to attack the epoxide to open its ring; or DMAP could weaken the bond between the metal and the nucleophile in the trans axial position [25].
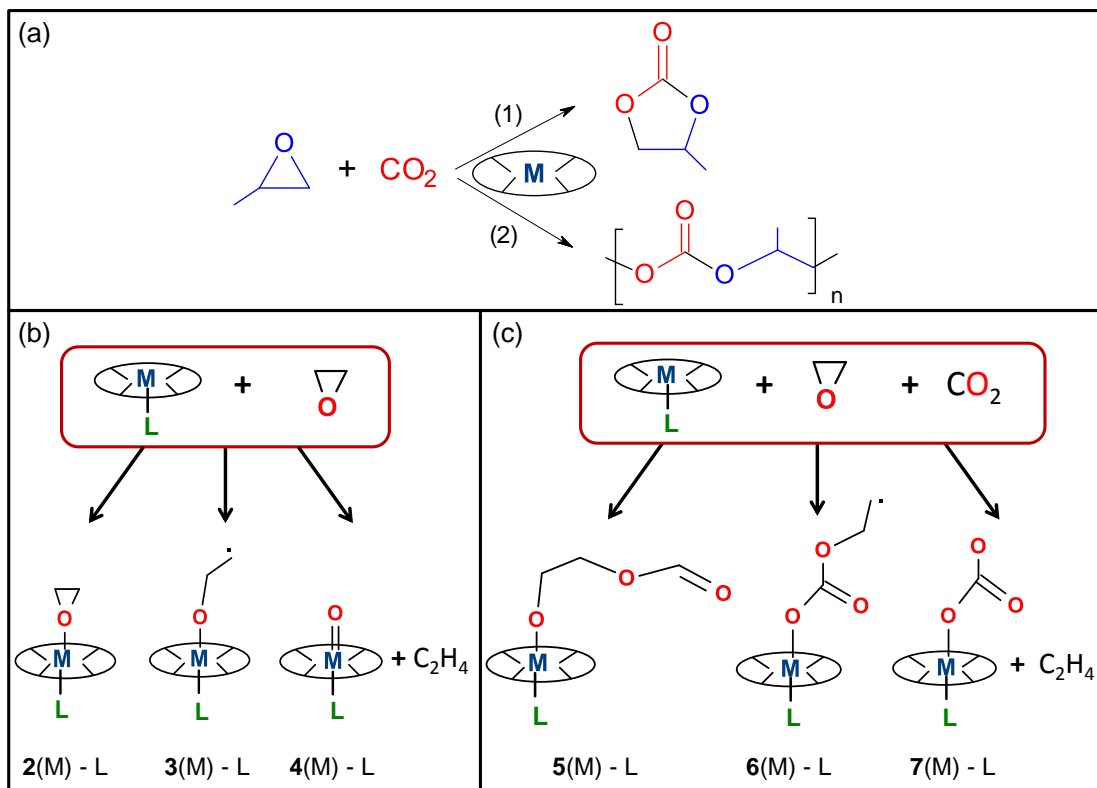
Fig. 6.2. Diagrams of: (a) the reaction of CO_2 with an epoxide using metal-salen catalysts, (b) possible complexes formed by the reactions involving ethylene oxide and **1**(M)-L, (c) possible complexes formed by the reactions involving CO_2, ethylene oxide and **1**(M)-L.

Adhikari and coworkers recently carried out a computational study of the formation of cyclic carbonates through the reaction of CO_2 with an epoxide catalyzed by [(salen)Cr+DMAP]. They evaluated a bimetallic mechanism, in which the ring of an epoxide bonded to the metal center of the catalyst is opened by the nucleophilic attack of an intermediate complex formed when CO_2 is activated by another catalyst molecule with DMAP as axial ligand [26]. The authors did not find evidence that proves that the reaction occurs through this bimetallic pathway or by simultaneous activation of both the epoxide

and CO_2, because the Cr-bound CO_2 complex formed is very high in energy. However, these findings are in good agreement with our previous density functional theory (DFT) study, in which we demonstrated that the bonding of CO_2 on chlorinated metal-salen complexes is not thermodynamically favorable, even when the epoxide is included in the system[27]. Thus according to these DFT studies, CO_2 cannot be directly activated by metal-salen complexes. A recent review article of Darensbourg and Yeung [24] summarizes relevant computational studies about the CO_2-epoxide reactions catalyzed by salens. However, to our knowledge, a systematic analysis with DFT methods to analyze the effect of the axial ligand and the metal center of the salen catalyst on the reaction energies of relevant reactions involving the activation of CO_2, and on the electronic properties of the catalysts still lacks in the literature. In the present study, we have analyzed these effects on the energies of reaction for the formation of relevant intermediates in the coupling of CO_2 and epoxides. Moreover, electronic properties such as electron density, charge distribution, HOMO and LUMO surfaces, LUMO energies, absolute hardness and absolute electronegativity of the metal-salen catalysts with Cl and DMAP as axial ligands have been studied to determine if a correlation exists between these properties and the reaction energies.

6.2. Theoretical Methods

DFT calculations were performed to obtain the energies and geometries of stable reaction intermediates, such as metal carbonates and metal alkoxide that could be produced through the reaction of CO_2 and ethylene oxide on metal-salen catalysts. The effects of the axial ligand and the metal center of the catalyst were analyzed by using two

axial ligands (L): chlorine and DMAP, and five different metal-salen centers (M): Co, Cr, Mn, Fe and Al. Salen complexes with Zn as metal center were also studied. However, albeit numerous attempts, no stable intermediates for the Zn systems were obtained with neither axial ligands. Hence, the results presented for Zn-complexes do not include an axial ligand. The specific metal-salen model analyzed, **1**(M)-L, is shown in Fig. 6.1. This model is a mimic of metal-salen catalysts that have been used in previous experiments for the reaction of CO_2 with epoxides.

Geometries and energies were obtained by performing full geometry optimization with no symmetry constraints on the three lowest spin states for each of the molecular systems studied. The unrestricted OPTX-based exchange functional [28] and the Perdew, Burke and Ernzerhof (PBE) correlation functional [29,30] were used to analyze the systems and perform a screening of the most favorable intermediates of reaction. Previous works have demonstrated that the O-PBE exchange–correlation functional accurately describes the electronic structure of the transition metals in the salens [31]. The basis set used in this screening was the effective core potential LANL2DZ [32–34], which is a double-ζ quality Dunning basis set that models the core electrons with a potential field to save computational cost. This basis set has been shown by many research groups to yield accurate energies of reaction with great computational efficiency, and additional test calculations using a larger basis set on similar systems provided similar results [35–37]. The intermediates formed with the lowest reaction energies from the screening were then exhaustively studied by re-optimizing their geometries, and calculating their energies. This second analysis was performed with the Becke three parameter hybrid functional [38] and the correlation functional of Lee, Yang, and Parr [39,40] (B3LYP). The B3LYP

functional was implemented because it has been exhaustively used, and it has been reported to yield reliable results. For instance, B3LYP has been used by others to accurately describe metal-salen complexes [24,26,41]. In this work, the performance of this hybrid method was also measured against the pure DFT method OPBE. Furthermore, the basis sets 6-311g** [42,43] was used to describe the organic part of the complexes, and LANL2DZ was used for the transition metal atoms. Wavefunction stability was confirmed using the methods described by Seeger and Pople, and Bauernschmitt and Ahlrichs [44,45]. Frequency calculations were carried out using the rigid-rotor and harmonic-oscillator approximation to ensure that the optimized geometries lied in a local energy minimum. The $<S^2>$ values were also verified in all calculations to corroborate that results do not have spin contamination. Natural bond orbital (NBO) analysis [46,47] was performed for the metal-salen catalysts and some relevant intermediate species to extract electronic structure information. Basis set superposition errors (BSSE) were estimated for some of the complexes using the counterpoise method proposed by Boys and Bernardi [48,49]. For the complexes analyzed in this work, BSSE was in the range of 13.7-21.9 kJ/mol. All calculations were performed with Gaussian 09 [50].

In this study, the effect of dichloromethane on the energies of reaction for the formation of the most favorable intermediates has been studied using the polarizable continuum model (PCM) scheme. In addition, the interaction of some metal-salen catalysts with a dichloromethane molecule was evaluated to explicitly analyze the solvent effect.

6.3. Results and Discussion

This section first compares the results obtained for the reactions of ethylene oxide with a metal-salen molecule, **1**(M)-L when the axial ligand is Cl or DMAP. Next, results for reactions of CO_2, ethylene oxide and a metal salen molecule, **1**(M)-L, are presented and compared for both axial ligands. Fig. 6.2 describes the systems that are discussed in this section. The OPBE functional accurately describes the electronic configuration of metal-salen complexes. Table 6.1 shows the relative energies for the three lowest spin states on **1**(M)-Cl, where zero energy is assigned to the ground state. These results are in good agreement with the experimental ground states obtained using electron paramagnetic resonance (EPR) spectroscopy for the high spin systems in Mn, Co, Cr and Fe-salen [51–54].

Table 6.1. Relative energies between spin states for **1**(M)-Cl obtained with the functional UOPBE. Zero energy correspond to electronic energy of the ground state.
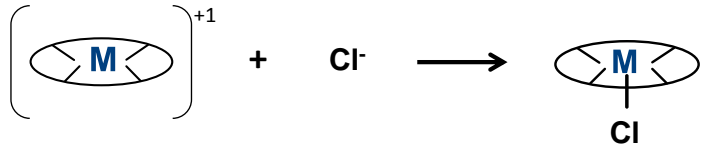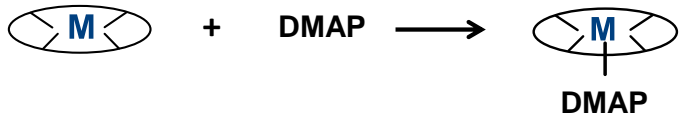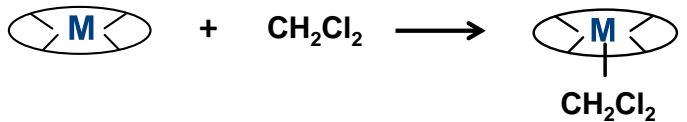
	Relative energy (kJ/mol)			Expected spin state
	$E_{singlet}$	$E_{triplet}$	$E_{quintet}$	
Mn-Salen	141	80	**0**	quintet [51]
Co-Salen	16	**0**	37	triplet [52]
Zn-Salen [a]	**0**	243	493	
Al-Salen	**0**	238	497	
	$E_{doublet}$	$E_{quartet}$	E_{sextet}	
Cr-Salen	91	**0**	155	quartet [53]
Fe-Salen	57	18	**0**	sextet [54]

[a] Zn-salen does not have axial ligand.

The interaction of the axial ligands Cl and DMAP with the metal center in **1**(Al)-L and **1**(Cr)-L was analyzed to corroborate that these metal-salen catalysts are stable. Also, a complex formed by the metal-salen catalyst with no axial ligand, **1**(Al) and **1**(Cr), where

the solvent dichloromethane is interacting with the metal center in the axial position was studied to determine if this interaction is favorable. Table 6.2 summarizes the results of this analysis for Al and Cr-salens. These results indicate that the formation of **1**(Al)-L and **1**(Cr)-Cl is highly favorable in the gas phase and in solvent. **1**(Cr) favorably interacts with DMAP in the gas phase with a reaction energy of -12.0 kJ/mol, while this interaction in solvent is almost thermoneutral with a reaction energy of 4.9 kJ/mol. However, no stable complexes involving the coordination of dichloromethane and the bare salen catalyst (**1**(Al)-CH_2Cl_2 and **1**(Cr)-CH_2Cl_2) were found albeit numerous attempts in the gas phase and in solvent, indicating that dichloromethane does not coordinate the Al or Cr center in the salen complexes.

Table 6.2. Electronic reaction energies for the interaction of the axial ligands Cl and DMAP, and the solvent dichloromethane with the salen complex **1**(M) to form the complexes **1**(M)-Cl, **1**(M)-DMAP and **1**(M)-CH_2Cl_2 with M= Cr, Al estimated with UOPBE/LANL2DZ in gas phase in solvent.

Reactions	Gas phase ΔE_{rxn} (kJ/mol)	Solvent ΔE_{rxn} (kJ/mol)
	M=Cr: -506.9 M=Al: -563.3	M=Cr: -121.7 M=Al: -185.5
	M=Cr: -12.0 M=Al: -106.5	M=Cr: 4.9 M=Al: -107.2
	M=Cr: no reaction M=Al: no reaction	M=Cr: no reaction M=Al: no reaction

6.3.1. The effect of the axial ligand, Cl and DMAP, in the reactions of epoxide and 1(M)-L

Three possible reactions were proposed for the interaction of ethylene oxide with **1**(M)-L as depicted in Fig. 6.2b. Complex **2**(M)-L is formed by the epoxide bonded to the metal atom of **1**(M)-L while maintaining the three-atom ring. Complex **3**(M)-L is a radical intermediate, which has been thoroughly suggested to be formed in the epoxide ring-opening step of the coupling reaction of CO_2 and epoxide [12,25,55]. Species **4**(M)-L is an oxo-metal-salen complex and it was analyzed to determine if the epoxide decomposition is a possible elementary step in the mechanism for the reaction of CO_2 with ethylene oxide. The optimized geometries of the complexes **2**(M)-L, **3**(M)-L and **4**(M)-L+C_2H_4 are shown in Figs. 6.3a and 6.3b with Cl and DMAP as the axial ligands, respectively, and with Co as the metal center. For **2**(M)-DMAP, Cr is the metal center because no stable intermediate was found for **2**(Co)-DMAP with this level of theory.

For all chlorinated salen complexes, **2**(M)-Cl is the intermediate with lowest electronic reaction energy in the reaction of ethylene oxide with **1**(M)-Cl (Fig. 6.3a). A negative electronic energy of reaction of -28.1 kJ/mol was obtained for **2**(Cr)-Cl, with a BSSE of 20.8 kJ/mol. For **2**(Co)-Cl, the reaction energy was almost thermoneutral with a value of -0.2 kJ/mol. For most of the metal centers that were studied, the order of the reaction energies were $E_{2(M)-Cl} < E_{3(M)-Cl} < E_{4(M)-Cl+C2H4}$. For the chlorinated system, the lowest energies of reaction were obtained for Cr-salens, while the highest energies of reaction were obtained for Al-salens.

When DMAP is the axial ligand, negative energies of reaction were only obtained for Al-systems, through the formation of **3**(Al)-DMAP and **2**(Al)-DMAP with reaction energies of -17.7 and -6.1 kJ/mol, respectively (Fig. 6.3b). These reaction energies have BSSEs

of 14.6 and 13.7 kJ/mol, respectively. In general, when comparing with the chlorinated systems, most radical species **3**(M)-DMAP and oxo-metal-salen species **4**(M)-DMAP + C_2H_4 are lower in energy than **3**(M)-Cl and **4**(M)-Cl + C_2H_4, indicating that DMAP has a higher promotion effect than Cl in the formation of these species. However, complexes **2**(Cr)-DMAP and **2**(Mn)-DMAP are higher in energy than the chlorinated counterparts, indicating that Cl is more efficient than DMAP in the formation of concerted epoxide-salen complexes with these metal centers. The complex **2**(Al) is only formed when DMAP is used as axial ligand and its formation is thermodynamically favorable with a reaction energy of -6.1 kJ/mol.

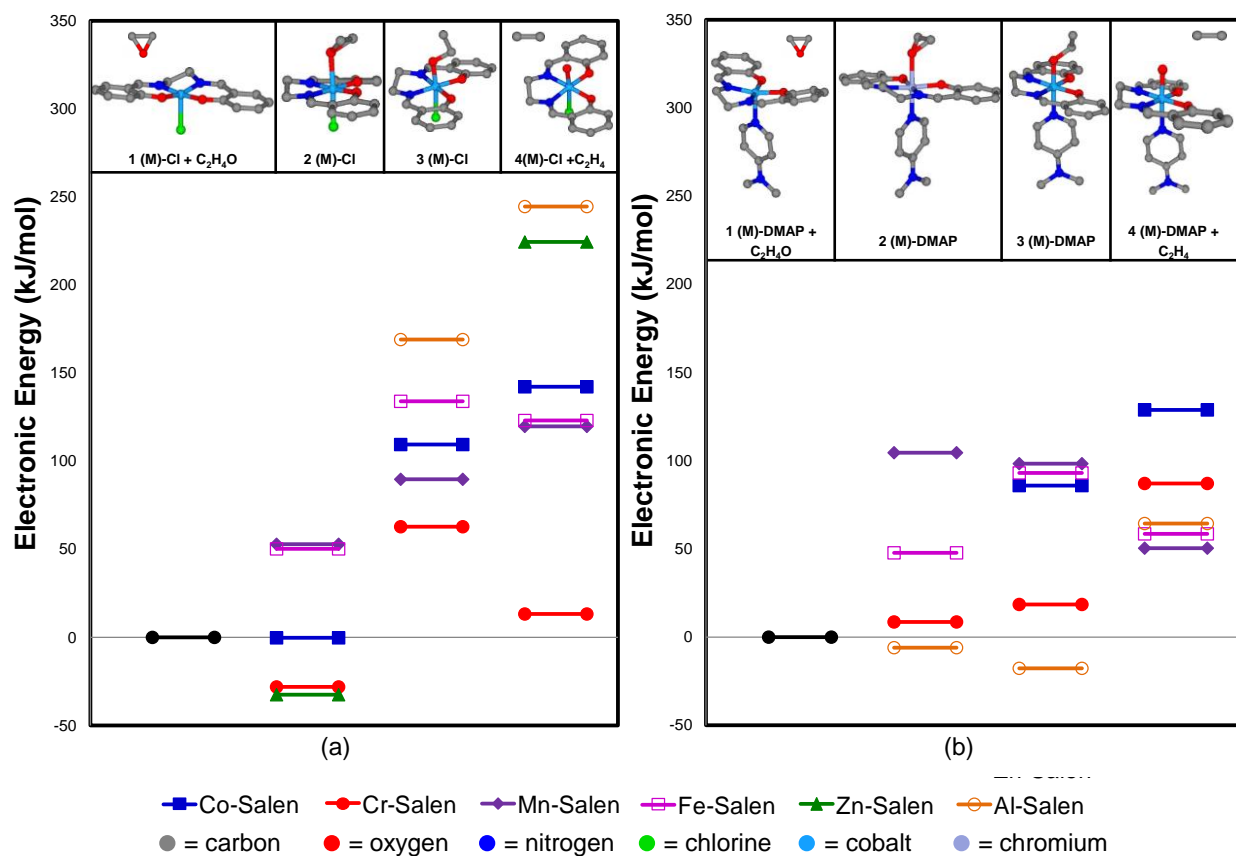**Fig. 6.3.** Relative electronic energies for **2**(M)-L, **3**(M)-L and **4**(M)-L+C_2H_4 produced by the interaction between ethylene oxide and **1**(M)-L, (a) L=Cl, (b) L=DMAP. Zero energy corresponds to the energy of the isolated species (C_2H_4O + **1**(M)-L) in gas phase. Complexes **2**(Al)-Cl, **2**(Co)-DMAP and **3**(Zn) were not observed in these calculations. Zn-complexes do not have axial ligand.

The activation of ethylene oxide to form **2**(Zn) is more exothermic (-32.5 kJ/mol) when compared to the energies obtained to form complexes **2**(M)-Cl and **2**(M)-DMAP, and it has a BSSE of 12.9 kJ/mol. However, the oxidation of the Zn-salen catalyst (formation of the complex **4**(Zn) + C_2H_4) is highly unfavorable in comparison with the oxidation of the other metal-salen catalysts.

Table 6.3. Electronic, zero point and Gibbs free energies for the reaction of ethylene oxide with: **1**(M)-Cl to produce **2**(M)-Cl with M= Co, Cr, Fe and **1**(M) to produce **2**(Zn) estimated using UOPBE/LANL2DZ, and B3LYP/6-311g**/LANL2DZ in gas phase and in solvent.

OC_2H_4 + **1**(M)-Cl → **2**(M)-Cl	UOPBE/LANL2DZ			B3LYP/6-311g**/LANL2DZ			B3LYP/6-311g**/ LANL2DZ + Solvent
	ΔE_{rxn} (kJ/mol)	ΔZPE_{rxn} (kJ/mol)	ΔG_{rxn} (kJ/mol)	ΔE_{rxn} (kJ/mol)	ΔZPE_{rxn} (kJ/mol)	ΔG_{rxn} (kJ/mol)	ΔE_{rxn} (kJ/mol)
M=Co	-0.2	7.5	62.6	-53.8	-45.2	9.6	-33.3
M=Cr	-28.1	-22.0	27.5	-61.0	-54.5	-4.2	-53.7
M=Fe	50.3	61.5	119.1	10.3	21.2	76.5	11.2
M=Zn [a]	-32.5	-28.7	14.2	-59.2	-54.5	-8.8	-30.6

[a] Zn-complex does not have axial ligand

Tables 6.3 and 6.4 compare the electronic, zero point and Gibbs free energies of reaction for the formation of the most stable species in complexes **2**(M)-L, **2**(Zn) and **3**(M)-DMAP obtained with the different DFT methods, and with the solvent. These results indicate that the electronic reaction energies calculated with B3LYP/6-311g**/LANL2DZ, are lower than the ones obtained with UOPBE/LANL2DZ. Moreover, the complex **2**(Co)-DMAP is energetically favorable when analyzed with B3LYP/6-311g**/LANL2DZ, while this complex is not stable with the other method. When the solvent is taken into account, the reaction energies slightly increase in comparison to the vacuum system, but in most cases the differences in energy are not significant. Furthermore, UOPBE/LANL2DZ and B3LYP/6-311g**/LANL2DZ yield similar minimum energy structures, as detailed in Tables B.1 to B.3 in the Appendix B.

Table 6.4. Electronic, zero point and Gibbs free energies for the reaction of ethylene oxide and **1**(M)-DMAP to produce **2**(M)-DMAP with M=Co, Cr, Al and **3**(M)-DMAP with M= Cr and Al estimated using UOPBE/LANL2DZ, and B3LYP/6-311g**/LANL2DZ in gas phase and in solvent.

OC$_2$H$_4$ + 1(M)-DMAP →2(M)-DMAP	UOPBE/LANL2DZ			B3LYP/6-311g**/LANL2DZ			B3LYP/6-311g**/ LANL2DZ + Solvent
	ΔE_{rxn} (kJ/mol)	ΔZPE_{rxn} (kJ/mol)	ΔG_{rxn} (kJ/mol)	ΔE_{rxn} (kJ/mol)	ΔZPE_{rxn} (kJ/mol)	ΔG_{rxn} (kJ/mol)	ΔE_{rxn} (kJ/mol)
M=Co	-	-	-	-34.1	-34.7	4.9	-15.8
M=Cr	8.5	17.7	79.6	2.9	11.0	69.0	18.8
M=Al	-6.1	-1.0	47.7	-40.3	-34.5	17.7	-26.3
OC$_2$H$_4$ + 1(M)-DMAP → 3(M)-DMAP							
M=Cr	18.5	18.5	72.5	0.7	-2.0	49.1	5.1
M=Al	-17.7	-20.3	24.0	-83.6	-84.8	-39.9	-78.9

The results of the reaction energies for the interactions of ethylene oxide and the catalysts indicate that DMAP as axial ligand facilitates the epoxide ring-opening step by making this reaction exothermic or decreasing the energy required for this step, when compared to the chlorinated salen systems. These results also indicate that the oxidation of the catalysts by the formation of the oxo complex 4(M)-L is not thermodynamically favorable by using either Cl or DMAP as axial ligand.

6.3.2. The effect of the axial ligand on the reaction of CO$_2$ and epoxide with 1(M)-L

The effect of the axial ligand on the interaction of CO$_2$ and ethylene oxide with **1**(M)-L was analyzed through the formation of three intermediates, as illustrated in Fig. 6.2c. In complex **5**(M)-L, CO$_2$ binds to the carbon atom with the unpaired electron of the radical species **3**(M)-L. In complex **6**(M)-L, CO$_2$ is inserted between the metal atom of **1**(M)-L and the opened-epoxide fragment. Complexes **5**(M)-L and **6**(M)-L are possible intermediates of the coupling reaction of CO$_2$ and epoxides, and have been widely

investigated [12,19,25,56]. Complex **5**(M)-L is a simple model of the intermediate formed in the copolymerization reaction of CO_2 and ethylene oxide, where the epoxide can be inserted in the polymer chain to form a metal-alkoxide intermediate. It has been proposed in the literature that cyclic carbonates are generated by the backbiting of a metal-alkoxide, such as **5**(M)-L or a dissociated alkoxide chain end [11]. Finally, in complex **7**(M)-L, CO_2 binds to the oxo-metal-salen species **4**(M)-L to form a carbonate intermediate. Metal-carbonate intermediates, such as **6**(M)-L and **7**(M)-L, have been suggested to be formed at elevated CO_2 pressures, conditions at which cyclic species are suppressed [23]. The optimized geometries for the three intermediates evaluated in this section with Co as the metal center are illustrated in Fig. 6.4.

Fig. 6.4a shows the electronic energies of reaction for the formation of **5**(M)-Cl, **6**(M)-Cl and **7**(M)-Cl + C_2H_4. When Cl is the axial ligand, the energies of reaction are positive for all the species and metal centers considered, indicating that the formation of these species is not energetically favored with this ligand. For the three intermediates analyzed, the order of the reaction energies was the same: $E_{Cr} < E_{Mn} < E_{Co} < E_{Fe} < E_{Al}$. In addition, the energy differences observed between the different metal centers are almost conserved in the three complexes.
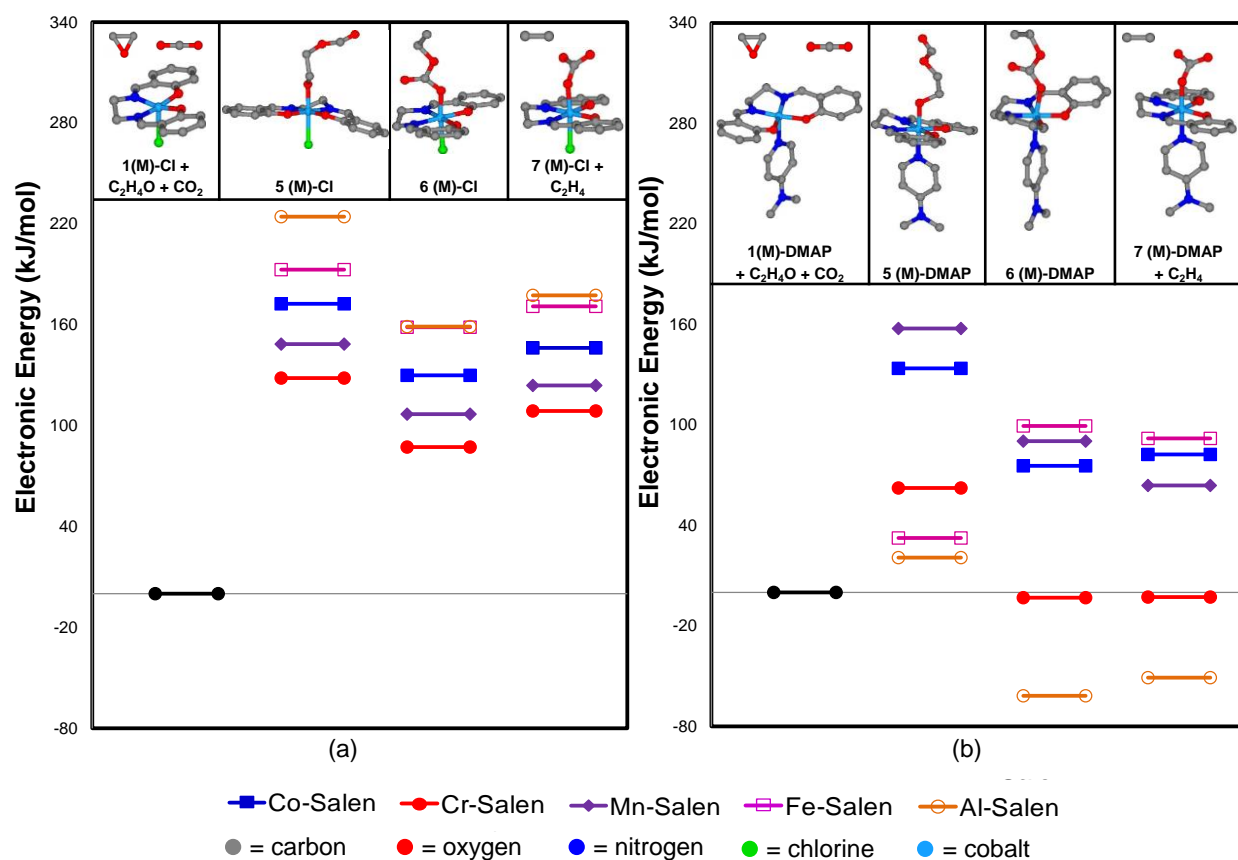
Fig. 6.4. Relative electronic energies for **5**(M)-L, **6**(M)-L, and **7**(M)-L+C_2H_4 produced by the interaction between CO_2, ethylene oxide and **1**(M)-L, (a) L=Cl, (b) L=DMAP. Zero energy corresponds to the energy of isolated species (CO_2 + C_2H_4O + **1**(M)-L) in gas phase.

As shown in Fig. 6.4b, when the axial ligand is DMAP, all the energies of reaction decrease when compared to the chlorinated counterparts, with the exception of **5**(Mn)-DMAP, in which an increase of 9.1 kJ/mol was observed. The lowest energies were obtained for Al, in complex **6**(Al)-DMAP followed by **7**(Al)-DMAP+C_2H_4, with values of -61.7 and -50.9 kJ/mol, respectively. Our results indicate that the formation of **6**(Al)-DMAP is the most energetically favorable reaction, and these results suggest that **3**(Al)-DMAP has the most nucleophilic center. The Cr-salen complexes also show negative reaction energies, albeit much higher than Al, with values of -3.2 and -2.8 kJ/mol for **6**(Cr)-DMAP

and **7**(Cr)-DMAP + C_2H_4. This is in good agreement with experimental findings of Lu and coworkers that demonstrated that Co-salens and Cr-salens used either alone or with a Lewis base as a cocatalyst hardly show catalytic activity for the CO_2/ethylene oxide coupling in comparison with Al-salens [17]. Luinstra and coworkers also demonstrated that Al-salens tend to favor the cyclic carbonates production because the dissociation of the growing polymer chain is easier with these salen complexes than with Cr-salens [57]. The formation energies for the intermediate **6**(M)-L are in most cases lower than the ones for **5**(M)-L, which is consistent with the mechanism proposed by many scientists where CO_2 is inserted in the metal alkoxide. Moreover, Liu and coworkers studied the alternating CO_2 and ethylene oxide insertions in a Zn-based catalyst and they found that the intermediates formed by the epoxide insertion after the CO_2 insertion are a little more thermodynamically favorable than the metal carbonate intermediates formed by the CO_2 insertion [58]. However, they found that the epoxide insertion intermediates have higher activation energies than the CO_2 insertion intermediates. The Gibbs free energies of reaction for the formation of **5**(M)-DMAP, **6**(M)-DMAP and **7**(M)-DMAP + C_2H_4 are illustrated in Fig. B.1, which indicate that the production of **7**(Al)-DMAP+C_2H_4 is a spontaneous reaction.

The electronic, zero point and Gibbs free energies of reaction for the minimum energy complexes of **6**(M)-DMAP and **7**(M)-DMAP + C_2H_4 with Cr and Al as metal centers were calculated using B3LYP/6-311g**/LANL2DZ and with solvent to establish a comparison between the methods. As shown in Table 6.5, there are significant changes in the reaction energies between both methods. Moreover, the formation of these intermediates is even more thermodynamically favorable when the solvent is incorporated in the reaction of

140

CO_2, epoxide and metal-salens, with the exception of **7**(Cr)-DMAP + C_2H_4 for which the reaction energy notably increases with B3LYP/6-311g**/LANL2DZ. However, the solvent causes minimal changes (2.1-12.4 kJ/mol) in the reaction energies for these complexes. Furthermore, there are no significant differences between the structural parameters of **6**(M)-DMAP obtained with UOPBE/LANL2DZ or B3LYP/6-311g**/LANL2DZ (Table B.5).

Table 6.5. Electronic, zero point and Gibbs free energies for the reaction of CO_2, ethylene oxide and **1**(M)-DMAP to produce **6**(M)-DMAP and **7**(M)-DMAP + C_2H_4 with M= Cr and Al estimated using UOPBE/LANL2DZ, and B3LYP/6-311g**/LANL2DZ in gas phase and in solvent.

CO_2 + OC_2H_4 + **1**(M)-DMAP → **6**(M)-DMAP	UOPBE/LANL2DZ			B3LYP/6-311g**/LANL2DZ			B3LYP/6-311g**/ LANL2DZ + Solvent
	ΔE_{rxn} (kJ/mol)	ΔZPE_{rxn} (kJ/mol)	ΔG_{rxn} (kJ/mol)	ΔE_{rxn} (kJ/mol)	ΔZPE_{rxn} (kJ/mol)	ΔG_{rxn} (kJ/mol)	ΔE_{rxn} (kJ/mol)
M=Cr	-3.2	5.2	103.6	-26.2	-18.7	76.1	-31.7
M=Al	-61.7	-53.4	31.7	-124.5	-114.7	-23.8	-126.6
CO_2 + OC_2H_4 + **1**(M)-DMAP→ **7**(M)-DMAP + C_2H_4							
M=Cr	-2.7	-2.7	54.2	113.2	112.0	161.4	100.8
M=Al	-50.9	-51.5	-11.8	-80.3	-78.2	-32.0	-89.2

The energies of reaction for the bonding of CO_2 to **4**(M)-L to form **7**(M)-L were also calculated. As shown in Fig. 6.5a, when Cl is the axial ligand, the lowest electronic energy of reaction (-67.1 kJ/mol) for the formation of a chlorinated carbonate complex was obtained for Al-salen, while the highest energy of reaction was obtained for the Cr-salen. The formation of **7**(Zn), which has no axial ligand, has even lower reaction energy than **7**(Al)-Cl. The reaction energies to form **7**(Al)-Cl and **7**(Zn) have BSSEs of 21.0 and 20.7 kJ/mol, respectively. The **7**(Al)-Cl and **7**(Zn) complexes also have negative Gibbs free energies of reaction of -28.9 and -51.2 kJ/mol, respectively, indicating a spontaneous formation of these complexes (Fig. B.2a).
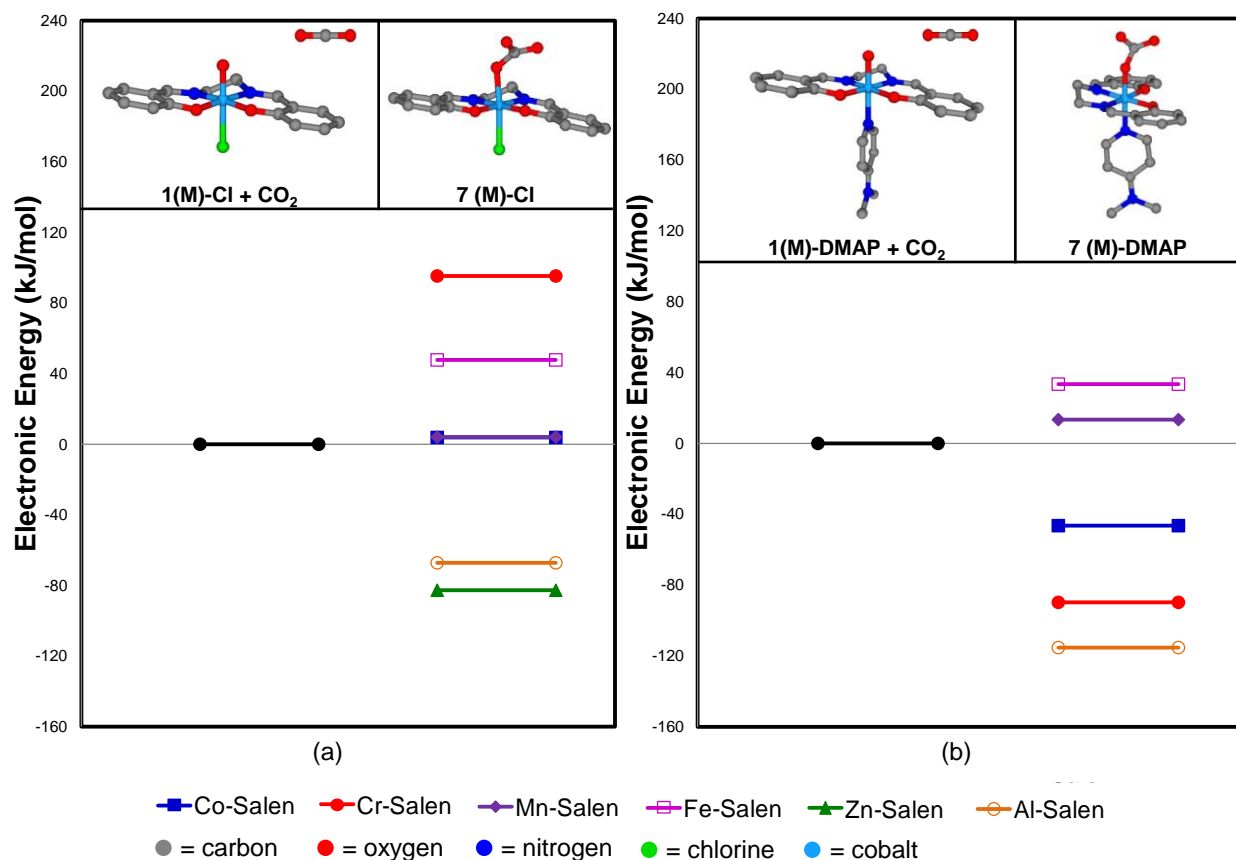
Fig. 6.5. Relative electronic energies for **7**(M)-L produced by the interaction between CO_2 and **4**(M)-L, (a) L=Cl, (b) L=DMAP. Zero energy corresponds to the energy of isolated species (CO_2 + **4**(M)-L) in gas phase. Zn-complexes do not have axial ligand.

Fig. 6.5b illustrates that the energies of reactions for the formation of **7**(M)-DMAP are lower than the chlorinated complexes for all metals, except for Mn. Negative reaction energies of -115.2, -89.8 and -46.4 kJ/mol with BSSEs of 21.9, 19.7 and 21.3 kJ/mol were obtained for Al, Cr and Co-salen complexes, respectively. The formation of these complexes are also spontaneous with Gibbs free reaction energies of -74.5, -40.7 and -0.7 kJ/mol for **7**(M)-DMAP with Al, Cr and Co, respectively (Fig. B.2b). In fact, the formation of **7**(Al)-DMAP is the most energetically favorable reaction analyzed in this study. When DMAP is the axial ligand, the reaction of CO_2 with the oxo-Cr or Al salens

is more exothermic than with the oxo-Zn-salen, which demonstrates the higher promotion effect of DMAP in comparison with Cl for the formation of **7**(M)-L.

Tables 6.6 and 6.7 show the electronic, zero point and Gibbs free reaction energies for **7**(M)-Cl with Co, Mn and Al, and **7**(M)-DMAP with Co, Cr, Mn and Al. Complex **7**(Zn) is also included in the analysis. The calculated reaction energies notably change with the DFT method. For instance, on the basis of B3LYP the formation of **7**(Co)-Cl and **7**(Mn)-Cl is exothermic, while it is thermoneutral on the basis of UOPBE. However, the solvent does not cause significant differences in the reaction energies. The structural parameters for the geometries of these complexes are found in Tables B.7 and B.9 in the Appendix B.

Table 6.6. Electronic, zero point and Gibbs free energies for the reaction of CO_2 with: **4**(M)-Cl to produce **7**(M)-Cl with M= Co, Mn, Al and **4**(M) to produce **7**(Zn) estimated using UOPBE/LANL2DZ, and B3LYP/6-311g**/LANL2DZ in gas phase and in solvent.

CO_2 + 4(M)-Cl → 7(M)-Cl	UOPBE/LANL2DZ			B3LYP/6-311g**/LANL2DZ			B3LYP/6-311g**/LANL2DZ + Solvent
	ΔE_{rxn} (kJ/mol)	ΔZPE_{rxn} (kJ/mol)	ΔG_{rxn} (kJ/mol)	ΔE_{rxn} (kJ/mol)	ΔZPE_{rxn} (kJ/mol)	ΔG_{rxn} (kJ/mol)	ΔE_{rxn} (kJ/mol)
M=Co	3.9	5.3	45.6	-56.3	-51.6	-10.1	-48.5
M=Mn	4.1	4.1	41.4	-19.2	-15.2	26.0	-14.3
M=Al	-67.1	-68.0	-28.9	-37.9	-40.4	-0.7	-46.8
M=Zn [a]	-82.6	-85.6	-51.2	5.6	2.7	41.3	11.2

[a] Zn-complex does not have axial ligand

Due to the differences in the reaction energies obtained with both methods, additional calculations were carried out to assess the reliability of the methods implemented in this study. Thus, the enthalpies for the reaction of CO_2 with ethylene oxide to produce ethylene carbonate in gas phase were calculated and the results were compared with the results obtained with higher level methods. The details of these results, and the comparison with other calculated enthalpies obtained with higher level methods are in the

Appendix B (Table B.12). In summary, the UOPBE/LANL2DZ describes the enthalpy for this reaction better than B3LYP/6-311g**. The performance of the basis sets was also evaluated analyzing this reaction with UOPBE/6-311g**, which yields a less reliable value of the reaction enthalpy than UOPBE/LANL2DZ. Thus, the D95V basis set as implemented in LANL2DZ is better than the 6-311g** basis sets in describing the organic species involved in this reaction. This is due to the Dunning-Huzinaga basis sets (e.g., D95V) do not have the restriction of equal exponents for the s and p functions that the Pople basis sets (e.g., 6-311g) have, which makes D95V more flexible, but computationally more expensive than 6-311g [59].

Table 6.7. Electronic, zero point and Gibbs free energies for the reaction of CO_2 and **4**(M)-DMAP to produce **7**(M)-DMAP with M= Co, Cr, Mn, Al estimated using UOPBE/LANL2DZ, and B3LYP/6-311g**/LANL2DZ in gas phase and in solvent.

CO_2 + 4(M)-DMAP → 7(M)-DMAP	UOPBE/LANL2DZ			B3LYP/6-311g**/LANL2DZ			B3LYP/6-311g**/ LANL2DZ + Solvent
	ΔE_{rxn} (kJ/mol)	ΔZPE_{rxn} (kJ/mol)	ΔG_{rxn} (kJ/mol)	ΔE_{rxn} (kJ/mol)	ΔZPE_{rxn} (kJ/mol)	ΔG_{rxn} (kJ/mol)	ΔE_{rxn} (kJ/mol)
M=Co	-46.4	-42.5	-0.7	-53.4	-47.6	-4.7	-59.2
M=Cr	-89.8	-84.8	-40.7	10.7	16.2	60.6	11.0
M=Mn	13.4	16.5	56.7	23.8	28.1	71.3	25.4
M=Al	-115.2	-110.2	-74.5	-102.3	-96.2	-53.5	-97.2

While the aim of this work was to analyze the interaction of CO_2 with metal-salen systems, another possible route for the activation of CO_2 could be through its interaction with DMAP. Results of this reaction indicate that the formation of a CO_2-DMAP complex is thermodynamically favorable, with an energy of -8.3 kJ/mol. This finding is consistent with other studies that have demonstrated that CO_2 can be activated by DMAP and other organic bases [56,60,61]. The C-N bond length on this complex is 1.8 Å and the CO_2 angle is 146°. The reaction energy and the geometry for this CO_2-DMAP complex was also evaluated with the method B3LYP/6-311g** and dichloromethane as solvent. When

the optimization is performed in solvent, the bending configuration of CO_2 is kept, reducing the CO_2 angle to 139° and the C-N bond length to 1.7 Å (Fig. 6.6). The CO_2-DMAP complex optimized in solvent has a reaction energy of -0.5 kJ/mol.
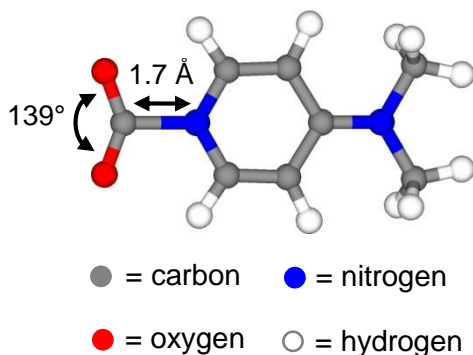

Fig. 6.6. Optimized geometry for the CO_2-DMAP complex using the B3LYP/6-311g**/LANL2DZ method with solvent.

● = carbon   ● = nitrogen

● = oxygen   ○ = hydrogen

6.3.3. Electron configuration, charge distribution, HOMO and LUMO, LUMO energies, absolute hardness (η) and absolute electronegativity (χ)

The axial ligand has a significant effect in the electronic properties of the catalyst, which is also manifested on the calculated reaction energies. The descriptors discussed in this section can explain some of the results obtained for the reactions analyzed in this study. Fig. 6.7 illustrates the electron configuration of Cr, the charge distribution and the surfaces of the highest occupied molecular orbitals (HOMO) and the lowest unoccupied molecular orbitals (LUMO) for **1**(Cr)-Cl and **1**(Cr)-DMAP. As noted when comparing the electron configurations of Cr on both complexes, Cr has a lower electron density on the valence orbitals when it is bonded to DMAP. The differences in the electron density of the Cr atom in both complexes are also manifested in the natural charges of the metal. As shown in Fig. 6.7, the charge of Cr is more positive when Cr-salen has DMAP as axial ligand compared to the chlorinated system. Differences between the two axial ligands are

also reflected in the HOMO and LUMO surfaces of **1**(Cr)-L. The HOMO's of **1**(Cr)-Cl and

1(Cr)-DMAP show two different interactions between the M d-orbitals and the L p-orbitals.

1(Cr)-DMAP is the only transition metal-salen that shows an interaction between the

HOMO orbitals of M and DMAP. Overlaps of the M d-orbitals with the L p-orbitals are not

observed in the HOMO's of **1**(Co)-DMAP, **1**(Mn)-DMAP and **1**(Fe)-DMAP (see Fig. B.11).

The unoccupied electron density around the Cr atom, illustrated on the LUMO of **1**(Cr)-Cl

(Fig. 6.7), suggests that the electron transfer from other species to the Cr atom on the

chlorinated system might be easier than in the DMAP system. Similarly to the HOMO

surfaces, a LUMO surface with main contributions of the M d-orbitals and the L p-orbitals

is only observed in **1**(Cr)-Cl. The M d-orbitals observed in the LUMO surface of the Cr

atom in **1**(Cr)-Cl with a d_z^2 symmetry suggest that we should expect lower electronic

energies of reactions for the activation of ethylene oxide by **1**(Cr)-Cl and the insertion of

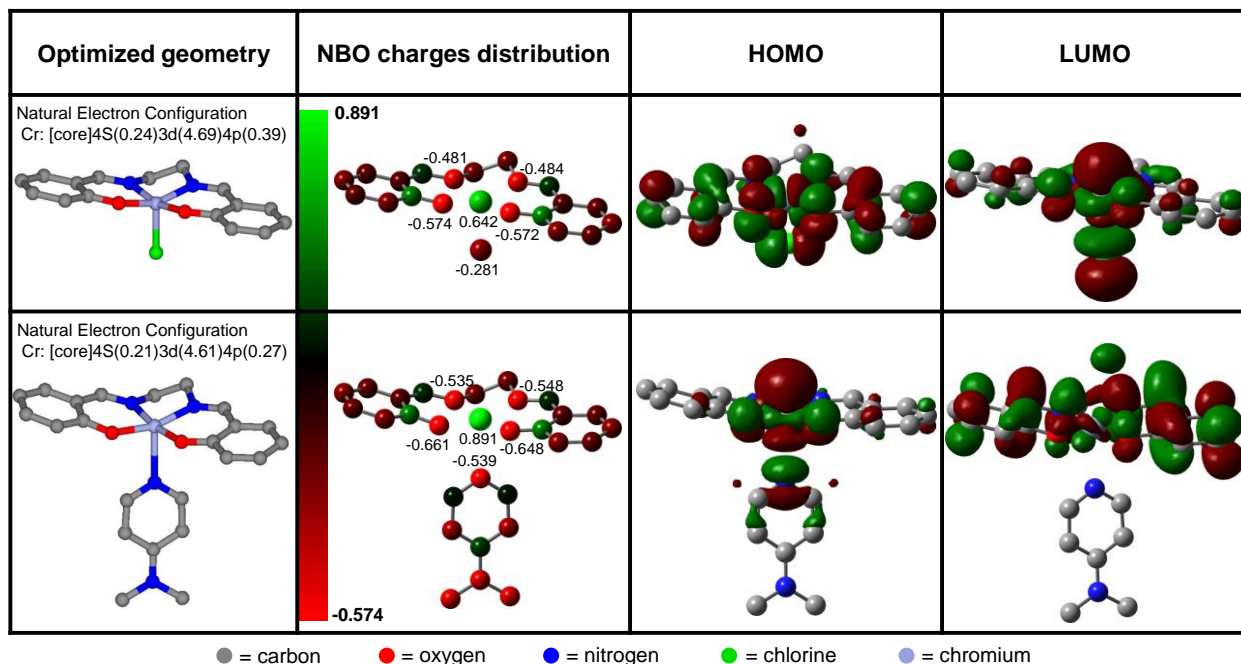CO_2 to form **6**(Cr)-Cl, in comparison with the other chlorinated metal-salen catalysts.

Fig. 6.7. Electron configuration of Cr, NBO charge distribution, HOMO and LUMO for **1**(Cr)-L.

Table 6.8 shows the LUMO energies (ε_{LUMO}), absolute hardness (η) and absolute electronegativity (χ) of **1**(M)-L for the five metal centers. These descriptors have been correlated by others with properties of materials, such as acidity/basicity and reactivity [62–64]. The Lewis acidity has been related to ε_{LUMO} such that the lower the ε_{LUMO} of a molecule, the higher is its Lewis acidity or its ability to gain electron density [62]. As shown in Table 6.8, when Cl is the axial ligand, the ε_{LUMO}'s are smaller than in the DMAP system, and the **1**(Zn) complex has an intermediate acidity between the chlorinated and the DMAP systems.

Table 6.8. LUMO energies, absolute hardness and absolute electronegativity for **1**(M)-L.

	1 (M)-Cl					
	Cr	**Al**	**Co**	**Mn**	**Fe**	**Zn**[a]
ε_{LUMO} **(eV)**	-3.51	-2.92	-3.34	-3.54	-2.74	-2.41
η **(eV)**	0.96	2.31	1.50	1.09	2.39	2.39
χ **(eV)**	3.99	4.07	4.09	4.09	3.94	3.61
	1 (M)-DMAP					
	Cr	**Al**	**Co**	**Mn**	**Fe**	
ε_{LUMO} **(eV)**	-1.88	-1.90	-1.82	-1.79	-1.80	
η **(eV)**	1.27	0.36	1.80	1.57	1.91	
χ **(eV)**	2.51	2.08	2.72	2.57	2.76	

[a] Zn-salen does not have axial ligand.

The hardness of a material has also been used as a descriptor to characterize or even predict the reactivity of chemical species and it could be approximated as the energy gap between the two frontier orbitals [63]. As shown in Table 6.8, the metal atom and the axial ligand impact the hardness of the salen complex. The electronic reaction energies were correlated to the hardness of **1**(M)-L, as illustrated in Fig. 6.8 for the chlorinated system and Fig. 6.9 for the DMAP complexes. These plots indicate that there is a trend between the energies of reactions and η, such that the reaction energies increases with increasing η. However, this trend was not accurately captured by the acidity.
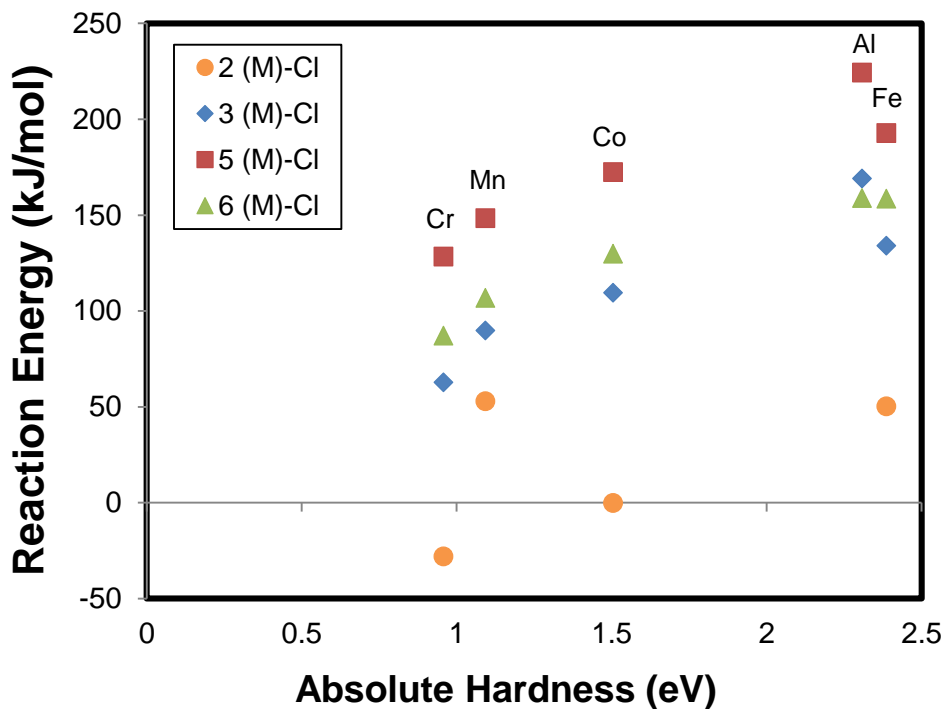
Fig. 6.8. Reaction energy to produce **2**(M)-Cl, **3**(M)-Cl, **5**(M)-Cl and **6**(M)-Cl as a function of the absolute hardness of the catalysts, **1**(M)-Cl.

The electronegativity, which is the average value between ε_{HOMO} and ε_{LUMO}, is also shown in Table 6.8. The chlorinated complexes are more electronegative than the DMAP complexes. Only the electronegativity for **1**(M)-DMAP follows a similar trend in the metal centers to the hardness of these catalysts with DMAP ($\eta_{Al}<\eta_{Cr}<\eta_{Mn}<\eta_{Co}<\eta_{Fe}$). As shown in Fig. B.13, the more electronegative catalysts with DMAP have higher hardness, and have higher reaction energies. However, this correlation was not observed for the chlorinated complexes (see Fig. B.14). An analysis of natural charges was performed to quantify the charge transfer in the reaction of **1**(M)-L with ethylene oxide to form **2**(M)-L (Table B.11). However, a trend is not observed between the electronegativity and the charge transfer for these salen complexes.
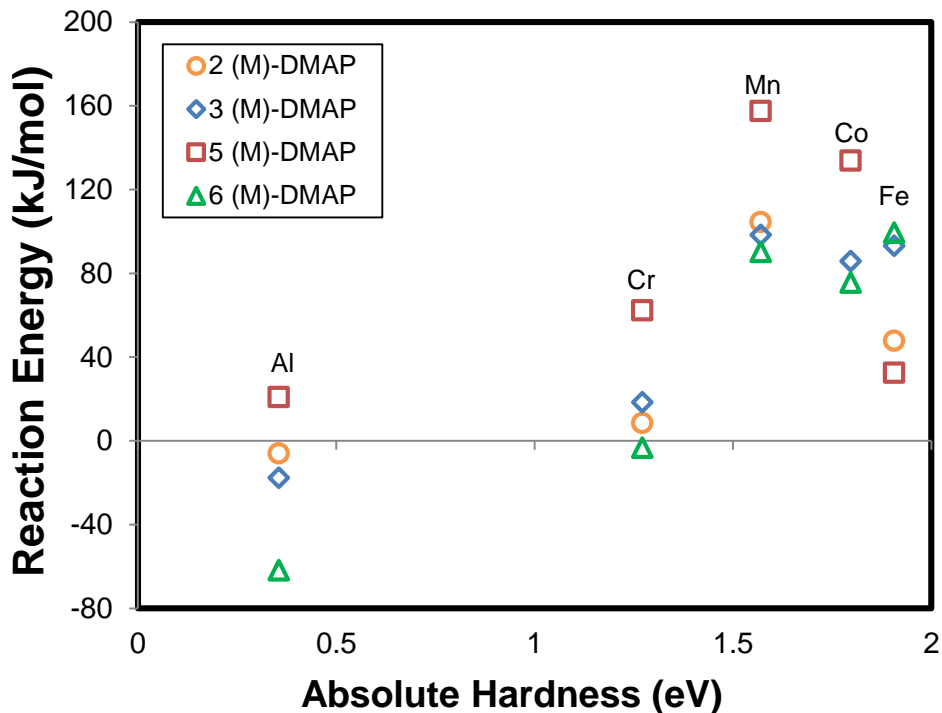
Fig. 6.9. Reaction energy to produce **2**(M)-DMAP, **3**(M)-DMAP, **5**(M)-DMAP and **6**(M)-DMAP as a function of the absolute hardness of the catalysts, **1**(M)-DMAP.

The descriptors analyzed in this study, including the LUMO energies, the hardness and the electronegativity, do not follow an exact correlation among them or with the reaction energies for the formation of the intermediates in the coupling reaction of CO_2 and ethylene oxide for all the metal centers and axial ligands studied. However, when considering salen complexes with the same ligand, a trend was observed between the reaction energies and hardness of the catalyst.

6.4.   Conclusions

DFT calculations have been used to study Cl and DMAP as axial ligands of the Co, Cr, Mn, Fe and Al-salen catalysts. We have also studied stable complexes formed through the interactions of these catalysts with ethylene oxide and CO_2 using the effective

core potential LANL2DZ together with the UOPBE functional to perform a screening of the most favorable intermediates for these reactions. For the reaction of ethylene oxide with the catalysts, the formations of the complexes **2**(Cr)-Cl, **2**(Zn), **2**(Al)-DMAP and **3**(Al)-DMAP are thermodynamically favorable. The decreasing tendency in the electronic energies of reaction for the formation of **3**(M)-DMAP demonstrates that DMAP as axial ligand facilitates the epoxide ring-opening step. The oxidation of the catalysts by the formation of complex 4(M)-L is not favorable by using Cl or DMAP as axial ligand. When DMAP is the axial ligand, the reaction energies for the formation of CO_2-epoxide-metal(salen) complexes are lower than the energies of reaction obtained for the chlorinated systems. The intermediates with lowest reaction energies have been exhaustively studied using the B3LYP/6-311g**/LANL2DZ method and taking in account the solvent effect with the PCM method. In general, there are significant differences for the reaction energies obtained using UOPBE/LANL2DZ and B3LYP/6-311g**/LANL2DZ. The trend for most evaluated complexes is that their formations are more favorable when the electron density is described by B3LYP/6-311g**/LANL2DZ. The complexes with Al as metal center and DMAP as axial ligand are the most energetically favorable intermediates for the coupling of CO_2 and ethylene oxide when the B3LYP/6-311g**/LANL2DZ method in solvent is implemented. In fact, negative energies as low as -126.6, -97.2 and -89.2 kJ/mol are obtained for the complexes **6**(Al)-DMAP, **7**(Al)-DMAP and **7**(Al)-DMAP + C_2H_4, respectively. The implementation of B3LYP/6-311g**/LANL2DZ does not cause significant changes in the geometry of the complexes. In general, reaction energies obtained with the solvent are comparable to those in vacuum. Furthermore, dichloromethane does not interact with the metal center of the **1**(Al) and **1**(Cr) complexes

in the gas phase or in solvent. Additional calculations were carried out to estimate the enthalpy of the reaction of CO_2 with ethylene oxide to produce ethylene carbonate. These calculations demonstrated that OPBE/LANL2DZ describes the enthalpy for this reaction better than B3LYP/6-311g**.

The activation of CO_2 by DMAP is thermodynamically favorable for the two DFT methods used in this study and when dichloromethane is incorporated as solvent in the reaction. Thus, the interaction of this CO_2-DMAP complex with the metal-salen catalysts and the epoxides warrant further study. In addition, the axial ligand has a significant effect in the electronic properties of the catalyst as manifested in the HOMO and LUMO, and by descriptors as LUMO energies, hardness and electronegativity. For salen catalyst with same axial ligand, the reaction energies can be correlated to the hardness of the salen catalyst as modified with different metal centers.

References

[1] T. Sakakura, J.-C. Choi, H. Yasuda, Transformation of Carbon Dioxide, Chem. Rev. 107 (2007) 2365–2387.
[2] A.-A.G. Shaikh, S. Sivaram, Organic Carbonates, Chem. Rev. 96 (1996) 951–976.
[3] After Major Downturn, Global Demand for Polycarbonate Growing Again, Says IHS Chemical Report, IHS Online Pressroom. (2012) http://press.ihs.com/press-release/commodities-pricing-cost/after-major-downturn-global-demand-polycarbonate-growing-agai (accessed Feb 3, 2015).
[4] S. Inoue, H. Koinuma, T. Tsuruta, Copolymerization of carbon dioxide and epoxide, J. Polym. Sci. [B]. 7 (1969) 287–292.
[5] D.J. Darensbourg, J.C. Yarbrough, Mechanistic Aspects of the Copolymerization Reaction of Carbon Dioxide and Epoxides, Using a Chiral Salen Chromium Chloride Catalyst, J. Am. Chem. Soc. 124 (2002) 6335–6342.
[6] E. Jacobsen, M. Tokunaga, J. Larrow, Stereoselective Ring Opening Reactions, WO/2000/009463 (2000) https://patentscope.wipo.int/search/en/detail.jsf?docId= WO2000009463 (accessed Feb 12, 2015).

[7] R.L. Paddock, S.T. Nguyen, Alternating Copolymerization of CO_2 and Propylene Oxide Catalyzed by CoIII(salen)/Lewis Base, Macromolecules. 38 (2005) 6251–6253.

[8] X.-B. Lu, R. He, C.-X. Bai, Synthesis of ethylene carbonate from supercritical carbon dioxide/ethylene oxide mixture in the presence of bifunctional catalyst, J. Mol. Catal. Chem. 186 (2002) 1–11.

[9] F. Jutz, J.-D. Grunwaldt, A. Baiker, Mn(III)(salen)-catalyzed synthesis of cyclic organic carbonates from propylene and styrene oxide in "supercritical" CO_2, J. Mol. Catal. Chem. 279 (2008) 94–103.

[10] H. Jing, S.K. Edulji, J.M. Gibbs, C.L. Stern, H. Zhou, S.T. Nguyen, (Salen)Tin Complexes: Syntheses, Characterization, Crystal Structures, and Catalytic Activity in the Formation of Propylene Carbonate from CO_2 and Propylene Oxide, Inorg. Chem. 43 (2004) 4315–4327.

[11] G.W. Coates, D.R. Moore, Discrete Metal-Based Catalysts for the Copolymerization of CO_2 and Epoxides: Discovery, Reactivity, Optimization, and Mechanism, Angew. Chem. Int. Ed. 43 (2004) 6618–6639.

[12] D.J. Darensbourg, Making Plastics from Carbon Dioxide: Salen Metal Complexes as Catalysts for the Production of Polycarbonates from Epoxides and CO_2, Chem. Rev. 107 (2007) 2388–2410.

[13] X.-B. Lu, D.J. Darensbourg, Cobalt catalysts for the coupling of CO_2 and epoxides to provide polycarbonates and cyclic carbonates, Chem. Soc. Rev. 41 (2012) 1462–1484.

[14] W.J. Kruper, D.D. Dellar, Catalytic Formation of Cyclic Carbonates from Epoxides and CO_2 with Chromium Metalloporphyrinates, J. Org. Chem. 60 (1995) 725–727.

[15] S. Inoue, Immortal polymerization: The outset, development, and application, J. Polym. Sci. Part Polym. Chem. 38 (2000) 2861–2871.

[16] E.N. Jacobsen, Asymmetric Catalysis of Epoxide Ring-Opening Reactions, Acc. Chem. Res. 33 (2000) 421–431.

[17] X.-B. Lu, X.-J. Feng, R. He, Catalytic formation of ethylene carbonate from supercritical carbon dioxide/ethylene oxide mixture with tetradentate Schiff-base complexes as catalyst, Appl. Catal. Gen. 234 (2002) 25–33.

[18] D.J. Darensbourg, J.C. Yarbrough, C. Ortiz, C.C. Fang, Comparative Kinetic Studies of the Copolymerization of Cyclohexene Oxide and Propylene Oxide with Carbon Dioxide in the Presence of Chromium Salen Derivatives. In Situ FTIR Measurements of Copolymer vs Cyclic Carbonate Production, J. Am. Chem. Soc. 125 (2003) 7586–7591.

[19] X.-B. Lu, B. Liang, Y.-J. Zhang, Y.-Z. Tian, Y.-M. Wang, C.-X. Bai, H. Wang, R. Zhang, Asymmetric Catalysis with CO_2: Direct Synthesis of Optically Active Propylene Carbonate from Racemic Epoxides, J. Am. Chem. Soc. 126 (2004) 3732–3733.

[20] X.-B. Lu, Y.-J. Zhang, B. Liang, X. Li, H. Wang, Chemical fixation of carbon dioxide to cyclic carbonates under extremely mild conditions with highly active bifunctional catalysts, J. Mol. Catal. Chem. 210 (2004) 31–34.

[21] Y.-M. Shen, W.-L. Duan, M. Shi, Chemical Fixation of Carbon Dioxide Catalyzed by Binaphthyldiamino Zn, Cu, and Co Salen-Type Complexes, J. Org. Chem. 68 (2003) 1559–1562.

[22] R.L. Paddock, S.T. Nguyen, Chemical CO_2 Fixation: Cr(III) Salen Complexes as Highly Efficient Catalysts for the Coupling of CO_2 and Epoxides, J. Am. Chem. Soc. 123 (2001) 11498–11499.

[23] R. Eberhardt, M. Allmendinger, B. Rieger, DMAP/Cr(III) Catalyst Ratio: The Decisive Factor for Poly(propylene carbonate) Formation in the Coupling of CO_2 and Propylene Oxide, Macromol. Rapid Commun. 24 (2003) 194–196.

[24] D.J. Darensbourg, A.D. Yeung, A concise review of computational studies of the carbon dioxide–epoxide copolymerization reactions, Polym. Chem. 5 (2014) 3949–3962.

[25] P.P. Pescarmona, M. Taherimehr, Challenges in the catalytic synthesis of cyclic and polymeric carbonates from epoxides and CO_2, Catal. Sci. Technol. 2 (2012) 2169–2187.

[26] D. Adhikari, S.T. Nguyen, M.-H. Baik, A computational study of the mechanism of the [(salen)Cr + DMAP]-catalyzed formation of cyclic carbonates from CO_2 and epoxide, Chem. Commun. 50 (2014) 2676–2678.

[27] M. Curet-Arana, P. Meza, R. Irizarry, R. Soler, Quantum Chemical Determination of Stable Intermediates on CO_2 Adsorption Onto Metal(Salen) Complexes, Top. Catal. 55 (2012) 260–266.

[28] N.C. Handy, A.J. Cohen, Left-right correlation energy, Mol. Phys. 99 (2001) 403–412.

[29] J.P. Perdew, K. Burke, M. Ernzerhof, Generalized Gradient Approximation Made Simple, Phys. Rev. Lett. 77 (1996) 3865–3868.

[30] J.P. Perdew, K. Burke, M. Ernzerhof, Generalized Gradient Approximation Made Simple [Phys. Rev. Lett. 77, 3865 (1996)], Phys. Rev. Lett. 78 (1997) 1396.

[31] J. Conradie, A. Ghosh, Electronic Structure of Trigonal-Planar Transition-Metal−Imido Complexes: Spin-State Energetics, Spin-Density Profiles, and the Remarkable Performance of the OLYP Functional, J. Chem. Theory Comput. 3 (2007) 689–702.

[32] T.H. Dunning Jr., P.J. Hay, in: Mod. Theor. Chem., H. F. Schaefer III, Plenum, New York, 1976: pp. 1–28.

[33] P.J. Hay, W.R. Wadt, Ab initio effective core potentials for molecular calculations. Potentials for the transition metal atoms Sc to Hg, J. Chem. Phys. 82 (1985) 270–283.

[34] W.R. Wadt, P.J. Hay, Ab initio effective core potentials for molecular calculations. Potentials for main group elements Na to Bi, J. Chem. Phys. 82 (1985) 284–298.

[35] M.C. Curet-Arana, G.A. Emberger, L.J. Broadbelt, R.Q. Snurr, Quantum chemical determination of stable intermediates for alkene epoxidation with Mn-porphyrin catalysts, J. Mol. Catal. Chem. 285 (2008) 120–127.

[36] J.S. Sears, C.D. Sherrill, Assessing the Performance of Density Functional Theory for the Electronic Structure of Metal−Salens: The 3d0-Metals, J. Phys. Chem. A. 112 (2008) 3466–3477.

[37] T. Takatani, J.S. Sears, C.D. Sherrill, Assessing the Performance of Density Functional Theory for the Electronic Structure of Metal−Salens: The d6-Metals, J. Phys. Chem. A. 113 (2009) 9231–9236.

[38] A.D. Becke, Density-functional thermochemistry. III. The role of exact exchange, J. Chem. Phys. 98 (1993) 5648–5652.

[39] C. Lee, W. Yang, R.G. Parr, Development of the Colle-Salvetti correlation-energy formula into a functional of the electron density, Phys. Rev. B. 37 (1988) 785–789.

[40] B. Miehlich, A. Savin, H. Stoll, H. Preuss, Results obtained with the correlation energy density functionals of becke and Lee, Yang and Parr, Chem. Phys. Lett. 157 (1989) 200–206.

[41] T. Shi, Y. Luo, X.-L. Wang, S. Lu, Y.-L. Zhao, J. Zhang, Theoretical Studies on the Mechanism, Enantioselectivity, and Axial Ligand Effect of a Ru(salen)-Catalyzed Asymmetric Cyclopropanation Reaction, Organometallics. 33 (2014) 3673–3682.

[42] A.D. McLean, G.S. Chandler, Contracted Gaussian basis sets for molecular calculations. I. Second row atoms, Z=11–18, J. Chem. Phys. 72 (1980) 5639–5648.

[43] R. Krishnan, J.S. Binkley, R. Seeger, J.A. Pople, Self-consistent molecular orbital methods. XX. A basis set for correlated wave functions, J. Chem. Phys. 72 (1980) 650–654.

[44] R. Seeger, J.A. Pople, Self-consistent molecular orbital methods. XVIII. Constraints and stability in Hartree–Fock theory, J. Chem. Phys. 66 (1977) 3045–3050.

[45] R. Bauernschmitt, R. Ahlrichs, Stability analysis for solutions of the closed shell Kohn–Sham equation, J. Chem. Phys. 104 (1996) 9047–9052.

[46] J.P. Foster, F. Weinhold, Natural hybrid orbitals, J. Am. Chem. Soc. 102 (1980) 7211–7218.

[47] A.E. Reed, L.A. Curtiss, F. Weinhold, Intermolecular interactions from a natural bond orbital, donor-acceptor viewpoint, Chem. Rev. 88 (1988) 899–926.

[48] S.F. Boys, F. Bernardi, The calculation of small molecular interactions by the differences of separate total energies. Some procedures with reduced errors, Mol. Phys. 19 (1970) 553–566.

[49] J. Sauer, Molecular models in ab initio studies of solids and surfaces: from ionic crystals and semiconductors to catalysts, Chem. Rev. 89 (1989) 199–255.

[50] M. J. Frisch, G. W. Trucks, H. B. Schlegel, G. E. Scuseria, M. A. Robb, J. R. Cheeseman, G. Scalmani, V. Barone, B. Mennucci, G. A. Petersson, H. Nakatsuji, M. Caricato, X. Li, H. P. Hratchian, A. F. Izmaylov, J. Bloino, G. Zheng, J. L. Sonnenberg, M. Hada, M. Ehara, K. Toyota, R. Fukuda, J. Hasegawa, M. Ishida, T. Nakajima, Y. Honda, O. Kitao, H. Nakai, T. Vreven, J. A. Montgomery, Jr., J. E. Peralta, F. Ogliaro, M. Bearpark, J. J. Heyd, E. Brothers, K. N. Kudin, V. N. Staroverov, R. Kobayashi, J. Normand, K. Raghavachari, A. Rendell, J. C. Burant, S. S. Iyengar, J. Tomasi, M. Cossi, N. Rega, J. M. Millam, M. Klene, J. E. Knox, J. B. Cross, V. Bakken, C. Adamo, J. Jaramillo, R. Gomperts, R. E. Stratmann, O. Yazyev, A. J. Austin, R. Cammi, C. Pomelli, J. W. Ochterski, R. L. Martin, K. Morokuma, V. G. Zakrzewski, G. A. Voth, P. Salvador, J. J. Dannenberg, S. Dapprich, A. D. Daniels, Ö. Farkas, J. B. Foresman, J. V. Ortiz, J. Cioslowski, and D. J. Fox, Gaussian 09, Revision A.02, Gaussian, Inc., Wallingford CT, 2009.

[51] L. Cavallo, H. Jacobsen, Electronic Effects in (salen)Mn-Based Epoxidation Catalysts, J. Org. Chem. 68 (2003) 6202–6207.

[52] S. Kemper, P. Hrobárik, M. Kaupp, N.E. Schlörer, Jacobsen's Catalyst for Hydrolytic Kinetic Resolution: Structure Elucidation of Paramagnetic Co(III) Salen Complexes in Solution via Combined NMR and Quantum Chemical Studies, J. Am. Chem. Soc. 131 (2009) 4172–4173.

[53] K.P. Bryliakov, E.P. Talsi, CrIII(salen)Cl Catalyzed Asymmetric Epoxidations: Insight into the Catalytic Cycle, Inorg. Chem. 42 (2003) 7258–7265.

[54] H.-L. Shyu, H.-H. Wei, G.-H. Lee, Y. Wang, Structure, magnetic properties and epoxidation activity of iron(III) salicylaldimine complexes, J. Chem. Soc. Dalton Trans. (2000) 915–918.

[55] K.B. Hansen, J.L. Leighton, E.N. Jacobsen, On the Mechanism of Asymmetric Nucleophilic Ring-Opening of Epoxides Catalyzed by (Salen)CrIII Complexes, J. Am. Chem. Soc. 118 (1996) 10924–10925.

[56] D.J. Darensbourg, R.M. Mackiewicz, Role of the Cocatalyst in the Copolymerization of CO_2 and Cyclohexene Oxide Utilizing Chromium Salen Complexes, J. Am. Chem. Soc. 127 (2005) 14026–14038.

[57] G.A. Luinstra, G.R. Haas, F. Molnar, V. Bernhart, R. Eberhardt, B. Rieger, On the Formation of Aliphatic Polycarbonates from Epoxides with Chromium(III) and Aluminum(III) Metal–Salen Complexes, Chem. – Eur. J. 11 (2005) 6298–6314.

[58] Z. Liu, M. Torrent, K. Morokuma, Molecular Orbital Study of Zinc(II)-Catalyzed Alternating Copolymerization of Carbon Dioxide with Epoxide, Organometallics. 21 (2002) 1056–1071.

[59] F. Jensen, Introduction to Computational Chemistry, 2nd ed., John Wiley & Sons, Ltd, West Sussex, England, 2007.

[60] E.R. Pérez, M.O. da Silva, V.C. Costa, U.P. Rodrigues-Filho, D.W. Franco, Efficient and clean synthesis of N-alkyl carbamates by transcarboxylation and O-alkylation coupled reactions using a DBU–CO_2 zwitterionic carbamic complex in aprotic polar media, Tetrahedron Lett. 43 (2002) 4091–4093.

[61] M. George, R.G. Weiss, Chemically Reversible Organogels: Aliphatic Amines as "Latent" Gelators with Carbon Dioxide, J. Am. Chem. Soc. 123 (2001) 10393–10394.

[62] G. Sastre, A. Corma, Relation between structure and Lewis acidity of Ti-Beta and TS-1 zeolites: A quantum-chemical study, Chem. Phys. Lett. 302 (1999) 447–453.

[63] R.G. Pearson, Chemical hardness and density functional theory, J. Chem. Sci. 117 (2005) 369–377.

[64] G. Yang, L. Zhou, X. Han, Lewis and Brönsted acidic sites in M^{4+}-doped zeolites (M = Ti, Zr, Ge, Sn, Pb) as well as interactions with probe molecules: A DFT study, J. Mol. Catal. Chem. 363–364 (2012) 371–379.

Chapter 7: Conclusions and Recommendations

This dissertation contributes to the development of novel and inexpensive heterogeneous catalysts for the conversion of CO_2 through its hydrogenation to valuable organic compounds in an effort to mitigate the negative effects of CO_2 in our planet and search for renewable sources of fuels and feedstocks.

The thermochemical potential energy surfaces for different decomposition, oxidation and hydrogenation reactions have been calculated, giving insight into the thermochemistry on gold nanoparticles. From these potential energy surfaces, we have concluded that the hydrogenation of CO_2 and CO to formic acid, formaldehyde and methanol on Au(111) probably will not be thermodynamically favorable, because CO_2 is not adsorbed on the Au(111) surface. Despite that the adsorption of CO and the formation of HCO are favorable on this surface, the dissociative adsorption of H_2 is an endothermic reaction, while it is highly favorable on other catalytic surfaces analyzed in this dissertation.

We have studied the thermochemistry for the synthesis of methanol, formic acid and formaldehyde through the CO_2/CO hydrogenation on Cu(111) doped with Ga, Ti, and Mg. Among these Cu-based surface alloys, our results suggest that Ga/Cu(111) and Mg/Cu(111) surfaces might have good catalytic performance. CO_2 is activated by chemisorption on Mg/Cu(111) and Ti/Cu(111), but the latter surface has a strong interaction with O, which inhibits the last reaction steps and the desorption of the products. The reaction mechanism proposed for the synthesis of these products varies depending on the dopant incorporated on the Cu(111) surface. The Cu surfaces doped with Ga and

Mg are predicted to selectively produce methanol from CO_2. To our knowledge, these doped Cu surfaces have not been studied for the hydrogenation of CO_2 and CO, therefore, these findings provides new insights in the sequestration and catalytic conversion of CO_2.

There are still many questions left unanswered. Future works could include determining the transition states and calculate the activation energies for the elementary steps evaluated for the synthesis of formic acid, formaldehyde and methanol on the Cu(111) surfaces doped with Ga and Mg. The effect of temperature in the thermochemistry for the hydrogenation of CO_2 to formic acid, formaldehyde and methanol over the Ga and Mg-doped Cu(111) surfaces could be evaluated by performing frequency calculations. From this analysis, the zero point energies, the enthalpies and Gibbs free energies of reaction could be calculated. This is important, especially for Mg/Cu(111), because this would help to predict if methanol and water could be desorbed from the surface at reaction conditions. Furthermore, different reaction temperatures could be investigated for the hydrogenation of CO_2 on these surfaces to determine if these added-value organic compounds can be generated at low temperature conditions. The analysis of the thermochemistry for the formation of methane from CO_2 and CO hydrogenation catalyzed by Ga/Cu(111) and Mg/Cu(111) surfaces might be an interesting approach. Finally, the effect of the dopant concentration in the reaction energies for the elementary steps in the proposed mechanisms could be also investigated by increasing the coverage of Ga and Mg in the Cu(111) surface or designing Cu-Ga and Cu-Mg alloys.

DFT calculations have been used to evaluate the thermochemistry of plausible elementary steps for the reaction of CO_2 with ethylene oxide catalyzed by metal-salen

157

complexes consisting of Co, Cr, Mn, Fe, Al and Zn. The effect of the metal centers and the axial ligands, Cl and DMAP, on the energies of reaction was studied. Our results have demonstrated that when chlorine is the axial ligand, the formation of CO_2-epoxide-salen complexes was an endothermic reaction for all metal-salens considered. However, the energies of reaction decreased for these complexes with DMAP as axial ligand. While differences were found in the reaction energies estimated with UOPBE/LANL2DZ and B3LYP/6-311g**/LANL2DZ, both methods yield similar minimum energy structures on the intermediates that were analyzed. We have demonstrated that the UOPBE/LANL2DZ method describe this reaction system better than B3LYP/6-311g**/LANL2DZ. The most energetically favorable intermediates for the coupling of CO_2 and ethylene oxide obtained with the UOPBE/LANL2DZ method were the complexes with Al and Cr as metal center and DMAP as axial ligand. The inclusion of dichloromethane as a solvent did not have a significant effect in the reaction energies with the B3LYP/6-311g**/LANL2DZ method. We have also analyzed the incorporation of DMAP as cocatalyst, and our results indicated that CO_2 is activated by DMAP forming a stable CO_2-DMAP complex. Therefore, this finding deserves further study in the interactions of the CO_2-DMAP complex with the epoxide and salen complexes to get a better understanding of the reaction mechanism for the formation of ethylene carbonate from CO_2 and ethylene oxide. This analysis could be performed evaluating different metal centers, axial ligands and solvents to investigate if they decrease the energies of reaction.

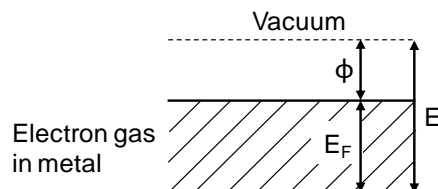# Appendix A: Supplementary Material for Chapter 5

Fig. A.1. Schematic illustration of the work function.

A.1. Screening Results for Cu(111) and M-Doped Cu(111) Surfaces

A.1.1. Adsorption of H on Cu(111) and M/Cu(111)

The binding energies of H on Ni/Cu(111), Pd/Cu(111), Ti/Cu(111), Mg/Cu(111), Al/Cu(111) and Ga/Cu(111) relative to the pure Cu(111) surface are shown in Fig. A.2a, which assigns a zero-energy to Cu(111). As illustrated in Fig. A.2a, Cu(111) doped with Ni presents the strongest adsorption of H while the weakest adsorption of H is predicted to be on Ga/Cu(111), when the M-doped Cu surfaces are compared. When the impurities Ni, Pd or Ti are added to the Cu(111), the adsorption of H is moderate and stronger than on the pure surface. While the addition of Mg, Al or Ga in Cu(111) increases the binding energy of H, when compared with Cu(111). However, H is chemisorbed on all the surfaces, including the Cu(111) surface. The label over each bar in Fig. A.2a indicates the preferred adsorption site for H on Cu(111) and M/Cu(111). The adsorption sites closed by parentheses are the sites that follow to the adsorption site with minimum energy, which is the site outside the parentheses. We are presenting two adsorption sites for each surface because the energy difference among both sites is only 0.01-0.04 eV,

which means the fcc and hcp sites are degenerated when H is adsorbed on Cu(111) and M/Cu(111). This degeneration in the binding energies is maintained even when the Cu surface is doped with Ni, Pd, Ti, Mg, Al and Ga. The difference between Cu(111), Mg/Cu(111), Al/Cu(111) and Ga/Cu(111), and the other M/Cu(111) is that in the former ones, H is only coordinated to Cu atoms while in the last ones, H prefers to adsorb on the mixed sites.
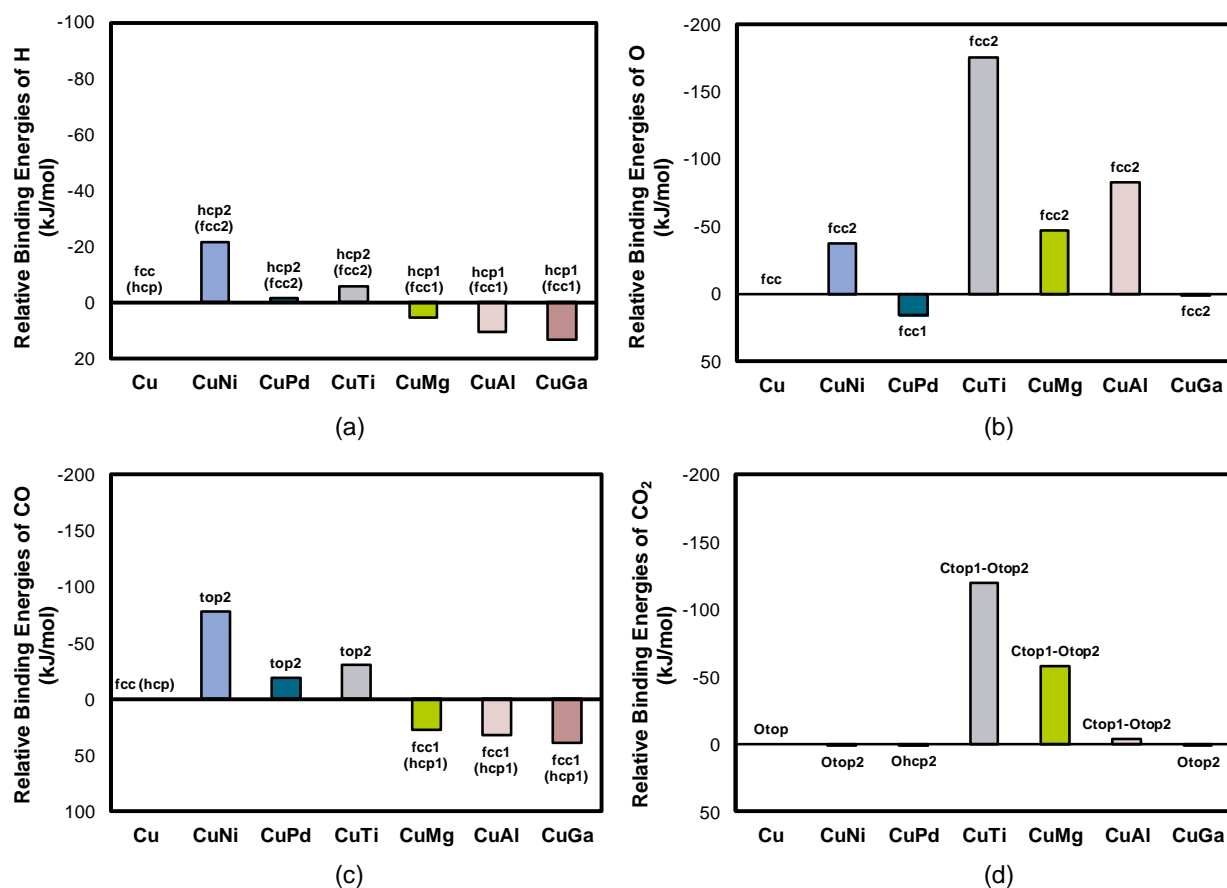

Fig A.2. Relative binding energies of: (a) H, (b) O, (c) CO and (d) CO_2 on M/Cu(111) with respect to Cu(111). M = Ni, Pd, Ti, Mg, Al, or Ga. The preferred adsorption sites for each surface are indicated in the label above of each bar.

A.1.2. Adsorption of O on Cu(111) and M/Cu(111)

Results of the adsorption of O on the pure and M-doped Cu surfaces indicate that O is strongly adsorbed on Ti/Cu(111) in comparison with the other surfaces, obtaining a binding energy 176 kJ/mol lower than the energy estimated on Cu(111), as depicted in Fig. A.2b. The highly strong chemisorption of O on Ti/Cu(111) (a binding energy of -638 kJ/mol) causes surface deformation because the Ti atom is displaced upward from the surface plane. While on Ni/Cu(111) and Mg/Cu(111), the adsorption of O is moderately stronger than on Cu(111); and on Pd/Cu(111) and Ga/Cu(111), O is adsorbed weaker than on Cu(111). An important tendency that we observed from this study is that substituting a Cu atom by Pd does not present a notably improvement effect in the adsorption of these species on Cu(111). This hypothesis is clearly observed in the results for O adsorption, because the preferred adsorption site for O on Pd/Cu(111) and Cu(111) is the same, which is the pure Cu fcc site. While on the other M-doped Cu surfaces, O prefers the mixed fcc sites.

A.1.3. Adsorption of CO on Cu(111) and M/Cu(111)

As shown in Fig. A.2c, the strongest adsorption of CO is predicted to be on Ni/Cu(111) with a lower binding energy than Cu(111) by 78 kJ/mol. While the weakest adsorption of CO is observed on Ga/Cu(111). Mg, Al and Ga impurities do not improve the capacity of CO adsorption on Cu(111). Ti and Pd have a moderate effect of promotion in the adsorption of CO on Cu(111). According to our results, the preferred adsorption site of CO on Cu(111) is different to the one on M/Cu(111) surfaces with M=Ni, Pd or Ti. However, the prediction of CO adsorption site using DFT non-hybrid functionals such as

the PW91 functional has caused controversy, because it has been reported in the literature that these functionals tend to fail in predicting the correct adsorption site for strong pi-acceptor molecules such as CO [1]. Experimentally, CO is adsorbed at the top site on Cu(111) [2], while our calculations and other theoretical studies indicate that the adsorption is on the fcc site [3,4]. A comparison of the results for CO adsorption on M/Cu(111) with M=Ni, Pd or Ti and the experimental observations indicate the adsorption preference of CO (the top site) does not change when the Cu surface is doped with Ni, Pd or Ti. But, CO prefers to adsorb on the dopant atom in the presence of these impurities rather than on the Cu atom.

A.1.4.   Adsorption of CO_2 on Cu(111) and M/Cu(111)

The results in Fig. A.2d indicate that CO_2 is favorably adsorbed on all the M/Cu(111) surfaces. Physical adsorption of CO_2 is observed on Ni/Cu(111), Pd/Cu(111) and Ga/Cu(111) as on Cu(111). CO_2 is activated by chemisorption on Ti/Cu(111), Mg/Cu(111) and Al/Cu(111) with binding energies of -125, -63 and -9 kJ/mol, respectively, being Ti the dopant with the highest promotional effect in the CO_2 activation. This CO_2 activation is clearly shown in the illustrations in Fig. A.3, where CO_2 is adsorbed on Ti/Cu(111) at a tridentate configuration, which is the same conformation adopted by CO_2 adsorbed on Mg/Cu(111) and Al/Cu(111). In this configuration, the nucleophilic C atom of CO_2 is bonded to a Cu atom at the top site, while each O atom of CO_2 is bonded to a Ti atom at the top site. In contrast, for Cu(111) and the other M/Cu(111), CO_2 keeps its linear configuration and large bonding distances among 3.3 – 3.6 Å are obtained. CO_2 adsorption causes surface deformation in Ti/Cu(111), Mg/Cu(111) and Al/Cu(111).
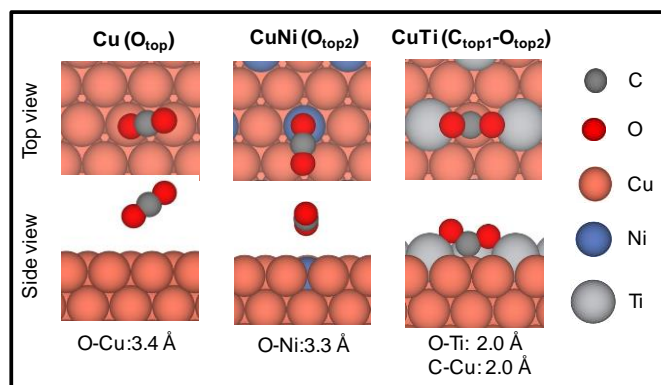
Fig. A.3. Adsorption geometries for CO_2 adsorbed on Cu(111), and Cu(111) doped with Ni and Ti.

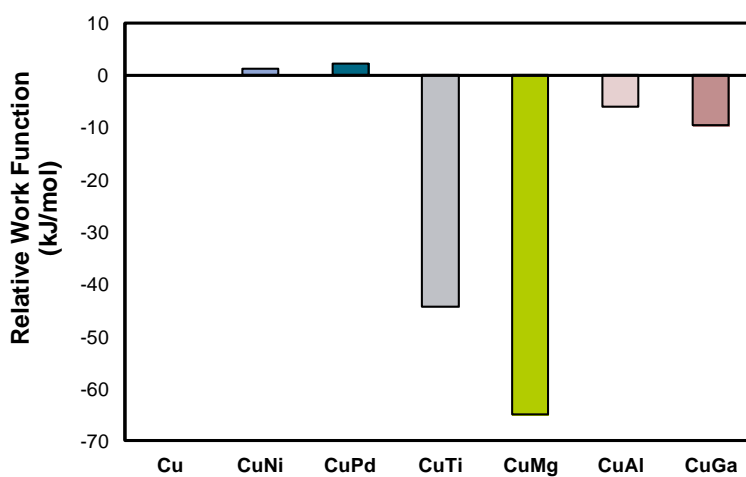## A.1.5. Work functions for Cu(111) and M/Cu(111)

Fig. A.4. Relative work function of M/Cu(111) with respect to Cu(111). M = Ni, Pd, Ti, Mg, Al, or Ga.

A.2. Results for the Systematic Study of the Ga-Doped Cu(111) Surface

Table A.1. Adsorption geometry on Ga/Cu(111).

Adsorbate	d_{A-Ga} (Å)	d_{A-Cu} (Å)	d_{Cu-Cu} (Å)	d_{Ga-Cu} (Å)[c]	d_{A-B} (Å)	ΔZ_{Cu} (Å)	ΔZ_{Ga} (Å)
H (hcp1)	-	1.74	2.56 [a]	2.58	-	0.00	-
O (fcc2)	1.86	1.94	2.75 [a]	2.86	-	0.00	0.01
C (fcc2)	1.90	1.85	2.69 [a]	3.11	-	0.00	0.03
CO (hcp1)	-	2.05	2.58 [a]	2.59	1.18	0.00	-
CO (fcc1)	-	2.05	2.59 [a]	2.58	1.18	0.00	-
OH (fcc1)		2.03	2.75 [a]	2.55	0.97	0.00	-
CO_2 (physisorption)	-	3.13	2.56 [a]	2.57	1.18	0.00	-
H_2O (physisorption)	-	2.37	2.56 [a]	2.60	0.98	0.00	-
COH (fcc1)	-	1.94	2.64 [a]	2.57	1.34 (CO) 0.98 (OH)	0.00	-
HCO (Ctop1)	-	1.95	2.61 [a]	2.57	1.24 (CO), 1.12 (CH)	0.01	-
HCO (Cbr1)	-	2.09	2.49 [a]	2.58	1.26 (CO), 1.11 (CH)	0.00	-
COOH (Ctop1-H down)	-	1.96	2.63 [a]	2.57	1.25 (CO),1.35 (C-OH) 0.98 (OH)	0.00	-
HCOO (Otop1-Otop1)	-	2.02	2.60 [a]	2.59	1.27 (CO), 1.11 (CH)	0.00	-
HCOOH (physisorption)	-	2.23	2.56 [a]	2.61	1.23 (CO), 1.32 (C-OH) 1.11 (CH), 1.01 (OH)	0.01	-
CO_3 (Otop2-Obr1)	1.92	2.02	2.76 [a]	2.80	1.21 (CO[d]), 1.32 (CO[e]) 1.42 (CO[f])	0.00	0.02
HCO_3 (Otop1-Otop1)	-	2.02	2.61 [a]	2.59	1.27 (CO), 1.36 (C-OH) 0.98 (OH)	0.00	-
CH_2O (Ctop1-Obr1)	-	2.07 (C) 2.12 (O)	2.68 [a]	2.58	1.34 (CO), 1.10 (CH)	0.00	-
CH_2OH (Ctop1)	-	2.03	2.57 [a]	-	1.43 (CO), 1.10 (CH) 0.98 (OH)	0.01	-
CH_2O_2 (Obr2-Obr2)	2.01	2.07	2.81 [b]	2.68	1.42 (CO) 1.11 (CH)	0.00	0.01
H_2COOH (Obr1)	-	2.03	2.74 [a]	2.50	1.42 (CO) 1.42 (C-OH) 1.10 (CH) 0.98 (OH)	0.00	-
CH_3O (fcc1)	-	2.02	2.74 [a]	2.55	1.43 (CO) 1.10 (CH)	0.00	-
CH_3O (fcc2)	2.04	2.09	2.73 [a]	2.79	1.44 (CO) 1.10 (CH)	0.00	0.00
CH_3OH (physisorption)	-	2.28	2.58 [a]	-	1.44 (CO) 1.10 (CH) 0.98 (OH)	0.00	-

See Fig. A.5 for geometric definitions of these parameters.
[a] These distances are compared to d_{Cu-Cu}= 2.56 Å for two adjacent Cu atoms on a relaxed clean surface.
[b] These distances are compared to d_{Cu-Cu}= 2.58 Å for the two Cu atoms at the bridge1' site that are bonded to two Ti atoms.
[c] These distances are compared to d_{Ga-Cu}= 2.58 Å for two adjacent Ga and Cu atoms on a relaxed clean surface.
[d] Refers to CO group that is not bonded to the Ga/Cu(111) surface in CO_3 molecule as depicted in Fig. 3.
[e] Refers to CO group bonded at the Otop2 site on Ga/Cu(111) in CO_3 molecule as depicted in Fig. 3.
[f] Refers to CO group bonded at the Obr1 site on Ga/Cu(111) in CO_3 molecule as depicted in Fig. 3.
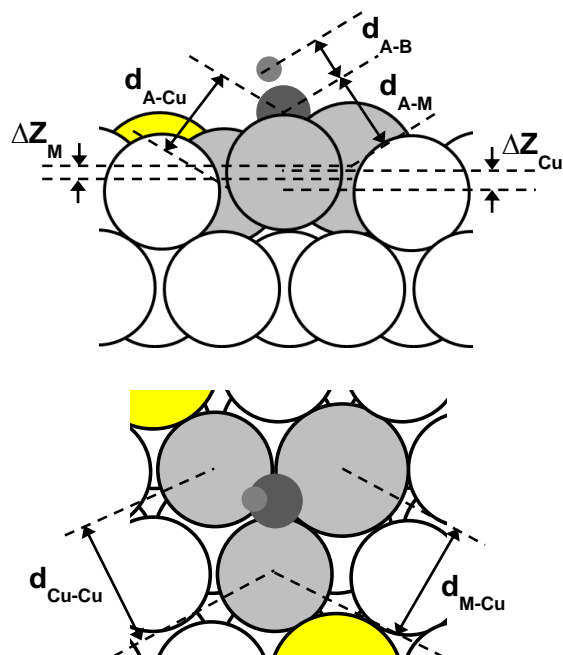
Fig. A.5. Top and side view of geometric parameters for the species adsorbed on M/Cu(111), where M= Ga, Ti, Mg. ΔZ_{Cu} (Å) is the change in vertical distance of the Cu atoms in contact with the adsorbate and the plane of Cu atoms on a clean relaxed surface; ΔZ_M (Å) is the change in vertical distance of the metal dopant (M) in contact with the adsorbate and the plane of M atoms on a clean relaxed surface; d_{Cu-Cu} (Å) is the average distance between adjacent Cu atoms in contact with the adsorbate (d_{Cu-Cu}= 2.53 Å for two adjacent Cu atoms on a relaxed clean surface while d_{Cu-Cu}= 2.63 Å for the two Cu atoms at the bridge1' site because these atoms are bonded to two M atoms); d_{M-Cu} (Å) is the average distance between adjacent M and Cu atoms in contact with the adsorbate, which is compared with the average distances d_{Ga-Cu}= 2.58 Å, d_{Ti-Cu}= 2.59 Å and d_{Mg-Cu} = 2.66 Å for adjacent M and Cu atoms on a relaxed clean surface; and d_{A-B} (Å) is the bond length within an adsorbed species.
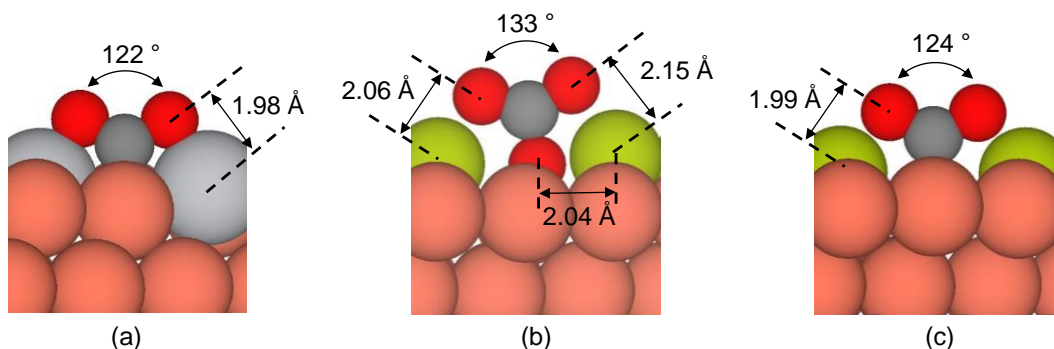

Fig. A.6. Side view of the adsorption geometry for: (a) CO_2 adsorbed on Ti/Cu(111), (b) CO_3 and (c) CO_2 adsorbed on Mg/Cu(111).

A.3. Results for the Systematic Study of the Ti-Doped Cu(111) Surface

Table A.2. Adsorption geometry on Ti/Cu(111).

Adsorbate	$d_{A\text{-}Ti}$ (Å)	$d_{A\text{-}Cu}$ (Å)	$d_{Cu\text{-}Cu}$ (Å)	$d_{Ti\text{-}Cu}$ (Å)[d]	$d_{A\text{-}B}$ (Å)	ΔZ_{Cu} (Å)	ΔZ_{Ti} (Å)
H (br1)	-	1.71	2.57 [b]	2.61	-	0.00	-
O (fcc2)	1.78	2.01	2.66 [b]	2.63	-	0.00	0.01
C (fcc2)	1.87	1.87	2.69 [b]	2.73	-	0.00	0.01
CO (Otop2-Cfcc2')	2.04 (C) 1.93 (O)	2.05	2.95 [c]	2.62 (Ti1) 2.53 (Ti2)	1.32	0.00	0.02
OH (top2)	1.77	-	2.53 [b]	2.64	0.96	-	0.02
CO_2 (Otop2-Ctop1[a])	1.98	2.05	2.73 [c]	2.59	1.30	0.00	0.02
CO_2 (Otop2-Cbr1' [a])	1.98	2.17	2.70 [c]	2.62	1.31	0.00	0.02
H_2O (top2)	2.15	-	2.55 [b]	2.61	0.99	-	0.01
COH (Cfcc2')	2.06	1.97	3.05 [c]	2.54	1.46 (CO), 0.98 (OH)	0.00	0.01
HCO (Cfcc2'-Otop2)	2.07 (C) 1.91 (O)	2.07	2.95 [c]	2.67 (Ti1) 2.54 (Ti2)	1.36 (CO) 1.16 (CH)	0.00	0.01
COOH (Otop2-Cbr1')	1.97	2.06	2.87 [c]	2.72	1.33 (CO),1.50 (C-OH) 0.98 (OH)	0.00	0.01
HCOO (Otop2-Ctop1[a])	1.86	2.16	2.54 [b]	2.54	1.38 (CO) 1.10 (CH)	0.00	0.02
HCOOH (top2-H down)	2.02	-	2.53 [b]	2.61	1.25 (CO), 1.30 (C-OH) 1.10 (CH), 1.04 (OH)	-	0.01
CH_2O (Otop2-Ctop1)	1.82	2.13	2.56 [b]	2.53	1.41 (CO) 1.10 (CH)	0.00	0.02
CH_2OH (Otop2-Ctop1)	2.06	2.10	2.57 [b]	2.51	1.49 (CO), 1.10 (CH) 0.99 (OH)	0.01	0.01
CH_2O_2 (Otop2-Otop2)	1.82	-	2.55 [b]	2.63	1.41 (CO), 1.11 (CH)	-	0.02
H_2COOH (Otop2)	1.86	-	2.56 [b]	2.61	1.37 (CO), 1.49 (C-OH) 1.10 (CH), 0.99 (OH)	-	0.02
CH_3O (top2)	1.77	-	2.52 [b]	2.65	1.41 (CO), 1.10 (CH)	-	0.02
CH_3OH (top2)	2.08	-	2.54 [b]	2.60	1.44 (CO), 1.10 (CH) 0.99 (OH)	-	0.01

See Fig. A.5 for geometric definitions of these parameters.
[a] Indicates that two oxygen atoms of the species are respectively adsorbed on two metal atoms at the preferred site specified, forming a tridentate configuration because the C atom is also bonded to the surface at the preferred site specified.
[b] These distances are compared to $d_{Cu–Cu}$= 2.53 Å for two adjacent Cu atoms on a relaxed clean surface.
[c] These distances are compared to $d_{Cu–Cu}$= 2.63 Å for the two Cu atoms at the bridge1' site that are bonded to two Ti atoms.
[d] These distances are compared to $d_{Ti–Cu}$= 2.59 Å for two adjacent Ti and Cu atoms on a relaxed clean surface.

A.4. Results for the Systematic Study of the Mg-Doped Cu(111) Surface

Table A.3. Adsorption geometry on Mg/Cu(111).

Adsorbate	d_{A-Mg} (Å)	d_{A-Cu} (Å)	d_{Cu-Cu} (Å)	d_{Mg-Cu} (Å)[e]	d_{A-B} (Å)	ΔZ_{Cu} (Å)	ΔZ_{Mg} (Å)
H (br1')	-	1.71	2.65 [d]	2.67	-	0.00	-
O (br1' [a])	2.03	1.98	3.00 [d]	2.63	-	0.00	0.01
C (br1')	-	1.84	2.98 [d]	2.74	-	0.00	-
CO (fcc1)	-	2.05	2.56 [c]	2.66	1.19	0.00	-
OH (fcc2)	1.92	2.14	2.58 [c]	2.81	0.97	0.00	0.00
CO_2 (Otop2-Otop2)	1.99	-	2.53 [d]	2.82	1.28	-	0.01
CO_2(Otop2-Ctop1[b])	1.98	2.10	2.55 [d]	2.80	1.28	0.00	0.01
H_2O (physisorption)	2.12	-	2.57 [c]	2.71	0.99	-	0.00
COH (fcc1)	-	1.95	2.62 [c]	2.62	1.34 (CO), 0.98 (OH)	0.00	-
HCO (Otop2-Cbr1)	2.00	2.09	2.45 [c]	2.79	1.29 (CO), 1.11 (CH)	0.00	0.01
COOH (Ctop1-H up)	-	1.96	2.55 [c]	2.74	1.26 (CO),1.42 (C-OH) 0.99 (OH)	0.00	0.01
HCOO (Otop2-Otop2)	1.98	-	2.54 [c]	2.74	1.27 (CO) 1.11 (CH)	-	0.01
HCOOH (top2-H down)	2.05	-	2.53 [c]	2.70	1.24 (CO) 1.31 (C-OH) 1.10 (CH), 1.03 (OH)	-	0.01
CO_3 (Otop2-Ofcc2')	2.04 (Mg1) 2.06 (Mg2)	2.00	2.92 [d]	3.18 (Mg1) 2.95 (Mg2)	1.26 (CO), 1.40 (CO)	0.00	0.03
HCO_3 (Otop2-Otop2)	1.97	-	2.54 [c]	2.74	1.27 (CO) 1.36 (C-OH) 0.98 (OH)	-	0.01
CH_2O (Otop2-Ctop1)	1.94	2.15	2.53 [c]	2.81	1.33 (CO), 1.11 (CH)	0.00	0.01
CH_2OH (Ctop1)	-	2.03	2.55 [c]	2.68	1.50 (CO), 1.10 (CH) 0.98 (OH)	0.01	0.01
CH_2O_2 (Otop2-Ofcc2')	1.94 (Mg1) 1.88 (Mg2)	2.09	2.75 [d]	2.82 (Mg1) 2.86 (Mg2)	1.35 (CO[f]), 1.49 (CO[g]) 1.11 (CH)	0.00	0.01
CH_2O_2 (Otop2-Ohcp2')	1.88 (Mg1) 1.94 (Mg2)	2.09	2.73 [d]	2.85 (Mg1) 2.81 (Mg2)	1.35 (CO[f]), 1.49 (CO[g]) 1.11 (CH)	0.00	0.01
H_2COOH (Otop2)	1.95	-	2.55 [c]	2.77	1.36 (CO) 1.48 (C-OH) 1.11 (CH) 0.99 (OH)	-	0.01
CH_3O (fcc2)	1.93	2.13	2.59 [c]	2.81	1.43 (CO) 1.11 (CH)	0.00	0.00
CH_3OH (physisorption)	2.11	-	2.53 [c]	2.72	1.45 (CO) 1.10 (CH) 1.00 (OH)	-	0.01

See Fig. A.5 for geometric definitions of these parameters.
[a] Indicates that this species is adsorbed through four metal atoms (two Cu and two Mg) on Mg/Cu(111).
[b] Indicates that two oxygen atoms of the species are respectively adsorbed on two metal atoms at the preferred site specified, forming a tridentate configuration because the C atom is also bonded to the surface at the preferred site specified.

[c] These distances are compared to d_{Cu-Cu}= 2.53 Å for two adjacent Cu atoms on a relaxed clean surface.
[d] These distances are compared to d_{Cu-Cu}= 2.64 Å for the two Cu atoms at the bridge1' site that are bonded to two Mg atoms.
[e] These distances are compared to d_{Mg-Cu}= 2.66 Å for two adjacent Mg and Cu atoms on a relaxed clean surface.
[f] Refers to CO groups bonded at or close to the Otop2 site on Mg/Cu(111) in CO_3 or CH_2O_2 molecule, as depicted in Fig. 11.
[g] Refers to CO group bonded at the 3-fold hollow (Ofcc2' or Ohcp2') site on Mg/Cu(111) in the CO_3 or CH_2O_2 molecule, as depicted in Fig. 11.

References

[1] F. Abild-Pedersen, M.P. Andersson, CO adsorption energies on metals with correction for high coordination adsorption sites – A density functional study, Surf. Sci. 601 (2007) 1747–1753.
[2] S. Vollmer, G. Witte, C. Wöll, Determination of Site Specific Adsorption Energies of CO on Copper, Catal. Lett. 77 (2001) 97–101.
[3] S.E. Mason, I. Grinberg, A.M. Rappe, First-principles extrapolation method for accurate CO adsorption energies on metal surfaces, Phys. Rev. B. 69 (2004) 161401.
[4] L.C. Grabow, M. Mavrikakis, Mechanism of Methanol Synthesis on Cu through CO_2 and CO Hydrogenation, ACS Catal. 1 (2011) 365–384.

Appendix B: Supplementary Material for Chapter 6
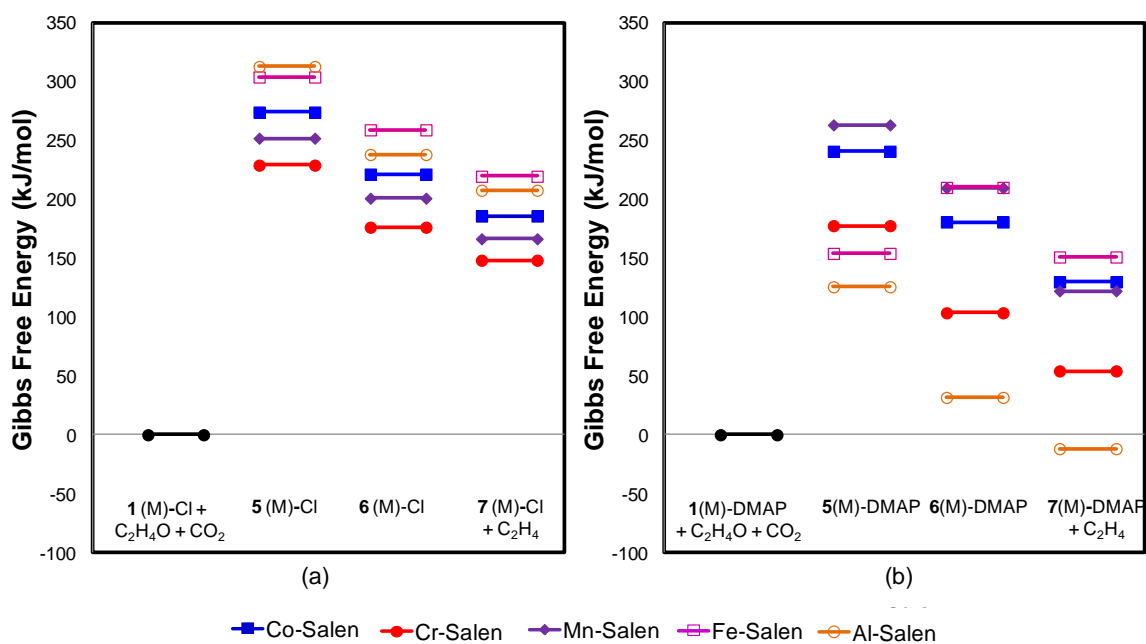
Fig. B.1. Relative Gibbs free energies for **5**(M)-L, **6**(M)-L and **7**(M)-L+C_2H_4 produced by the interaction between CO_2, ethylene oxide and **1**(M)-L with: (a) L=Cl and (b) L=DMAP. The reference zero corresponds to the energies of isolated species in gas-phase.
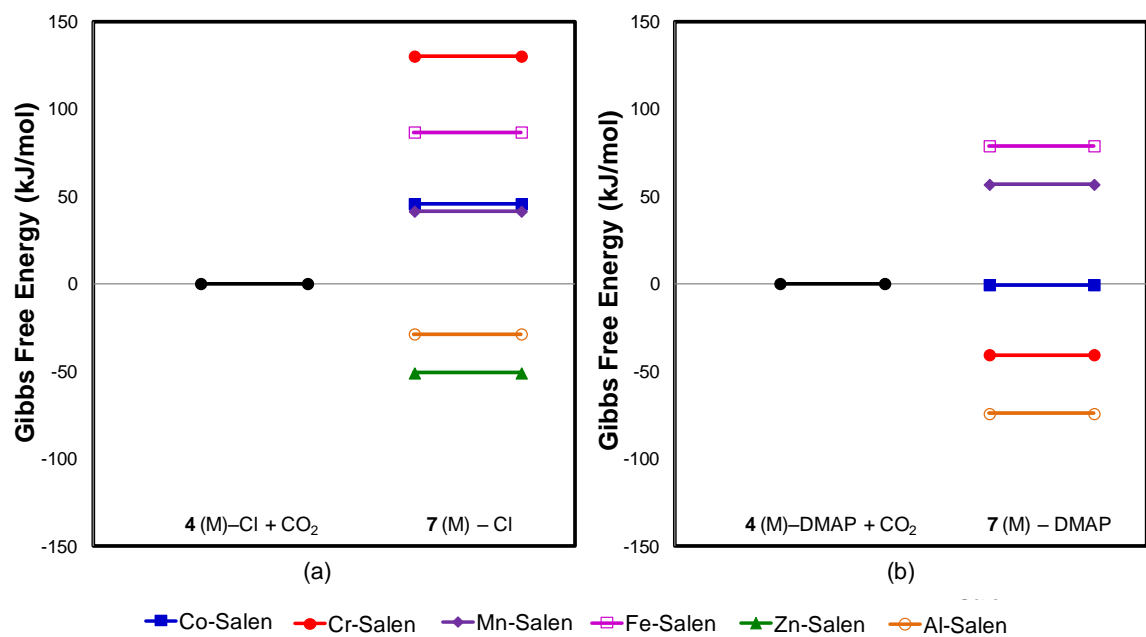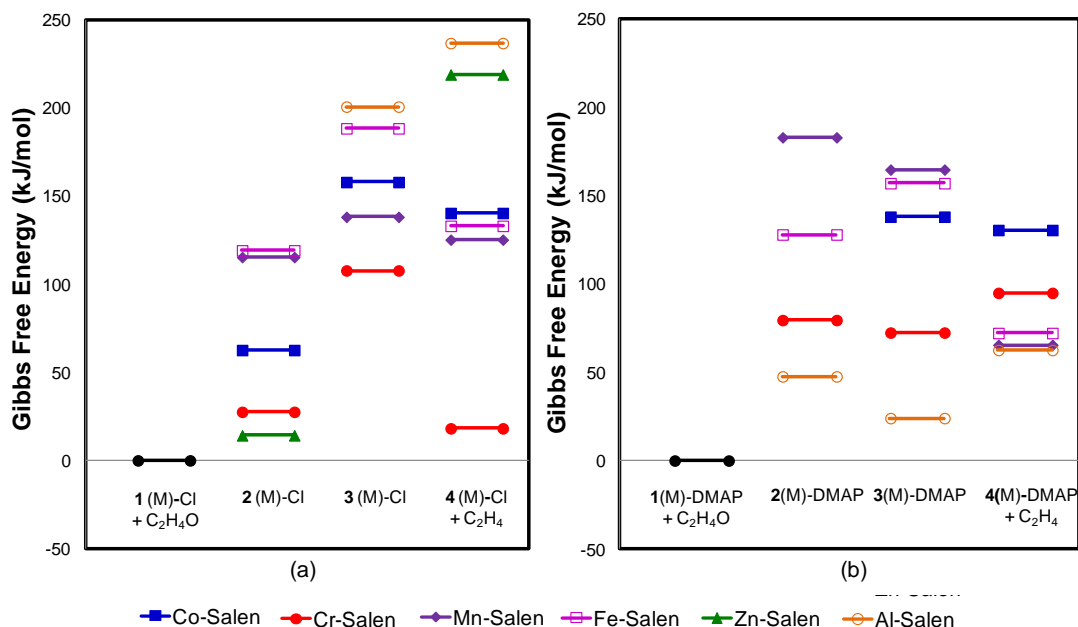

Fig. B.2. Relative Gibbs free energies for **7**(M)-L produced by the interaction between CO_2 and **4**(M)-L with: (a) L=Cl and (b) L=DMAP. The reference zero corresponds to the energies of isolated species in gas-phase. Zn-complexes do not have axial ligand.

Fig. B.3. Relative Gibbs free energies for **2**(M)-L, **3**(M)-L and **4**(M)-L+C_2H_4 produced by the interaction between ethylene oxide and **1**(M)-L with: (a) L=Cl and (b) L=DMAP. The reference zero corresponds to the energies of isolated species in gas-phase. Complexes **2**(Al)-Cl, **2**(Co)-DMAP and **3**(Zn) were not observed in these calculations. Zn-complexes do not have axial ligand.
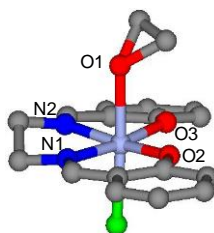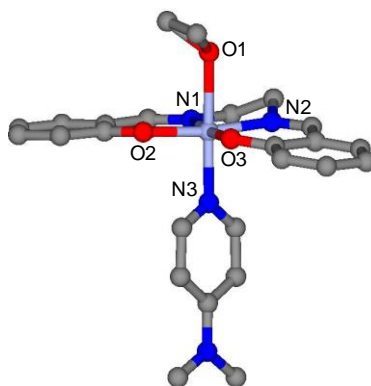

Fig. B.4. Optimized geometry for the complex **2**(M)-Cl. The color gray is for carbon atoms, red is for oxygen, blue is for nitrogen, green is for chlorine and gray-blue is for the metal centers: Cr, Co, Fe and Zn.

Table B.1. Structural parameters for relevant atoms in the most favorable complexes **2**(M)-Cl as illustrated on Fig. B.4 estimated using the methods UOPBE/LANL2DZ and B3LYP/6-311g**/LANL2DZ.

2(M)-Cl	UOPBE/LANL2DZ						B3LYP/6-311g**/LANL2DZ					
	M-O1 (Å)	M-O2 (Å)	M-O3 (Å)	M-N1 (Å)	M-N2 (Å)	M-Cl (Å)	M-O1 (Å)	M-O2 (Å)	M-O3 (Å)	M-N1 (Å)	M-N2 (Å)	M-Cl (Å)
Co (m1)	2.185	1.904	1.904	1.877	1.876	2.261	2.112	1.897	1.895	1.923	1.917	2.249
Cr (m4)	2.262	1.938	1.946	2.001	2.005	2.330	2.203	1.938	1.942	2.045	2.045	2.312
Fe (m2)	2.249	1.893	1.891	1.875	1.876	2.288	2.176	1.904	1.894	1.934	1.932	2.279
Zn[a] (m1)	2.297	2.014	2.010	2.128	2.118	-	2.228	2.004	1.999	2.152	2.144	-

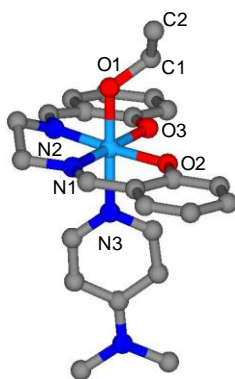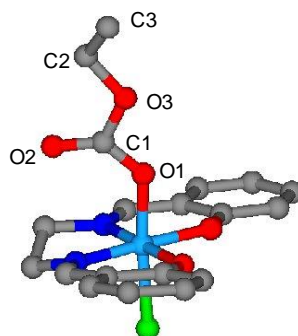[a] Zn-salen complexes do not have axial ligand

Fig. B.5. Optimized geometry for the complex **2**(M)-DMAP. The color gray is for carbon atoms, red is for oxygen, blue is for nitrogen, green is for chlorine and gray-blue is for the metal centers: Cr, Co and Al.

Table B.2. Structural parameters for relevant atoms in the most favorable complexes **2**(M)-DMAP as illustrated on Fig. B.5 estimated using the methods UOPBE/LANL2DZ and B3LYP/6-311g**/LANL2DZ.

2(M)-DMAP	UOPBE/LANL2DZ						B3LYP/6-311g**/LANL2DZ					
	M-O1 (Å)	M-O2 (Å)	M-O3 (Å)	M-N1 (Å)	M-N2 (Å)	M-N3 (Å)	M-O1 (Å)	M-O2 (Å)	M-O3 (Å)	M-N1 (Å)	M-N2 (Å)	M-N3 (Å)
Co (m4)	-	-	-	-	-	-	2.426	2.020	2.022	2.146	2.117	2.219
Cr (m3)	2.296	1.943	1.941	1.953	1.951	2.048	2.226	1.965	1.956	2.007	1.996	2.121
Al (m2)	2.440	1.859	1.864	1.969	1.963	2.094	2.217	1.869	1.844	2.016	1.956	2.116

Fig. B.6. Optimized geometry for the complex **3**(M)-DMAP. The color gray is for carbon atoms, red is for oxygen, blue is for nitrogen, green is for chlorine and light blue is for the metal centers: Cr and Al.

Table B.3. Structural parameters for relevant atoms in the most favorable complexes **3**(M)-DMAP as illustrated on Fig. B.6 estimated using the methods UOPBE/LANL2DZ and B3LYP/6-311g**/LANL2DZ.

| 3(M)-DMAP	UOPBE/LANL2DZ							B3LYP/6-311g**/LANL2DZ						
	M-O1 (Å)	M-O2 (Å)	M-O3 (Å)	M-N1 (Å)	M-N2 (Å)	M-N3 (Å)	O1-C1-C2 (°)	M-O1 (Å)	M-O2 (Å)	M-O3 (Å)	M-N1 (Å)	M-N2 (Å)	M-N3 (Å)	O1-C1-C2 (°)
Cr (m5)	1.893	1.979	1.976	2.019	2.007	2.239	106.552	1.872	1.968	1.964	2.061	2.059	2.259	110.911
Al (m2)	1.842	1.895	1.907	2.034	2.034	2.253	112.416	1.824	1.884	1.885	2.064	2.061	2.286	111.963

Fig. B.7. Optimized geometry for the complex **6**(M)-Cl. The color gray is for carbon atoms, red is for oxygen, blue is for nitrogen, green is for chlorine and light blue is for the metal centers: Cr, Co, Mn, Fe, Al and Zn.

Table B.4. Natural charges (top) and spin densities (bottom) of CO_2 and relevant atoms in complex **6**(M)-Cl as illustrated on Fig. B.7.

| 6(M)-Cl	metal atom	O1	O2	O3	C1	C3	Cl
Co (triplet)	0.33308 0.400030	-0.54298 -0.011432	-0.71276 0.021658	-0.56840 0.030770	1.00529 -0.000707	-0.29450 1.088932	-0.28111 -0.011096
Cr (quartet)	0.40819 2.553782	-0.56491 0.005459	-0.69509 0.000552	-0.56271 0.003610	1.01583 0.003061	-0.29417 1.044954	-0.27366 -0.019543
Mn (quintet)	0.52045 2.847421	-0.55396 0.044367	-0.69000 0.028485	-0.55909 0.031661	1.01331 -0.001776	-0.28658 1.09374	-0.23404 -0.011503
Fe (quartet)	0.34963 1.582244	-0.53013 0.057917	-0.68915 0.033802	-0.56011 0.031877	1.01049 -0.004906	-0.28847 1.095798	-0.21180 0.035154
Al (triplet)	1.89487 -0.020597	-0.82147 0.042852	-0.68537 0.058627	-0.56334 0.016980	1.02606 -0.009959	-0.33242 1.133191	-0.50879 0.179914
Zn (triplet)	1.40357 -0.007698	-0.77720 0.052596	-0.67743 0.121887	-0.56867 0.021984	1.01293 -0.015961	-0.33070 1.131480	N/A [a]

[a] Zn-salen complexes do not have axial ligand
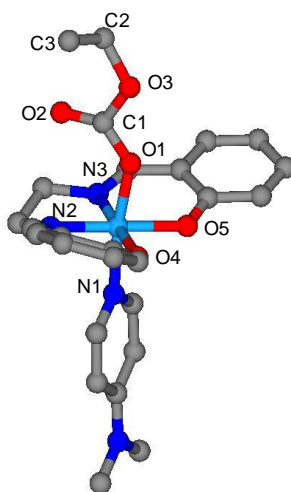
Fig. B.8. Optimized geometry for the complex **6**(M)-DMAP. The color gray is for carbon atoms, red is for oxygen, blue is for nitrogen, green is for chlorine and light blue is for the metal centers: Cr, Co, Mn, Fe and Al.

Table B.5. Structural parameters for relevant atoms in the most favorable complexes **6**(M)-DMAP as illustrated on Fig. B.8 estimated using the methods UOPBE/LANL2DZ and B3LYP/6-311g**/LANL2DZ.

6(M)-DMAP	UOPBE/LANL2DZ							B3LYP/6-311g**/LANL2DZ						
	M-O1 (Å)	M-O4 (Å)	M-O5 (Å)	M-N1 (Å)	M-N2 (Å)	M-N3 (Å)	O1-C1-O2 (°)	M-O1 (Å)	M-O4 (Å)	M-O5 (Å)	M-N1 (Å)	M-N2 (Å)	M-N3 (Å)	O1-C1-O2 (°)
Cr (m5)	1.964	1.967	1.962	2.135	1.998	2.011	129.672	1.954	1.957	1.954	2.165	2.039	2.055	128.945
Al (m2)	1.895	1.883	1.883	2.202	2.030	2.023	128.627	1.900	1.875	1.868	2.189	2.051	2.064	128.494

Table B.6. Natural charges (top) and spin densities (bottom) of CO_2 and relevant atoms in complex **6**(M)-DMAP as illustrated on Fig. B.8.

| 6(M)-DMAP	metal atom	O1	O2	O3	C1	C3	N1
Co (doublet)	0.41419	-0.54527	-0.72903	-0.56715	1.00630	-0.30284	-0.40921
	0.011229	0.000665	0.001549	0.072150	-0.007872	1.102989	0.002128
Cr (quintet)	0.65785	-0.59447	-0.72140	-0.57224	1.01874	-0.32819	-0.46192
	3.041876	-0.007575	0.020271	0.016009	0.000637	1.124713	-0.051136
Mn (doublet)	0.47117	-0.56167	-0.71817	-0.57135	1.01742	-0.33386	-0.42722
	2.168034	-0.039335	0.006185	-0.010844	0.000329	-1.128881	-0.031774
Fe (triplet)	0.34873	-0.54474	-0.72437	-0.57181	1.01363	-0.32329	-0.41490
	0.922577	-0.008921	0.017599	0.020994	-0.001526	1.118987	-0.020670
Al (doublet)	2.04762	-0.84200	-0.72267	-0.57558	1.02877	-0.33815	-0.62628
	-0.000040	0.001172	0.004328	0.009088	-0.001144	1.130508	0.000001
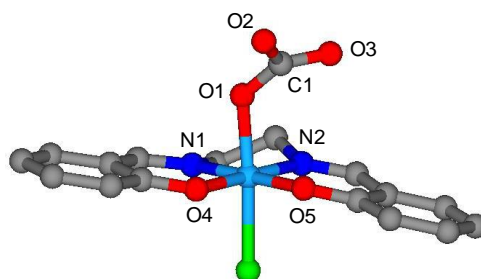
Fig. B.9. Optimized geometry for the complex **7**(M)-Cl. The color gray is for carbon atoms, red is for oxygen, blue is for nitrogen, green is for chlorine and light blue is for the metal centers: Cr, Co, Mn, Fe, Al and Zn.

Table B.7. Structural parameters for relevant atoms in the most favorable complexes **7**(M)-Cl as illustrated on Fig. B.9 estimated using the methods UOPBE/LANL2DZ and B3LYP/6-311g**/LANL2DZ.

	UOPBE/LANL2DZ							B3LYP/6-311g**/LANL2DZ						
7(M)-Cl	M-O1 (Å)	M-O4 (Å)	M-O5 (Å)	M-N1 (Å)	M-N2 (Å)	M-Cl (Å)	O1-C1-O2 (°)	M-O1 (Å)	M-O4 (Å)	M-O5 (Å)	M-N1 (Å)	M-N2 (Å)	M-Cl (Å)	O1-C1-O2 (°)
Co (m3)	1.951	1.888	1.880	1.874	1.872	2.312	116.774	1.947	1.896	1.898	1.907	1.907	2.298	120.420
Mn (m3)	1.920	1.864	1.856	1.973	1.974	2.310	117.898	1.921	1.853	1.844	1.998	1.994	2.304	119.997
Al (m3)	1.909	1.900	1.893	2.015	2.019	2.411	120.832	1.906	1.912	1.876	2.054	2.034	2.399	121.293
Zn[a] (m1)	2.016	2.071	2.063	2.166	2.147	-	122.808	2.043	2.031	2.028	2.183	2.161	-	121.024

[a] Zn-salen complexes do not have axial ligand

Table B.8. Natural charges (top) and spin densities (bottom) of carbonate and relevant atoms in complex **7**(M)-Cl as illustrated on Fig. B.9.

7(M)-Cl	metal atom	O1	O2	O3	C1	Cl
Co (triplet)	0.31720	-0.53955	-0.45460	-0.52375	0.95978	-0.26109
	0.373157	0.236241	0.437919	0.380988	-0.092101	-0.023133
Cr (quartet)	0.38626	-0.58572	-0.42867	-0.48915	0.96395	-0.25820
	2.513287	0.075413	0.543780	0.476969	-0.085124	-0.010487
Mn (triplet)	0.48719	-0.54147	-0.42228	-0.49818	0.96571	-0.21215
	2.791010	-0.150376	-0.489706	-0.404740	0.099599	-0.010604
Fe (quartet)	0.35072	-0.49073	-0.50011	-0.54657	0.95765	-0.23667
	1.707086	0.304449	0.287792	0.305321	-0.068368	0.012713
Al (triplet)	1.88816	-0.80779	-0.42822	-0.52317	0.96990	-0.50033
	-0.021873	0.119165	0.552863	0.448385	-0.092739	0.185535
Zn (singlet)	1.39916	-0.78541	-0.45092	-0.55589	0.96049	N/A [a]
	-0.005484	-0.114567	-0.531840	-0.422988	0.088058	

[a] Zn-salen complexes do not have axial ligand
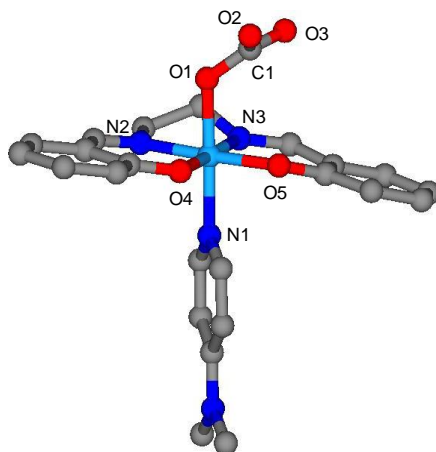
Fig. B.10. Optimized geometry for the complex **7**(M)-DMAP. The color gray is for carbon atoms, red is for oxygen, blue is for nitrogen, green is for chlorine and light blue is for the metal centers: Cr, Co, Mn, Fe and Al.

Table B.9. Structural parameters for relevant atoms in the most favorable complexes **7**(M)-DMAP as illustrated on Fig. B.10 estimated using the methods UOPBE/LANL2DZ and B3LYP/6-311g**/LANL2DZ.

7(M)-DMAP	UOPBE/LANL2DZ							B3LYP/6-311g**/LANL2DZ						
	M-O1 (Å)	M-O4 (Å)	M-O5 (Å)	M-N1 (Å)	M-N2 (Å)	M-N3 (Å)	O1-C1-O2 (°)	M-O1 (Å)	M-O4 (Å)	M-O5 (Å)	M-N1 (Å)	M-N2 (Å)	M-N3 (Å)	O1-C1-O2 (°)
Co (m2)	1.923	1.918	1.916	1.978	1.898	1.883	117.327	1.928	1.912	1.903	2.016	1.936	1.919	120.582
Cr (m3)	1.894	1.942	1.942	2.155	2.018	2.000	117.029	1.968	1.927	1.927	2.169	2.054	2.036	120.647
Mn (m4)	1.763	1.911	1.894	2.219	1.976	1.957	109.379	1.973	1.912	1.892	2.108	1.989	1.986	120.388
Al (m2)	1.924	1.879	1.880	2.182	2.025	2.023	121.101	1.926	1.870	1.865	2.172	2.049	2.061	121.473

Table B.10. Natural charges (top) and spin densities (bottom) of carbonate and relevant atoms in complex **7**(M)-DMAP as illustrated on Fig. B.10.

7(M)-DMAP	metal atom	O1	O2	O3	C1	N1
Co (doublet)	0.41806 0.060492	-0.52897 0.278869	-0.48274 0.398637	-0.53932 0.363852	0.96740 -0.093035	-0.41265 -0.006706
Cr (triplet)	0.62440 2.881893	-0.53084 -0.220547	-0.50345 -0.357312	-0.55607 -0.331944	0.97008 0.086678	-0.46460 -0.048240
Mn (quartet)	0.60974 2.626550	-0.46677 0.339056	-0.57867 0.020126	-0.66670 0.078156	0.95495 -0.012676	-0.48173 -0.028001
Fe (triplet)	0.37861 1.174862	-0.45752 0.360871	-0.53237 0.255081	-0.62394 0.194008	0.95871 -0.060890	-0.43592 -0.024693
Al (doublet)	2.04308 -0.001037	-0.80939 0.106999	-0.44675 0.536345	-0.54372 0.433041	0.97418 -0.090298	-0.63363 0.000025
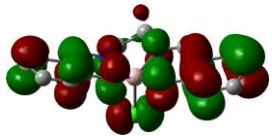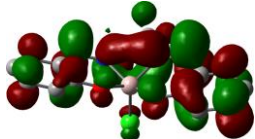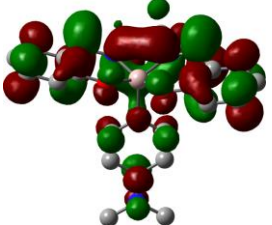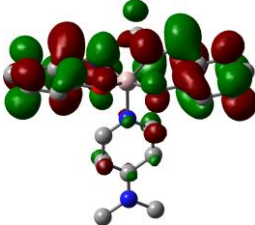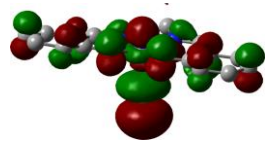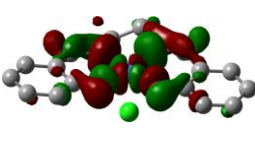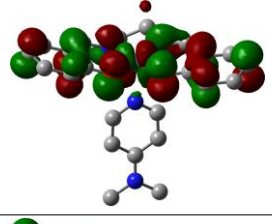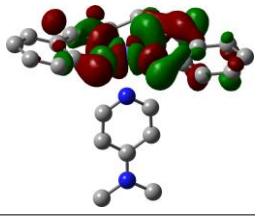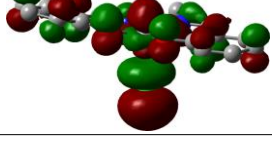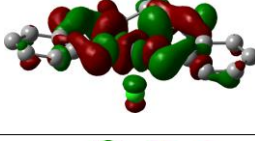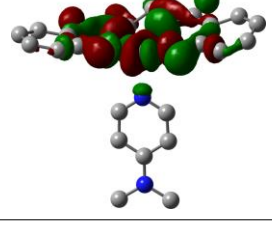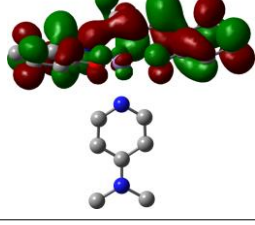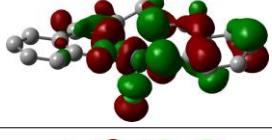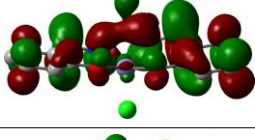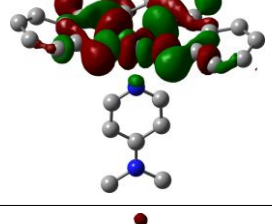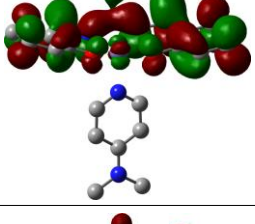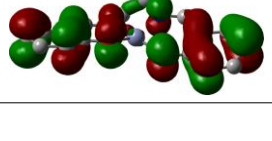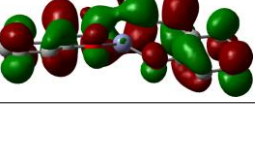
Metal-salen	HOMO	LUMO
1(Al)-Cl		
1(Al)-DMAP		
1(Co)-Cl		
1(Co)-DMAP		
1(Mn)-Cl		
1(Mn)-DMAP		
1(Fe)-Cl		
1(Fe)-DMAP		
1(Zn)		

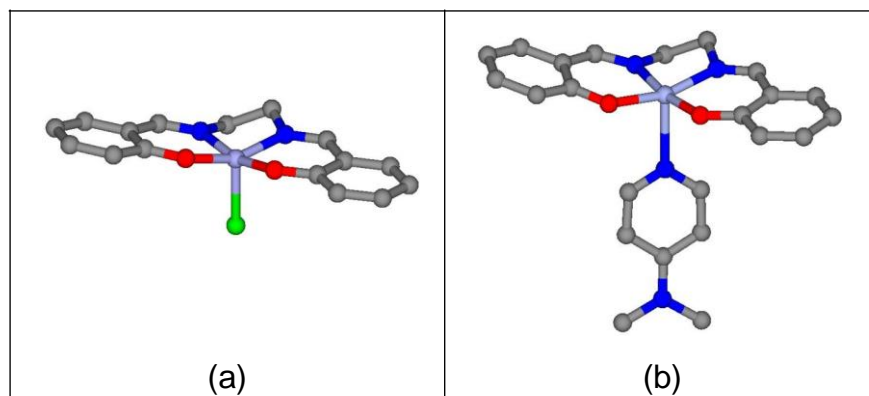**Fig. B.11.** HOMO and LUMO for the metal-salen catalysts, **1** (M)-L, illustrated in Fig. B.12.

Fig. B.12. Optimized geometries for the metal-salen catalyst, **1**(M)-L with (a) L=Cl and (b) L=DMAP. The color gray is for carbon atoms, red is for oxygen, blue is for nitrogen, green is for chlorine and gray-blue is for the metal centers: Cr, Co, Mn, Fe, Al and Zn.
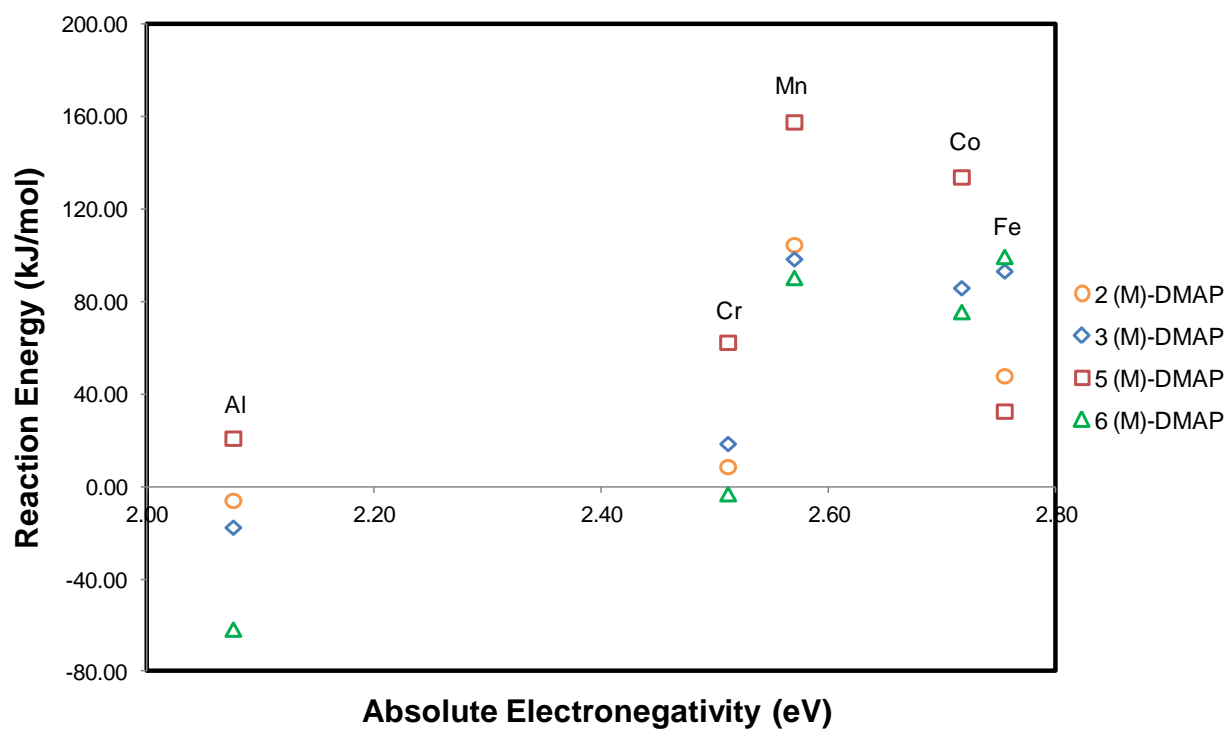

Fig. B.13. Reaction energy to produce **2**(M)-DMAP, **3**(M)-DMAP, **5**(M)-DMAP and **6**(M)-DMAP as a function of the absolute electronegativity of the catalysts, **1**(M)-DMAP.
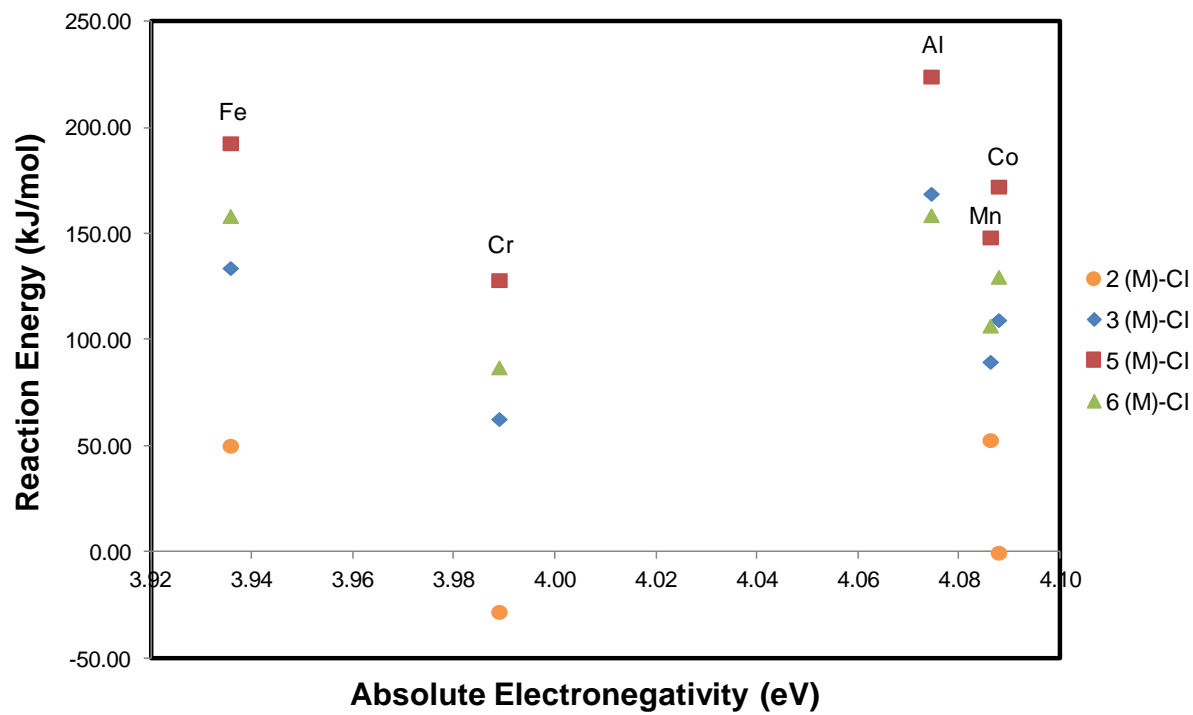
Fig. B.14. Reaction energy to produce **2**(M)-Cl, **3**(M)-Cl, **5**(M)-Cl and **6**(M)-Cl as a function of the absolute electronegativity of the catalysts, **1**(M)-Cl.

Table B.11. NBO analysis of the complexes **1**(M)-Cl and **1**(M)-DMAP and changes in the atomic charges upon the bonding of the epoxide with **1**(M)-L.

	Cr	Al	Co	Mn	Fe	Zn[a]
Sum of partial atomic charges of epoxide bonded to the metal in 2(M)-Cl complex	0.174	-	0.195	0.176	0.179	0.061
Atomic charge of the metal in 1(M)-Cl complex	0.642	1.847	0.581	0.867	1.042	1.428
Atomic charge of the metal in 2 (M)-Cl complex	0.522	-	0.320	0.392	0.279	1.417
Change of partial atomic charge of the metal in (M)-Cl complexes upon bonding of epoxide	-0.120	-	-0.261	-0.475	-0.763	-0.011
Change of partial atomic charge of Cl in salen complexes upon bonding of epoxide	-0.001	-	0.186	0.235	0.170	-
Sum of partial atomic charges of epoxide bonded to the metal in 2(M)-DMAP complex	0.168	0.068	-	0.164	0.182	
Atomic charge of the metal in 1(M)-DMAP complex	0.891	2.029	0.606	1.221	1.092	
Atomic charge of the metal in 2(M)-DMAP complex	0.524	2.080	-	0.370	0.219	
Change of partial atomic charge of the metal in (M)-DMAP complexes upon bonding of epoxide	-0.367	0.051	-	-0.851	-0.873	
Change of partial atomic charge of DMAP in salen complexes upon bonding of epoxide	0.251	0.038	-	0.171	0.210	

[a] Zn-salen complexes do not have axial ligand

Table B.12. Comparison between the reaction enthalpies for the reaction of CO_2 and ethylene oxide to ethylene carbonate in gas phase estimated with UOPBE/LANL2DZ, UOPBE/6-311g**, B3LYP/6-311g** and some methods implemented by Darensbourg and Yeung (reference [37] in Chapter 2) together with their deviations from the critically evaluated thermodynamic data published by the National Institute of Standards and Technology (NIST).

Method	ΔHrxn (kJ/mol)	ΔHrxn (kcal/mol)	Deviation from NIST (kcal/mol)
NIST [a]		-15.2	
UOPBE/LANL2DZ	-59.7	-14.3	0.9
UOPBE/6-311g**	-26.1	-6.2	9.0
B3LYP/6-311g**	-48.1	-11.5	3.7
B3LYP/6-311g (2df,p) [a]		-11.9	3.2
MP2/6-311g (3d2f,p) [a]		-12.8	2.4
CCSD/6-311g (3d2f,p) [a]		-16.7	-1.5
CBS-4M [a]		-15.1	0.1

[a] Means that these data were extracted from the reference [37] in Chapter 2.